Improving the Monitoring, Verification, and Accounting of CO_2 Sequestered in Geologic Systems with Multicomponent Seismic Technology and Rock Physics Modeling

Final Report

DOE Award Number: DE-FE0001317

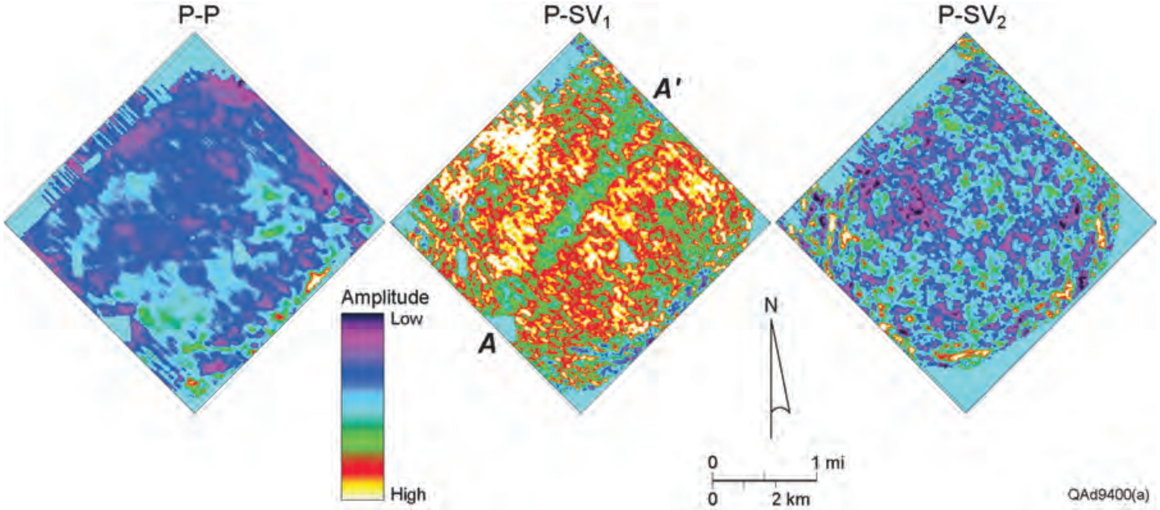

December 2012

Principal Investigator: Bob A. Hardage

Submitted by: Bureau of Economic Geology
The University of Texas at Austin

Subcontractor: Battelle Pacific Northwest Division

Research Team: Engin Alkan, Michael DeAngelo, Bob Hardage,
Diana Sava, Charlotte Sullivan, and Donald Wagner

Abstract

Research done in this study showed that P-SV seismic data provide better spatial resolution of geologic targets at our Appalachian Basin study area than do P-P data. This finding is important because the latter data (P-P) are the principal seismic data used to evaluate rock systems considered for CO_2 sequestration. The increase in P-SV_1 resolution over P-P resolution was particularly significant, with P-SV_1 wavelengths being approximately 40-percent shorter than P-P wavelengths. CO_2 sequestration projects across the Appalachian Basin should take advantage of the increased resolution provided by converted-shear seismic modes relative to P-wave seismic data.

In addition to S-wave data providing better resolution of geologic targets, we found S-wave images described reservoir heterogeneities that P-P data could not see. Specifically, a channel-like anomaly was imaged in a key porous sandstone interval by P-SV_1 data, and no indication of the feature existed in P-P data. If any stratigraphic unit is considered for CO_2 storage purposes, it is important to know all heterogeneities internal to the unit to understand reservoir compartmentalization. We conclude it is essential that multicomponent seismic data be used to evaluate all potential reservoir targets whenever a CO_2 storage effort is considered, particularly when sequestration efforts are initiated in the Appalachian Basin.

Significant differences were observed between P-wave sequences and S-wave sequences in data windows corresponding to the Oriskany Sandstone, a popular unit considered for CO_2 sequestration. This example demonstrates that S-wave sequences and facies often differ from P-wave sequences and facies and is a principle we have observed in every multicomponent seismic interpretation our research laboratory has done. As a result, we now emphasis elastic wavefield seismic stratigraphy in our reservoir characterization studies, which is a science based on the concept that the same weight must be given to S-wave sequences and facies as is given to P-wave sequences and facies. This philosophy differs from the standard practice of depending on only conventional P-wave seismic stratigraphy to characterize reservoir units.

The fundamental physics of elastic wavefield seismic stratigraphy is that S-wave modes sense different sequences and facies across some intervals than does a P-wave mode because S-wave displacement vectors are orthogonal to P-wave displacement vectors and thus react to a different rock fabric than do P waves. Although P and S images are different, both images can still be correct in terms of the rock fabric information they reveal.

Disclaimer

Table of Contents

Comparison of Goals and Actual Accomplishments

Summary of Project Activities

Technology Transfer and Products Developed

List of Figures

Tables

Executive Summary

The 3C3D seismic data used in this study provided the most dramatic contrast between P-wave and S-wave imaging of geologic targets that our research teams has observed in the 12 years our laboratory has been engaged in multicomponent seismic interpretation. The impressive aspect of these data was that both the P-SV_1 (fast-S) seismic mode and P-SV_2 (slow-S) seismic mode provided better spatial resolution of key geologic targets than did P-P (compressional) seismic data. Comparisons of P-P and P-SV seismic resolution are shown in Chapter 9.

The finding that P-SV seismic data provide better spatial resolution of geologic targets than do P-P data is important because the latter data (P-P) are the principal seismic data used to evaluate reservoir systems considered for CO_2 sequestration. The increase in P-SV_1 resolution over P-P resolution was particularly significant, with P-SV_1 wavelengths being approximately 40-percent shorter than P-P wavelengths. Research findings discussed in Chapter 9 should be considered by all CO_2 sequestration projects, but particularly for projects across the Appalachian Basin, so seismic interpreters can take advantage of the increased resolution provided by converted-shear seismic modes relative to P-wave seismic data.

In addition to S-wave data providing better resolution of geologic targets, we found S-wave images described reservoir heterogeneities that P-P data could not see. Specifically, a channel-like feature was imaged in the Tully-to-Tichenor interval by P-SV_1 data, and no indication of the feature existed in P-P data. This research finding is documented in Chapter 9 also.

The increased geologic information and insight provided by converted-S seismic data is important because the Middle Devonian stratigraphic interval illustrated in Chapter 9 contains attractive sandstones that can be utilized as reservoirs for CO_2 sequestration. If any stratigraphic unit is considered for CO_2 storage purposes, it is essential to know all heterogeneities internal to the unit to understand reservoir compartmentalization. We conclude it is essential that multicomponent seismic data be used to evaluate all potential reservoir targets whenever a CO_2 storage effort is considered, particularly when sequestration efforts are initiated in the Appalachian Basin.

Significant differences were observed between P-wave sequences and S-wave sequences in data windows corresponding to the Oriskany Sandstone, a popular unit considered for CO_2 sequestration. Unfortunately, no deep-well data existed local to our study site that allowed P and S reflectivities to be calculated for the Oriskany and its bounding rock units. Consequently, the observed distinctions between these P sequences and S sequences cannot be associated with specific petrophysical properties.

This Oriskany Sandstone example that shows that S-wave sequences/facies differ from P-wave sequences/facies is a principle that has been observed in every multicomponent seismic interpretation our research laboratory has done. As a result, we now emphasis elastic wavefield seismic stratigraphy in our reservoir characterization studies, which is a science based on the concept that the same weight must be given to S-wave sequences/facies as is given to P-wave sequences/facies. This philosophy differs from the standard practice of depending on only conventional P-wave seismic stratigraphy to characterize reservoir units. We emphasize that in this study, as in all other studies we have done, S-wave seismic sequences and facies differ from P-wave sequences and facies only in some stratigraphic intervals, not throughout the entirety of a stratigraphic section.

The fundamental physics of elastic wavefield seismic stratigraphy is that S-wave modes sense different sequences and facies across an interval than does a P-wave mode because S-wave displacement vectors are orthogonal to P-wave displacement vectors and thus react to different rock fabric than do P waves. Although P and S images are different, both images can still be correct. Each seismic mode provides a distinct insight into reservoir compartmentalization because each mode often senses a different rock fabric than does its companion wave modes.

Comparison of Goals and Actual Accomplishments

Chapter 1

Objectives of Study and Summary of Research Findings

Introduction

The overarching objective of this study was to demonstrate multicomponent seismic technology has greater value than conventional, single-component P-wave seismic technology for evaluating porous rock units where CO_2 can be injected for long-term storage. Our study considered porous brine-filled sandstones and carbonates in an area of the Appalachian Basin in northeastern Pennsylvania. Concepts and principles documented in this study can be used in areas other than the Appalachian Basin and can be applied to rock facies other than those present at our research site.

To achieve the broad objective of establishing the value of multicomponent seismic technology in CO_2 sequestration, several secondary objectives were embedded in our research tasks. The purposes of these secondary objectives were to compile information and evidence describing the physics of compressional (P) and shear (S) wave propagation in Earth layering associated with CO_2 storage reservoirs. Among these secondary goals were seismic field tests that established: (1) cable-free seismic data-acquisition systems provide 3-component (3C) seismic data having quality equal to that of data acquired with conventional cable-based seismic recording systems, (2) data acquired with a cable-based recording system have signal spectra extending to frequencies approximately 10-percent higher than signal spectra of data acquired with cable-free systems, and (3) 3C geophones and 3C accelerometers provide equivalent-quality multicomponent seismic data, but accelerometers enhance low-frequency components of P and S wave modes slightly better than do typical 10-Hz geophones. Enhanced lower frequencies can be important for some seismic applications.

Seismic test data were also acquired to compare attributes of P and S wave modes produced by explosive, accelerated-weight impact, and vibratory energy sources and to document the relative merits of these seismic sources for illuminating CO_2 reservoir targets and their associated stratigraphic and structural seals. These tests contributed to an important principle documented in this study; that being that full-elastic wavefield data can be acquire with vertical-force seismic sources. This research finding eliminates the need to use both vertical-force and horizontal-force seismic sources to produce full-elastic wavefield data for many seismic applications and simplifies multicomponent seismic data acquisition.

The most common seismic source used to study subsurface geology is a vertical-force source such as a vertical vibrator, a vertical impact, or a shot-hole explosive. When 3C seismic data are acquired with a vertical-force source, traditionally the only S-wave information that is utilized is the upgoing converted-SV mode (P-SV mode) created when a downgoing P wave arrives at rock interfaces at incident angles different than zero (normal incidence) and creates upgoing SV reflection events. One focus of our research was to demonstrate that valuable S-wave modes are produced directly at the point where a vertical-force source applies its force vector to the Earth, which allows S-wave modes other than P-SV data to be utilized in CO_2 sequestration studies. The recognition and use of these direct-S modes introduce new seismic imaging options into CO_2 sequestration projects and provide expanded suites of seismic attributes that can be used to infer rock and fluid properties across CO_2 reservoir systems.

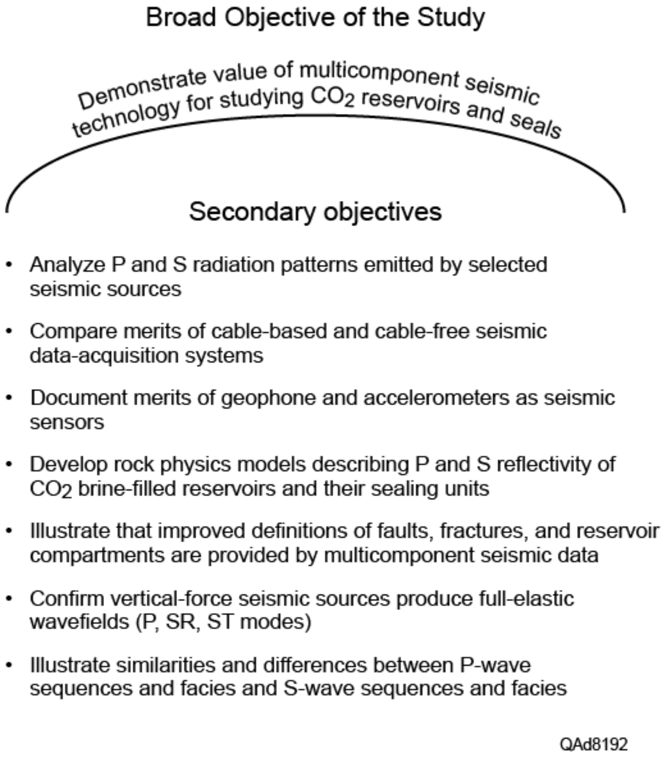

Broad Objective of the Study

Demonstrate value of multicomponent seismic technology for studying CO_2 reservoirs and seals

Secondary objectives

- Analyze P and S radiation patterns emitted by selected seismic sources
- Compare merits of cable-based and cable-free seismic data-acquisition systems
- Document merits of geophone and accelerometers as seismic sensors
- Develop rock physics models describing P and S reflectivity of CO_2 brine-filled reservoirs and their sealing units
- Illustrate that improved definitions of faults, fractures, and reservoir compartments are provided by multicomponent seismic data
- Confirm vertical-force seismic sources produce full-elastic wavefields (P, SR, ST modes)
- Illustrate similarities and differences between P-wave sequences and facies and S-wave sequences and facies

Figure 1.1. Objectives of study. Numerous secondary objectives were implemented to achieve the basic, overarching objective of demonstrating the value of multicomponent seismic technology for characterizing CO_2 reservoirs and seals.

Broad Objective: Demonstrate Value of Multicomponent Seismic Technology for Evaluating CO_2 Reservoir Systems

The fundamental objective of this study was to demonstrate the value of multicomponent seismic technology in CO_2 sequestration projects. The approach to achieving this objective was to subdivide this general objective into a series of smaller, secondary objectives that collectively allowed a rigorous documentation of the basic principles that need to be demonstrated. This research strategy is illustrated by the graphic exhibited as Figure 1.1.

Objective 1: Measure P and S Radiation Patterns Emitted by Selected Seismic Sources

The most common type of energy source used to acquire exploration seismic data is a source that applies a vertical force vector to the Earth. Examples of such sources are vertical vibrators, vertical-impact weights, and shot-hole explosives. For decades, geophysicists have considered vertical-force sources to be only P-wave sources. One objective of this research was to demonstrate that full elastic wavefields, consisting of a P-wave mode, a radial-S mode, and a transverse-S mode, are produced by vertical-force sources. The implication of this principle is significant because, when proven to be true, it is no longer necessary to use horizontal-force sources (either horizontal vibrators or inclined-impact sources) to generate S-wave modes directly at a source station. Instead, simpler and more common vertical-force sources can be used to produce S waves directly at source stations, in addition to producing converted-SV waves at interfaces remote from a source station.

Vertical-force sources can be classified into three categories—vertical vibrators, vertical impacts, and shot-hole explosives. Test data were collected at the Devine Test Site operated by the Bureau of Economic Geology to evaluate each of these source types. Sources that were tested were:

- Vertical vibrator: An Input/Output Model AHV IV PLS 362 with a hold-down weight of 60,000 lb (27,733 kg).

- Explosive: One kilogram (2.2 lbs) of pentolite placed at a depth of 6 m (20 ft).

- Vertical impact: A VSX source manufactured by United Services Alliance—a 33,000-lb vehicle with a 1000-psi nitrogen-spring weight acceleration system that delivers impact energy of 22,276 ft-lb (30,202 joules) to its base plate.

The fundamental physics documented by these seismic-source tests was:

Research Finding 1

Vertical-force seismic sources produce full elastic wavefields having robust compressional (P), radial-shear (SR), and transverse-shear (ST) modes.

A conclusion reached in this study is that these full elastic wavefields are created directly at the point where each source applies its vertical force vector to the Earth. The data and methodology used to achieve this objective and to produce this research finding are described in Chapter 6.

This research finding adds additional confirmation to previous conclusions reached by our research laboratory, this being that full elastic wavefields can be acquired with simple vertical-force sources. The fact that three, independent, and orthogonal force vectors (vertical, inline horizontal, crossline horizontal) do not have to be applied at a source station to produce full elastic wavefields can have significant impact on lowering the cost of acquiring multicomponent seismic data.

Objective 2: Compare Merits of Cable-Based and Cable-Free Seismic Data-Recording Systems

Three seismic recording systems were used to collect multicomponent seismic test data at our Devine Test Site. One system was the popular Sercel 428 used by many seismic crews around the world. A Sercel 428 is a cable-based system, meaning data outputs from sensors deployed across a seismic prospect are transmitted to a central recorder and data storage unit by a series of interconnecting cables. If there are several thousand sensor stations distributed across a sizeable area, there is only one data recorder and one data storage unit, but there are many kilometers of interconnecting cable that interface this central recorder/storage system to all sensor stations distributed across the area.

The other two recording systems involved in the field tests were cable-free systems. Cable-free seismic data acquisition is a relatively new technology, with the first prototypes introduced in the late 1990s. As is the case with many technologies, the reliability and versatility of cable-free equipment has increased on an annual basis, and today, cable-free systems appear to be fully competitive with standard cable-based systems. The attraction of cable-free seismic data acquisition is that by avoiding spread cables, a seismic contractor eliminates a huge amount of equipment (hundreds of kilometers of cable, hundreds of thousands of kilograms of weight, and several millions of dollars of capital investment), reduces the number of equipment-transport trucks, avoids expensive daily cable repair, and operates with fewer field personnel. Cable-free data-acquisition systems thus have economic appeal to seismic contractors. However, skeptics still demand proof that cable-free systems provide seismic data of the same quality provided by cable-based systems that have been used for decades. This attitude is what caused the objective of comparing 3C seismic data acquired with cable-based and cable-free systems to be incorporated into this study.

In cable-free data acquisition, a small data-recording and data-storage box is connected directly to the sensors at each receiver station. Data outputs from the sensors at a particular station are recorded only by the box deployed at that station. If there are several thousand 3C receiver stations across a sizeable area, there is an equivalent (or larger) number of data recorders and data-storage boxes (one 3-channel box, or three 1-channel boxes at each 3C station). The only cable required at each receiver station is a short cable of less than a meter that connects the data-recorder box to the geophone string. There are no interconnecting spread cables; there is no central data recorder or central data storage unit. Instead at appropriate clock/calendar times, a replacement box is deployed at each receiver station while the boxes that were active at those stations are transported to a local field office where data are downloaded onto the same digital media used by cable-based data acquisition systems.

The two cable-free systems utilized in our field tests were EUnite boxes provided by Sercel, and Sigma boxes provided by Seismic Source and iSeis. Photos of these cable-free boxes can be seen on Figure 6.4 of Chapter 6. Data acquired with the Sercel 428 cable-based system and with EUnite and Sigma cable-free systems are displayed and discussed throughout Chapter 6. The principal research finding developed from analyzing these data was:

Research Finding 2

There are negligible differences in the quality of multicomponent seismic data acquired with cable-free data-acquisition systems and data acquired with cable-based data-acquisition systems. Cable-based data had slightly broader signal spectra than did cable-free data in our tests.

This research finding is important in CO_2 sequestration programs because cable-free systems allow seismic data to be acquired in areas of high culture (houses, streets, roads, industrial plants, and so forth) more easily than can be done with cable-based systems. CO_2 sequestration projects are often located in close proximity to high levels of human activity. Cable-free seismic data acquisition will thus be important for studying CO_2 reservoirs and seals across urban, industrial, and heavy-use properties.

Objective 3: Compare Merits of Geophone and Accelerometer Sensors

The standard sensor used to acquire seismic data for evaluating CO_2 sequestration reservoirs is the moving-coil geophone that has been used by seismic contractors for more than 70 years. In the decade of the 1990s, solid state accelerometers called MEMS (micro-electronic mechanical systems) were introduced as seismic sensors. Today both sensor types—geophones and accelerometers—are used to acquire multicomponent seismic data. Several companies and groups have done tests to compare P and S seismic data acquired with these two sensor types. Most of these tests are proprietary to the companies that did the tests. Publicly available comparisons of data recorded by geophones and accelerometers are limited. Thus an objective integrated into this research was to collect test data that allowed similarities and differences between geophone data and accelerometer data to be provided to the CO_2 sequestration community. These data should allow better informed decisions to be made when setting parameters and equipment standards for seismic data acquisition across CO_2 sequestration areas.

The 3C geophones deployed for testing at the Devine Test Site were Oyo Geospace Model 20DX, which had 10-Hz resonance suspension springs in their vertical and horizontal moving-coil elements. The 3C accelerometers were Sercel DSU3 MEMS. Surface spreads of these sensors used to collect test data are shown on the photographs displayed as Figure 6.4 of Chapter 6. Although other types of geophones with suspension springs having different resonances could have been utilized, the data collected in our field test with these 10-Hz geophones will be used to make generalized statements about attributes of P and S data acquired with geophones and accelerometers. Specifically, the research finding resulting from analyzing geophone and accelerometer data was:

Research Finding 3

Accelerometers provide better low-frequency data (frequencies less than 8 Hz) than do geophones. Otherwise geophone data and accelerometer data are equivalent.

This research finding can be important for acquiring optimal-quality S-wave data because S-modes tend to be lower frequency than P-wave data. When S waves are critical to evaluating a CO_2 sequestration system, serious consideration should be given to using accelerometers for seismic data acquisition. Geophone manufacturers counter with the argument that the frequency roll-off exhibited by geophones below their natural spring resonance can be removed during data processing because the amplitude and phase character of each type of geophone is documented by careful laboratory measurements for frequencies less than resonant frequency. This argument has merit, but in practice few geophysicists apply such numerical adjustments to geophone data. Geophone and accelerometer test data are displayed and discussed in Chapter 6.

Objective 4: Develop Rock Physics Models Describing P and S Reflectivities

The log data, physical principles, and analysis procedures used to develop rock physics models for CO_2 sequestration reservoirs are discussed in Chapter 5. Regarding rock units considered for CO_2 storage reservoirs, we found porosities of 12 to 16 percent existed in most brine-filled rock units across our study area in northeast Pennsylvania. These porosity magnitudes are sufficient for these units to accept significant volumes of injected CO_2 and lead to the following conclusion:

Research Finding 4

From the viewpoint of in situ porosity only, there are sandstone units in the northeast portion of the Appalachian Basin that can be used for CO_2 sequestration. Our seismic-based study did not consider the viability of these porous units from the viewpoint of whether they posses adequate permeability for efficient injection of large volumes of CO_2.

Objective 5: Illustrate Increased Reservoir Information Provided by Multicomponent Seismic Data

The type, quality, and amount of geological information embedded in multicomponent seismic data is compared to the information content of single-component P-wave data in Chapter 9. Comments here will be limited to observations related to stratigraphic resolution and to detecting and characterizing faults. Additional comments related to seismic sequence and seismic facies are provided in the discussion of Objective 7. As documented in Chapter 9, we found the following advantage of multicomponent seismic technology which will be invaluable in evaluating CO_2 reservoir systems.

Research Finding 5

Converted-shear (P-SV) seismic data provided better vertical resolution of strata related to CO_2 sequestration systems and also detected and resolved fractures and faults better than did P-wave seismic data.

In addition to these findings, the combination of fast-S and slow-S seismic modes estimated approximately the same magnitude of S-wave anisotropy as did local dipole sonic-log data. Thus multicomponent seismic technology allows fracture densities inside targeted rock units to be estimated and fractured reservoir-sealing units to be detected across broad areas where CO_2 reservoir systems are located. To date, single-component P-wave seismic data do not provide reliable fracture-detection capability unless data are acquired with extremely long offsets that are sufficient to allow S-wave properties to be inferred by amplitude-vs-angle reflectivity behavior.

Objective 6: Confirm Vertical-Force Sources Produce Full Elastic Wavefields

Multicomponent wave modes propagating away from a source station can be best evaluated if they are captured by a vertical array of downhole receivers. Such data define the properties of all downgoing source-generated wavefields that illuminate geologic targets. Analyzing vertical-array data allows all P and S modes embedded in illuminating wavefields to be identified and quantified. Because of this insight, analyzing vertical-array data is the preferred way to evaluate seismic source performance and was the method used in this study. Analysis of vertical-array data acquired at the Devine Test Site showed:

Research Finding 6

Each tested vertical-force source generated radial-shear and transverse-shear modes directly at each source station in addition to the expected compressional-wave mode. The energy content and data quality of these S modes equaled or exceeded those of the P mode.

This research finding was further verified by recording reflected wavefields with horizontal arrays of 3C geophones and extracting P and S reflection events from single-fold data having low signal-to-noise ratios. These data processing results are illustrated and discussed in Chapter 6. In terms of fundamental seismic wavefield physics and the impact of these principles on future seismic data-acquisition projects, this research finding is one of the more important research results achieved in this study.

Objective 7: Use Multicomponent Seismic Data to Evaluate Potential CO_2 Sequestration Reservoirs

Seismic data interpretation examples used to achieve this objective are discussed in Chapter 9. Interpretation results summarized here relate to seismic sequences and seismic facies observed in poststack P and S image volumes.

Research Finding 7

S-wave data revealed intra-reservoir compartmentalization features in an interval dominated by transgressive Middle Devonian sandstone that could not be seen with P-wave data.

Detecting intra-reservoir depositional features such as we document in Chapter 9 is critical for describing the internal architecture of potential CO_2 sequestration reservoirs. The implications of this finding are significant. Such features can be either an enhancement or an impediment to fluid flow, depending on the lithological nature of the fill material of each intra-reservoir anomaly. If only P-wave data were used to evaluate our prospect area, the existence of these internal reservoir-compartment features would not be suspected. With the inclusion of S-wave data into the interpretation, the presence of these features is known, and a different thought process has to be implemented as to the fluid-flow behavior that could be expected within Middle Devonian sandstone units targeted for CO_2 sequestration local to our study area.

Conclusions

A broad spectrum of secondary research objectives was implemented to achieve our principle research objective of demonstrating the value of multicomponent seismic technology for studying CO_2 sequestration reservoirs and seals. Important research findings were documented as each secondary objective was accomplished. The cumulative effect of these research findings is presented as definitive proof that multicomponent seismic data provide more information about geological sequences and facies, and allow better estimation of rock and fluid properties, than do single-component P-wave seismic data. These research findings need to be distributed among companies and individuals engaged in CO_2 sequestration projects so the advantages of multicomponent seismic technology are considered in future evaluations of CO_2 sequestration reservoir systems.

As a general observation, the research accomplishments achieved in this study equaled or exceeded the goals that were established at the start of the project.

Summary of Project Activities

Chapter 2

Study Site

Introduction

The fundamental objective of this research was to demonstrate the value of multicomponent seismic technology for evaluating CO_2 sequestration systems. In concept, sequestration reservoirs can be any porous, brine-filled rock unit deeper than 3000 ft (914 m), and reservoir seals can be a variety of impermeable rock layering above a sequestration interval. A burial depth of 3000 ft (914 m) is required to ensure pore pressure is sufficient to keep injected CO_2 in a super-critical state. Such rock conditions are widespread across all basins. From a geological perspective, we had considerable leeway in selecting a study site for this project.

An early decision was that the study should focus on porous, brine-filled sandstones and carbonates across the Appalachian Basin. The most constraining criterion for selecting a research study site within the basin was the availability of appropriate multicomponent seismic data. More interest has risen in acquiring multicomponent seismic surveys the past several years as companies have begun to appreciate that S-wave modes are more valuable than P-wave data for evaluating fracture systems embedded in fractured-rock units. Because of industry interest in using multicomponent seismic data to evaluate fractured shale units, we were able to combine attractive CO_2 sequestration geology with modern multicomponent seismic data in the Marcellus Shale trend of northeast Pennsylvania. The result was an excellent study site located in Bradford County, Pennsylvania.

Selection Criteria

The rock facies targeted for CO_2 sequestration can be porous, brine-filled sandstones or carbonates, and possibly even fractured shales. Intervals selected for CO_2 sequestration must be deeper than 3000 ft (914 m) so CO_2 remains in a super-critical phase after injection. The selection of our study site was largely dictated by whether one or more porous, brine-filled rock facies acceptable for CO_2 sequestration, together with one or more impermeable sealing units above these potential sequestration targets, were present across an area of interest. Once general geographical boundaries were defined that encompassed these necessary geological conditions, locations for specific study sites were then dictated by where essential research data, particularly 3D multicomponent seismic data and high-quality subsurface calibration data, were located within the designated area.

The end result of this site-search strategy led us to the Appalachian Basin where deep, porous, brine-filled sandstones span broad areas and several stratigraphic intervals with near-zero permeability are positioned above these potential CO_2 reservoir targets to serve as sealing units. For example, the distribution of the Potsdam Sandstone, a proposed CO_2 sequestration target across the Midwest Regional Carbon Sequestration Partnership (MRCSP) area, is illustrated on Figure 2.1. This map was taken from the *2008 Carbon Sequestration Atlas of the United States and Canada* (U.S. DOE, 2008).The map does not show anticipated distributions of the Tuscarora and Oriskany Sandstones, which are additional candidates for CO_2 sequestration in the northeastern portion of the Appalachian Basin where our study site is located. The potential CO_2 storage capacities of sandstones across the MRCSP region are tabulated on Figure 2.2. Additional possibilities for sequestration reservoirs not listed on this figure are discussed in Chapter 3 (Geological Analysis).

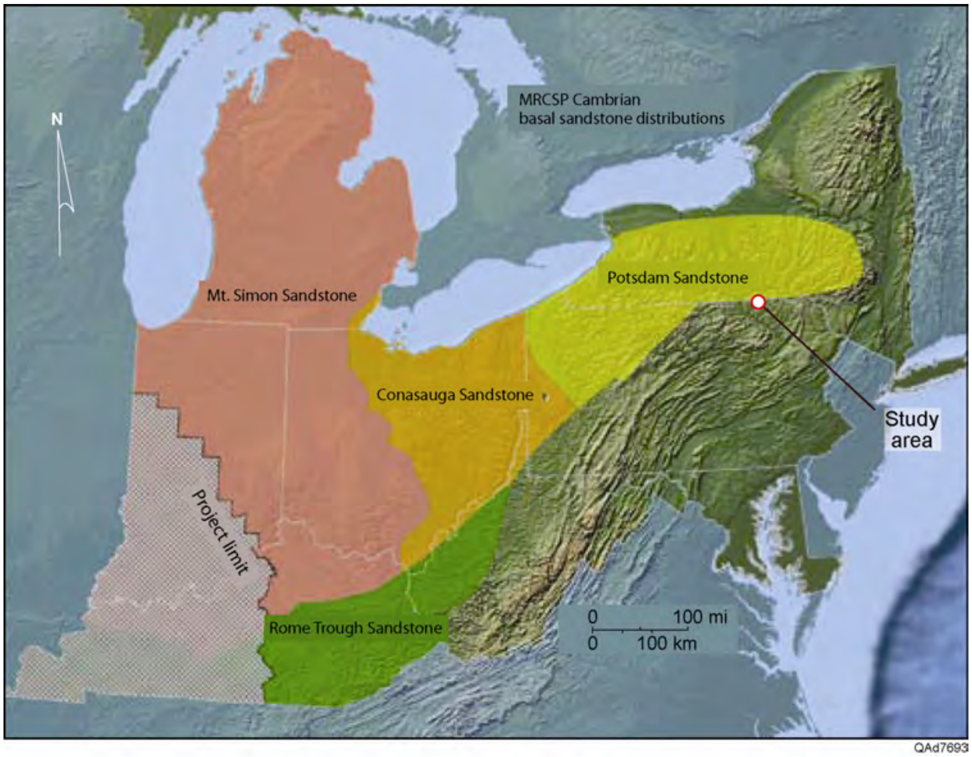

Figure 2.1. Generalized map showing distributions of Cambrian basal sandstones across the Midwest Regional Carbon Sequestration Partnership (MRCSP) area. The position labeled “Study area” identifies the location of the 3C3D seismic data that will be used in this study. Map is taken from the DOE 2008 Carbon Sequestration Atlas of the United States and Canada (U.S. DOE, 2008).

The location of our study site is labeled on Figure 2.1. The position of the site was dictated by the availability of 3D multicomponent seismic data needed for the study. This generalized map implies the Potsdam Sandstone terminates near our study site. However, the orogenic movement that formed the

Appalachian Basin caused the basin to deepen and abruptly terminate along a trend that approximately follows the southern edge of the Potsdam Sandstone distribution drawn on this map. This asymmetrical basin geometry causes brine-filled sandstone reservoir targets such as the Potsdam, Tuscarora, and Oriskany (Fig. 2.3) to be relatively deep local to our study site, which is an attractive feature that ensures CO_2 injected into these units will remain in a super-critical phase after injection. In addition, basin deepening should cause some sequestration targets to thicken across the area of our study site, which is a second attractive geological feature local to our study location. As will be shown in Chapter 3, our study site is also on the edge of the Rome Trough, the last CO_2 sequestration target listed on Figure 2.2. This proximity to the Rome Trough is a third attraction of our study area as an excellent location for evaluating possible CO_2 sequestration reservoirs.

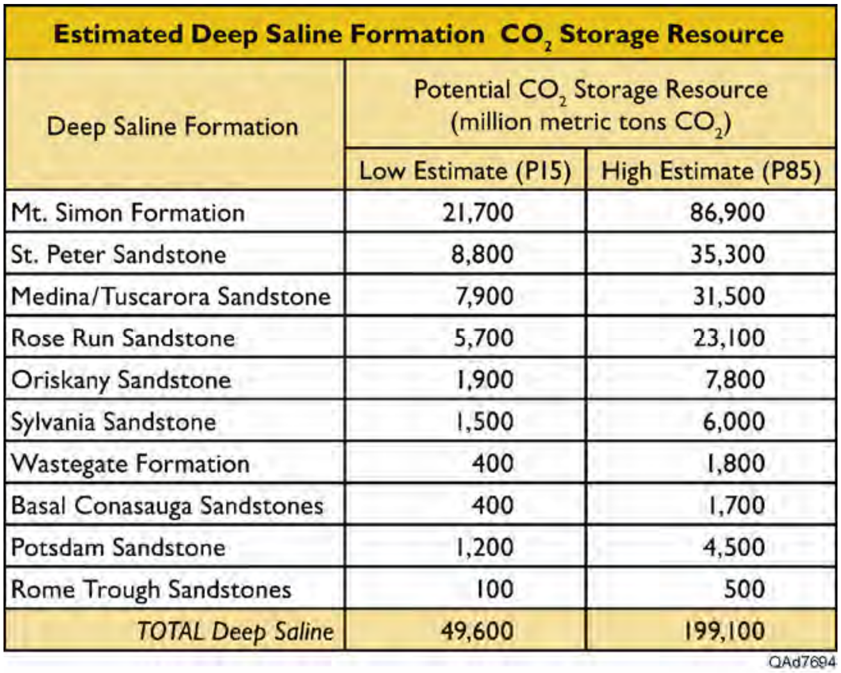

Estimated Deep Saline Formation CO_2 Storage Resource

Deep Saline Formation	Potential CO_2 Storage Resource (million metric tons CO_2)	
	Low Estimate (P15)	High Estimate (P85)
Mt. Simon Formation	21,700	86,900
St. Peter Sandstone	8,800	35,300
Medina/Tuscarora Sandstone	7,900	31,500
Rose Run Sandstone	5,700	23,100
Oriskany Sandstone	1,900	7,800
Sylvania Sandstone	1,500	6,000
Wastegate Formation	400	1,800
Basal Conasauga Sandstones	400	1,700
Potsdam Sandstone	1,200	4,500
Rome Trough Sandstones	100	500
TOTAL Deep Saline	49,600	199,100

Figure 2.2. Estimated CO_2 storage capacities of deep saline formations that could transgress across our study area. Data are reproduced from the DOE 2008 Carbon Sequestration Atlas of the United States and Canada (U.S. DOE, 2008).

A generalized stratigraphic column of the northeast Appalachian Basin is displayed on Figure 2.3 to indicate the relative stratigraphic positions of potential sandstone CO_2 sequestration targets local to our study site. A fifth sandstone sequestration target, the Catskill Sandstone, identified on this stratigraphic column may exist beneath the study site, which broadens the research opportunity and increases the value of the multicomponent seismic survey identified on Figure 2.1 as a research database. The absence of deep well data local to our study site does not allow the presence of deeper CO_2 reservoir targets to be known with confidence.

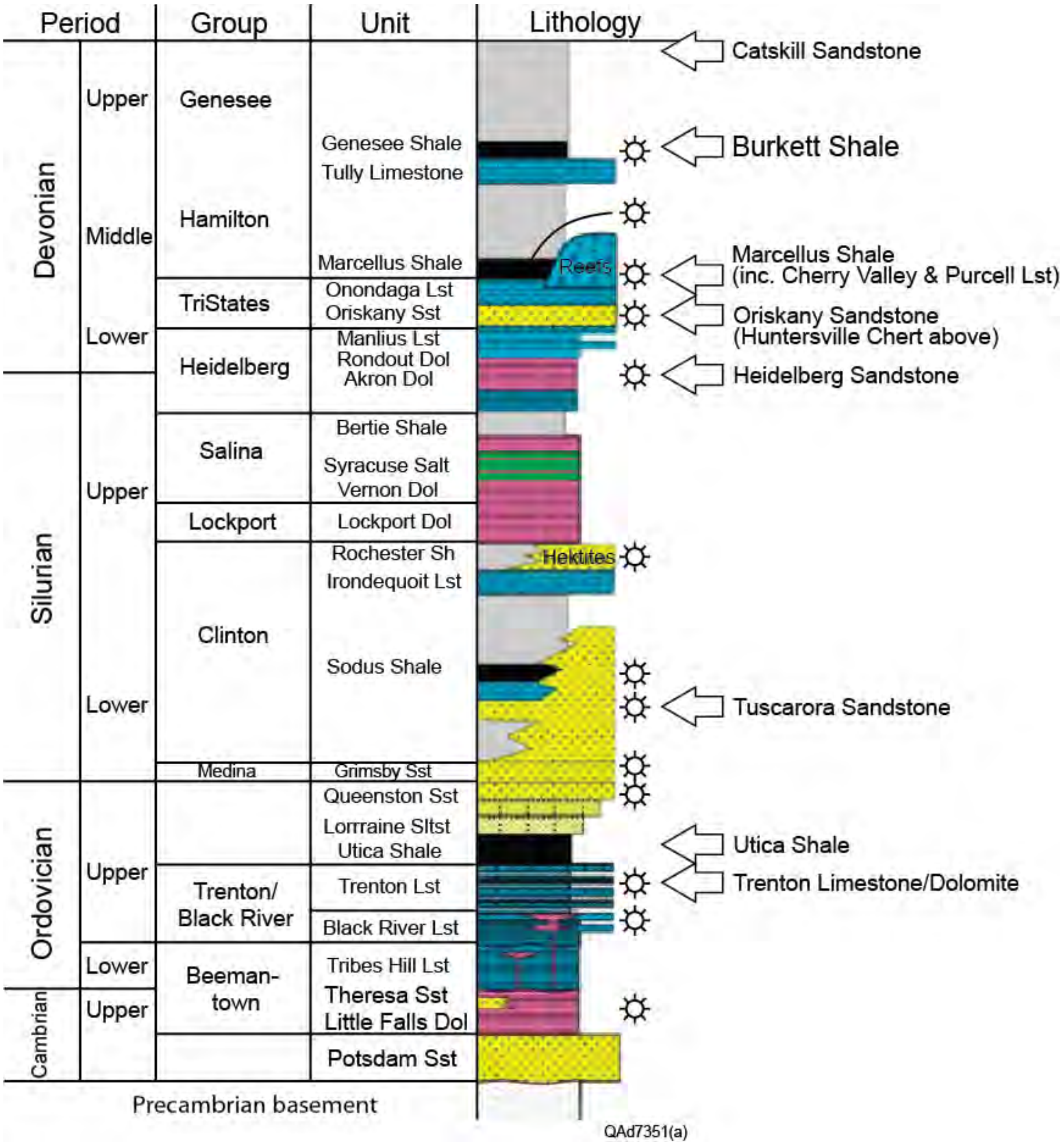

Figure 2.3. Stratigraphic column for the study area showing additional brine sandstones (Catskill, Oriskany, Heidelberg,and Tuscarora) that can be considered as CO2 sequestration reservoirs in addition to the Potsdam Sandstone. Shale units (Burkett, Marcellus, Utica) are noted that also can be analyzed as CO_2 sequestration reservoirs using multicomponent seismic data. From Nyahay, et al. (2007).

Our study focused on porous, brine-filled sandstone and carbonate sequestration targets. However, across the MRCSP area, Devonian shales are also considered by some scientists as potential CO_2 sequestration reservoirs (Fig. 2.4). Our selected seismic survey is positioned atop attractive thicknesses of the Burkett, Genesee, Bertie, Rochester, Sodus, Utica, and Marcellus Shales which allows these shale units to be included in our study to illustrate the value of multicomponent seismic technology for evaluating shales, as well as sandstones, as possible CO_2 sequestration targets.

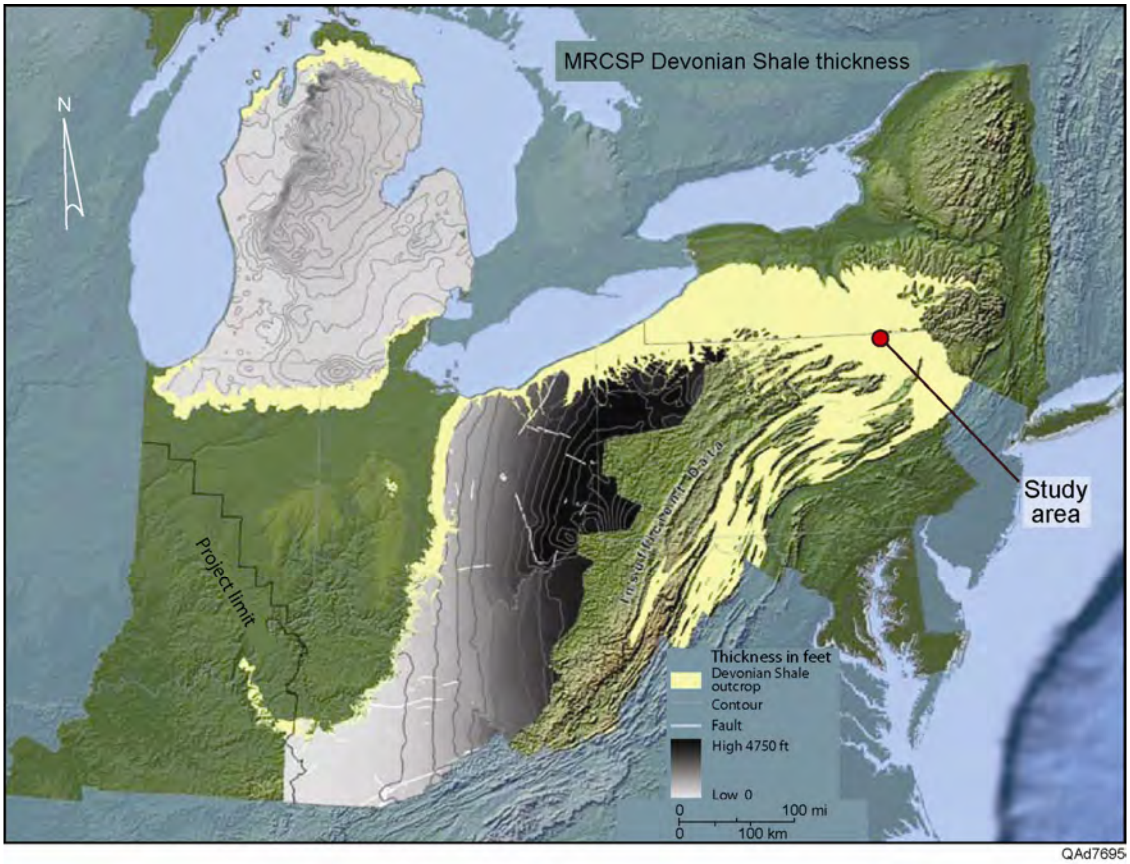

Figure 2.4. Thicknesses of Devonian shales that could serve as CO_2 sequestration reservoirs. Figure is reproduced from the DOE 2008 Carbon Sequestration Atlas of the United States and Canada (U.S. DOE, 2008).

Availability of Multicomponent Seismic Data

An opportunity arose to utilize a high-quality, 3C3D seismic survey acquired by Geokinetics and Geophysical Pursuit for the purpose of multi-client leasing to companies wishing to develop Marcellus Shale prospects. Our research team succeeded in negotiating acceptable data-confidentiality terms that allowed us to use these data to demonstrate the value of multicomponent seismic data for evaluating porous fluid-storage reservoirs. The availability of these 3C3D seismic data was the dominant factor that determined the exact position of our study site. A map showing the generalized location of this multicomponent seismic survey is presented as Figure 2.5. An attraction of positioning the study area in this part of the Appalachian Basin is that the study site sits atop some of the thickest Devonian strata in the basin. Several potential CO_2 sequestration units that need to be evaluated are Devonian age. The value of this site was further enhanced by an operator drilling a Marcellus Shale well in the exact center of the 3C3D seismic grid and acquiring valuable geological calibration data in that well consisting of a full suite of modern well logs and vertical seismic profile (VSP) data.

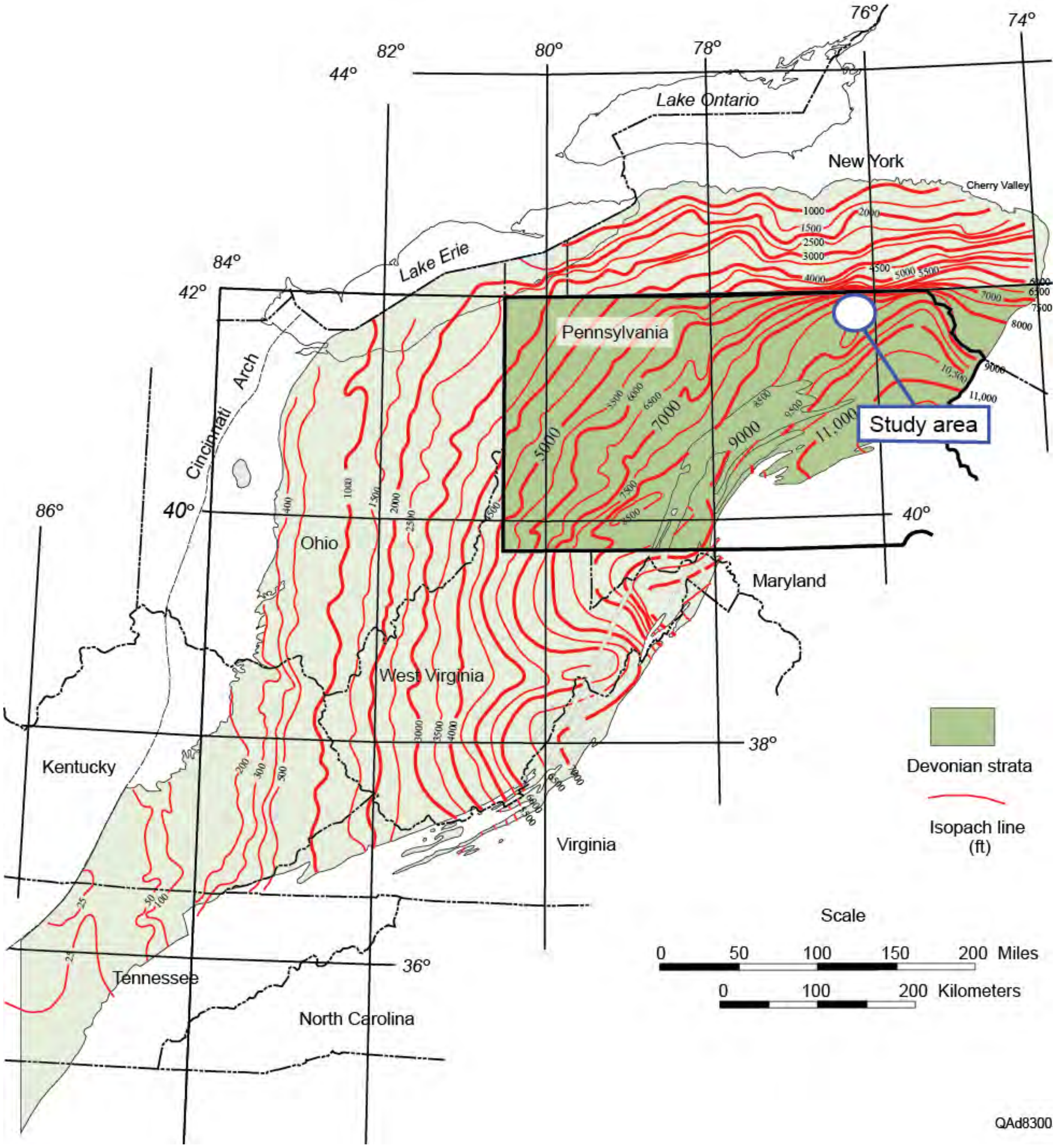

Figure 2.5. Thickness of Devonian strata and location of the multicomponent seismic data used in this study. The study area defined for this project was the area local to this seismic image space. An appeal of the study site is that it sits atop thick Devonian strata, which enhances the possibility that several potential CO_2 sequestration units are present. Modified from Milici and Swezey (2006).

Detailed maps showing the location of the study site on geological maps are illustrated and discussed in Chapter 3 (Geological Analysis). Additional maps showing the configuration of the seismic data-acquisition grid, the position of the central calibration well, and the locations of several local wells that provide additional calibration data are displayed and discussed in Chapter 4 (Research Database).

Conclusions

The selection of an appropriate study site was the initial step in our proposed research plan. Our efforts led to the selection of an ideal site that not only sat atop a sequence of potential CO_2 sequestration reservoirs but that also provided access to a modern multicomponent seismic survey. The site selected for this study is in Bradford County, Pennsylvania, in the northeastern portion of the Appalachian Basin. The study area traverses numerous brine-filled sandstones and carbonates that are potential CO_2 sequestration targets. Most importantly, a modern (Year 2009) 3C3D seismic survey spans the site, and an exploratory well was drilled in Year 2009 at the center point of this 3D seismic image space. Invaluable seismic-to-geology calibration data were acquired in this well and made available to the research team.

The multicomponent seismic data provided by Geophysical Pursuit and Geokinetics have allowed the research team to do innovative seismic data analysis to expand the number and type of P and S seismic attributes that can be used to define rock and fluid properties associated with CO_2 sequestration systems. These multicomponent seismic data also allowed elastic wavefield seismic stratigraphy to be practiced, which is a science based on the principles:

(1) S-wave seismic data provide seismic facies and seismic sequences that differ from P-wave seismic facies and seismic sequences, and

(2) S-wave seismic facies and sequences have equal importance to P-wave seismic facies and sequencies, and these two sets of data must be treated as equals during seismic interpretation.

These principles of elastic wavefield seismic stratigraphy are emphasized in Chapter 9 (Multicomponent Seismic Interpretation).

Chapter 3

Geology of Rock Units Suitable for CO_2 Sequestration

Introduction

Numerous saline aquifers across the Appalachian Basin are candidates for sequestering CO_2. This chapter presents an overview of the geology of the northeastern portion of the Appalachian Basin where our study site was located in Bradford County, Pennsylvania. The primary focus of our geological analysis was to describe porous brine-filled units throughout the entire stratigraphic column to ensure all possible CO_2 storage targets were considered local to Bradford County. Geological descriptions start with Lower Devonian sequestration candidates and proceed to deeper Basal Cambrian sandstones.

Because of the recent, intense focus by the gas industry on the Marcellus Shale, new geological information about Appalachian Basin geology has been published. Our objectives in this chapter are to only summarize key aspects of this growing body of papers describing basin geology and to create a reasonable number of references that provide readers more geological detail than we include in this short treatise.

Geological Overview

Bradford County, Pennsylvania, lies in the northeastern part of the asymmetric Appalachian foreland basin. The preserved elongate axis of the Appalachian Basin extends southwest-northeast across the western half of Pennsylvania. The eastern margin of the basin is overthrust by the Appalachian Mountains, and the western margin extends into Ohio and Kentucky. Appalachian sedimentation is controlled by repetition of passive margin environments, basin deepening, sediment starvation, and advances of immature siliciclastic units in a general east-to-west direction.

Delineating deep subsurface geology across Pennsylvania is largely controlled by hydrocarbon exploration. Recent exploration for tight-gas sand plays and post-2005 seismic-based exploration for Marcellus Shale and other shale-gas plays have provided new geological information. There are few penetrations of the sub-Oriskany interval in Pennsylvania. As of 2009, only 170 sub-Oriskany well had been drilled in central and eastern Pennsylvania (DCNR, 2009a). Much of the reconstruction of deep geology comes from projections of trends outside of Bradford County compiled by the Pennsylvania Geologic Survey (Harper, 1990; Harper, 2008), the West Virginia Geologic Survey (Roen and Walker, 1996), and the U.S. Geological Survey (Milici and Swezey, 2006).

The stratigraphy and basin structure of northern Pennsylvania reflect Precambrian rifting and sediment deposition in a passive margin setting during most of the Cambrian through Early/Middle Ordovician. Structural features EC, RR, RS, RT, and RW shown on Figure 3.1 are elements of the Precambrian Rome Trough. The RT arm of the Rome Trough extending across Pennsylvania is offset by several regional faults and passes in the immediate vicinity of our study site. Late Cambrian events included plate movement of the present-day Appalachian area into the evaporative subtropical trade winds belt (Fig. 3.2) where it remained until late Mississippian time (Miall and Blakely, 2009).

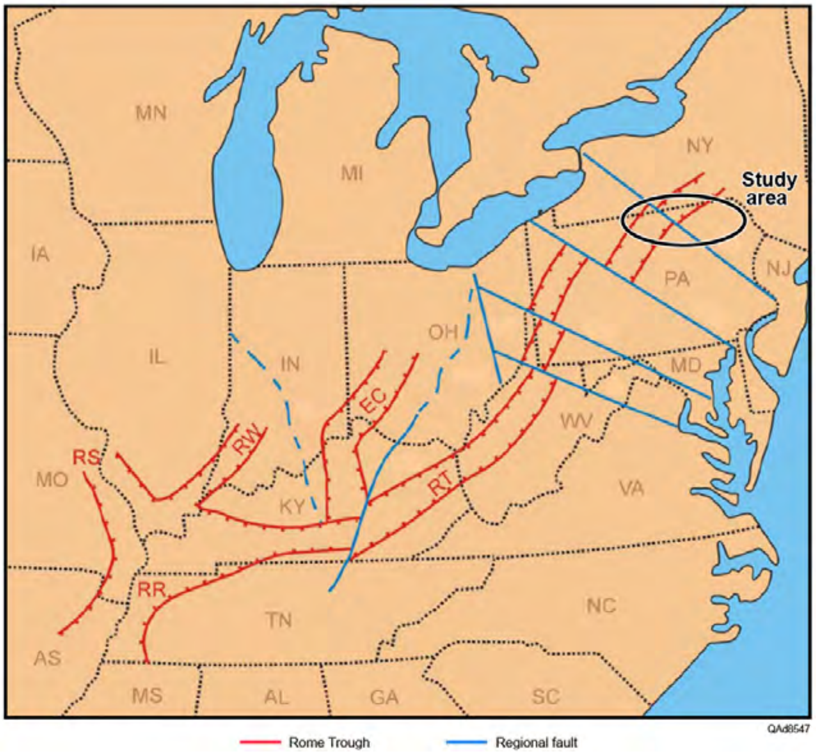

Figure 3.1. Red outline shows segments of the Precambrian Rome Trough (RR, RS, RW, RT, EC) and their offsets by later strike-slip faults (blue). After Harper (2005). Our study site in Bradford County, Pennsylvania is at the northern terminus of the Rome Trough.

Overprinted on this early depositional setting are the effects of continental collisions and tectonic movements that produced various uplifts, downwarps, foreland basin formation and fill, and burial by prograding clastic wedges during Late Ordovician/Early Silurian Taconic, Devonian Acadian, and Pennsylvanian Alleghenian orogenies. The Alleghenian collision resulted in late-stage, warm (110° C), reactive basinal fluids being flushed toward the Cincinnati Arch (Fig. 3.2), resulting in vugular porosity development in some Cambrian–Ordovician carbonates (Rowan et al., 2008). Of importance to our study, collision dynamics caused both thick-skin and thin-skin fault developments that include décollement surfaces associated with the Silurian Salina evaporite beds (Harper, 1990; Harper and Patchen, 1996; Fig. 3.3). This thin-skin faulting is well documented in northern Pennsylvania and across Bradford County, the location of our study site. Line drawings are shown on Figure 3.4 of the configurations of faulted and deformed Salina evaporates observed on two regional seismic lines.

Figure 3.2. Middle Devonian paleo-reconstruction of Laurentia showing location of our study site in Bradford County, Pennsylvania. Our study area was proximal to the Acadian Mountains, the Catskill clastic wedge/delta, and the subsequent Alleghenian front (not labeled). Modified from Harper and Kostelnik (2010).

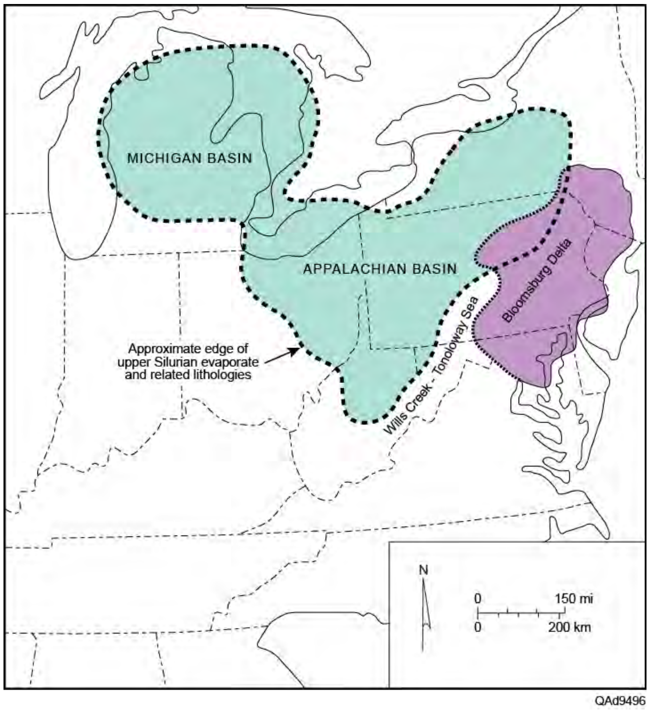

Figure 3.3. Depocenters for Silurian evaporites. Thick, deformed evaporite layers are present in some seismic profiles from Bradford County, Pennsylvania. The Bloomsburg Delta is contemporaneous with the lower part of the Salina evaporites (after DCNR, 2009a).

CO_2 Storage Units

CO_2-storage reservoir targets across the Appalachian Basin are most attractive when they demonstrate large storage capacity and injectivity and have no transmissive faults or fracture zones. Reservoir targets include deep saline reservoirs and downdip water legs of known hydrocarbon bearing zones.

Most of the units in the stratigraphic column of Pennsylvania can be considered as confining zones or seals. In general, the best regional porosity development in the Appalachian Basin is associated with laterally extensive unconformities. Fortunately, several unconformities traverse the basin as documented on Figure 3.5. The most widespread sandstone reservoirs are transgressive sandstones developed immediately above, or between, regional and local unconformities. These transgressive systems tend to grade upward into carbonates and shales. Sandstone porosity can develop locally in association with still stands or in association with tectonically forced regressions during progradations of clastic wedges. Such sandstone porosity development is observed in the Upper Devonian Venango and Lock Haven Groups (Fig. 3.6).

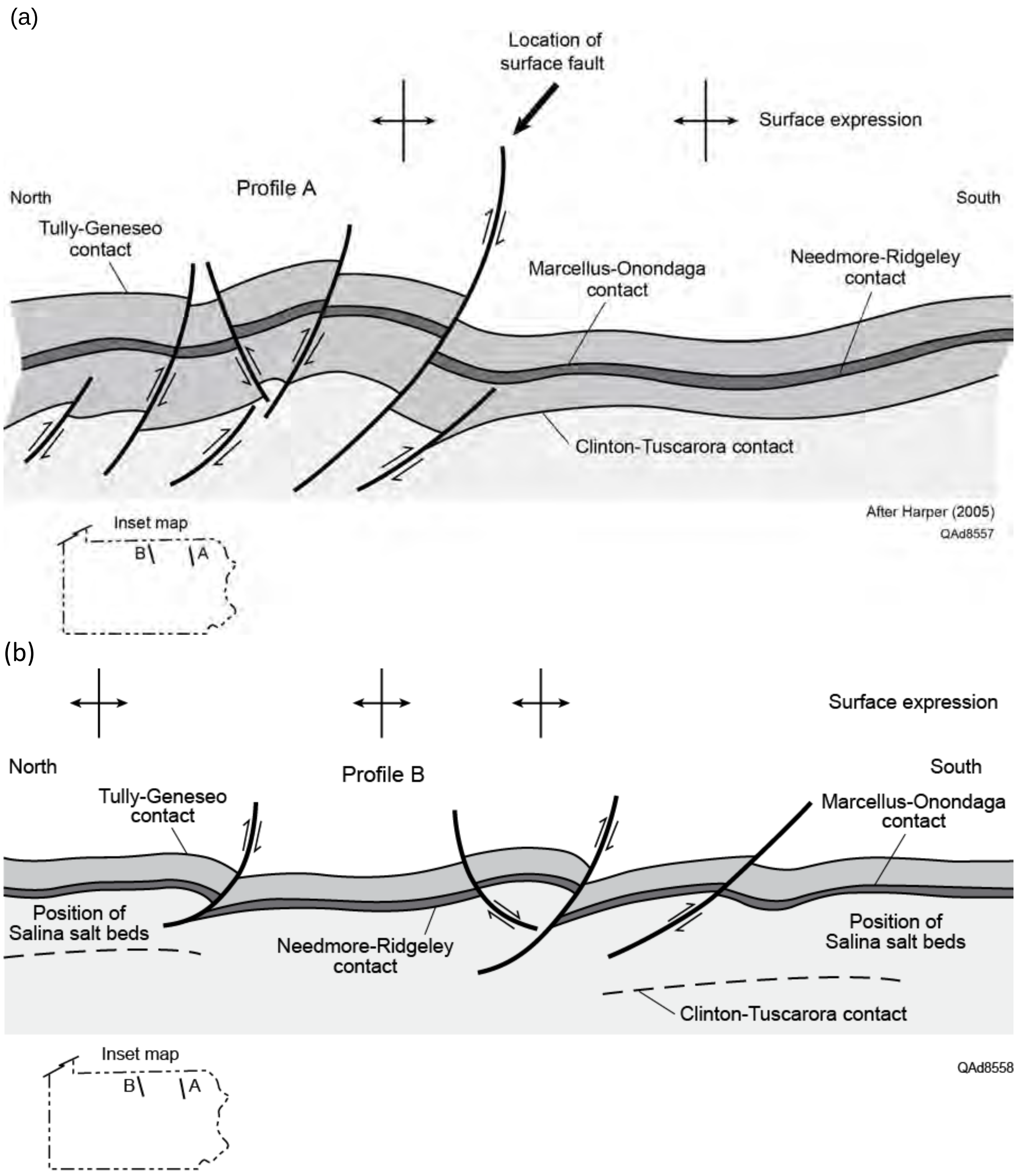

Figure 3.4. Thin-skinned, evaporite-soled faults interpreted on two seismic lines in northern Pennsylvania. These exhibits are line drawings of interpreted seismic horizons (after Harper, 1990).

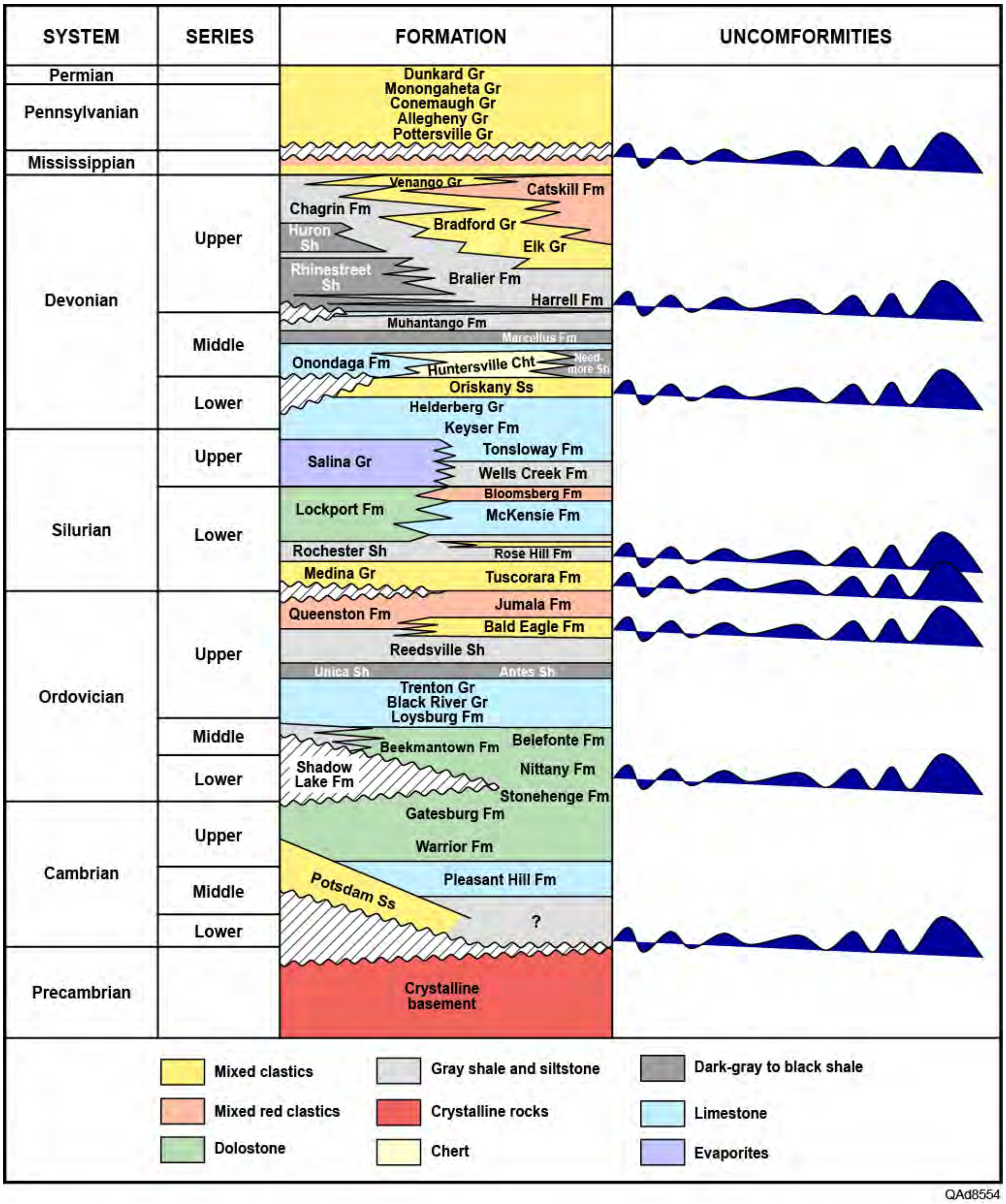

Figure 3.5. The most prospective CO_2-storage reservoirs in Pennsylvania are sandstones and carbonates associated with unconformities. Porous transgressive sandstones often occur above unconformities, and porous carbonates often are created below unconformities by dissolution and dolomitization processes. Numerous unconformity surfaces are present across the Appalachian Basin, as shown (modified from DCNR 2009a).

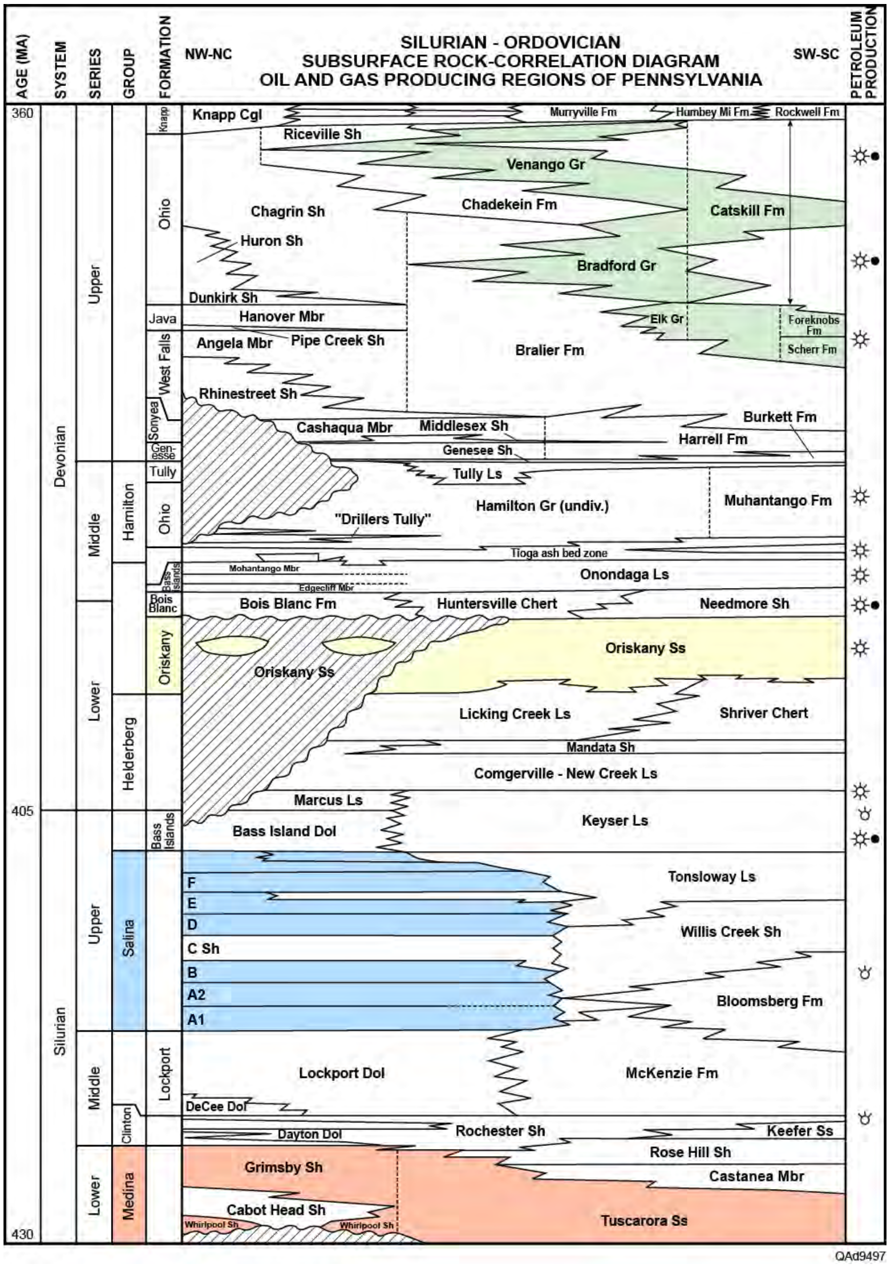

Figure 3.6. Four potential Silurian—Devonian CO_2-storage targets in Pennsylvania are: (1) the Upper Devonian Venango-Bradford-Lock Haven/Elk clastic wedge, (2) Lower Devonian Oriskany sandstones, (3) Upper Silurian Salina evaporites, and (4) the Lower Silurian Tuscarora Formation (after DCNR, 2009a).

Porosity in carbonates may develop below unconformities as a result of karsting, dissolution, and dolomitization of grain-rich lithofacies. Dolomitization or leaching of carbonates can also result from contact with migrating basinal and hydrothermal fluids. Dolomitized reef rubble is reported to generate reservoir quality porosity in the Silurian Lockport Formation of Pennsylvania (Harper 2005).

In Pennsylvania, the most regionally prospective CO_2-storage reservoirs are sandstones. Referring to Figures 3.5 and 3.6, these sandstone units are, from younger to older (Harper 2011; DCNR 2009a):

- Upper Devonian Venango and Elk/Lock Haven sandstones,
- Middle Devonian transgressive sandstones immediately below the Tully Limestone,
- Lower Devonian Oriskany (or Ridgeley), and
- Lower Silurian Tuscarora (Clinton/ Medina).

Although the Cambrian Potsdam Sandstone is likely present in the subsurface of eastern Pennsylvania, it has few penetrations and is probably too deeply buried to have retained porosity in that part of the State (DCNR 2009b). Cambrian and Lower Devonian sandstones were typically deposited as transgressive, shore-parallel sandstones. Middle Devonian and Lower Silurian siliciclastic depositional environments also include incised fluvial deposits. Upper Devonian reservoir-quality sandstones were deposited in a variety of fluvial, deltaic, and shallow marine environments. In general, fluvial sandstones in the Appalachian Basin are thought to be better able to retain porosity in the subsurface.

Petrophysical Properties of CO_2 Storage Units

Within the western Pennsylvania area studied by Kostelnik and Carter (2009a), average porosities in Oriskany sandstones ranged from 1.4 to 14 percent. They report three main porosity types:

1. Primary intergranular porosity related to stratigraphic pinch-out zones near the Oriskany no-sand area and at the western limit of the Oriskany Sandstone,

2. Secondary dissolution of carbonate constituents that dominate combination stratigraphic/structural gas plays in western Pennsylvania, western West Virginia, and eastern Ohio, and

3. Fracture porosity that dominates gas plays in the central Appalachian Plateau Province and the Valley and Ridge Province**.**

Kostelnik and Carter (2009a) report permeability in the Oriskany ranges from 0.2 to 42.7 md, with stratigraphic pinch-outs at the northern and western edges of the basin having the highest permeabilities. In most of Pennsylvania, the development of secondary dissolution or fractures is important for developing permeability in the Oriskany.

Upper Devonian CO_2 Storage Sandstones

Prospective Upper Devonian sandstones in Pennsylvania belong to the Venango, Bradford, and Elk Groups (Fig. 3.6), which are associated with the Middle to Upper Devonian Catskill delta that formed in response to the Acadian orogeny (Fig. 3.2). Devonian strata are thickest in eastern Pennsylvania, where they reach a thickness of 12,000 ft (3658 m). Reservoir quality sandstones were deposited primarily in deltaic and turbidite environments associated with tectonically forced low stands of the progradational Devonian clastic wedge (Milici and Swezey, 2006).

The Venango group, including the Murrysville (Brea in part), Hundred-Foot Zone, and Gordon Formations, produces oil and gas in southwestern Pennsylvania (Sager, 2007) and has considerable potential for CO_2 storage in western Pennsylvania. In southwestern Pennsylvania where the Murrysville depositional environment is interpreted as a high-energy braid delta, porosity can exceed 20-percent, and permeability may exceed one Darcy (Smosna and Sager, 2008). When large pore volumes are found, porosity is retained or enhanced by coarse grain size, moderate compaction, leaching of unstable grains, lack of externally derived carbonate cement, and the presence of detrital and authigenic chlorite that inhibited quartz cement overgrowths (Sager, 2007). Unfortunately, Venango Group sandstone lithofacies do not extend into eastern Pennsylvania where our study site is located.

The most important Upper Devonian target in Bradford County may be the Lock Haven sandstones of the Catskill clastic wedge that are hydrocarbon productive in north-central Pennsylvania's Centre and Clinton Counties. The Council Run field covers about 290 mi^2 (742 km^2) and has approximately 700 wells with a cumulative production of 56 Bcf as of 2001 and an estimated ultimate recovery of 250 Bcf (Laughery et al., 2004). The most prolific of the Council Run reservoirs are in the Lock Haven Formation and were deposited in deltaic and nearshore marine environments associated with a lowstand systems tract of a third-order tectonically forced regression. Multicomponent seismic mapping of this or other Upper Devonian lowstands may allow similar reservoirs to be identified for CO_2 storage. At the Council Run Field, core porosity in lithic to feldspathic reservoir sandstones ranges up to 16-percent. Permeabilities are generally low and require hydraulic fracture stimulation. Original porosity has been reduced by diagenesis and compaction, enhanced by grain dissolution of deformable lithic fragments, and preserved, in part, by pore-lining clay cements and early hydrocarbon emplacement (Laughery et al., 2004). It is important to note that this mode of porosity formation and retention appears to be a regional phenomenon along the Alleghany structural front (Bruner and Smosna, 1994; Laughery et al., 2004).

Middle Devonian CO_2 Storage Sandstones

Middle Devonian sandstones are regionally less extensive, but include transgressive sandstones immediately below the Tully Limestone, a strong seismic marker at the top of the Hamilton Group or Mahantango Formation (Fig. 3.7). These transgressive units are interpreted as being coincident with the regional erosion of the Moscow Shale observed in upstate New York by Lash (2007). On regional seismic lines, these sandstones display channel-shaped morphologies, are quite likely incised into underlying shales, and might possibly develop reservoir quality porosity in Bradford County.

A striking example of such a channel-like morphology defined by our Bradford County seismic data is illustrated in Chapter 9 (Figs. 9.15, 9.22). An intriguing aspect of this channel facies is that it is prominent in converted-shear data but is absent in conventional P-wave data, the latter being the primary seismic data used to evaluate CO_2 sequestration targets. This study thus presents evidence that multicomponent seismic data should be used to evaluate CO_2 reservoirs and their seals rather than having total reliance on P-wave data.

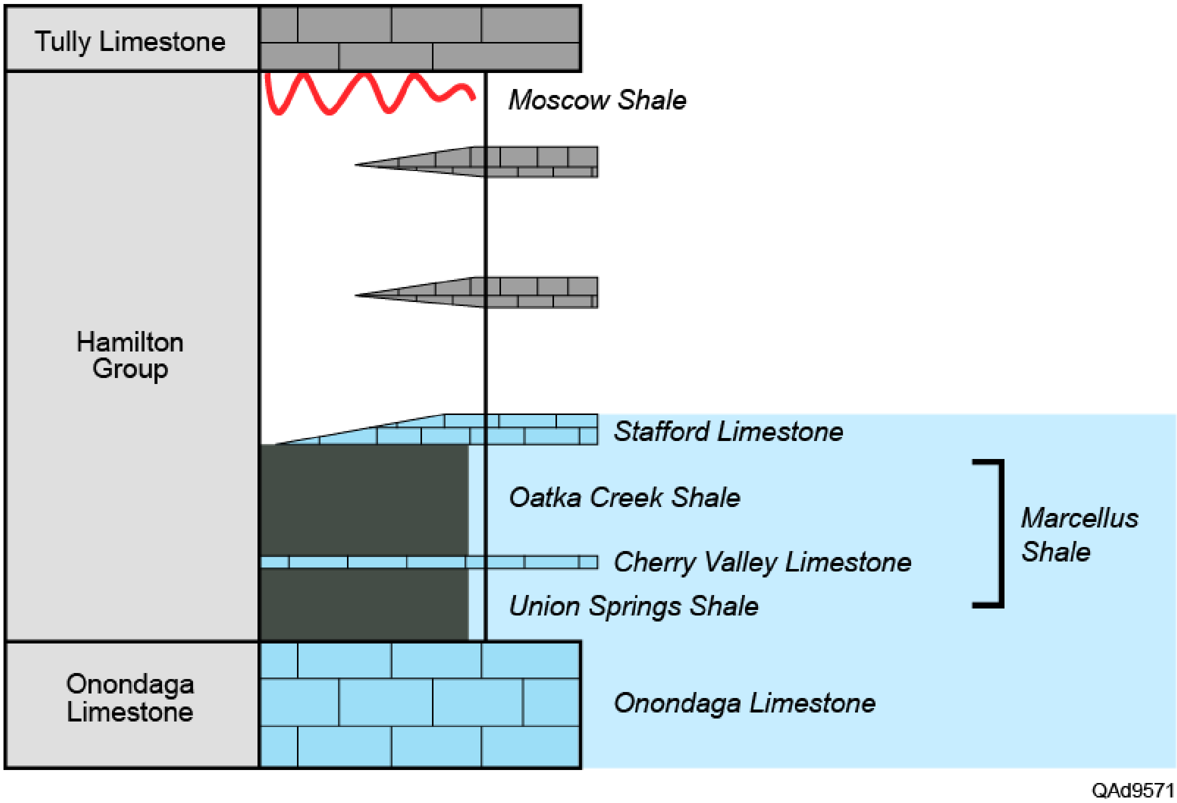

Figure 3.7. Middle Devonian stratigraphy in New York and Northern Pennsylvania. Unconformity related sandstones below the Tully Limestone may form potential CO_2 storage reservoirs in Bradford County. Modified from Lash, 2007.

Lower Devonian CO_2 Storage Sandstones

The Oriskany (Ridgeley) Sandstone is considered the most promising siliciclastic saline reservoir for CO_2 sequestration in northeastern Pennsylvania (Skeen and Carr, 2009; Kostelnik and Carter, 2009b; DCNR, 2009a). The Oriskany Formation occurs across New York, Pennsylvania, Ohio, Maryland, West Virginia, Virginia, and Kentucky (Diecchio, 1985; Bruner and Smosna, 2008; Dilmore et al., 2008). As a facies, the Oriskany is a fossiliferous shallow-marine quartzarenite, variably cemented with calcite or quartz. Depositionally, the Oriskany is a transgressive sandstone that unconformably overlies the Helderberg Limestone or equivalents, and is overlain by more siliciclastic-poor lithologies of the Onondaga Limestone, Huntersville Chert, or Needmore Shale (Fig. 3.8). These units may locally be arenaceous (Diecchio, 1985; Skeen, 2010).

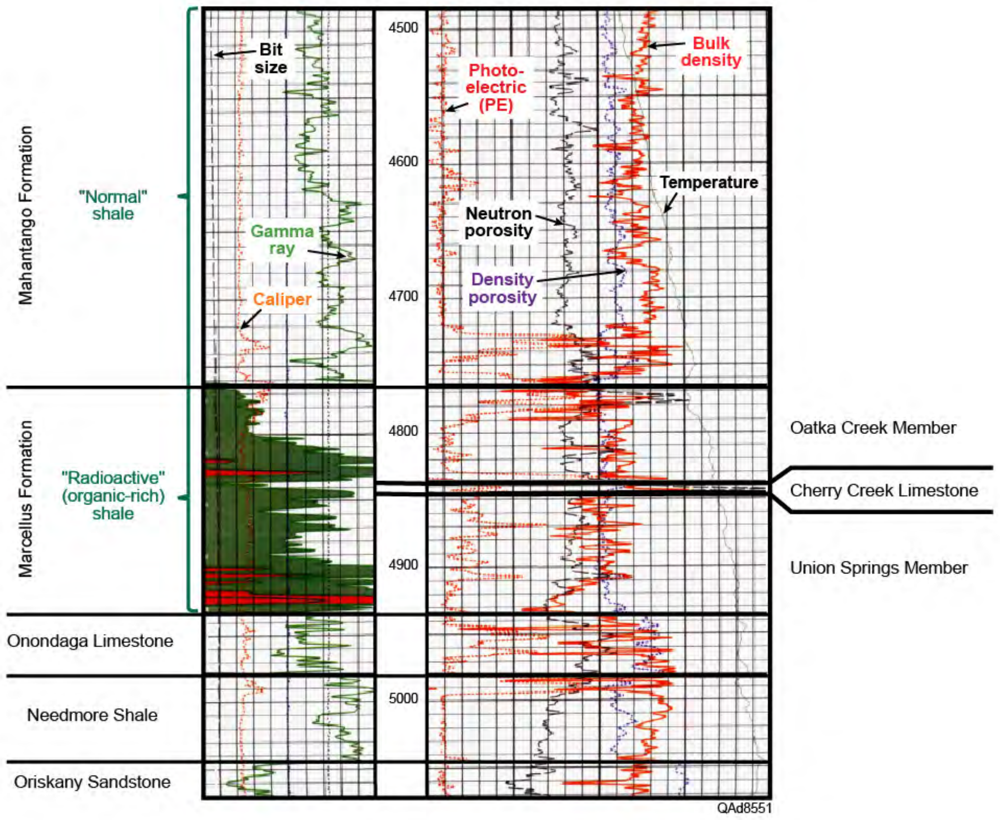

Figure 3.8. Type log for the Oriskany Sandstone in the Bradford County area. After Harper and Kostelnik (2010).

The Oriskany sandstone was generally deposited on an unconformity and in many places also has an erosional upper contact (Fig. 3.9). Locally in parts of central Pennsylvania, the Oriskany appears to be in conformable contact with the underlying Helderberg Group limestones and cherts (DCNR, 2009a). The

Oriskany (Ridgeley) is an orthoquartzite that is locally conglomeratic and was deposited in a shallow marine environment. In central Pennsylvania, the Oriskany was deposited in a high-energy shoreface environment with shallow marine shoreline parallel bars, and tidally influenced sandstone bodies (Kostelnik and Carter, 2009a). Within our study area the Oriskany is estimated to have a thickness between 50 and 100 ft (15 and 30 m), as shown on Figure 3.10.

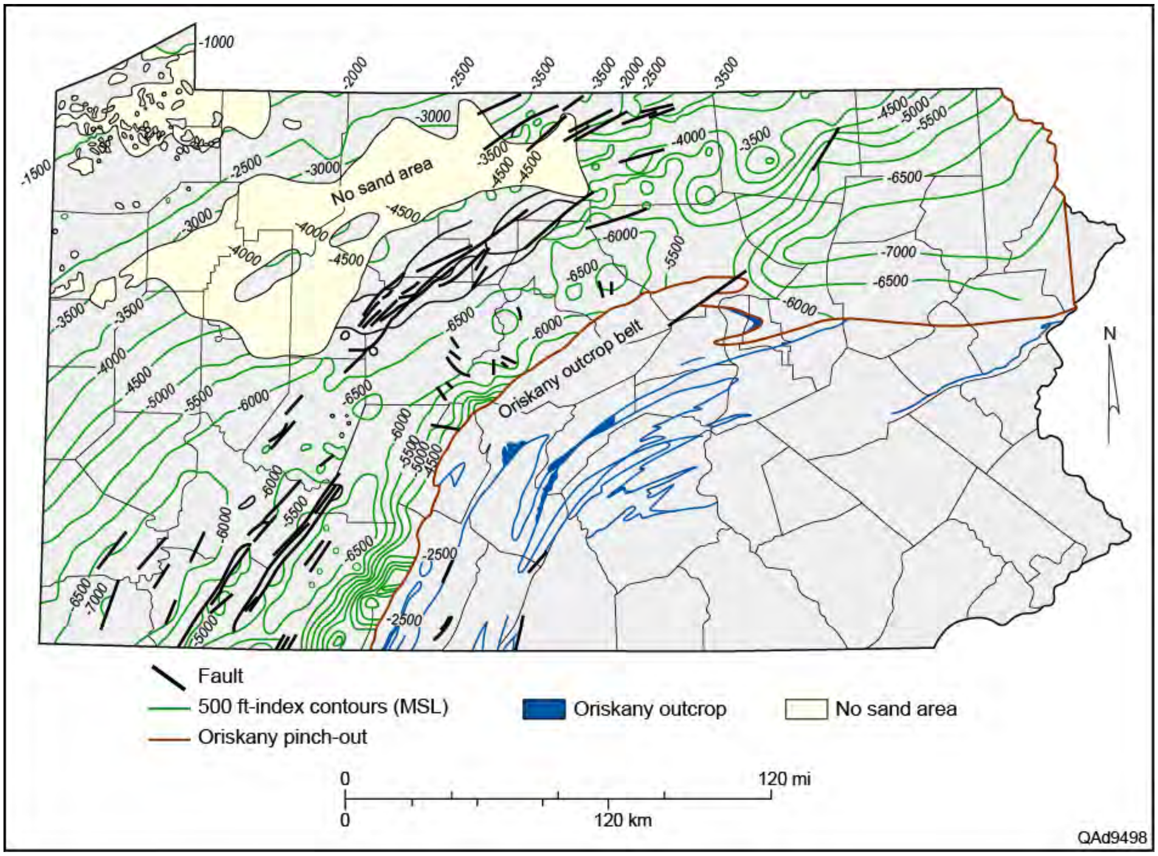

Figure 3.9. Structure on top of the Oriskany. Depths are subsea. Note the areas of nondeposition in northwestern Pennsylvania. The depth of the Oriskany changes rapidly local to our study area. (After DCNR 2009a)

The Oriskany produces oil and gas from permeability pinch-outs in northwestern and north-central Pennsylvania and from fractured reservoirs in southwestern Pennsylvania (Opritza, 1996; Patchen and Harper, 1996; Kostelnik and Carter, 2009a). Depth of the Oriskany in these areas is generally between 1700 and 3100 ft (518 and 945 m). Some Oriskany gas fields in the central Appalachian Basin coincide with the boundary of higher and lower salinities and appear to reflect geologic-scale basinal fluid flow (Skeen 2010). In addition to being hydrocarbon productive, the Oriskany has been used for injection of industrial wastes. There are 32 Oriskany gas storage fields with a cumulative total of over one Tcf storage capacity (Skeen, 2010). The primary risk for Oriskany CO_2

storage in Bradford County, and elsewhere parallel to the Alleghany structural front, is the presence of fractured and leaky caprock (Kostelnik and Carter 2009b). Seismic detection of faults and fracture systems is therefore critical to evaluating the non-hydrocarbon bearing Oriskany for CO_2 storage potential. Fracture detection and evaluation can be done far better with seismic S waves than with seismic P waves, which is a principal justification for utilizing multicomponent seismic technology to evaluate CO_2 reservoir systems.

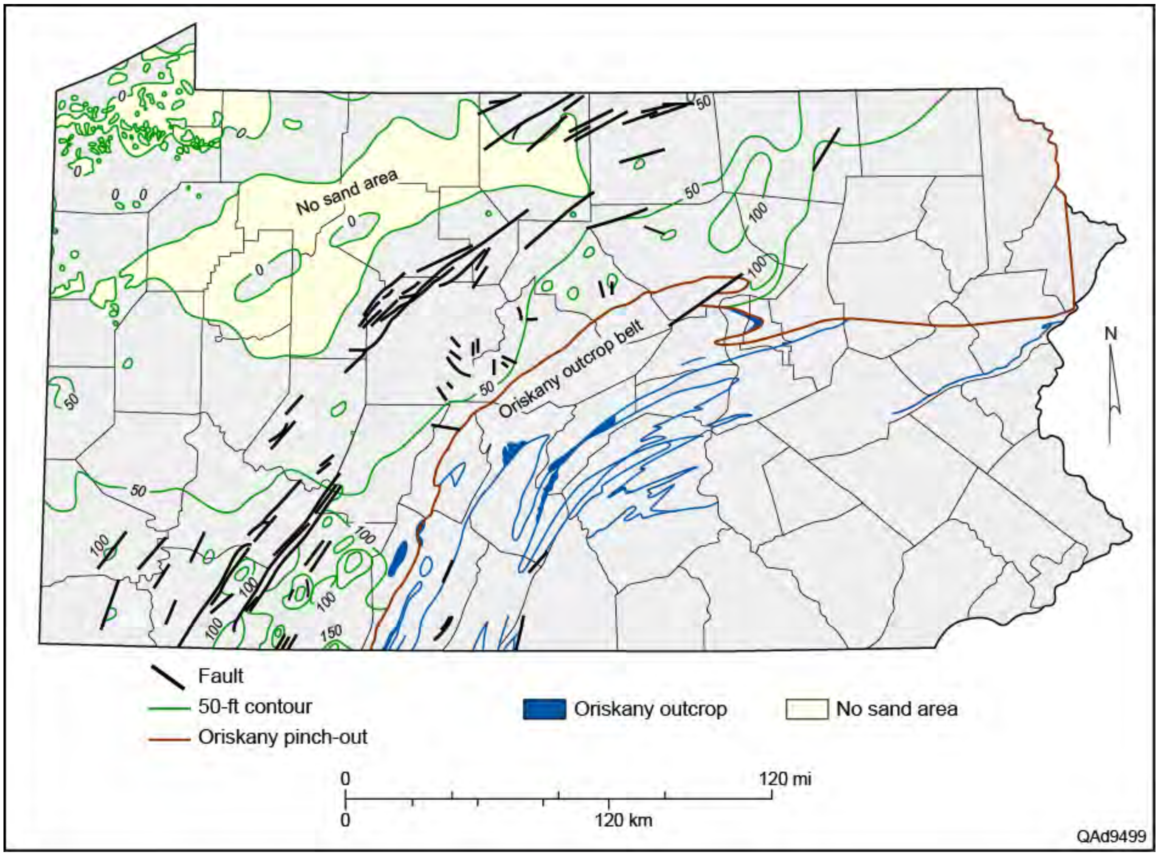

Figure 3.10. Thickness of the Oriskany Sandstone. The Oriskany can be expected to be between 50 and 100 feet thick across Bradford County. After DCNR 2009a.

Lower Silurian Medina Group/Tuscarora Sandstone CO_2 Storage Units

Within a sequence stratigraphic framework, Medina Group sandstones of northwestern Pennsylvania and Tuscarora sandstones of northeastern Pennsylvania unconformably overlie the Upper Ordovician Queenston Shale to the west and the time-equivalent siliciclastics of the Juniata Formation to the east (Fig. 3.5). The Tuscarora is correlative to the Shawangunk Formation in eastern Pennsylvania (DCNR 2009b). Tuscarora sandstones are derived from the Taconic highlands to the east. Lithologies include fine-grained to coarse-grained quartz arenite, subgraywacke, siltstone with occasional thin shales, and conglomerates. Deposition of these sandstones occurred near the end of the Taconic orogeny, and depositional environments ranged from fluvial to shallow marine. Depositional processes commonly produced shoreline-parallel sand bodies. Of six lithofacies identified by Castle and Byrnes (2005) in the Lower Silurian sandstones of the Appalachian basin, those associated with incised fluvial channels had the highest porosities and permeabilities. Lithofacies of the Medina and Tuscarora sandstones in Northern Pennsylvania have variable lithologies, low porosity, and burial depths of 7,000–10,000 ft (2,134–3,048 m) subsea (Fig. 3.11) across Bradford County (DCNR, 2009a).

Although Medina Group sandstones (including the Clinton) are relatively thick and form oil and gas reservoirs in Crawford and Erie counties, Pennsylvania, their north-central and northeastern Pennsylvania equivalents are thin, tight, have variable lithologies, and are less attractive as CO_2 storage units. The Tuscarora Formation can be expected to be between 150 and 200 ft (46 and 61 m) thick in Bradford County. For comparison, sandstone lithologies across the state generally range from 3–50 ft (1–15 m) with an average of about 23 ft (7 m) as shown on Figure 3.12 (DCNR, 2009a).

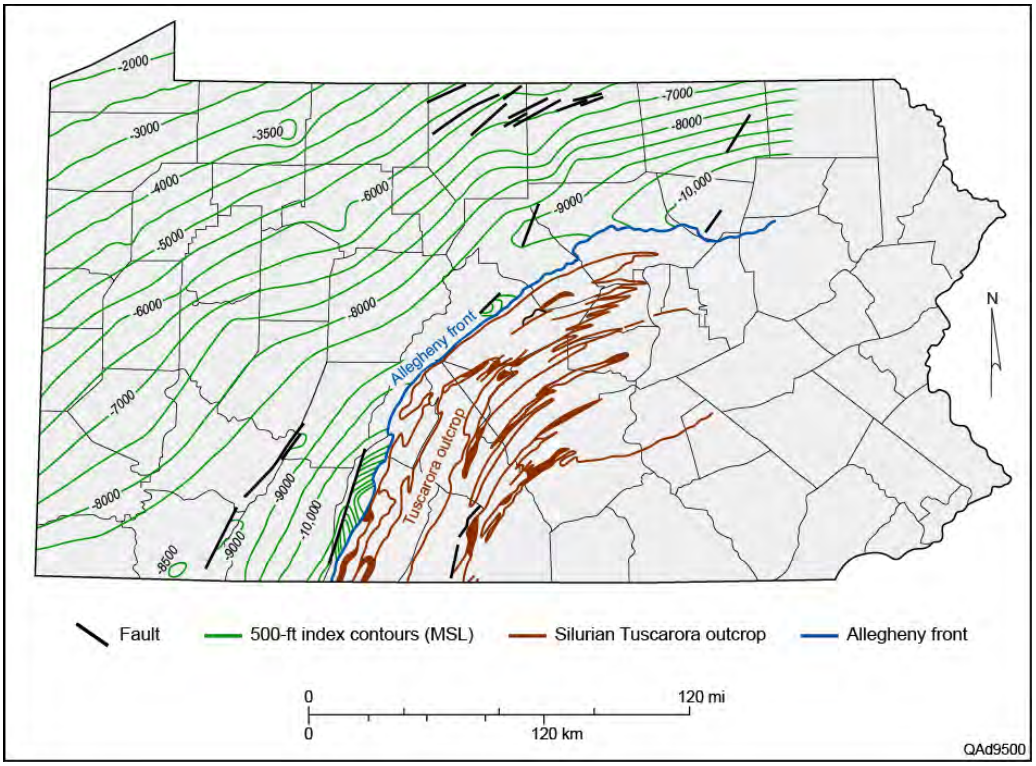

Figure 3.11. Structure across top of Silurian Tuscarora in Pennsylvania. Depths are subsea (after DNRC, 2009a).

Ordovician CO_2 Storage Reservoirs

The greatest number of siliciclastics in the Ordovician section is associated with unconformities and sea-level stillstands of the Upper Ordovician Queenston clastic wedge (Fig. 3.5). These include sandstones of the Juniata and Bald Eagle Formations. In Juniata County, the Bald Eagle Formation comprises fine to coarse sandstones with some cross-stratification, and some conglomeratic intervals. The sandstones of the overlying Juniata formation also include siltstones and some shale.

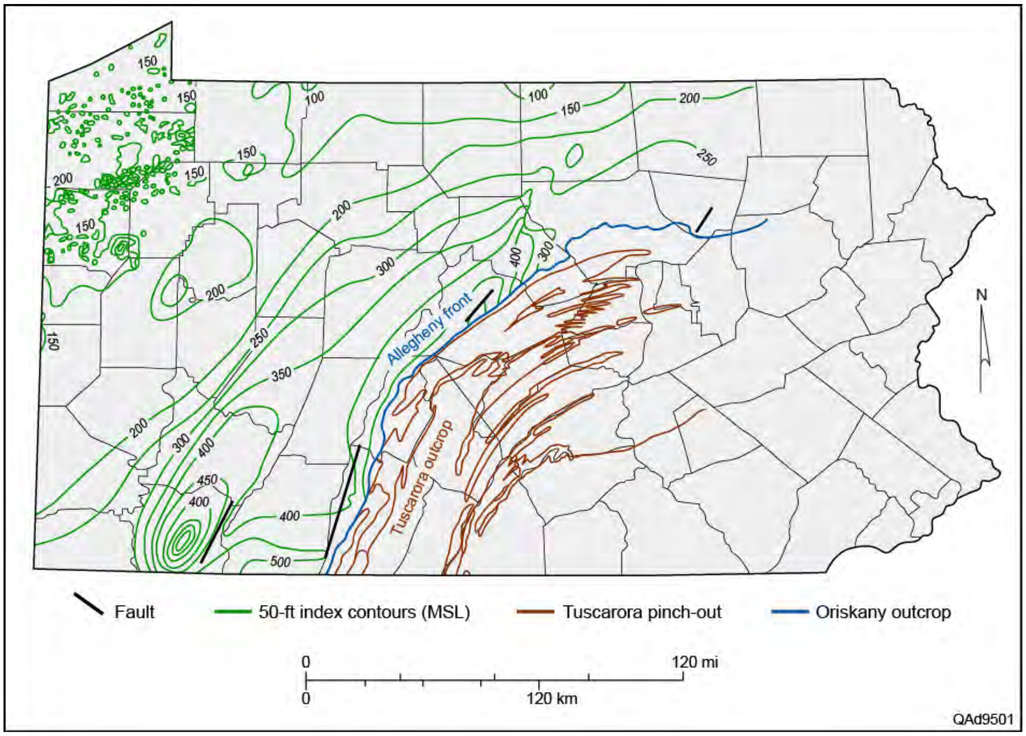

Figure 3.12.Gross thickness of the Silurian Tuscarora Formation. Actual sandstone lithology thickness averages less than 30 ft (9 m) (after DCNR 2009a).

Cambrian CO_2 Storage Sandstones

During the Cambrian, the North American landmass of Laurentia, containing Pennsylvania, was at the equator and rotated about 90 degrees clockwise of its present position. The collision of the passive margin of Laurentia with the Taconic island arc initiated during mid-Cambrian (Miall and Blakely, 2009) and culminated in the Ordovician, forming the Appalachian foreland basin and causing subaerial karstification of carbonates across of much of the craton.

In Pennsylvania, transgressive Cambrian sandstones are considered to have greater sequestration potential than Cambrian carbonates. Because of increasing depth of burial and lack of penetrations in northeastern Pennsylvania, the Midwestern Regional Sequestration Partnership (MRCSP) and the Department of Conservation and Natural Resources (DCNR) have assessed Cambrian sandstones only in the western part of Pennsylvania. Seismic surveys acquired in conjunction with shale-gas exploration are providing important new information on depth and porosity retention in the deeper part of the Appalachian Basin.

Gatesburg CO_2 Storage Sandstone

Cambrian sandstones in Pennsylvania include the Upper Cambrian Gatesburg and the transgressive basal sandstones of the Potsdam (Fig. 3.5). The Upper Sandy member of the Gatesburg is correlative to Rose Run sandstones, which produce hydrocarbons in eastern Ohio (Riley et al., 1993), especially where they subcrop beneath the Knox unconformity. Depositional environments of these sandstones in eastern Ohio include tidal channels, bays, estuaries, and shallow marine shelf (Riley et al., 1993, Nwaodua, 2008).

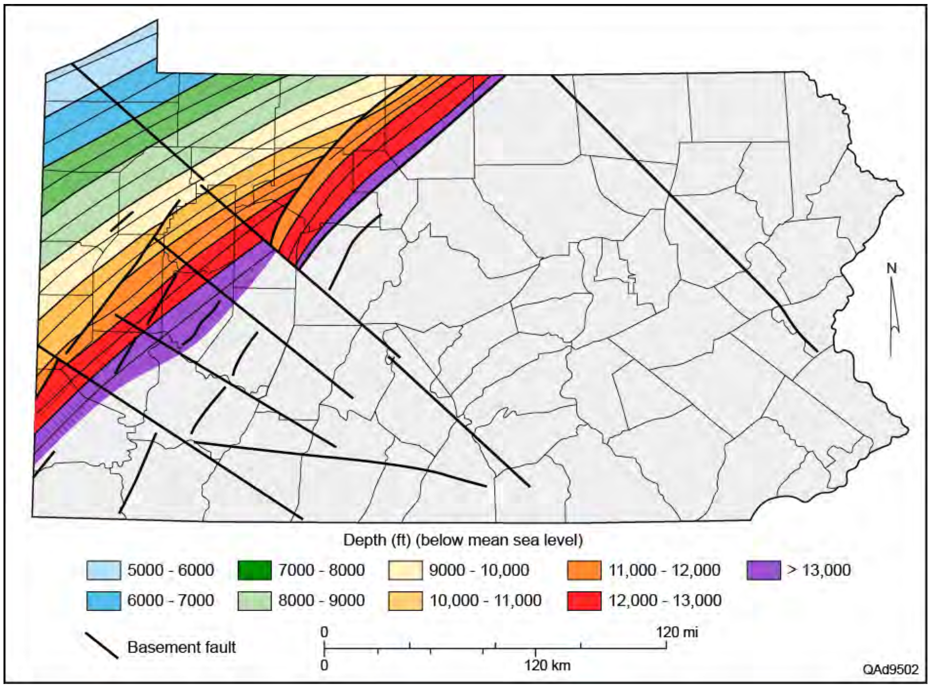

Figure 3.13. Structure on the Potsdam Sandstone. Increased acquisition of 3D seismic data should allow mapping to extend into northeastern Pennsylvania (after MRCSP, 2005, and DCNR, 2009b).

Structure and isopach maps of Cambrian sandstones across western Pennsylvania are shown on Figures 3.13 and 3.14, respectively, to illustrate the CO_2 sequestration potential of these deep rocks. One Gatesburg brine disposal well in northwest Pennsylvania demonstrates reservoir potential (DCNR, 2009b). Both Gatesburg and Potsdam sandstones are expected to be present in northern Pennsylvania, including Bradford County, but there are few well penetrations to provide evaluation data. The Rose Run Formation in Ohio and West Virginia includes dolomites as well as sandstones, and although the overall thickness of the correlative Upper Sandy Member increases into the deeper Appalachian Basin, the sandstone facies may decrease.

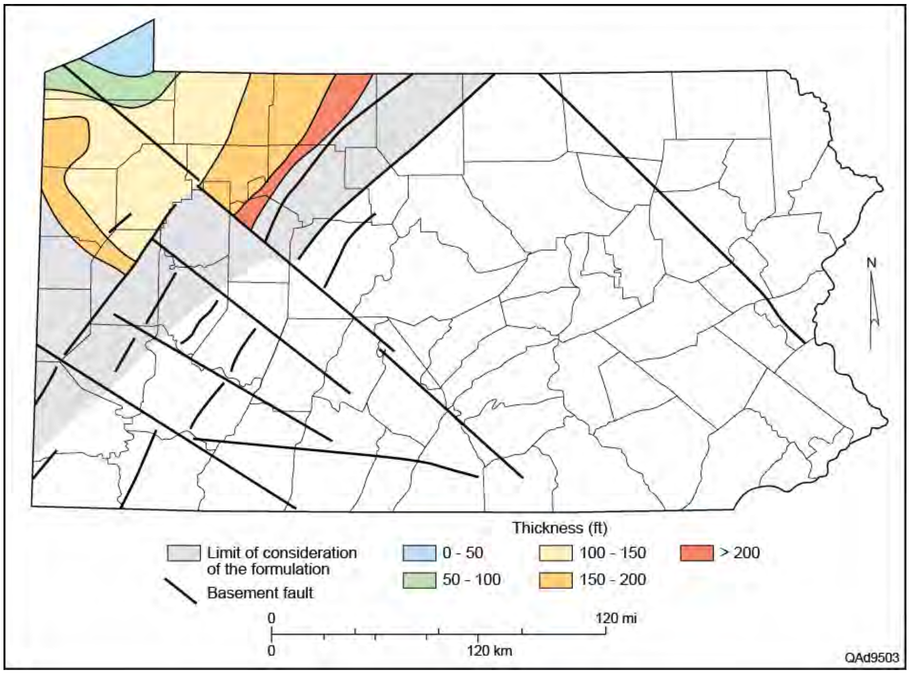

Figure 3.14. Thickness map of the Potsdam Sandstone (after MRCSP, 2005, and DCNR, 2009b).

Basal Cambrian CO_2 Storage Sandstones

Basal Cambrian sandstones directly and unconformably overlie Precambrian non-sedimentary basement. These include dolomitic sandstones of the Conasauga Group of the Rome Trough that extends into western Pennsylvania, and the stratigraphically older, but unnamed transgressive sandstones of both the Rome Trough and the eastern proto-Appalachian Basin of Pennsylvania (DCNR 2009b). These sandstones are expected to be 50 to 150 ft (15 to 45 m) thick.

Cap rock for the basal Cambrian sandstones includes the Queenston Shale and relatively thick, continuous, low-permeability Trenton and Black River limestones. Although the expected low porosities and depths of 10,000 ft (3,048 m) or greater generally make Cambrian sandstones less attractive as sequestration targets, the MRCSP (2005) concluded that paleotopographic and structural highs play a strong control on reservoir development. New 3D seismic data acquired in Bradford and other northeastern Pennsylvanian counties should identify structural highs and define porosity-sensitive seismic attributes.

Conclusions

Following the selection of our study site (Chapter 2), our next research step was to confirm that attractive CO_2 sequestration targets existed across the selected study area. The information compiled in this chapter verifies the stratigraphic sequence beneath our study site should contain several potential CO_2 sequestration intervals. We consider the outcome of this research step exceeds our expectations when the project was started.

Numerous unconformities have been observed in sections spanning Cambrian to Devonian rocks across the Appalachian Basin. Any unconformity surface traversing Bradford County, Pennsylvania (our study site) has the potential of being an interval where CO_2 sequestration reservoirs could be concentrated. Foremost among sequestration possibilities are porous, transgressive sandstone reservoirs deposited on unconformity surfaces during local subsidence. Other possibilities are porous carbonate units that have been exposed to dissolution processes and/or dolomitic replacement during uplift and surface exposure. Both of these conditions, commonly associated with unconformities, create rock units that could be attractive CO_2 storage reservoirs.

Almost no log data are available within and near Bradford County to evaluate porous rock units below the Marcellus Shale, which handicaps any analysis of reservoir targets older than Middle Devonian. Thus if seismic-based unconformities are observed below the Marcellus Shale, it is not possible to establish definitive relationships between P and S seismic attributes related to that unconformity and log-based porosity and rock type. Seismic characterization of pre-Marcellus CO_2 storage reservoirs must therefore be based on petrophysical speculation and assumption. For this reason, data interpretation will focus on post-Marcellus rock units where log data allow some degree of seismic calibration to be done to establish links between seismic attributes and reservoir quality.

The description of potential CO_2 sequestration reservoirs in this chapter spans what is thought to be the full geologic time period in which Appalachian Basin CO_2-storage reservoir units could have been deposited. As deeper wells are drilled and more modern-log data become available, the documentation in this chapter can be extended to deeper and deeper seismic data.

Chapter 4

Research Database

Introduction

An extensive database was amassed to support this research. Key elements of the database were well logs that defined petrophysical properties of rock units and pore fluids across the study site, vertical seismic profile data that established depth registration of P and S reflection events, and surface-based 3C3D seismic data that imaged geological units with P and S wavefields. This chapter illustrates critical components of the database and discusses strengths and weaknesses of the data that were assembled for the study.

Vertical Seismic Profiles

Vertical seismic profile (VSP) data are essential for a rigorous interpretation of multicomponent seismic data. Because P and S wave modes propagate with different velocities, P-wave data position a targeted stratigraphic interval in an image-time window that is significantly different from the image-time window where S-wave data position that same stratigraphy. In addition, P-P reflectivities of interfaces associated with a stratigraphic target often differ in phase and amplitude from S-S and P-SV reflectivities of those same interfaces. Thus not only do P and S images depict a geologic target at different image-time coordinates, but the reflection character of the target may look quite different in P-wave image space than it does in S-wave image space. As a result, the greatest challenge in interpreting multicomponent seismic data is to depth register P and S wave modes so there is a rigorous correlation between a stratigraphic depth interval and its associated P-mode and S-mode image-time windows.

VSP data provide several critical pieces of information that allow interpreters to correctly position stratigraphic depth on P-wave or S-wave time-based data. Notably, VSP data permit the following steps to be taken.

1. P-wave image time can be defined as a function of depth.

2. S-wave image time can be defined as a function of depth.

3. The depth of each interface where a VSP P-P reflection occurs can be identified, and the phase and amplitude properties of reflection events from each imaged interface are recorded.

4. The depth of each interface where a VSP S-S reflection occurs can be identified, and the phase and amplitude properties of reflection events from each imaged interface are recorded.

5. The depth of each interface where a VSP P-SV or SV-P reflection occurs is identified, and the phase and amplitude properties of reflection events from each imaged interface are recorded.

6. A P-P image can be constructed as a function of two-way P-wave time.

7. A P-P image can be expressed as a function of depth.

8. An S-S image can be created as a function of two-way S-wave time.

9. An S-S image can be expressed as a function of depth.

10. P-SV and SV-P images can be constructed as functions of image time.

11. P-SV and SV-P images can be expressed as functions of depth.

Collectively, these features of VSP data allow interpreters of multicomponent seismic data to create, analyze, and compare surface-based P and S seismic attributes in depth-equivalent windows that span specific geologic targets.

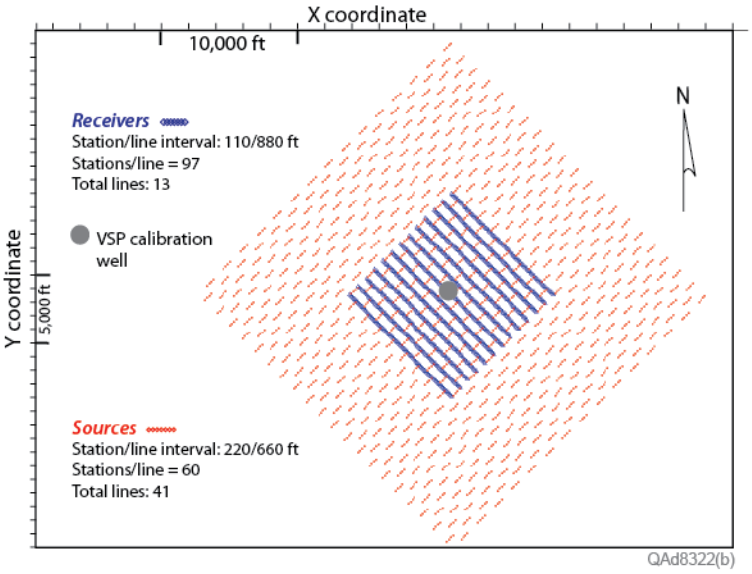

Figure 4.1. Map of study area showing location of VSP calibration well relative to planned positions of source and receiver stations used for the 3C3D seismic survey.

The VSP calibration data integrated into our database were acquired near the center of our 3C3D seismic study area as shown on Figure 4.1. The location of this calibration well was ideal for transferring VSP-based information into 3D seismic volumes for interpretation purposes. An extensive set of VSP data was acquired in this central-image well, consisting of:

- An outer walk-around survey involving 73 source stations that allowed P and S wave propagation to be analyzed at large offsets of 1 to 1.5 mi (1.6 to 2.4 km) in azimuth increments of approximately 5 degrees. Source stations occupied by this walk-around survey are shown by red station labels on Figure 4.2.

- An inner walk-around survey involving six source stations that allowed P and S velocities and images to be created at moderate offsets of 0.5 to 0.75 mi (0.8 to 1.2 km) in azimuth increments of approximately 60 degrees. These inner walk-around source stations are shown as yellow flags on Figure 4.2.

- An 18-station walk-away profile extending southeast from the receiver well approximately 1.5 mi (2.4 km). Walk-away source stations are shown as blue station flags (Fig. 4.2).

- An orthogonal-azimuth source station pair positioned approximately 0.8 mi (1.3 km) from the receiver well (green station flags, Fig. 4.2).

- A conventional zero-offset VSP with a source positioned at the walk-away station closest to the well.

The source used to generate all of these VSP data was a vertical vibrator. Wavefields generated by the orthogonal-azimuth vibrator source pair (green flags on Figure 4.2) will be used to illustrate the quality of the VSP data acquired for this study. Data from the southwest vibrator source station are exhibited on Figure 4.3, and data from the southeast station are shown on Figure 4.4. The data are transformed to a rotated coordinate system that isolates P, radial-shear (labeled as SR or SV), and transverse-shear (labeled as SH or ST) wave modes on Figures 4.3b and 4.4b. These displays show the data exhibit high-quality P and S wavefields that can be used for imaging and for P-to-S depth registration. Several downgoing and upgoing events are labeled on the wavefields to illustrate different wave modes contained in the data (Figs. 4.3b and 4.4b).

Data having quality equivalent to that shown on Figures 4.3 and 4.4 were generated at all VSP source stations. As a result, the VSP calibration data integrated into the project database are ideal for depth registering P and S data, assisting interpretation of P and S geological images, and analyzing P and S wave propagation across our study site. Interpretation applications of these VSP data are illustrated and discussed in Chapter 9.

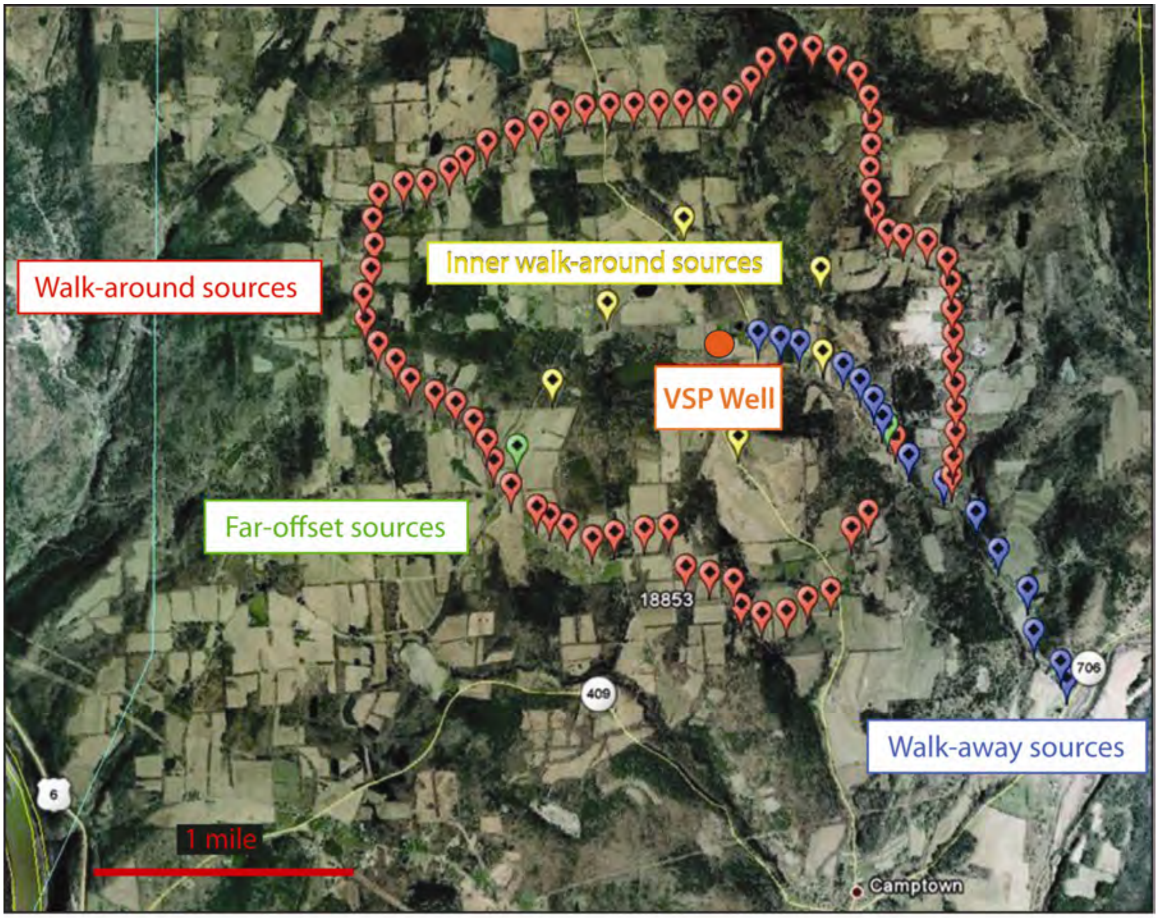

Figure 4.2. Source stations utilized in VSP data acquisition. Data acquisition included a 73-station outer walk-around (red stations), a 6-station inner walk-around (yellow stations), an 18-station walk-away (blue stations), a 2-station orthogonal-azimuth pair (green stations), and a zero-offset station (blue station closest to the well).

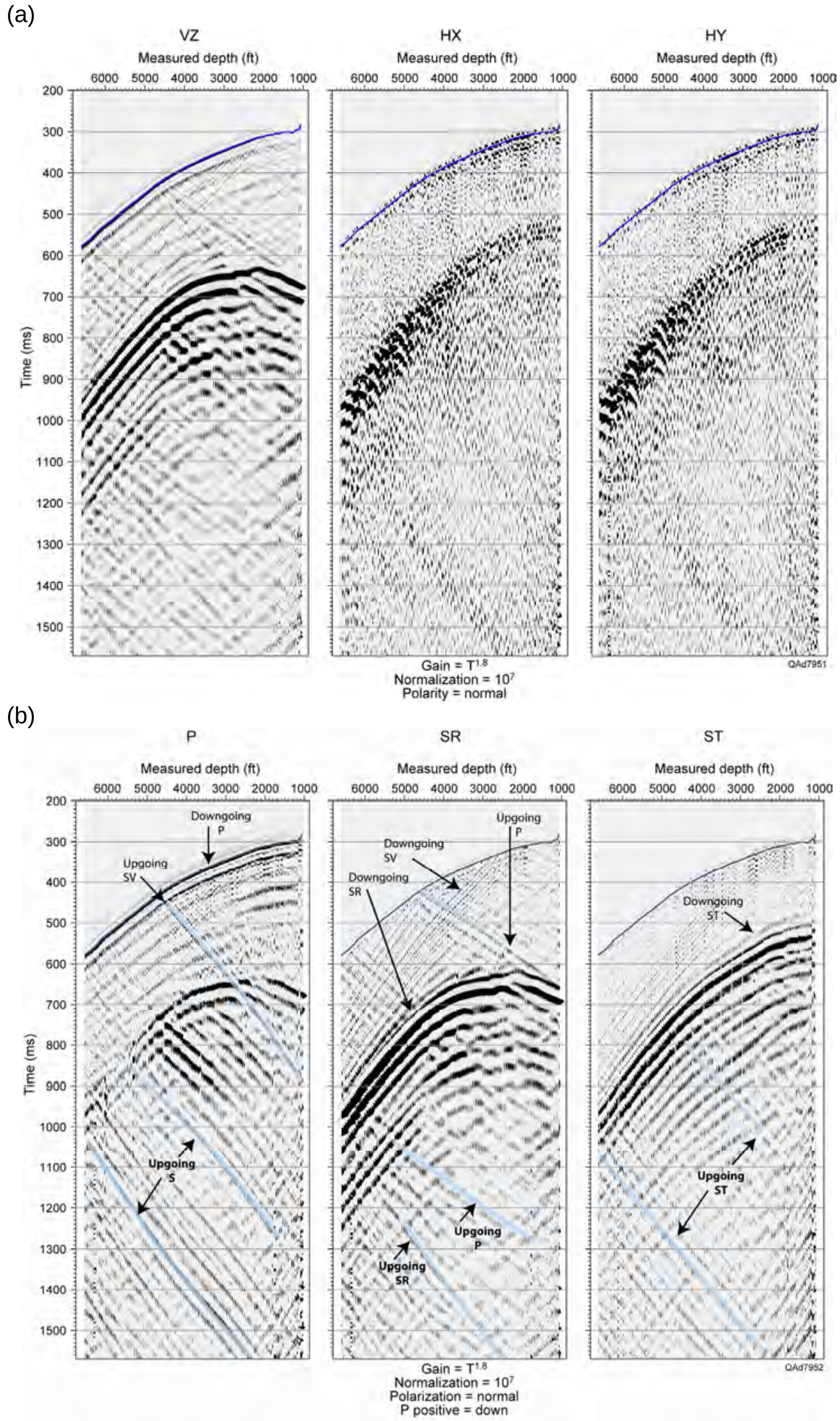

Figure 4.3. VSP data acquired when the source was at the green-flag station southwest of the receiver well. (a) Raw data as recorded. (b) Data after coordinate rotation to P, S-radial (labeled SR or SV), and S-transverse (labeled ST or SH) data space.

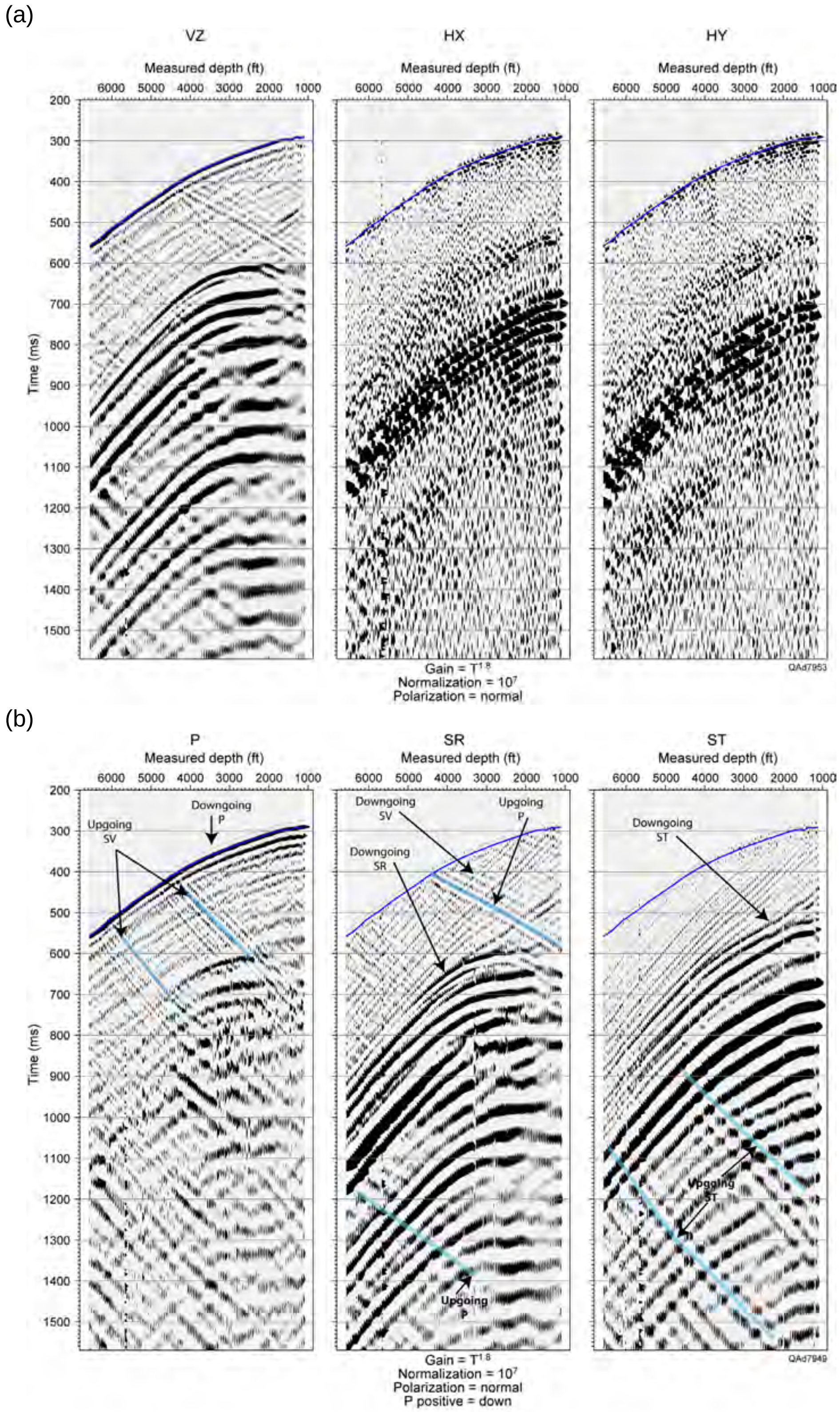

Figure 4.4. VSP data acquired when the source was at the green-flag station southeast of the receiver well. (a) Raw data as recorded. (b) Data after coordinate rotation to P, S-radial (labeled SR or SV), and S-transverse (labeled ST or SH) data space.

3C3D Seismic Data

The survey design that was supposed to be used to acquire 3C3D seismic data across the study site is illustrated on Figure 4.1. As discussed in Chapter 7, the source-receiver geometry shown on this presurvey plot had to be modified as equipment was deployed because surface conditions prevented a significant number of source stations, as well as several receiver stations, from being positioned where this design placed those stations. The final source-receiver arrangement that was deployed is illustrated and discussed in Chapter 7 and will not be repeated here.

The energy source used to generate surface-based P and S data across this 3D survey was an explosive charge of 1 kg (2.2 lb) positioned at a depth of 6 m (20 ft). This is a different source type than the vertical vibrator used to generate VSP data recorded in the calibration well at the center of the 3D image space. Examples of trace gathers created from responses of vertical, radial-horizontal, and transverse-horizontal surface geophones are displayed on Figures 4.5 and 4.6. These data are surface-sensor equivalents of the P, SR (or SV), and ST (or SH) data recorded by the downhole vertical-sensor array exhibited on Figures 4.3 and 4.4. Because the VSP calibration data show robust SR and ST shear modes propagate to deep depths and illuminate geological targets, reflected SR and ST events must be embedded in these surface-based sensor responses even though they are not easily seen in unprocessed data. One of the major challenges of this research was to extract reflected P and S modes embedded in the 3C3D data and to demonstrate the geological value of those modes. The interpreted reflections shown on Figure 4.6 are labeled “Tully” and “Marcellus” with question marks added to emphasize these data are not yet rigorously calibrated to subsurface geology. The intent is only to illustrate that robust S-wave reflections appear on radial-horizontal and transverse-horizontal geophones. Upon examination of several such trace gathers, a general observation that can be made is ***the 3C3D seismic data used in this study have good signal-to-noise properties and provide an excellent opportunity to demonstrate the value of multicomponent seismic data for evaluating CO_2 sequestration reservoirs and seals.***

Other valuable components of the 3C3D seismic database were three processed data volumes—a P-P volume and two P-SV volumes (a fast-S volume and a slow-S volume)—that Geokinetics produced from the 3C3D data and provided for our study. Interpretations of these 3D data volumes are illustrated and discussed in Chapter 9 and will not be presented here. Because the purpose of this chapter is only to describe the research database, it is sufficient to show selected examples of vertical slices through the image volumes to illustrate P and S data quality. Such example profiles are displayed on Figure 4.7a through 4.7d.

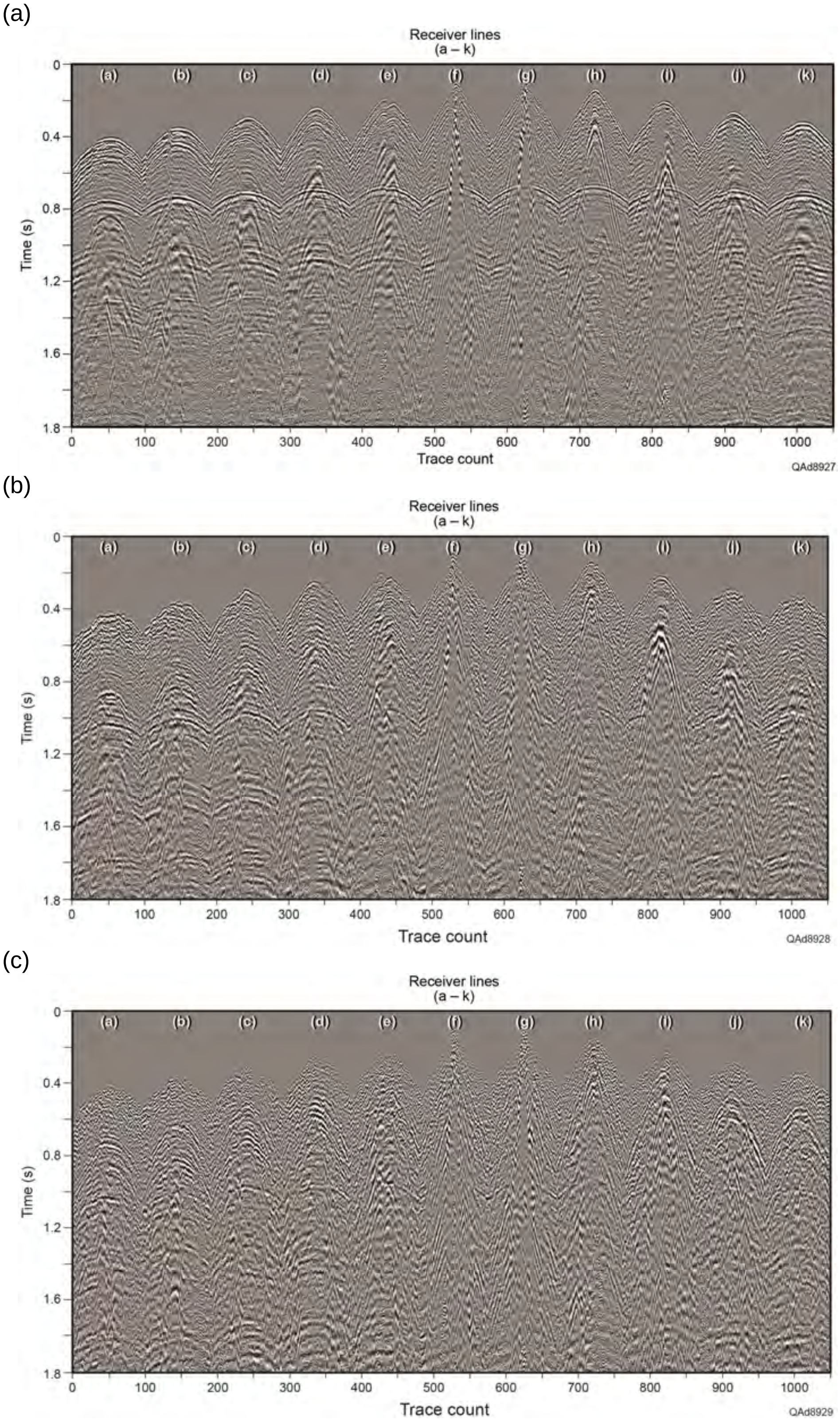

Figure 4.5. Trace gathers of responses of (a) vertical geophones, (b) radial-horizontal geophones, and (c) transverse-horizontal geophones from the 3C3D seismic data used in this investigation.

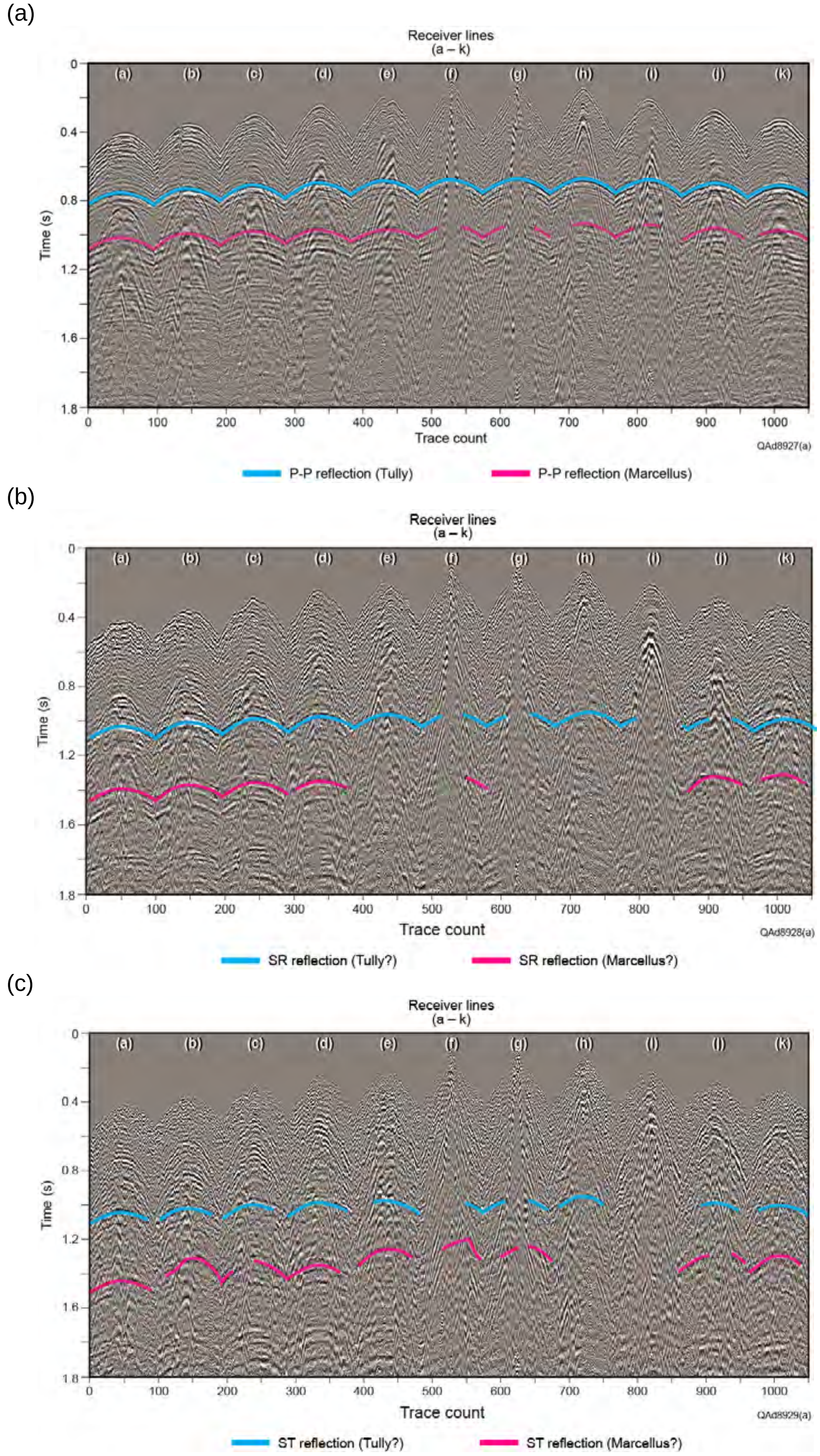

Figure 4.6. Interpreted trace gathers of responses of (a) vertical geophones, (b) radial-horizontal geophones, and (c) transverse-horizontal geophones.

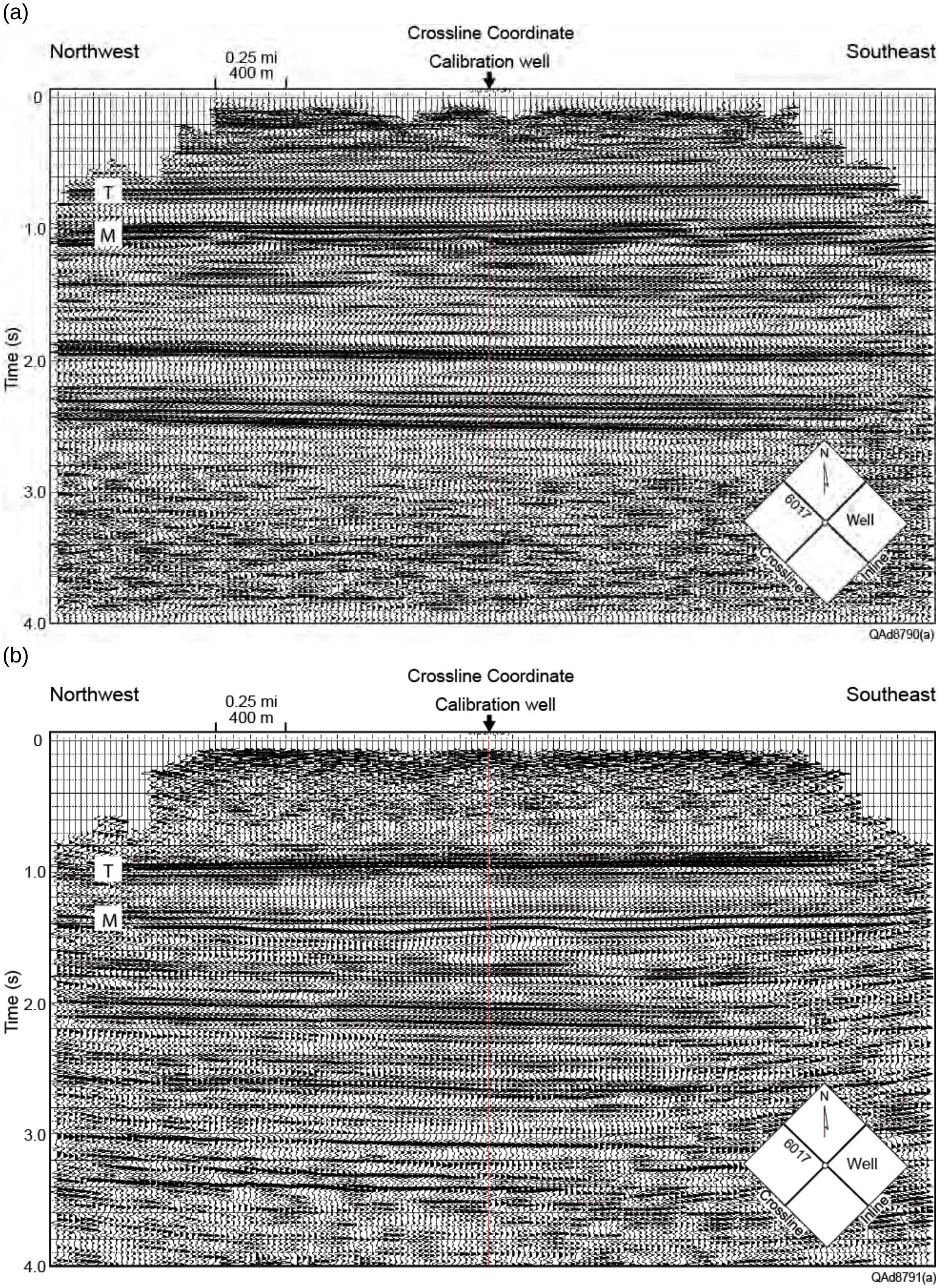

Figure 4.7. Vertical slices through (a) P-P, and (b) P-SV volumes constructed from the 3C3D seismic research data. These northwest-southeast profiles follow inline coordinate 6017 that passes through the central calibration well. T = Tully Limestone. M = Marcellus Shale.

(c)

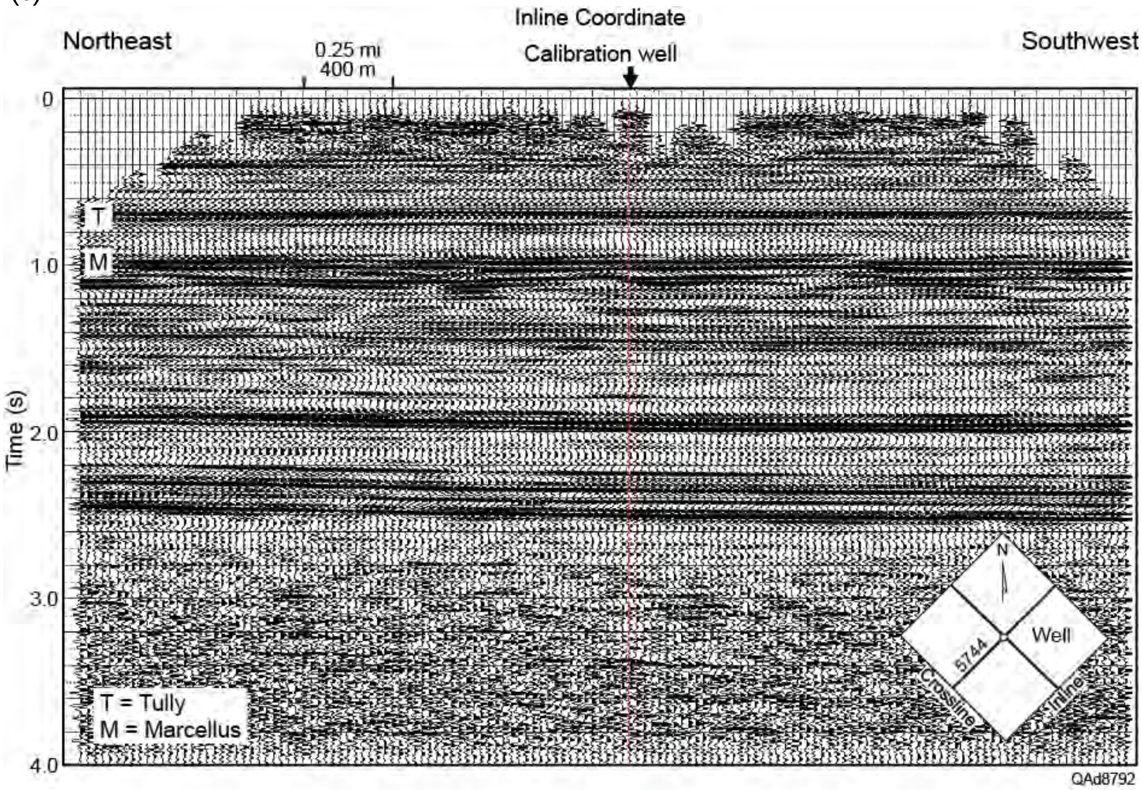

(d)

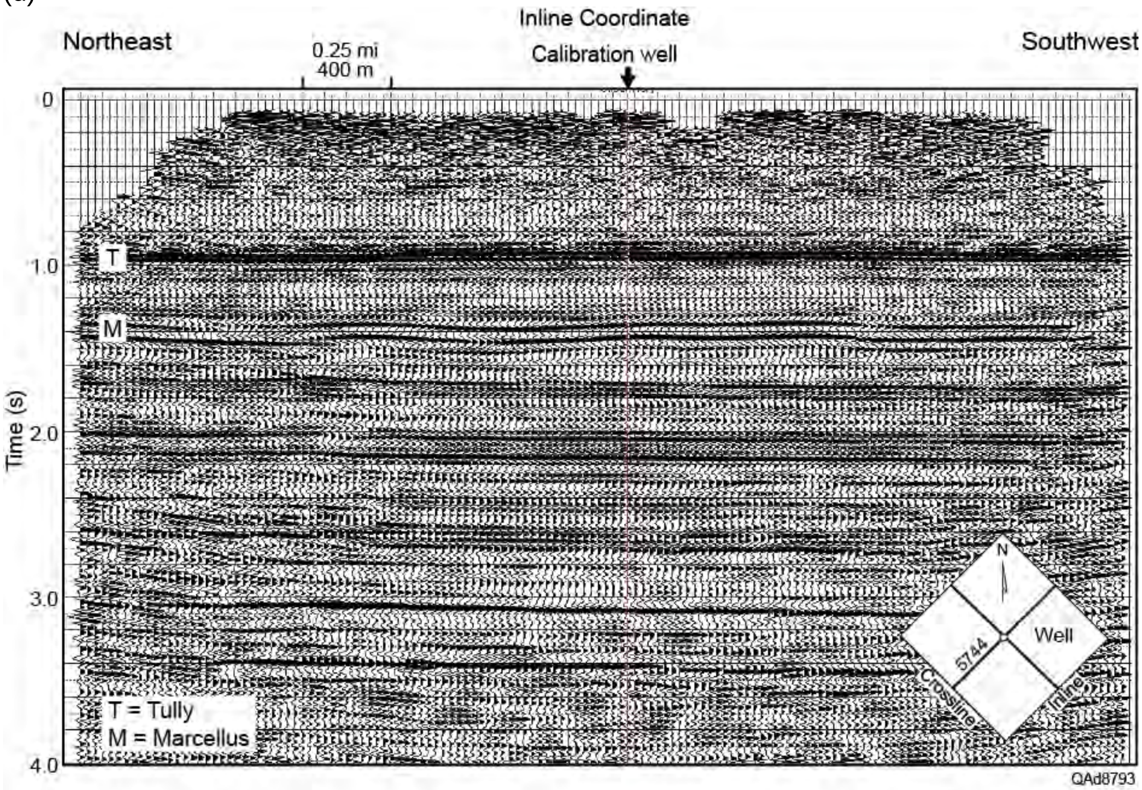

Figure 4.7 continued. (c) Vertical slice through P-P volume and (d) P-SV volume that follows southwest to northeast profile 5744.

These vertical slices verify that targeted geology is presented as high-quality P-P and P-SV images. Specific examples of P and S definitions of faults, sequences, and facies are provided in Chapter 9.

Well Log Data

Log data acquired in the VSP calibration well at the center of the 3D seismic image space (Fig. 4.1) were an important part of the research database. These logs allowed direct correlations between rock and fluid properties and multicomponent seismic attributes that spanned the well position. The logged well was a horizontal exploration well targeting the Marcellus Shale, and drilling terminated when the well reached the Onondaga Limestone immediately below the Marcellus. The well was then kicked-out from its vertical track a short distance above the Marcellus and drilled laterally through the Marcellus interval. Because of this drilling strategy, petrophysical properties of potential CO_2 sequestration reservoirs below the Oriskany Sandstone (a short distance below the Onondaga Limestone) were not logged.

Gamma-ray (GR) and velocity logs acquired in the central-image calibration well are displayed on Figure 4.8. The low-GR/high-velocity interval response between 4400 and 4500 ft (1341 and 1372 m) is the Tully Limestone. The high-GR/low-velocity interval response between 6100 and 6500 ft (1859 and 1981 m) is the Marcellus Shale. V_P and V_S velocities are also relatively high for the entire drilled interval, which is a second implication that porosity in all logged rock units is low to moderate. However, porosities in some intervals are still sufficient to justify evaluating those intervals for CO_2 storage potential.

Fast-S and slow-S velocities calculated from dipole sonic-log data by the well-log contractor (Halliburton) show only minor differences across the entire well depth (Fig. 4.8c). The anisotropy curve plotted on Figure 4.8d is a measure of the difference between slow-S velocity [V_S(slow)] and fast-S velocity [V_S(fast)] calculated as,

$$\text{(4.1)} \qquad \text{ANISO} = \{ [V_S(\text{fast}) - V_S(\text{slow})] \,/\, V_S(\text{slow}) \} \times 100.$$

In this equation, ANISO is the S-wave velocity anisotropy value plotted on Figure 4.8d. The anisotropy calculated for the entire logged interval is only 1 to 2 percent. This low value of S-wave anisotropy was unexpected, particularly for the Marcellus Shale, because the Marcellus supposedly has a dense population of orthogonal joints, which were initially assumed would produce significant azimuthal anisotropy. This dipole sonic log thus introduces an interesting and important research problem—the need to do independent measurement, quantification, and modeling of S-wave propagation in orthorhombic media associated with CO_2 sequestration reservoirs and particularly with sealing units above CO_2 storage reservoirs.

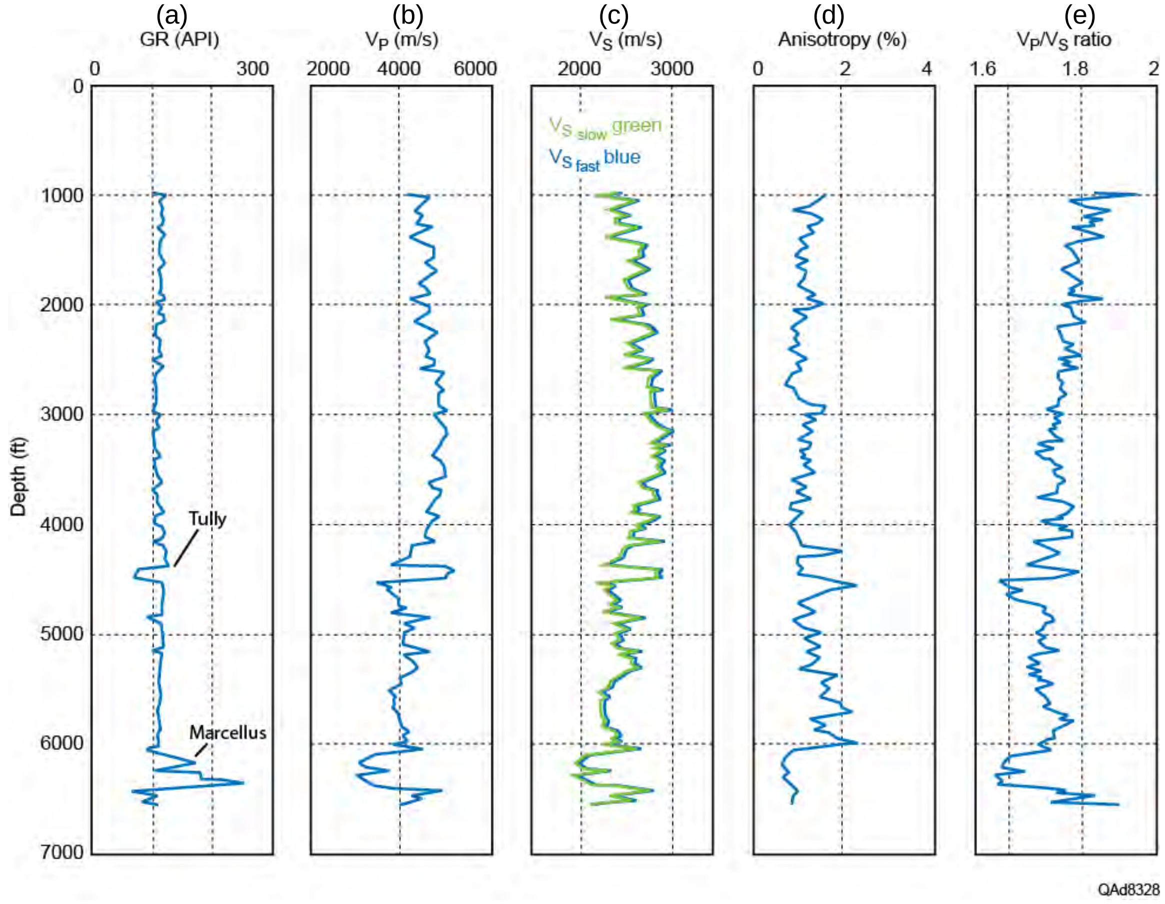

Figure 4.8. (a) Gamma-ray and (b) V_P and (c) V_S velocity logs acquired in the calibration well at the center of the 3D seismic image space. Both fast-S and slow-S velocities are shown on (c) and are used to calculate S-wave anisotropy (d). The V_P/V_S velocity ratio (e) uses the fast-S velocity.

Additional logs acquired in the central-image calibration well are displayed as Figure 4.9. The gamma-ray log is repeated to aid correlation with companion logs on Figure 4.8. The porosity log displayed on Figure 4.9c is particularly important because it indicates the interval below the Tully Limestone (below 4500 ft [1372 m]) has porosities of 15 percent to 18 percent. This porosity range is attractive for CO_2 sequestration reservoirs.

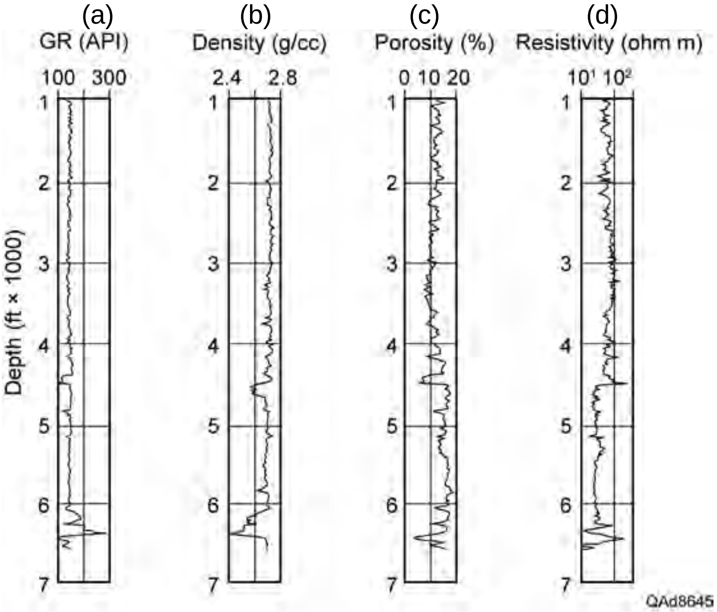

Figure 4.9. Additional logs acquired in the central-image calibration well. (a) Gamma-ray log. (b) Bulk density. (c) Neutron porosity. (d) Deep resistivity.

Commercial and public well log databases were searched to locate additional logs local to our study area. These efforts were moderately successful. Thousands of wells have been drilled and logged in Pennsylvania, but the majority of these wells are not of significant value to this research because they: (1) are shallow and do not reach depths of many CO_2 sequestration targets, or (2) have minimal logging suites often consisting of only a gamma-ray curve. Wells local to our Bradford County study area where logs were located are indicated on Figure 4.10. Gamma-ray logs along the three labeled profiles, AB, CD, and EF, are displayed in cross-section formats on Figure 4.11.

The logs are helpful in that they show the consistent nature of the Tully Limestone and Marcellus Shale over a wide area. They are not encouraging in the sense that they show no obvious thick, clean-sandstone intervals that could be candidates for CO_2 sequestration reservoirs. The decreased GR interval labeled “SS ?” (for “sandy ?”) on profile AB (Fig. 4.11a) is encouraging evidence of possible CO_2 storage reservoir rock, but that trend does not seem to extend to our study area. A message emphasized by these logs is that a principal challenge of our study would be to locate units with sufficient porosity to be considered as CO_2 sequestration reservoirs. As has been noted, porosities below the Tully Limestone follow a consistent trend of 15 percent to 18 percent (Fig. 4.9) within our 3D seismic image space. These porosities and their associated depths of more than 4500 ft (1372 m) make pre-Tully Middle Devonian units our preferred candidates for CO_2 sequestration reservoir targets.

A compilation of logged wells integrated into the database and the log suites associated with those wells are provided as Table 4.1.

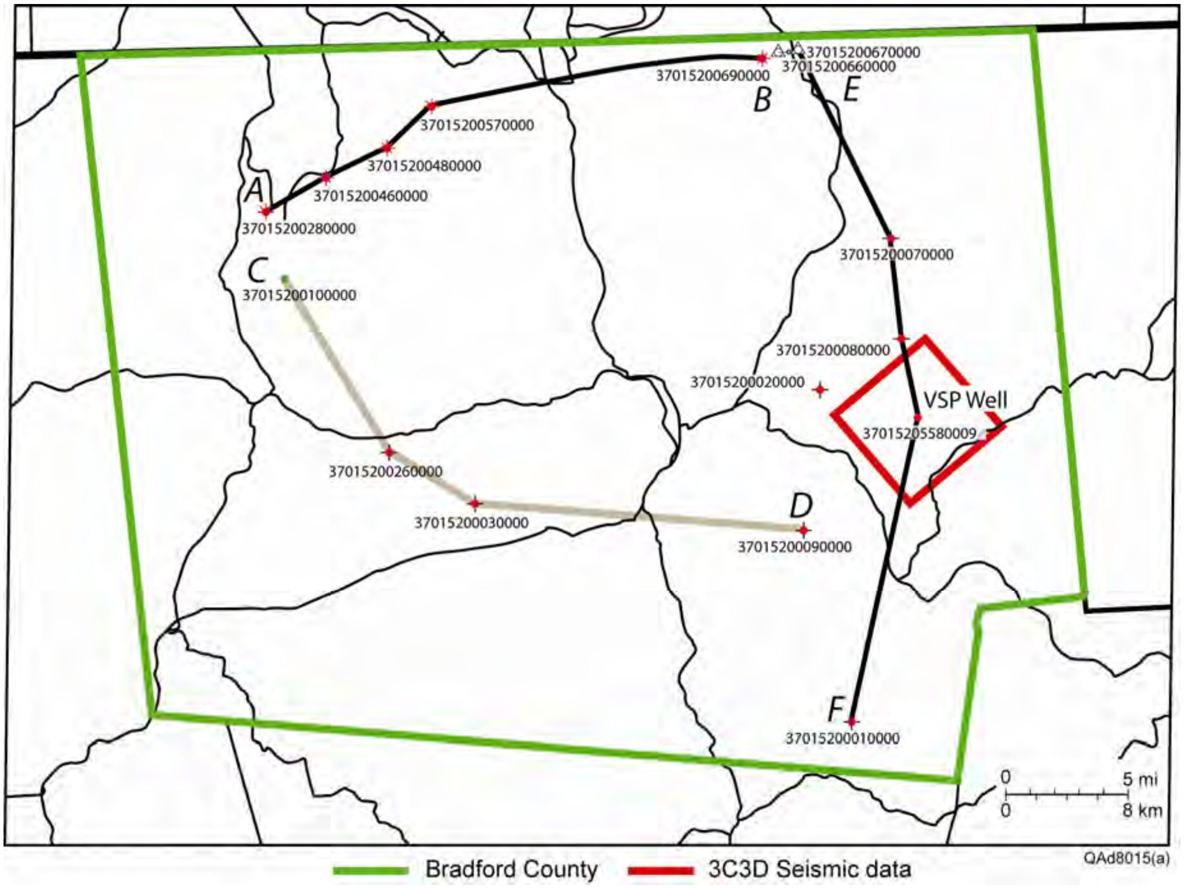

Figure 4.10. Logged wells local to the study site that were integrated into the research database.

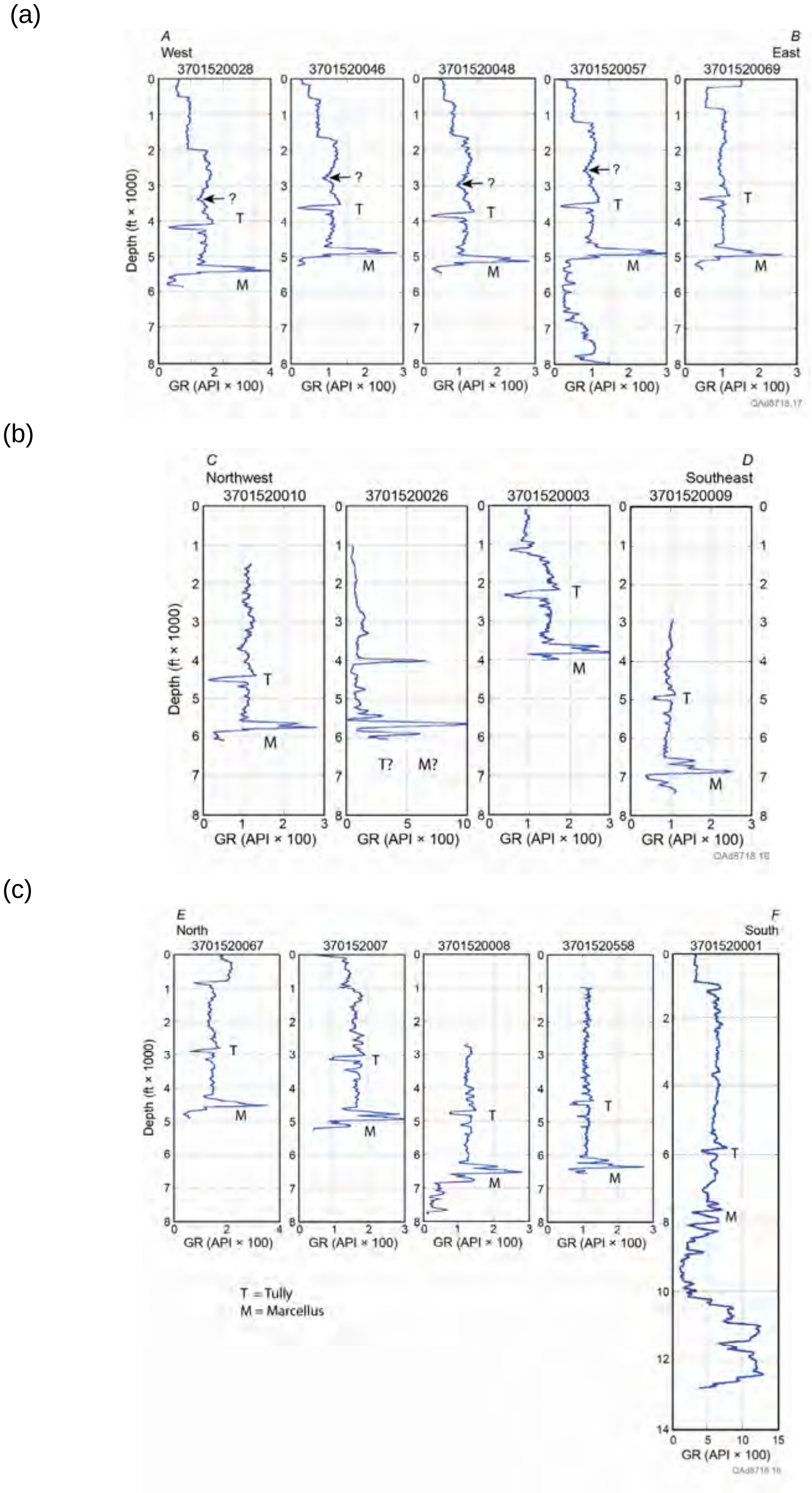

Figure 4.11. Gamma-ray logs along the three profiles labeled on Figure 4.10. (a) Cross section A-B. The label SS**?** identifies an interval above the Tully that is “possibly sandy.” (b) Cross section C-D. (c) Cross section E-F. **T** = Tully. **M** = Marcellus.

Table 4.1. Well Log Database

Well API	Depth (ft)	Log curves
3701520001	12,852	GR, ILD, rhob
3701520002	6617	GR, ILD, rhob
3701520003	4094	GR, rhob
3701520007	5267	GR, ILD, rhob
3701520008	7846	GR, rhob
3701520009	7505	GR, rhob
3701520010	6123	GR, ILD, ILM, rhob, NPHI
3701520026	6070	GR, LLD, LLS, rhob, cal, DT, NPHI, PEF
3701520028	5922	GR, ILD, ILM, rhob, NPHI, cal, PEF
3701520046	5280	GR, ILD, ILM, rhob, NPHI, cal, PEF
3701520057	5442	GR, rhob, NPHI, cal, PEF, gas temp
3701520066	4935	GR, rhob, RLA5, RLA3, RLA2, NPHI, cal, PEF
3701520067	4812	GR, rhob, RLA5, RLA3, RLA2, NPHI, cal, PEF
3701520069	5387	GR, rhob, RLA5, RLA3, RLA2, NPHI, cal, PEF
3701520070	5034	GR, TT
3701520558	6582	GR, RO90, RO60, RO30, RO20, RO10, RT90, RT60, RT30, RT10, RF90, RF60, RF30, RF20, RF10, rhob, cal, DT, DTFast, DTslow, ANISO, NPHI, PEF

Abbreviations:

ANISO : Shear-wave anisotropy (%)
cal: Caliper (inch)
DT: Compressional transit traveltime (microsec/ft)
DTFast: Fast polarization for the shear transit traveltime (microsec/ft)
DTSlow: Slow polarization for the shear transit traveltime (microsec/ft)
GR: GR (API units)
ILD: Deep induction log (ohm.m)
ILM: Medium induction log (ohm.m)
NPHI: Neutron porosity (%)
PEF: Photoelectric factor (V/V)
rhob: Bulk density (gm/cm^3)
RLA5, RLA3, RLA2, RO90, RO60, RO30, RO20, RO10, RT90, RT60, RT30, RT10, RF90, RF60, RF30, RF20, RF10: Various electrical resistivity measurements with different penetration depths (ohm.m)
TT: Transit time (microsec)

Conclusions

The database assembled for this study is excellent with respect to the quality of its 3C3D seismic data, which are the primary data needed for this research. The database is also excellent with respect to the calibration VSP data that were acquired at the center of the 3C3D seismic survey. Likewise, well logs acquired in the calibration well at the center of the seismic image space are modern, extensive, and excellent quality. In short, all data acquired within the immediate study area are high-quality and complete in almost every aspect required for our research.

A disappointing aspect of the database is that well logs acquired outside the study area are limited in type, variety, and quality from what is desired for detailed petrophysical analysis. It is difficult to define trends of attractive CO_2 sequestration reservoirs and to project these trends into the study area using these public logs. Some speculation will be required to identify CO_2 storage targets inside the 3C3D seismic image space, particularly those deeper than the Marcellus Shale because no local log data have been found that span pre-Marcellus geology.

Assembling an appropriate research database was a critical research step in our proposed work plan. Although the amount and quality of well log data surrounding our study area were not what we wished, the variety and quality of data inside the seismic image space were superb. The database we created has exceeded the expectations we had at the start of the project.

Chapter 5

Rock Physics

Introduction

Among the methods for monitoring sequestered CO_2, 3D seismic surveying provides the volumetric measurements needed to understand the distribution of CO_2 in 3D space. However, seismic-monitoring strategy and methods have to be implemented in ways that allow the effects of CO_2 saturation to be exhibited on P-wave and S-wave seismic attributes. It is thus essential to build quantitative links between measured seismic properties of rocks containing CO_2 and the CO_2 saturation in the porous spaces of those rocks. These quantitative links are defined by rock physics theories that describe elastic properties of porous media partially saturated with CO_2.

The elastic properties of rocks in which CO_2 is injected, and the effects of these properties on P and S seismic velocities, depend on

1. Elastic properties of the dry mineral frame,
2. Porosity and pore shapes (cracklike pores vs. spherical pores),
3. Elastic properties of the fluid phases in the pores,
4. Fluid saturations and the mixing law for the fluids (fine-scale, homogeneous mixing, or patchy saturation), and
5. In situ conditions, which include effective pressure, confining pressure, pore pressure, and temperature.

These topics are now considered in sequence.

Elastic Properties of Dry Mineral Frames

During CO_2 injection, the mineral matrix of a reservoir rock is affected by increasing pore pressure, which causes the in-situ stiffness of the mineral frame to weaken. To first order, the change in the stiffness of the mineral matrix is due to the change in effective pressure, which is the difference between lithostatic pressure and pore pressure. Therefore, we need to develop quantitative rock-physics models that take into account changes in elastic properties of a host rock that are related to fluid changes during CO_2 injection and also changes occurring in the mineral frame.

One possible theoretical model that accounts for changes in the elastic moduli of the mineral frame is the **self-consistent approximation (SCA)** introduced by Berryman (1995). This model accounts for changes that occur within the dry mineral frame due to variation in pore pressure. Changes in effective pressure affect the fraction of cracklike porosity that is most pressure dependent, these being pores with a small aspect ratio. Pores with small aspect ratios are considered to be soft, or compressible, and more easily closed. Pores with large aspect ratios are considered to be incompressible.

Porosity and Pore Shape

Figure 5.1 presents modeling results for the bulk modulus of a CO_2 host rock as a function of effective pressure for a theoretical dry sample with 14-percent porosity and calcite composition. Such a rock matrix is representative of Middle Devonian rock units positioned between the Tully Limestone and the Marcellus Shale at our study site. The boxes represent the dry mineral frame, with the black regions corresponding to the mineral frame and the white ellipsoids corresponding to pores with various aspect ratios. The bulk modulus increases with effective pressure because the mineral frame stiffens as cracklike pores (pores with low aspect ratios) close. The relationships between seismic-mode velocities and pressure depend on the shape (aspect ratio) of the cracks that close at a given effective pressure. Even if the fraction of porosity that is pressure dependent is small, perhaps only a few percentages of the total porosity, this fraction has a strong impact on velocity-pressure dependence.

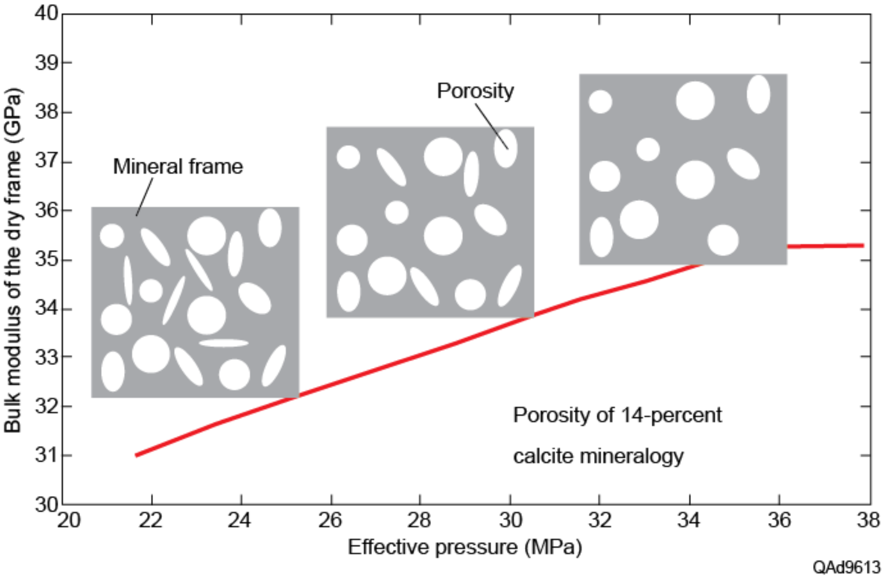

Figure 5.1. Bulk modulus of the dry mineral frame for a theoretical sample with 14-percent porosity as a function of effective pressure calculated using Berryman's (1995) self-consistent approach (black curve). The boxes represent the dry mineral frame. Black regions are the mineral framework, and white ellipsoids are pores with various aspect ratios. The bulk modulus increases with effective pressure because the mineral frame stiffens as more cracklike pores close.

The model assumes a distribution of pores with various aspect ratios. The distribution of aspect ratios for a particular host rock can be determined by measuring the velocity-pressure dependence in a laboratory using rock samples from a sequestering formation. If such laboratory measurements are not possible, analogs can be used from published laboratory data in which velocity versus effective pressure behavior has been studied using similar host rocks.

This analog approach is used here by referring to laboratory measurements made on stiff, West Texas carbonate rocks that are similar to possible host rocks local to our Bradford County study area. Figure 5.2 shows laboratory measurements performed on dry samples from the Sacroc EOR unit operated by Kinder Morgan in Scurry County, Texas. P-wave and S-wave velocities are shown as a function of effective pressure. Although these cores are not from our study area, these laboratory tests provide insights into the expected pressure dependence of elastic properties of host rocks similar to rocks at our Bradford County site and illustrate the applicability of the theoretical approach presented here.

Laboratory measurements indicate both P and S-wave velocities increase as effective pressure increases, due to closing of crack-like pores and stiffening of grain boundaries. Superimposed on both panels are our theoretical modeling results for P-wave velocity and S-wave velocity as a function of effective pressure, using Berryman self-consistent approach. There is an acceptable agreement between the modeling results and the actual laboratory measurements.

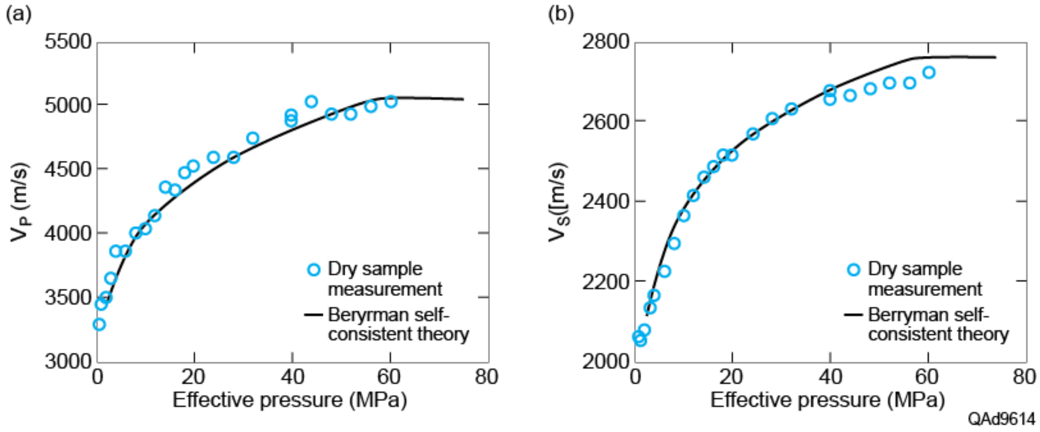

Figure 5.2. Laboratory measurements performed on dry samples from the Sacroc EOR unit (West Texas) presented in blue circles. (a) P-wave velocity, and (b) S-wave velocity as functions of effective pressure. Data courtesy of Chris Purcell and William Harbert, University of Pittsburgh. Superimposed as black curves are P-wave and S-wave velocity behaviors in the dry mineral frame calculated using Berryman (1995) self-consistent approach.

Elastic Properties of Fluid Phases (CO_2 and Brine)

Elastic properties of CO_2 and brine depend on pressure and temperature. Figure 5.3 shows the variation in density of CO_2 and brine as functions of pore pressure. In each plot, the suite of curves correspond to different temperature values, with the arrow indicating increasing temperature from 90°F to 180°F, by 10°F increments. The salinity of brine is assumed to be 59,000 ppm.

This analysis shows the density of CO_2 is much more sensitive to pressure and temperature than is brine. Also, the density of brine is higher than the density of CO_2 for all values of pressure and temperature considered. However, for high pore pressures (>20 MPa) and low temperature (90° F), the density of supercritical CO_2 is relatively high, and approaches the density of brine.

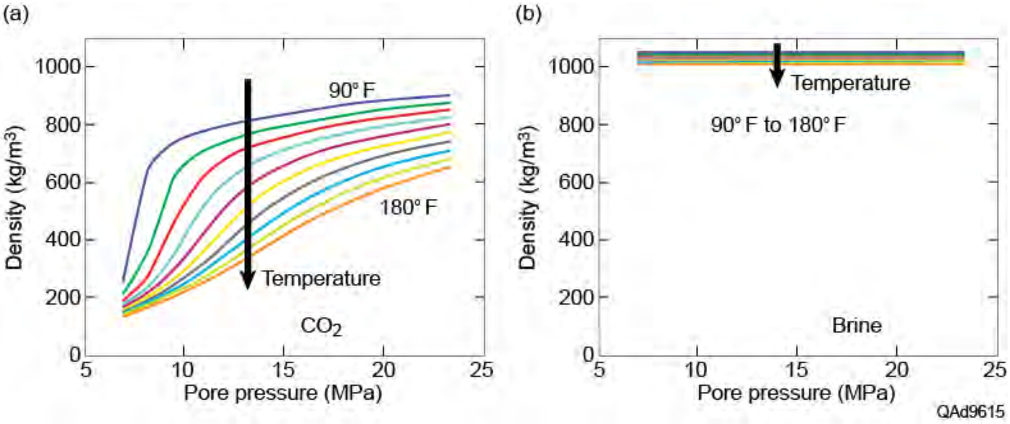

Figure 5.3. Density as a function of pore pressure for (a) CO_2 and (b) brine. Different curves correspond to different temperatures. The arrows indicate the direction of increasing temperature, which varies from 90^0 F to180^0 F in 10^0 F increments.

Figure 5.4 shows the P-wave velocity of CO_2 and brine as functions of pore pressure. Again, different curves correspond to different temperature values, with the arrow indicating increasing temperature from 90°F to 180°F at increments of 10°F.

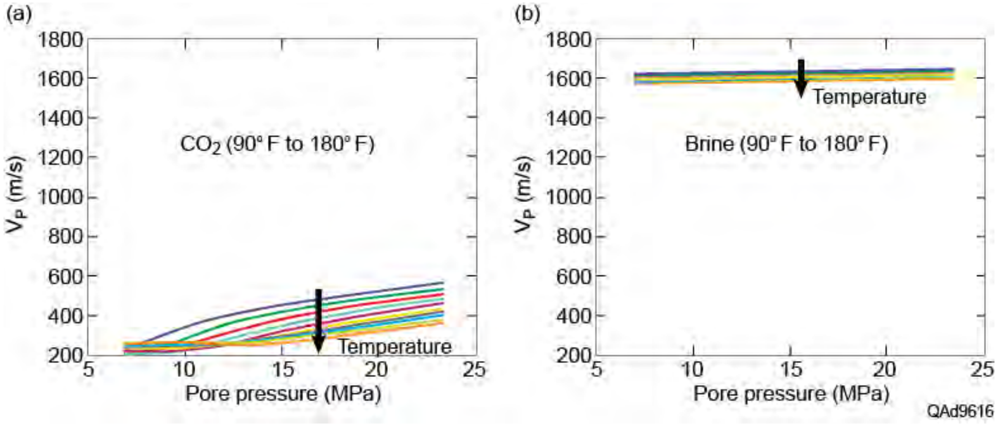

Figure 5.4. P-wave velocity as a function of pore pressure for (a) CO_2 and (b) brine. Different curves correspond to different temperatures. The arrow indicates the direction of increasing temperature from 90°F to 180°F at 10°F increments.

Fluid Saturation and Mixing Laws

When CO_2 is injected into a porous formation, it will mix with the brine present in the pore spaces. Brine and CO_2 can mix at two scales, either:

1. fine scale, which generates a homogeneous saturation, or
2. large scale, which generates a patchy saturation.

The elastic properties of a mixture of brine and CO_2 depend on the volumetric fraction of each of the fluid phases, and whether the mixing law applies to homogeneous saturation, or to patchy saturation. The bulk modulus of a fluid mixture with homogeneous saturation can be estimated using a Reuss average; whereas, the bulk modulus of a fluid mixture with patchy saturation can be estimated using a Voigt average. These Reuss and Voigt averages can be considered as lower and upper bounds,respectively, for the elastic properties of the fluid mixture.

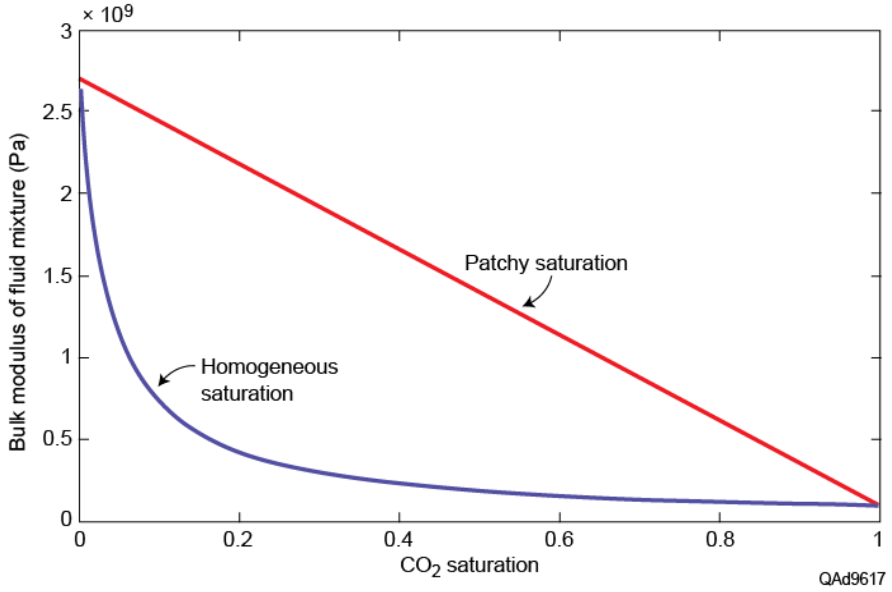

Figure 5.5. Bulk modulus for the mixture of CO_2 and brine for homogeneous (blue) and patchy (red) saturations.

Figure 5.5 presents the computed bulk modulus for mixtures of CO_2 and brine as a function of CO_2 saturation. The two curves represent upper and lower bounds for the bulk modulus of the mixture. The upper bound is represented by Voigt averaging (a patchy saturation assumption), while the lower bound is represented by Reuss averaging (a homogeneous saturation). In this example, pore pressure is 17.5 MPa, and temperature is 130° F. The bulk modulus of the fluid mixture decreases with increasing CO_2 saturation for both saturation cases: patchy and homogeneous. However, there is a large uncertainty in the elastic modulus for mixtures of CO_2 and brine which depends on the mixing scale of the two fluid phases. If the CO_2 phase is finely dispersed in the brine phase, then a change of a few percentage points in CO_2 can lower the bulk modulus significantly (Reuss averaging). In contrast, if the CO_2 is present in big patches, the bulk modulus of the mixture decreases linearly as CO_2 saturation increases (Voight averaging).

Effects of In Situ Conditions

We consider here the effects of in situ temperature and effective pressure on seismic velocities as CO_2 concentration varies in a CO_2 sequestration interval. After the elastic properties and V_P and V_S velocities of the dry mineral frame of the sequestering formation are modeled as functions of effective pressure, Gassmann (1956) theory can be used to predict velocities corresponding to a fluid-saturated mineral frame. This theory assumes the shear modulus of a rock does not change with fluid saturation, but bulk modulus does. This assumption is based on the principle that fluids have no shear strength. As a result, P-wave velocity is sensitive to changes in pore fluids, but S-wave velocity varies only when there are significant changes in fluid density across a fluid-contact boundary. When the difference between fluid densities is large, S-wave velocity and bulk density may be useful for mapping fluid distributions. In such applications, density information can be extracted from reflectivities of converted P-SV waves at large incidence angles.

To illustrate fluid effects on velocities, three theoretical reservoirs having porosity values of 5-percent, 10-percent, and 20-percent will be considered as potential targets for CO_2 sequestration. In this analysis, the theoretical rocks are fully saturated with either brine or CO_2 in order to calculate the maximum theoretical differences that can occur in elastic properties as CO_2 is injected. For any other mixture of CO_2 and brine, the magnitudes of P and S velocities are between these computed end members.

First, we consider the theoretical case of a sandstone with 5-percent porosity. This model could correspond to the Lower Devonian Oriskany/Ridgeley sandstone that lies below the Onandaga Limestone/Needmore Formation in our study area. This sandstone has relatively low porosity and limited storage capacity, but is considered as a potential target for CO_2 injection (Kostelnik and Carter, 2009b).

Figure 5.6 presents a plot of the differences between P-wave velocity in a brine-saturated rock and in a CO_2-saturated rock, as a function of effective pressure and temperature. Velocity differences are small, as expected for a rock with low porosity. The maximum difference is approximately 35 m/s, which occurs at low temperature and low effective pressure.

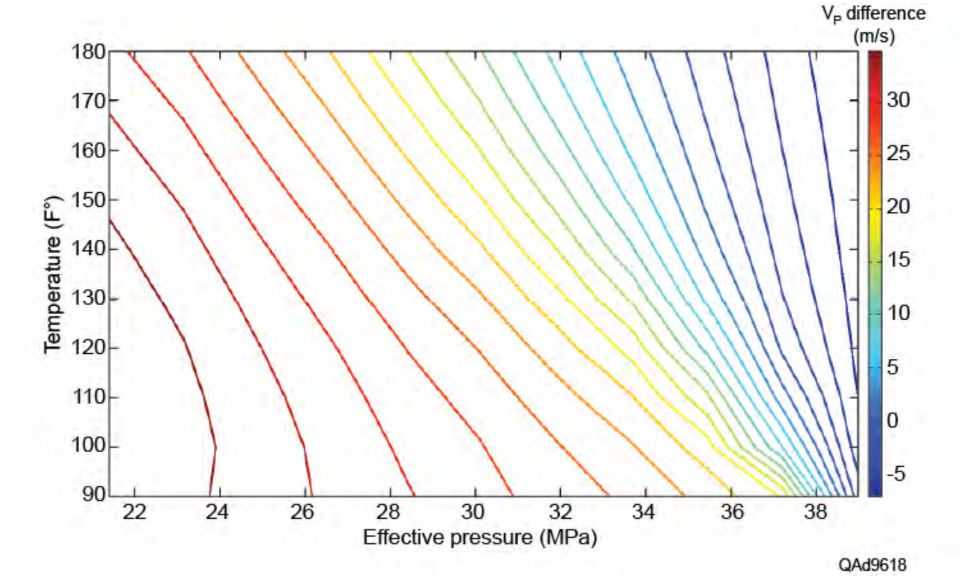

Figure 5.6. Model results showing differences in P-wave velocity for a sandstone saturated with brine versus a sandstone saturated with CO_2 as effective pressure and temperature are varied. The sandstone is assumed to have 5-percent porosity.

Figure 5.7 presents the plot of the differences between S-wave velocity in a brine-saturated rock and in a CO_2-saturated rock for the same ranges of effective pressure and temperature. As Gassmann fluid substitution theory predicts, differences in S-wave velocities occur because of changes in pore-fluid density. All velocity differences are negative because the bulk-density factor appears in the denominator of the V_S velocity equation. The larger density of a brine-saturated rock makes S-wave velocity less than it would be in a lower-density CO_2-saturated rock. The maximum difference is approximately 30 m/s at higher temperature and higher effective pressure, because as shown on Figure 5.3, the density difference between brine and CO_2 is larger at higher temperature and lower pore pressure. Lower pore pressure corresponds to higher effective pressure.

We conclude that for lower-porosity sandstones, with average porosities of 5-percent, it is difficult to use velocities (or bulk density) to determine whether CO_2 or brine fills the porous space of a reservoir.

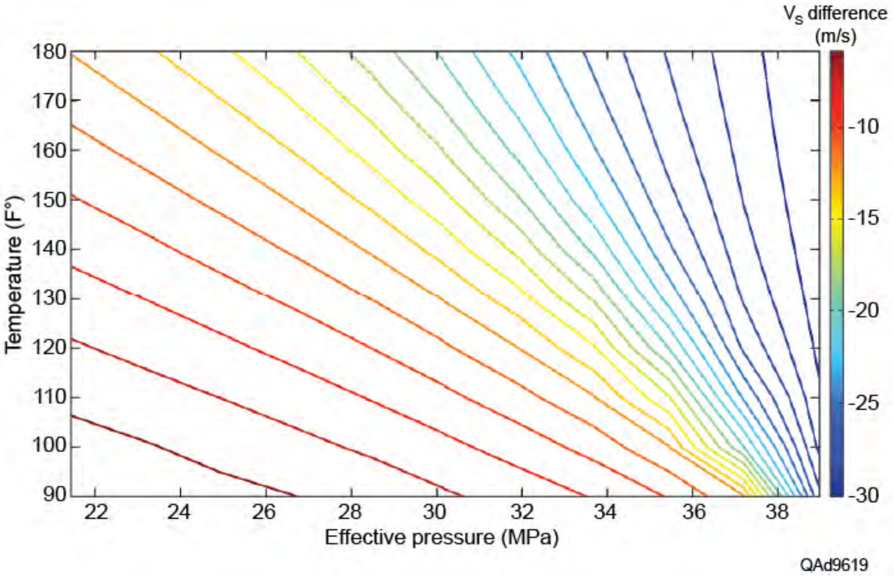

Figure 5.7. Model results showing differences between S-wave velocity in a sandstone saturated with brine versus a sandstone saturated with CO_2 as effective pressure and temperature vary. The sandstone is assumed to have 5-percent porosity.

Next we consider a theoretical sandstone with an average porosity of 10-percent, which is a reasonable approximation of Oriskany sandstones local to our study area. Figure 5.8 shows a plot of the differences between P-wave velocity in a brine-saturated rock and in a CO_2-saturated rock as a function of temperature and effective pressure. For a sandstone with 10-percent porosity, the differences in P-wave velocity due to fluids are larger than the differences plotted on Figure 5.6, as expected. The maximum difference again occurs at lower temperatures and lower effective pressure and is approximately 70 m/s. This difference is twice as large as the velocity difference associated with a sandstone having 5-percent porosity and may be a rock-fluid property that can be distinguished with high-quality seismic data.

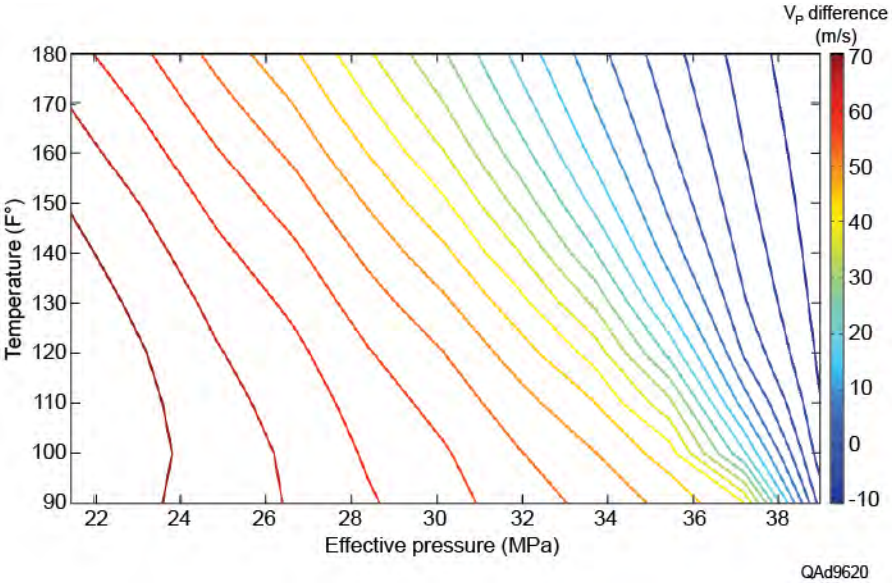

Figure 5.8. Model results showing differences between P-wave velocity in a sandstone saturated with brine and in a sandstone saturated with CO_2 as effective pressure and temperature vary. The sandstone is assumed to have 10-percent porosity.

Figure 5.9 shows differences in S-wave velocities as pore fluid changes from brine to CO_2. Because these differences are caused by variations in bulk density, they are larger for this sandstone with 10-percent porosity than for the sandstone with 5-percent porosity depicted on Figure 5.7. Again, the maximum difference occurs for higher temperature and higher effective pressure (lower pore pressure).

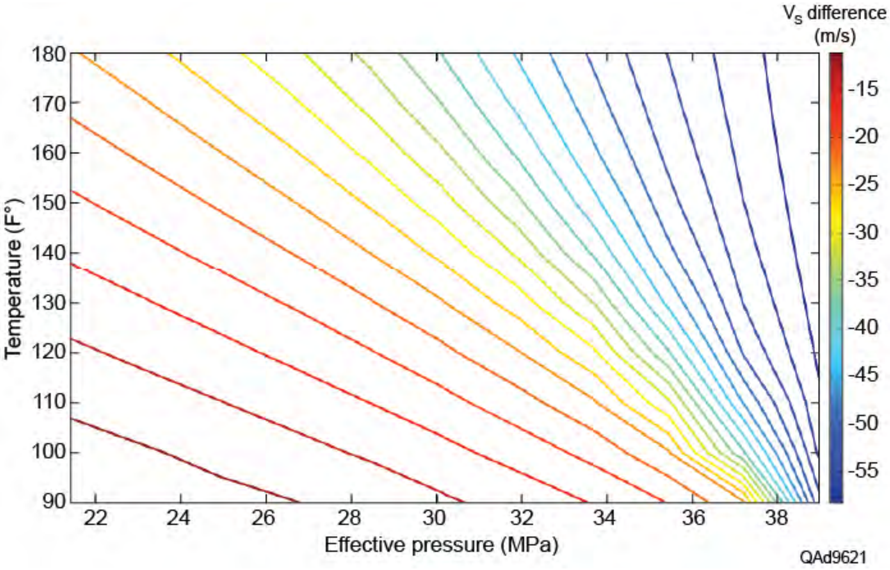

Figure 5.9. Model results showing differences between S-wave velocity in a sandstone saturated with brine and a sandstone saturated with CO_2 as effective pressure and temperature vary. The sandstone is assumed to have 10-percent porosity.

The third theoretical rock we consider is a sandstone with 20-percent porosity. Within our study area, the interval between the Tully limestone and the Marcellus Shale contains channel-like features having porosities that sometimes are as large as 20-percent (Fig. 5.10c). A formation within the Hamilton Group above the Marcellus with this magnitude of porosity should provide attractive storage capacity and also be imaged with seismic data having reasonable-quality signal-to-noise character.

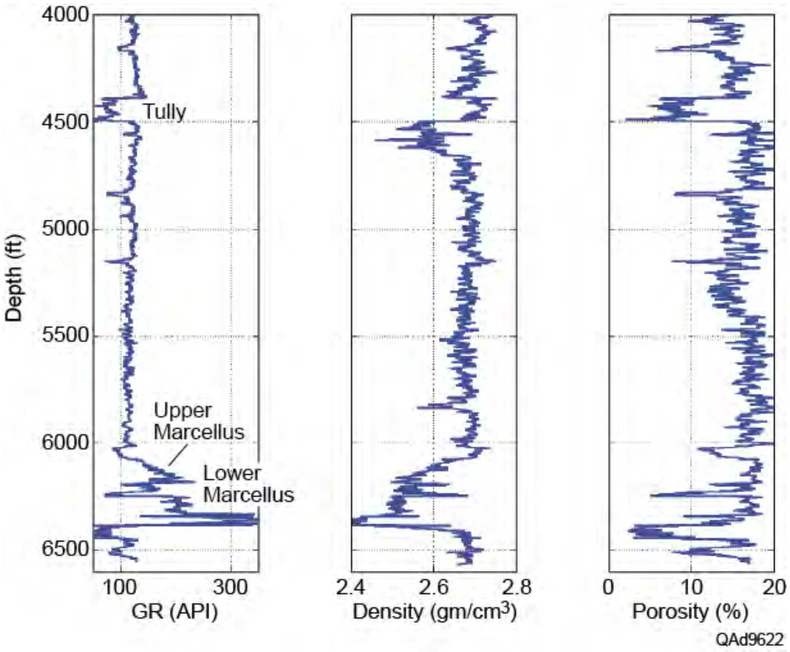

Figure 5.10. Well log data from central-image calibration well showing (a) gamma-ray response, (b) bulk density, and (c) and porosity. Devonian-age rocks between the Tully Limestone and Marcellus Shale have porosities that make them attractive candidates for CO_2 sequestration studies.

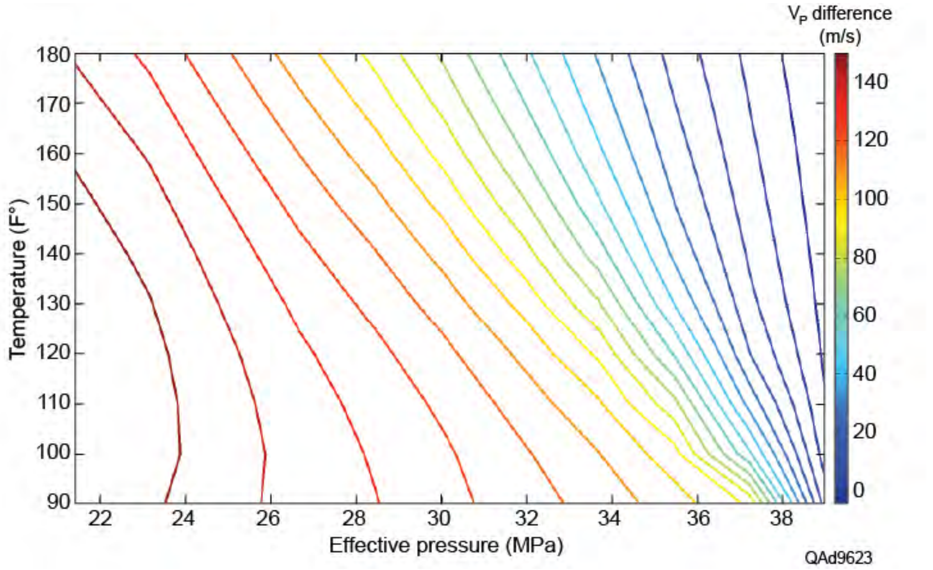

Figure 5.11. Model results showing differences between P-wave velocity in a sandstone saturated with brine and a sandstone saturated with CO_2 as effective pressure and temperature vary. The sandstone is assumed to have 20-percent porosity.

Figure 5.11 shows differences between P-wave velocity in a 20-percent porosity sandstone saturated with brine and then with CO_2 as temperature and effective pressure are varied over ranges appropriate for CO_2 sequestration near our study site. As expected, these differences are larger than those exhibited by lower porosity rocks, with a maximum velocity change of approximately 140 m/s occurring within the range of temperature and effective pressure considered.

Figure 5.12 shows differences in S-wave velocities in brine-saturated versus CO_2-saturated rocks. Because the density difference between brine and CO_2 is relatively large, especially for high temperature and low pore pressure, the change in S-wave velocity is larger than 100 m/s, which approaches the change observed in P-wave velocity (Fig. 5.11). However, the maximum change observed in S-wave velocities correponds to higher effective pressure and higher temperature, while the maximum increase in P-wave velocity corresponds to lower effective pressure and lower temperature. As a result, the V_P/V_S ratio does not change significantly across this wide range of reservoir temperature and effective pressure. Figure 5.13 presents the relative change in V_P/V_S ratio when CO_2 displaces brine. The V_P/V_S ratio decreases by only 4 or 5-percent when CO_2 displaces brine in this 20-percent porosity reservoir, which too small a change to be detected with seismic data.

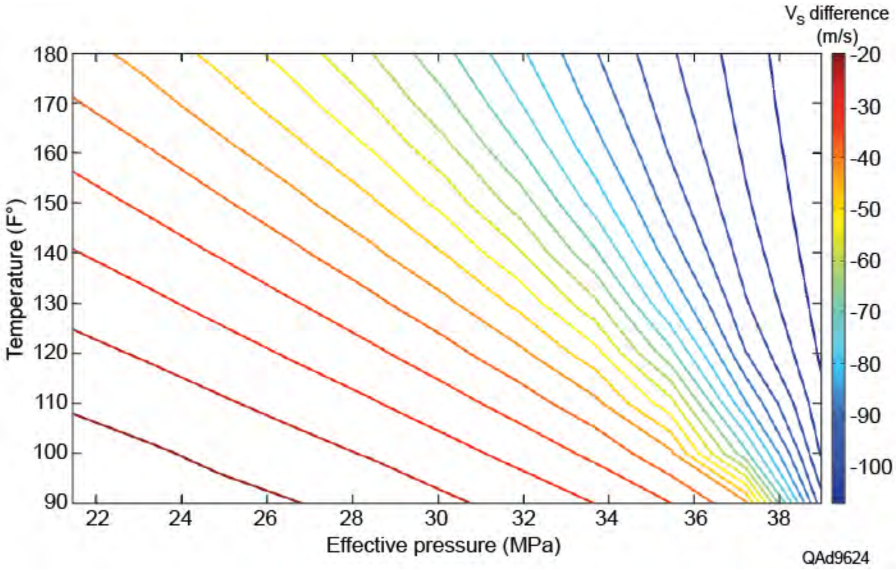

Figure 5.12. Model results showing differences between S-wave velocity in a sandstone saturated with brine and a sandstone saturated with CO_2 as effective pressure and temperature vary. The sandstone is assumed to have 20-percent porosity.

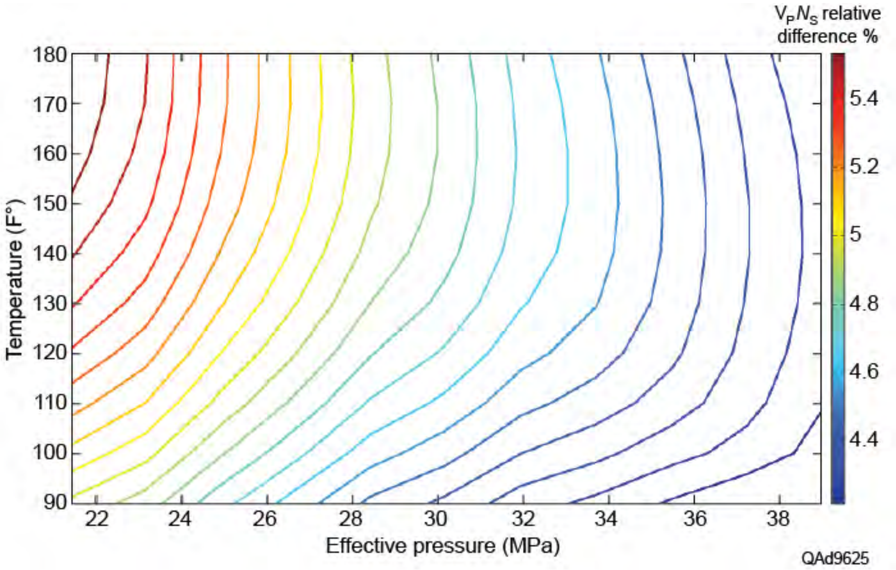

Figure 5.13. Model results showing relative differences in V_P/V_S ratio for a sandstone saturated with brine and a sandstone saturated with CO_2 as effective pressure and temperature vary. The sandstone is assumed to have 20-percent porosity.

Comparing results for these three hypothetical CO_2 sequestration reservoirs it is obvious that a formation with greater porosity not only offers more storage capacity for the same thickness and lateral extend of a reservoir unit, but it also allows better monitoring of CO_2 movement and saturation with seismic data because significant changes occur in P and S velocities as injected CO_2 replaces brine.

Well Log Data

A small subset of the well log data acquired in the calibration well at the center of the seismic image space has been shown as Figure 5.10. We now show the full log suite and segregate the log curves into two separate figures so log character can be illustrated in appropriate detail. Gamma-ray, density, porosity, and electrical resistivity data are displayed on Figure 5.14. The gamma-ray log is repeated on Figure 5.15 in combination with P-wave velocity, fast-S and slow-S velocities, S-wave anisotropy for waves traveling at normal incidence, and the $Vp:Vs_{fast}$ velocity ratio. The gamma-ray (GR) curve identifies two key formations: the Tully Limestone with a low GR response, and the Marcellus Shale with a high GR signature. The Marcellus Shale displays the lowest density of all rock units penetrated by the calibration well. The Marcellus also has a higher electrical resistivity than its bounding units because of its high gas content. Based on the preceding rock physics models for monitoring injected CO2, log measurements that are of most interest are P-wave and S-wave velocities.

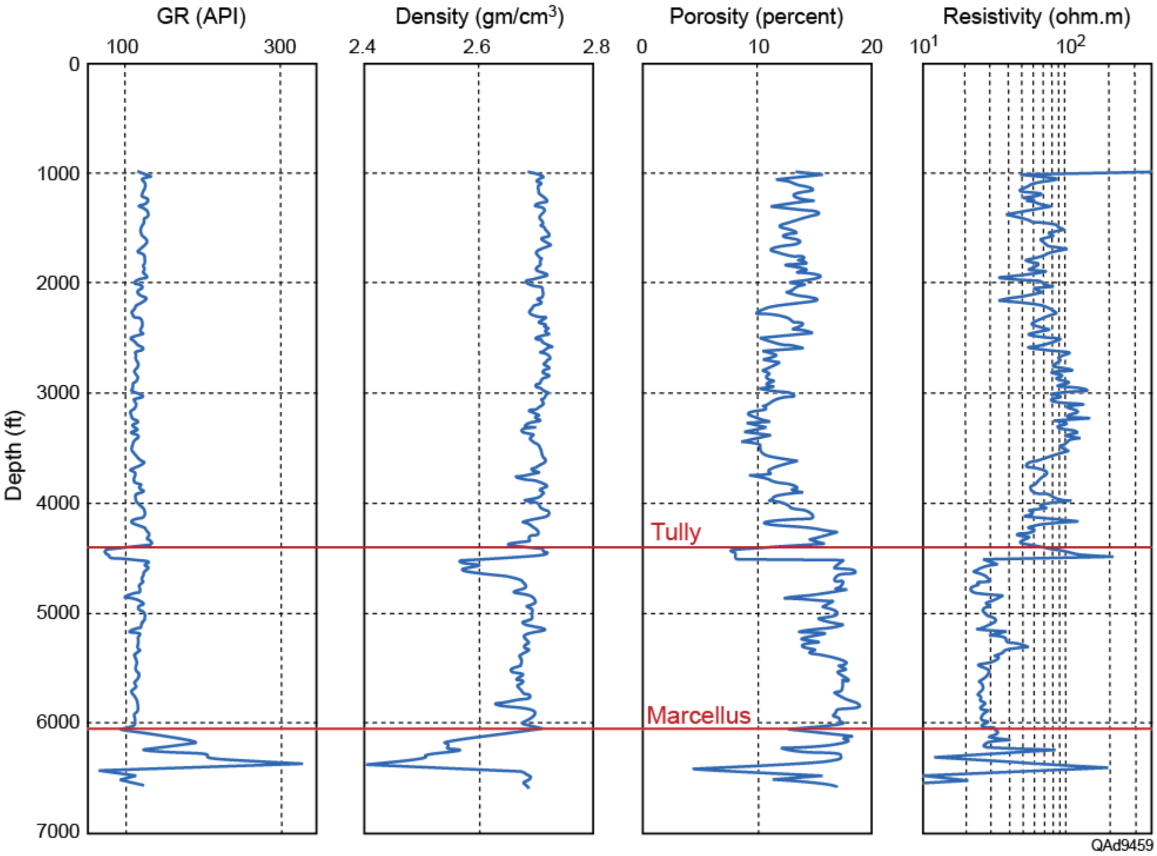

Figure 5.14. Well log data from local calibration well. From left to right are gamma ray (API units), density (gm/cm^3), porosity (percent), and electrical resistivity (ohm.m). The tops of the Tully Limestone and the Marcellus Shale are labeled.

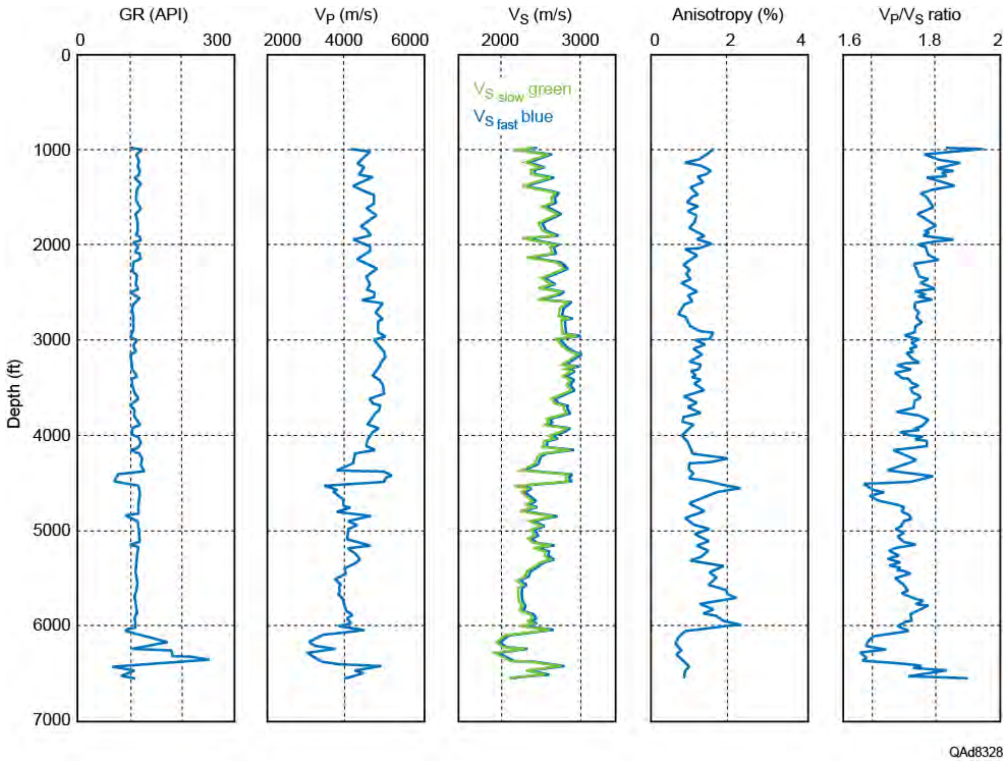

Figure 5.15. Well log data from the calibration well. From left to right: gamma ray (API units), Vp (km/s), Vs_{fast} (blue curve, km/s) and Vs_{slow} (green curve, km/s), S-wave anisotropy (percent), and Vp/Vs_{fast} ratio. There is little difference between Vs_{fast} and Vs_{slow}, and the curves in the third panel plot atop each other.

Porosity of Potential CO_2 Sequestration Units

The porosity curve displayed on Figure 5.14 is critical information for selecting geologic units that can serve as potential CO_2 sequestration reservoirs. The most attractive porosities occur in the Middle Devonian section between the Tully Limestone and the Marcellus Shale. We thus limited our analysis of possible CO_2 sequestration reservoirs to the Tully-to-Marcellus stratigraphic interval in this study. A particularly interesting reservoir target was found immediately below the Tully Limestone and is illustrated and discussed in Chapter 9.

Conclusions

It is essential to establish rock physics models that relate multicomponent seismic attributes to rock and fluid properties. Regarding interpretation of possible CO_2 sequestration reservoirs, log data showed rocks between the Tully Limestone and the Marcellus Shale have the highest porosities of the entire section drilled by the central-image calibration well, with porosities being in the range of 15-percent to 18-percent. This magnitude of pore volume is sufficient for these Tully-to-Marcellus units to be the focus of our efforts to demonstrate the advantages of evaluating CO_2 reservoir systems with multicomponent seismic data rather than with single-component P-wave seismic data.

The rock physics models developed in this chapter are based on sound physics. A part of the modeling theory has been verified by producing numerical estimates of P-wave and S-wave velocities that conform to laboratory measurements of these values on pressurized core-plug samples (Fig. 5.2). The remaining portions of the rock physics models that allow CO_2 concentration to be estimated using seismic-based P and S velocities cannot be verified because no CO_2 will be injected into any of the porous units inside the project's seismic image space during this study period.

Chapter 6

Seismic Sources, Sensors, and Recording Systems and Their Effects on P and S Wave Modes

Introduction

To fulfill the first three secondary objectives listed on Figure 1.1 of Chapter 1, a field-test program was done to: (1) quantify the relative strengths of compressional (P) wave and shear (S) wave modes produced by a variety of vertical-force seismic sources, (2) compare the relative merits of cable-based and cable-free data recording systems, and (3) document and compare the quality of 3C data acquired with moving-coil geophones and MEMS solid state accelerometers. These equipment tests were done at the Devine Test Site owned by The University of Texas at Austin. Vertical-force sources deployed for the tests were: 1-kg (2.2 lb) packages of explosive positioned at a depth of 6 m (20 ft), a 27,273-kg (60,000-lb) vertical vibrator, and a vertical impact accelerated-weight source that delivered 30,202 joules (22,276 ft-lb) of energy to the Earth. Horizontal-force sources used in the tests were this accelerated-weight source impacting at various non-vertical incident angles and a Mertz Model 18 horizontal vibrator operating with a drive force of 24,000 lbs (10,900 kg). Data were acquired with three recording systems—a Sercel 428 cable-based system, Sercel's EUnite cable-free boxes, and Sigma cable-free boxes provided by Seismic Source of Ponca City, Oklahoma, and iSeis of Denver, Colorado.

Field Test Procedure

The University's seismic test site is called the Devine Test Site because of its proximity to the community of Devine, Texas, shown on the map displayed as Figure 6.1a. An aerial photo of the test site property is included as Figure 6.1b. The most valuable assets on the property are the three equipment tests wells drilled and cased to depths of 3000 ft (914 m). The locations of these wells are indicated by the solid circles labeled 4, 2, 9 on Figure 6.1b.

The stratigraphy penetrated by the test wells is labeled on the well log curves displayed as Figure 6.2. These logs were recorded in well 4 and define compressional velocity V_P, shear velocity V_S, and gamma-ray readings across the rock units that form the first 3000 ft (914 m) of the seismic propagation medium beneath the property. These log measurements start immediately below the base of surface casing, which is at a depth of 532 ft (162 m) in well 4 where these logs were recorded.

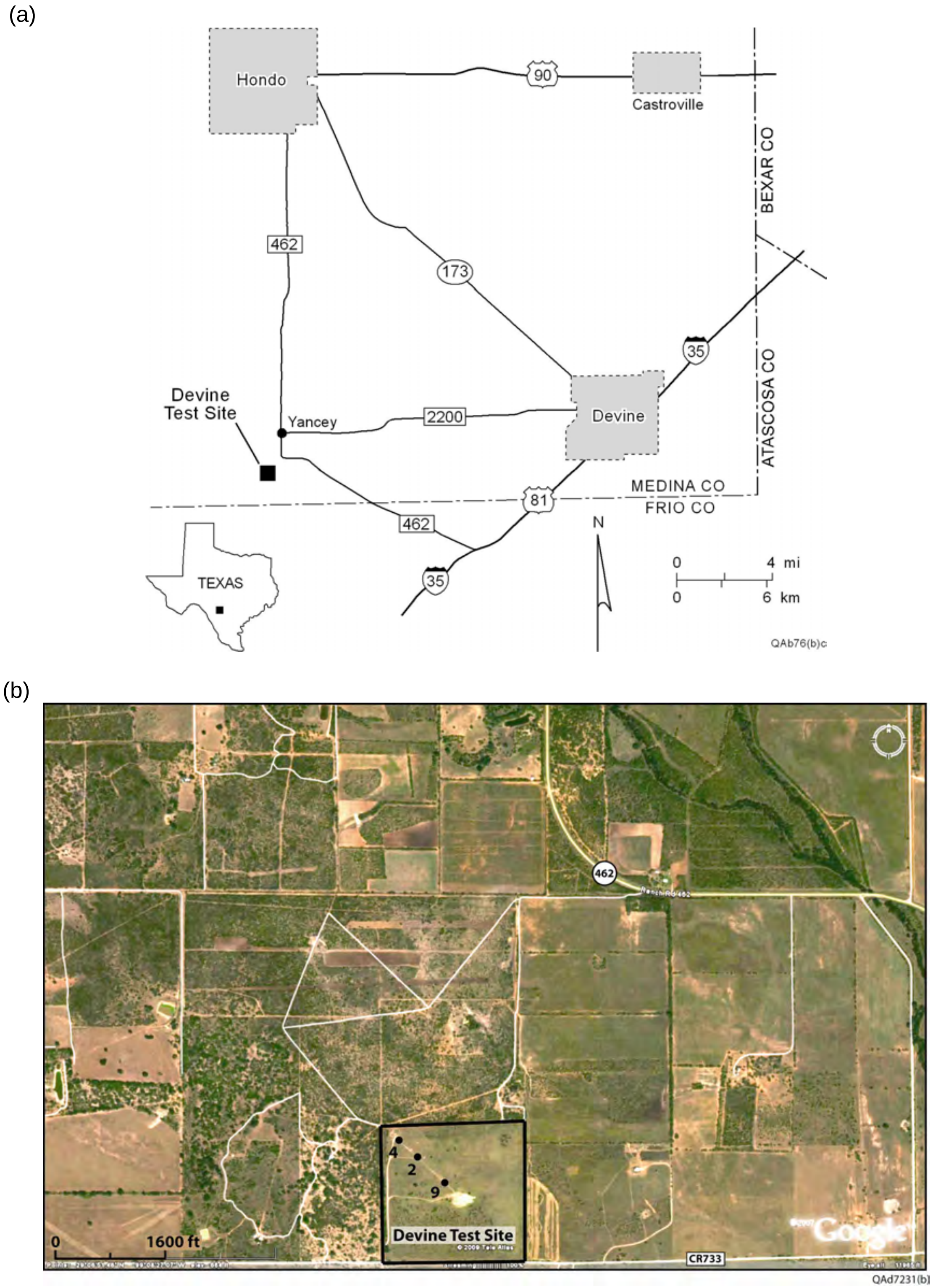

Figure 6.1. (a) Location of the Devine Test Site in Medina County, Texas. The city of San Antonio is approximately 50 km east of the town of Hondo shown on this map. (b) Aerial photo of the Devine Test Site. Test wells 4, 2, and 9 were constructed for the purpose of deploying downhole instrumentation, particularly seismic sources and receivers and well logging tools. All wells are 3000 ft (914 m) deep. The site spans 100 acres.

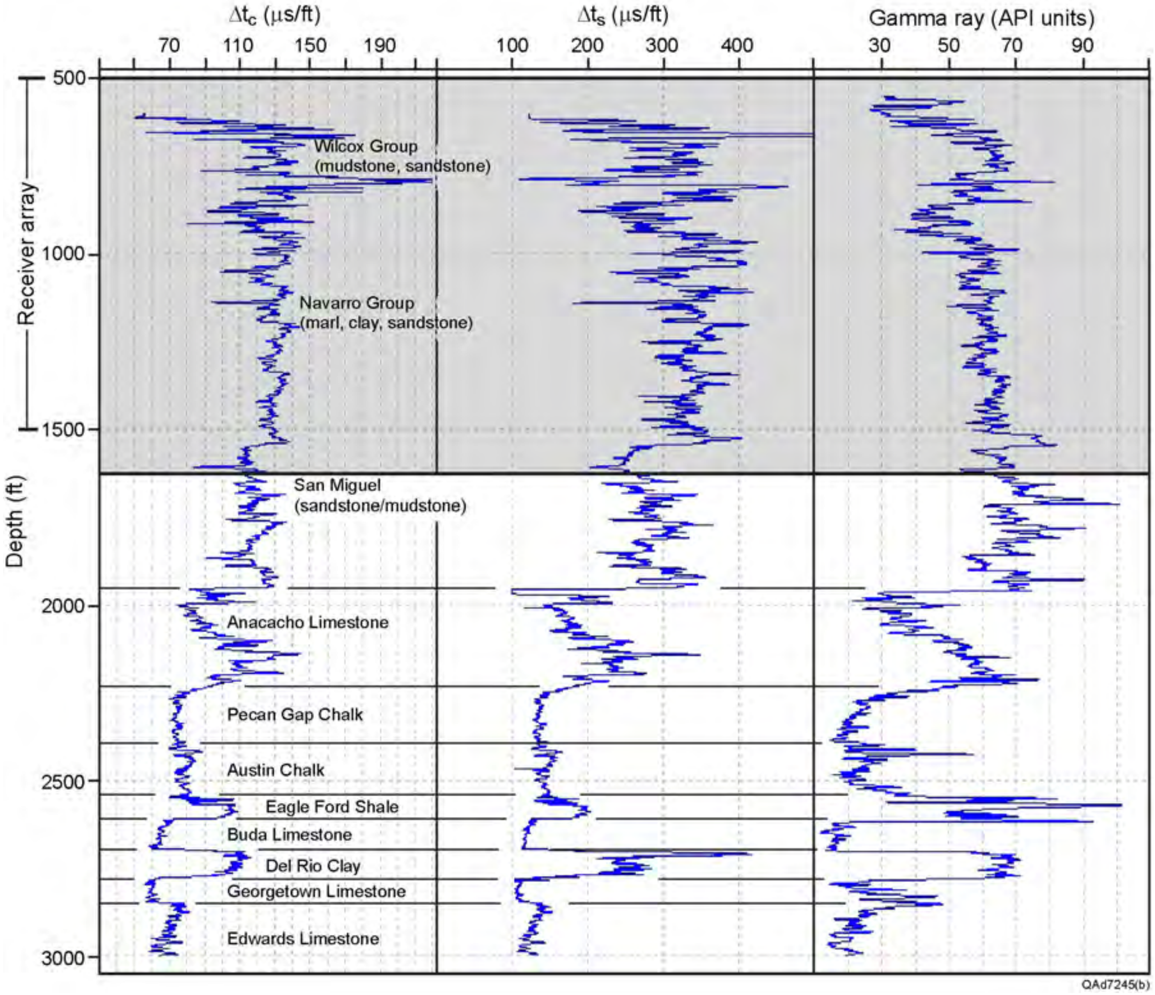

Figure 6.2. V_P and V_S velocity logs and gamma-ray log acquired in well 4 on the Devine Test Site. The shaded interval defines the depth range over which downhole geophones were deployed for source tests in this study.

Source-Receiver Test Geometry

The source-receiver geometry utilized for these tests combined the concepts of horizontal wave testing (involving only a horizontal receiver array) and vertical wave testing (involving only a vertical receiver array) as described by Hardage (2009, 2010).

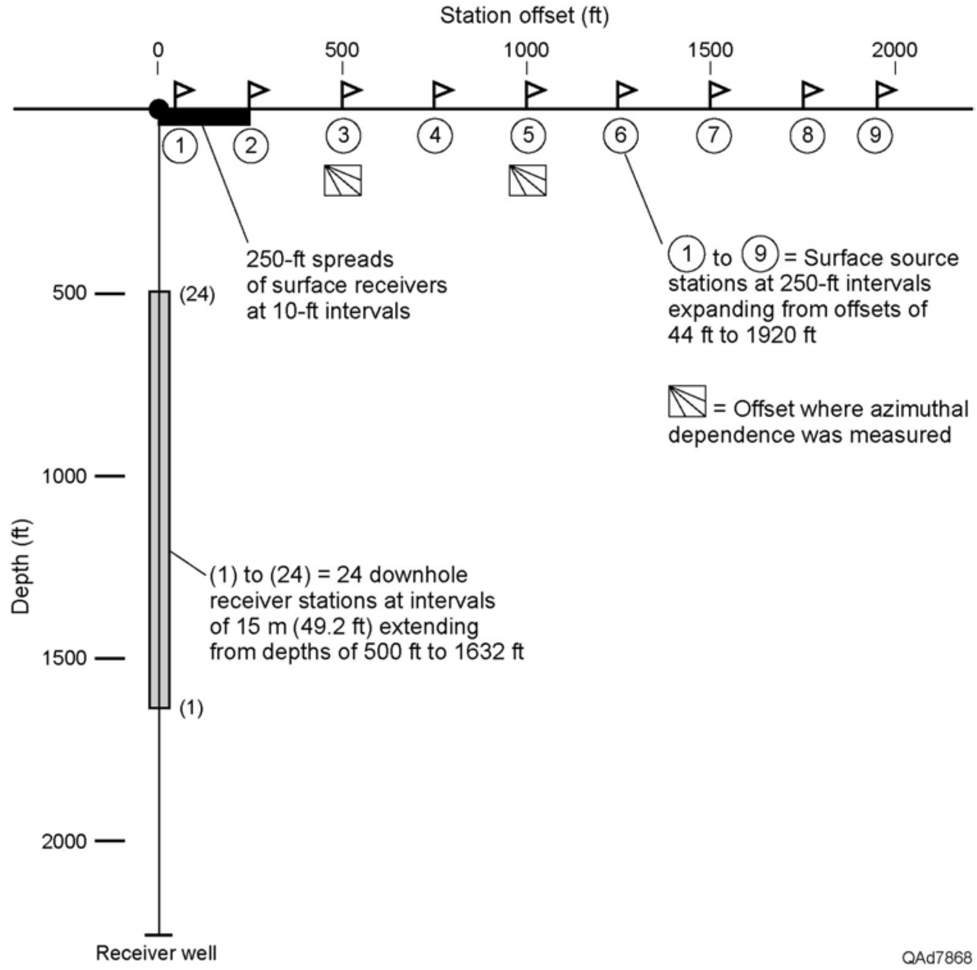

Figure 6.3. Source-receiver geometry used to compare relative merits of multicomponent seismic sources, sensors, and recording systems. A 24-station vertical array of 3C geophones spaced at intervals of 15 m (49.2 ft) spanned the depth interval from 500 to 1632 ft (152 to 497 m) in well 4. Several 25-station horizontal arrays of 3C sensors spaced 10 ft (3 m) apart spanned the offset range 0 to 250 ft (0 to 76 m) immediately next to well 4. Source stations were offset from the well at intervals of 250 ft (76 m), the linear dimension of the horizontal surface-receiver arrays.

Well 4 (Fig. 6.1b) was chosen for the location of the vertical receiver array. A 24-station MaxiWave receiver system provided by Mitcham Industries was deployed in this well, with receiver stations spanning a depth interval extending from 500 to 1632 ft (152 to 497 m). The velocity layering local to this vertical sensor array is defined by the log character inside the shaded interval shown on Figure 6.2. Several parallel arrays of 2D horizontal sensors extended eastward 250 ft (76 m) from well 4, and a series of nine inline source stations continued eastward a distance of 1920 ft (585 m), as illustrated on Figure 6.3. Within each 250-ft (76 m) horizontal-receiver array (the heavy black line between source stations 1 and 2 on Figure 6.3), a single 3C sensor was buried at inline intervals of 10 ft (3 m) so that the top of each sensor case was flush with the ground surface. The X,Y,Z sensor elements at each 3C sensor station were recorded as individual data channels.

Photographs of the surface equipment deployed for the tests are shown on Figure 6.4. Along each horizontal receiver array, the first sensor station was 10 ft (3 m) from well 4 and sensor station 25 ended at source station 2, offset 250 ft (76 m) from the receiver well (Fig. 6.3). As shown by the labeling on the photographs, the instrumentation deployed along these parallel arrays consisted of:

1. 25 stations of 3C geophones recorded by Sigma cable-free boxes provided by Seismic Source and i-Seis.

2. 25 stations of DSU3 MEMS sensors recorded by a Sercel 428 cable-based system.

3. 25 stations of 3C geophones recorded by Sercel's EUnite cable-free boxes.

4. 25 stations of 3C geophones recorded by a Sercel 428 cable-based system.

5. 5 stations at which OyoGeospace deployed high-sensitivity geophones and special packaging of 3C geophones with all sensors recorded by OyoGeospace GSR cable-free boxes.

The 3C geophones utilized in surface spreads 1, 3, and 4 of this list were Oyo Geospace Model 20DX (10-Hz resonance) geophones.

(a)

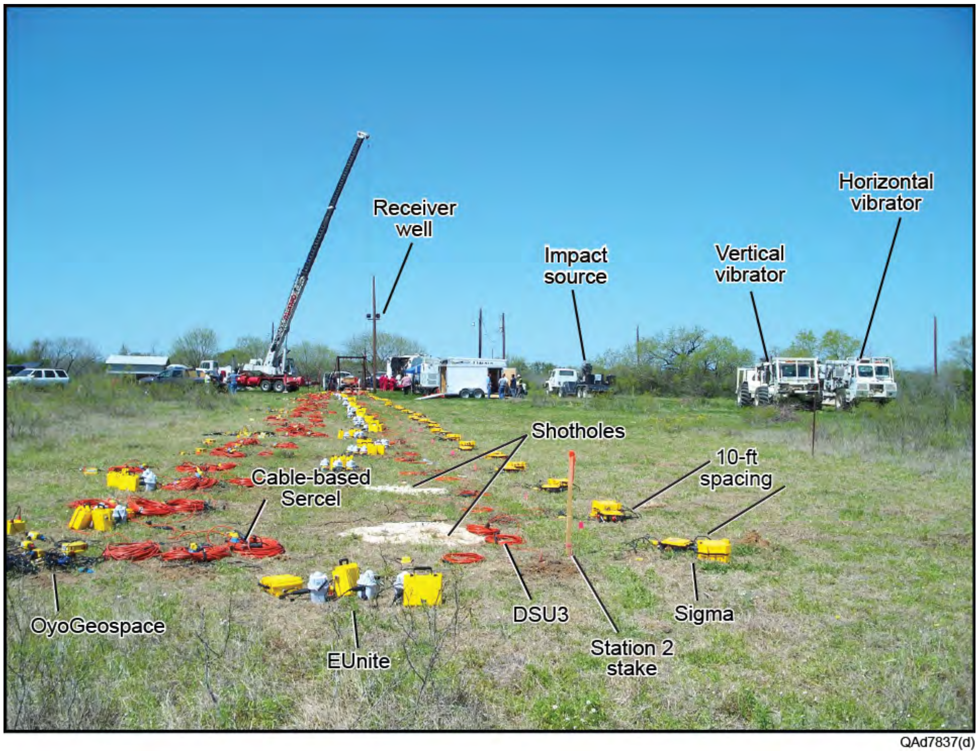

(b)

Figure 6.4. (a) View of the receiver well from a position near source station 2 on the source-station profile. This view shows parallel, 25-station arrays of horizontal-wave-test instrumentation deployed over the offset range 0 to 250 ft (0 to 76 m) and some of the source and data-acquisition technologies assembled for the test. (b) View from the receiver well looking down the source-station profile.

Vertical Aperture of Test Geometry

An important requirement of the test was to record downgoing P and S modes over a wide aperture of vertical takeoff angles from surface source stations. This requirement allowed the maximum amount of energy contained in each wave mode propagating away from source stations to be captured for analysis. The shallowest takeoff angle involved data generated at source station 9 (offset 1920 ft [585 m]) and recorded at downhole receiver station 24 (depth of 500 ft [152 m]). The steepest takeoff angle involves source station 2 (offset 250 ft [76 m]) and downhole receiver station 1 (depth of 1632 ft [497 m]). A first-order approximation of the aperture range created by the source-receiver geometry can be done by assuming straight raypaths from source to downhole receiver, which yields the result shown on Figure 6.5.

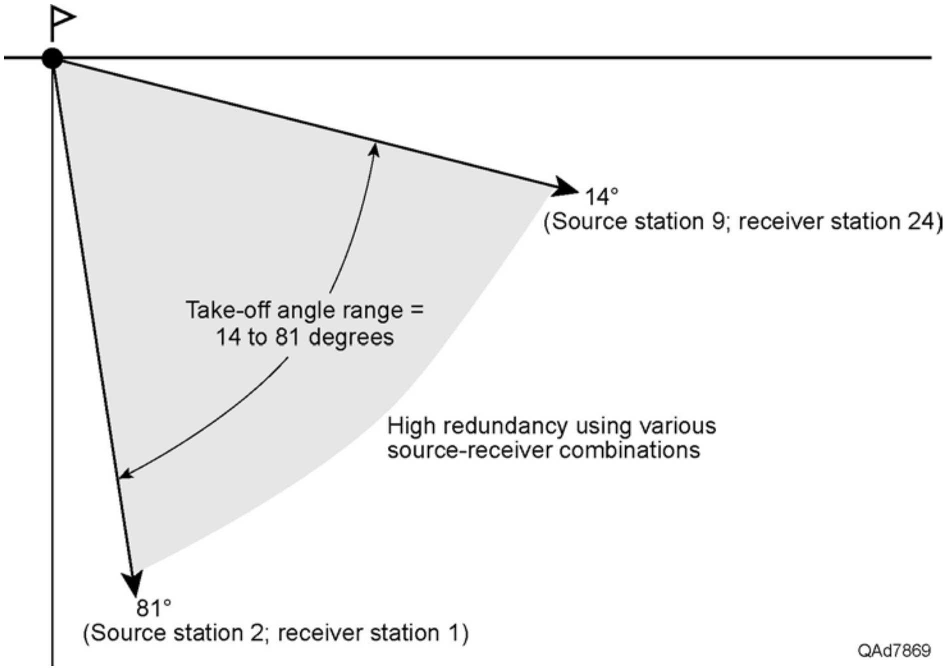

Figure 6.5. Takeoff angle aperture when straight raypaths are assumed between surface sources and downhole receivers.

Wave Components Embedded in Test Data

Three independent, vector-based, seismic wave modes propagate in a simple homogeneous Earth**:** a compressional mode, **P**, and two shear modes, **SV** and **SH** (Fig. 6.6). These are the wave modes the seismic industry creates when wavefields produced by three orthogonal source-displacement vectors are recorded with three orthogonal vector sensors. These are the wave modes that were evaluated in the wavefields generated by the seismic sources evaluated at the Devine Test Site.

Each mode of an elastic wavefield travels through the Earth at a different velocity, and each mode distorts the Earth in a different direction as it propagates. In a homogeneous medium, the orientations of the P, SV, and SH displacement vectors relative to the propagation direction of each mode are defined on Figure 6.6. The propagation velocities of SH and SV shear modes differ by only a few percent, but both shear velocities (**V_S**) are significantly less than P-wave velocity (**V_P**). The velocity ratio V_P/V_S can vary by an order of magnitude in Earth media, from a value of 50 or more in deep-water, unconsolidated, near-seafloor sediment to a value of approximately 1.5 in a few dense, well-consolidated rocks.

A convenient way to distinguish between SH and SV shear modes in a homogeneous medium is to imagine a vertical plane passing through a source station and a receiver station. SV vector displacement occurs in this vertical plane; SH vector displacement is normal to the plane (Fig. 6.7). This vertical plane passing through the coordinates of a source station, a receiver station, and a reflection point produced by that source-receiver pair is called a **sagittal plane**.

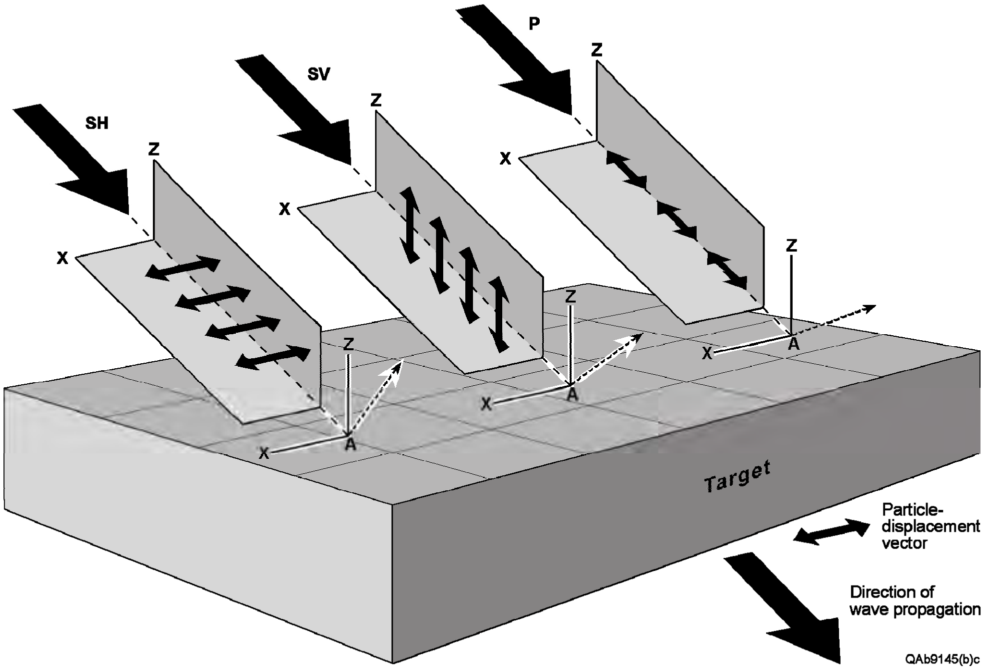

Figure 6.6. A full-elastic, multicomponent seismic wavefield propagating in a homogeneous Earth consists of a compressional mode P and two shear modes, SV and SH. A key distinction among these wave modes is that each mode distorts the Earth in a different direction along its propagation path. The direction in which each mode displaces the Earth is indicated by double-headed arrows.

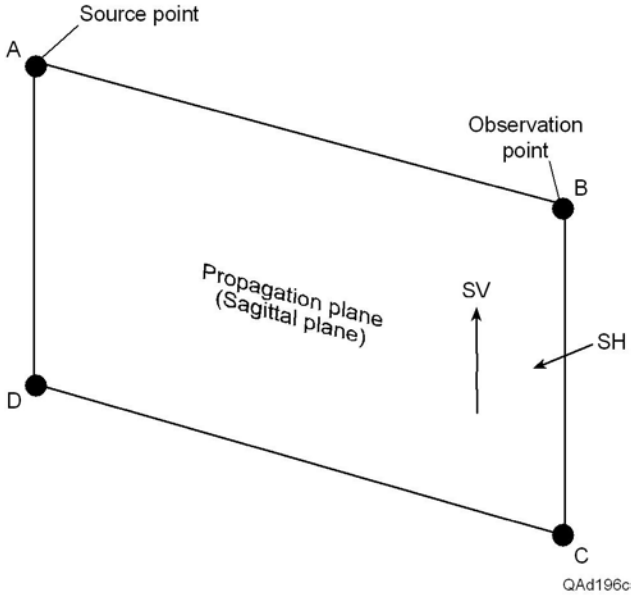

Figure 6.7. Distinction between SH and SV shear wave displacements in a homogeneous medium. SV displacement occurs in the vertical plane that passes through a source station and an observation point. SH displacement is normal to this plane.

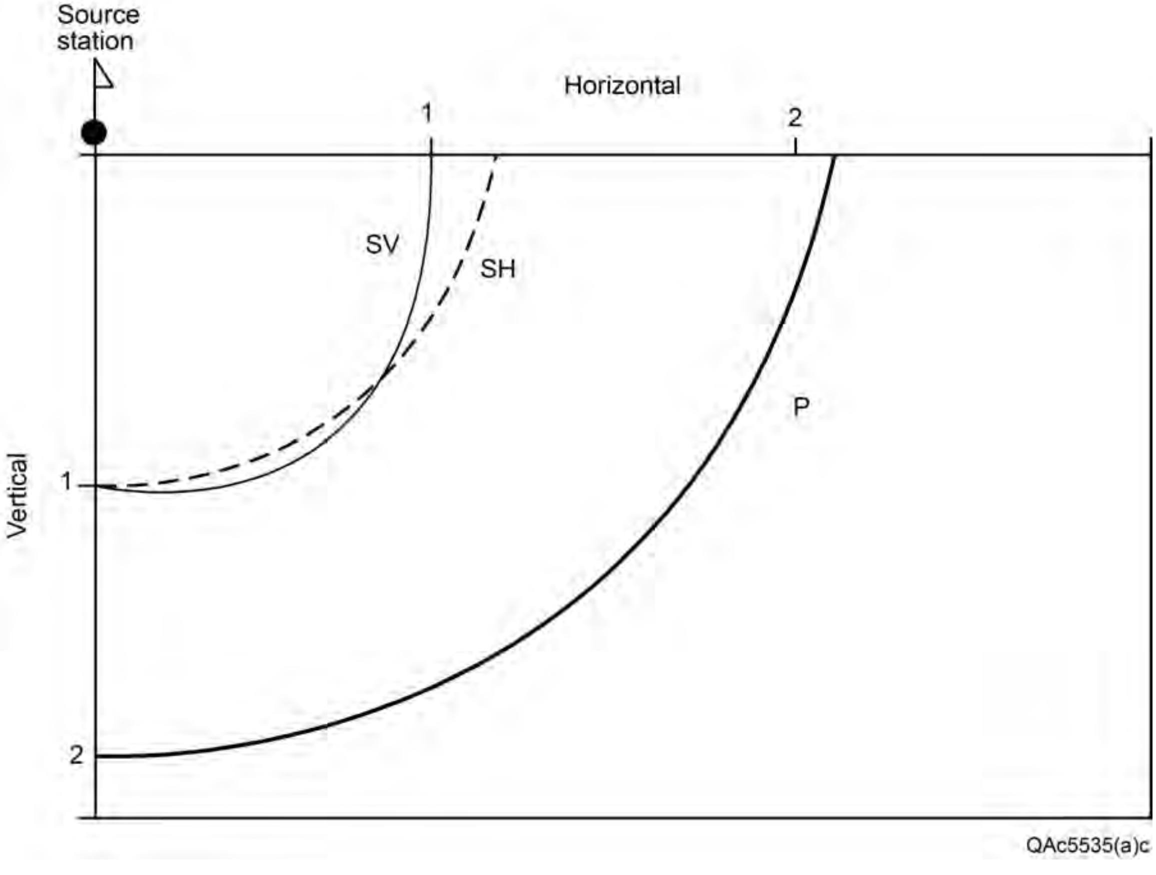

Figure 6.8. Comparison of SH, SV, and P velocity behavior for elastic wave propagation in horizontally layered [vertical transverse isotropic (VTI)] media. From Levin (1979, 1980).

Because SV and SH modes cause orthogonal displacements with these orientations, some geophysicists prefer to use the terms **radial-S** (**SR**) and **transverse-S** (**ST**) when describing S-wave propagation in layered media and to restrict the terms SV and SH to S-wave propagation in homogeneous media, or to S-wave modes that propagate only in symmetry-axis planes. Both styles of nomenclature are used in this study.

Levin (1979, 1980) expanded the physics of S-modes from a homogeneous Earth to a layered Earth and found SH and SV modes propagating through a layered medium exhibit velocity behaviors like those displayed on Figure 6.8. An important point to note is that at all take-off angles from the source station, except for true vertical and for the one angle that points to the subsurface coordinate where the SH and SV wavefronts intersect, SV and SH modes propagate with different velocities, with the SH mode having a significantly faster velocity at shallow take-off angles from a source station. This wave physics will be important when examining seismic test data shown later.

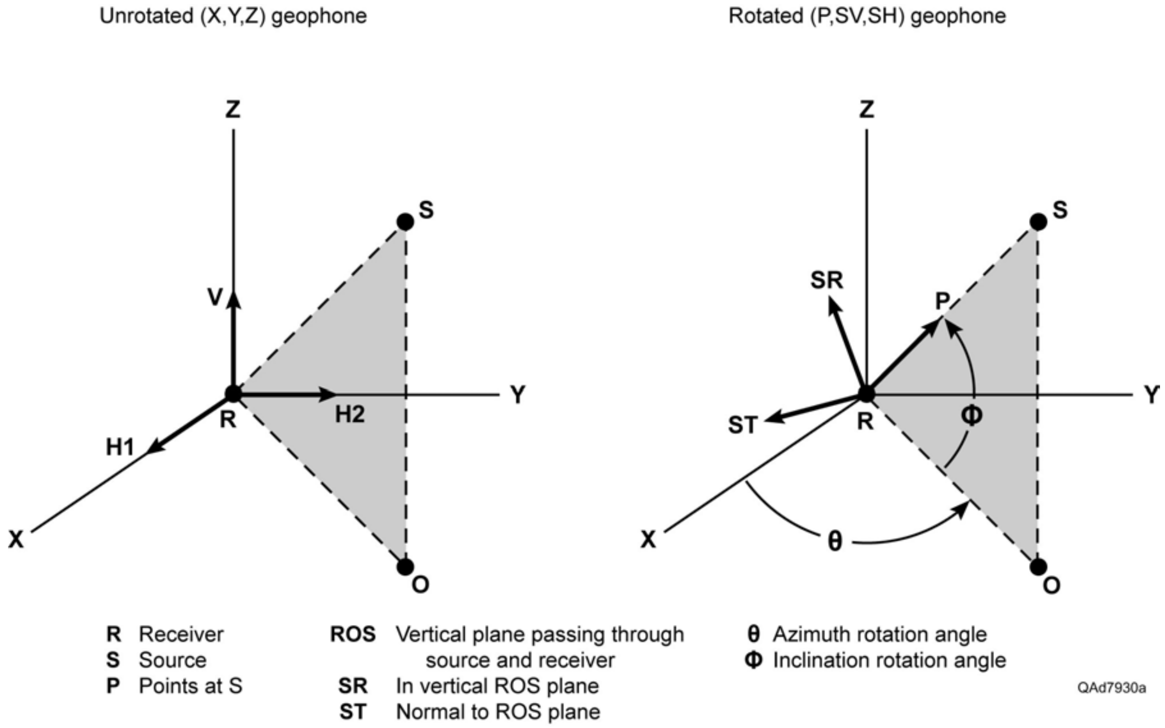

Figure 6.9. Reorientation of X, Y, Z receivers to P, SR, and ST receivers.

Transforming VSP Test Data to Wave-Mode Data

In a vertical receiver well, azimuth orientations of X,Y horizontal geophones differ at each downhole station because sensor packages are deployed on twisted-wire cable that rotates as it spools off a cable reel. As a result, sensors rotate by different amounts when they reach different deployment depths. Phase shifts and amplitude variations introduced into horizontal-sensor data by station-to-station variations in receiver orientation do not allow individual events or distinct wave modes to be recognized, particularly S-wave events that dominate horizontal-sensor response. Receivers must be mathematically oriented to consistent azimuths and to proper inclinations to define downgoing and upgoing P and S modes.

Transformations of borehole receivers from in situ X, Y, Z orientations to a data space where receivers are oriented to emphasize P, radial-shear (SR), and transverse-shear (ST) events have been practiced in VSP technology for several decades. A graphical description of the transformation of receivers from X, Y, Z data space to P, SR, ST data space is shown on Figure 6.9. Azimuth rotation angle θ and inclination angle Φ have to be calculated at each receiver station so that P-wave displacement vectors are aligned along raypath RS, SV displacement vectors are confined to vertical plane ROS, and SH displacement vectors are orthogonal to plane ROS.

Vertical Array Measurements of Wave-Mode Amplitudes and Frequencies Produced by Test Sources

Examples of this receiver orientation procedure applied to vertical-impact, shot-hole explosive, and vertical-vibrator sources positioned at selected source stations are illustrated on Figures 6.10, 6.11, and 6.12. The data windows used to determine geophone azimuth θ and inclination angle Φ (Fig. 6.9) to apply at each receiver station spanned 40 ms immediately following the onset of the interpreted P-wave direct arrival (top row of Figures 6.10, 6.11, 6.12).

Because each of the three seismic sources (explosive, vertical vibrator, vertical impact) generated a different amount of seismic energy, a different plot gain was used to display data produced by each source. However, a constant plot gain is used within individual figures (Figs. 6.10, 6.11, 6.12) so that P, SR, and ST wave mode amplitudes produced by each specific source can be compared visually to judge their relative energy levels. Such comparisons confirm S modes radiating away from a vertical-force source often have amplitudes greater than their companion P mode (for example, Figs 6.10 and 6.11). Because data-display gains differ for each source, P and S amplitudes produced by one source should not be visually compared with P and S amplitudes produced by other sources.

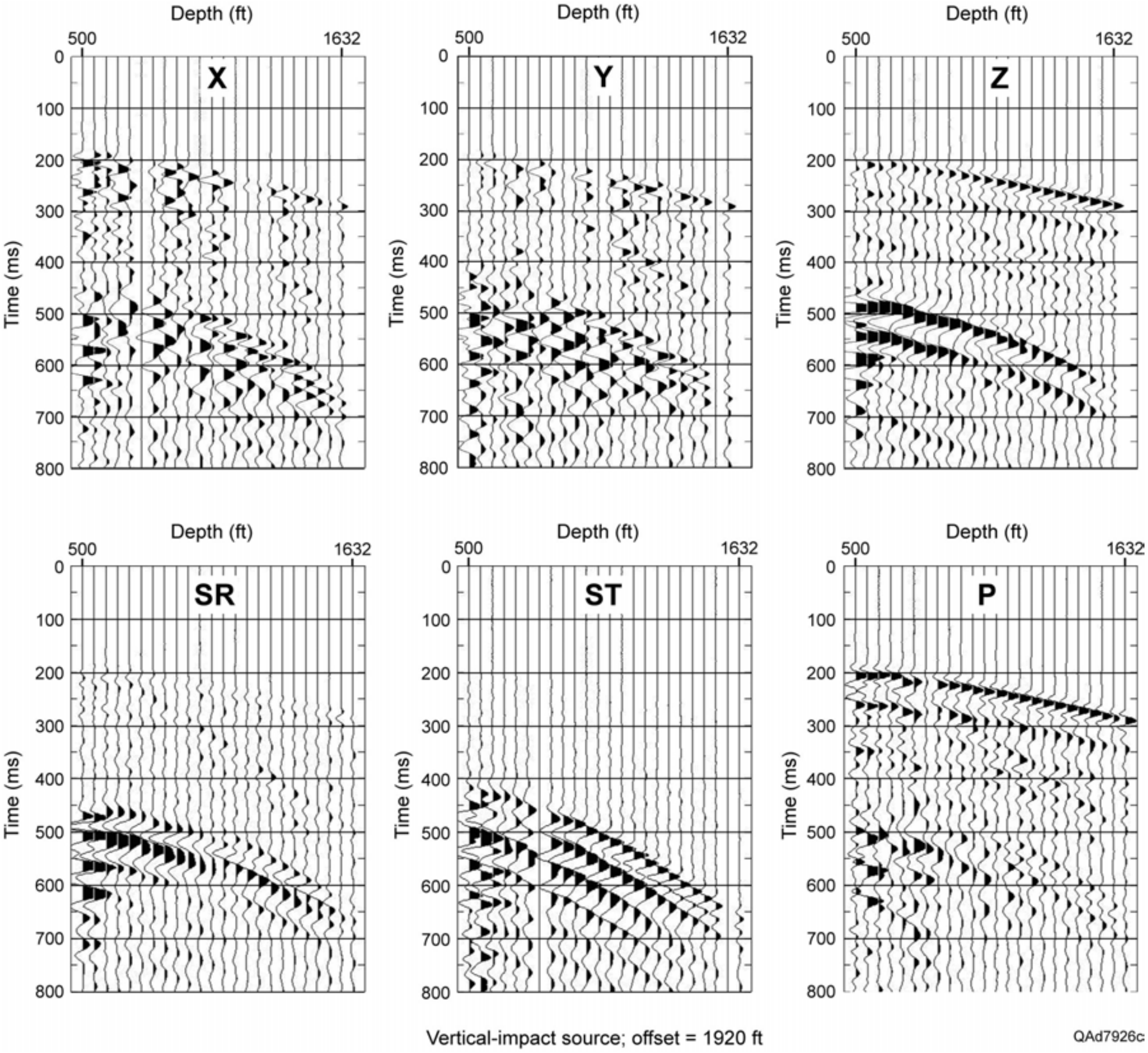

Figure 6.10. (a) Example of X, Y, Z data acquired with the test-site vertical sensor array when a vertical-impact source was positioned at source station 9, offset 1920 ft (585 m) from the array. (b) Data rotated to P, SR, and ST data space. All data panels are shown with a constant display gain.

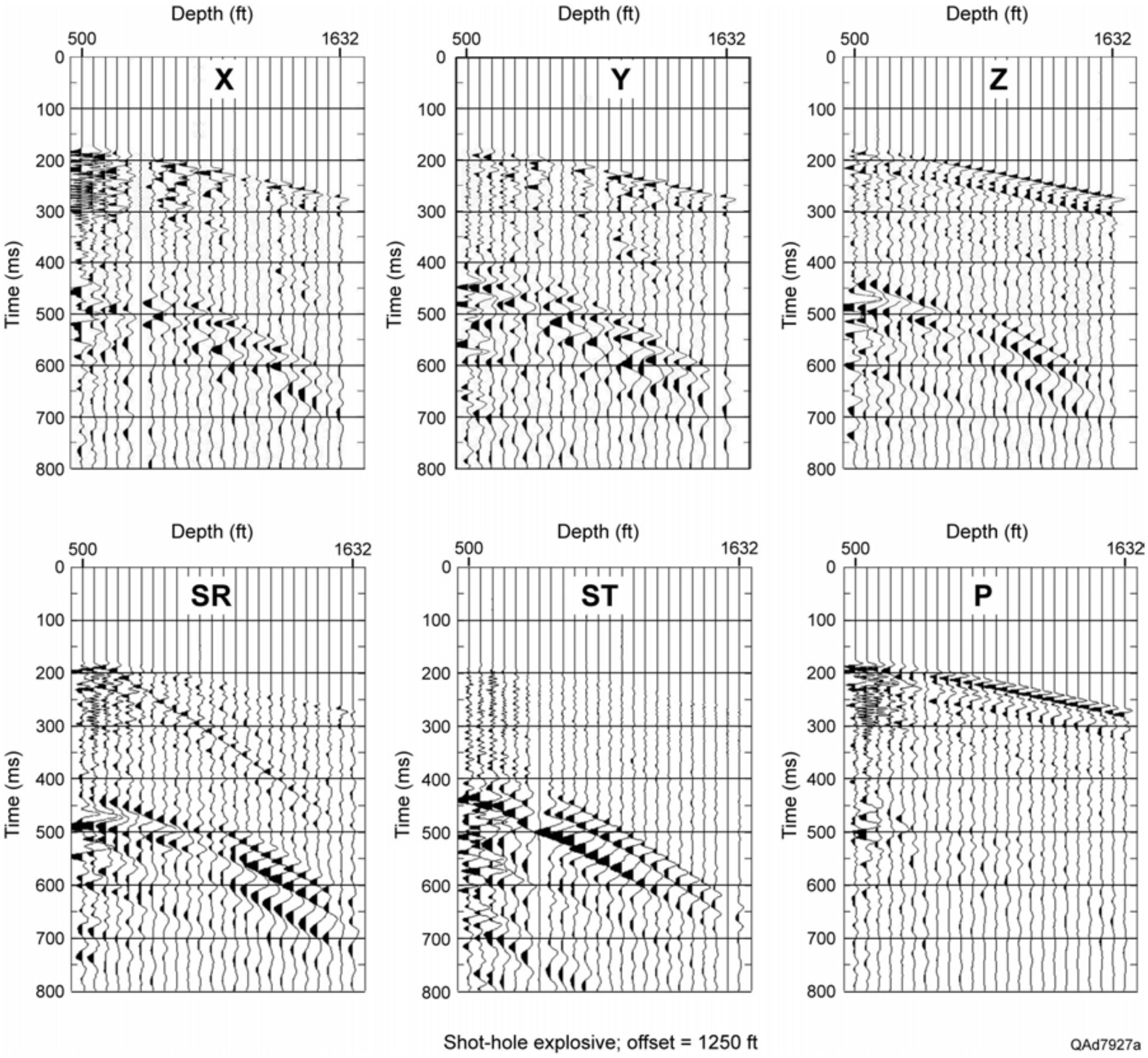

Shot-hole explosive; offset = 1250 ft

Figure 6.11. (a) Example of X, Y, Z data acquired with the test-site vertical sensor array when a shot-hole explosive source was positioned at source station 5, offset 1250 ft (381 m) from the array. (b) Data rotated to P, SR, and ST data space. All data panels are shown with a constant display gain.

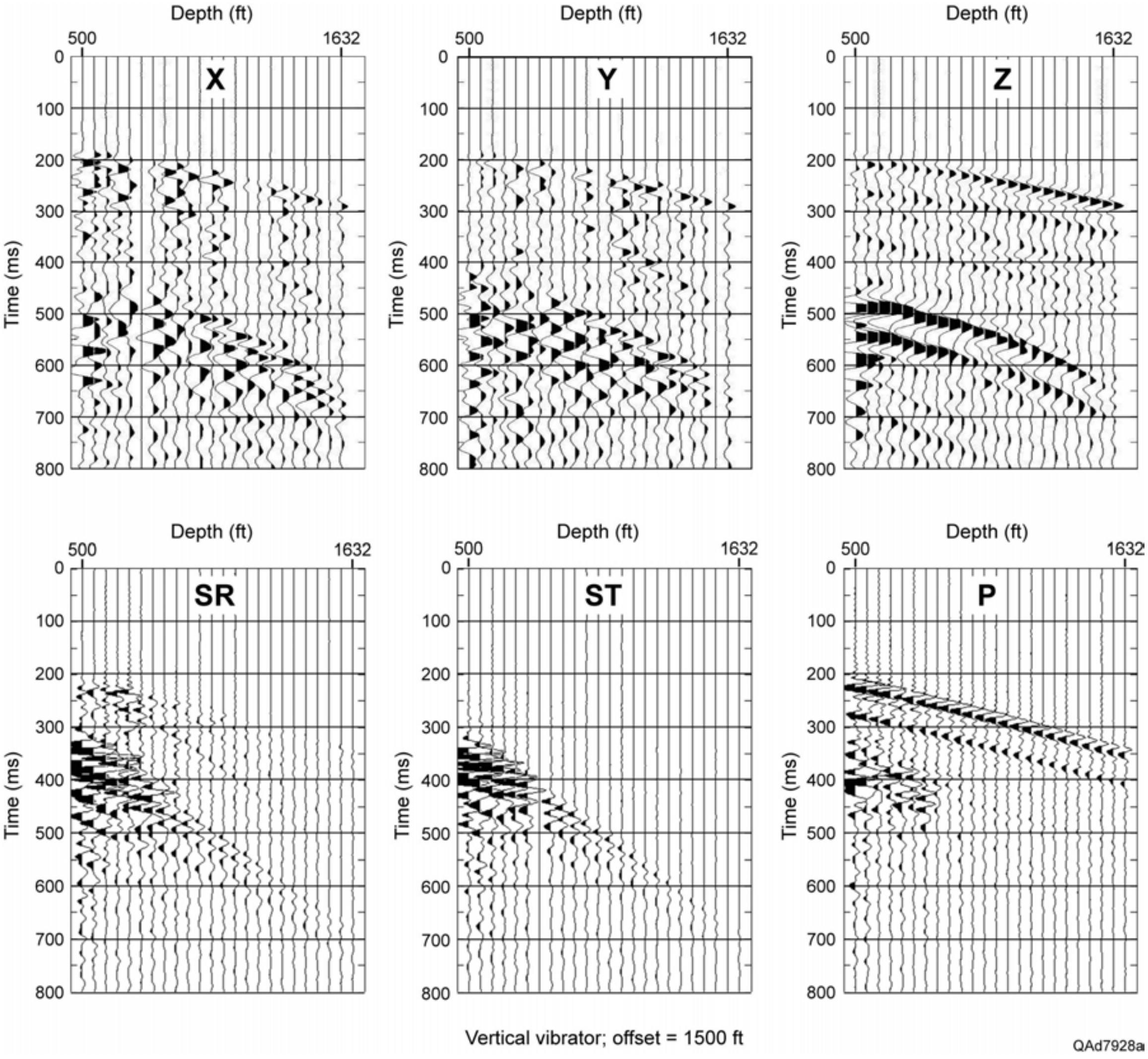

Figure 6.12. (a) Example of X, Y, Z data acquired with the test-site vertical sensor array when a vertical-impact source was positioned at source station 6, offset 1500 ft (457 m) from the array. (b) Data rotated to P, SR, and ST data space. All data panels are shown with a constant display gain.

Only data rotated to coordinate axes that isolate downgoing P, SR, and ST modes (the bottom rows of Figures 6.10, 6.11, and 6.12) were analyzed for energy content. Examination of these rotated data shows it is reasonably simple to define narrow windows that span the downgoing first arrivals of P, SR, and ST modes. After defining first-arrival times at each receiver station for each wave mode produced by each source, wavelet amplitudes were analyzed in 40-ms windows starting at the interpreted first-break times of each arriving mode. Wavelets inside these data windows represent the downgoing illumination wavelets for each wave mode. Curves of root-mean-square (rms) wavelet amplitudes calculated in these first-arrival windows for data generated at various source stations are exhibited on Figures 6.13 through 6.15.

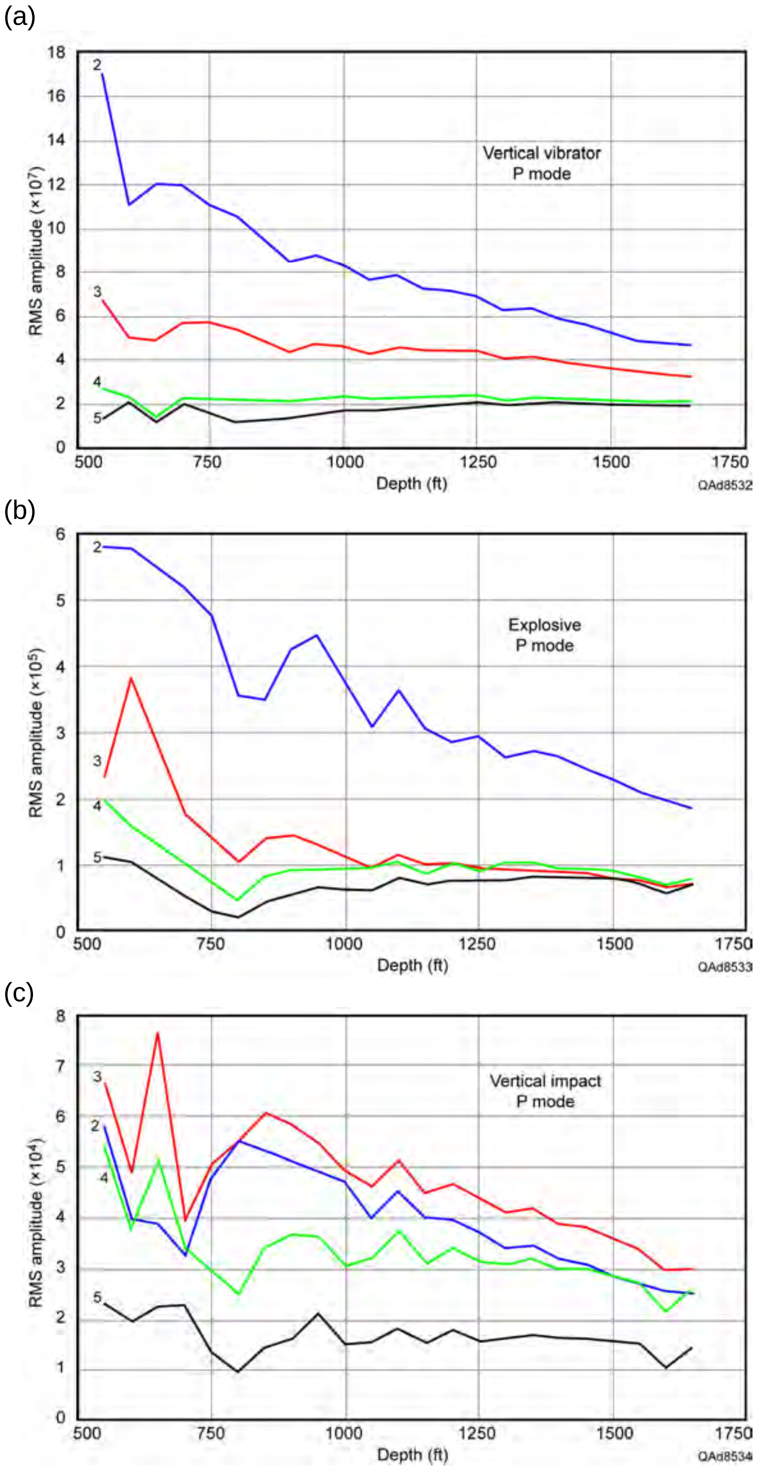

Figure 6.13. Root-mean-square (rms) amplitudes of downgoing P modes measured across the downhole vertical sensor array when sources are positioned at offset stations 2 through 5 (Fig. 6.3). Source station locations are indicated by the numbers on the curves. (a) Source is 60,000-lb (27,733-kg) vertical vibrator. (b) Source is 1 kg charge at depth of 6 m. (c) Source is an accelerated-weight impact delivering 22,276 ft-lb (30,202 joules) to the Earth.

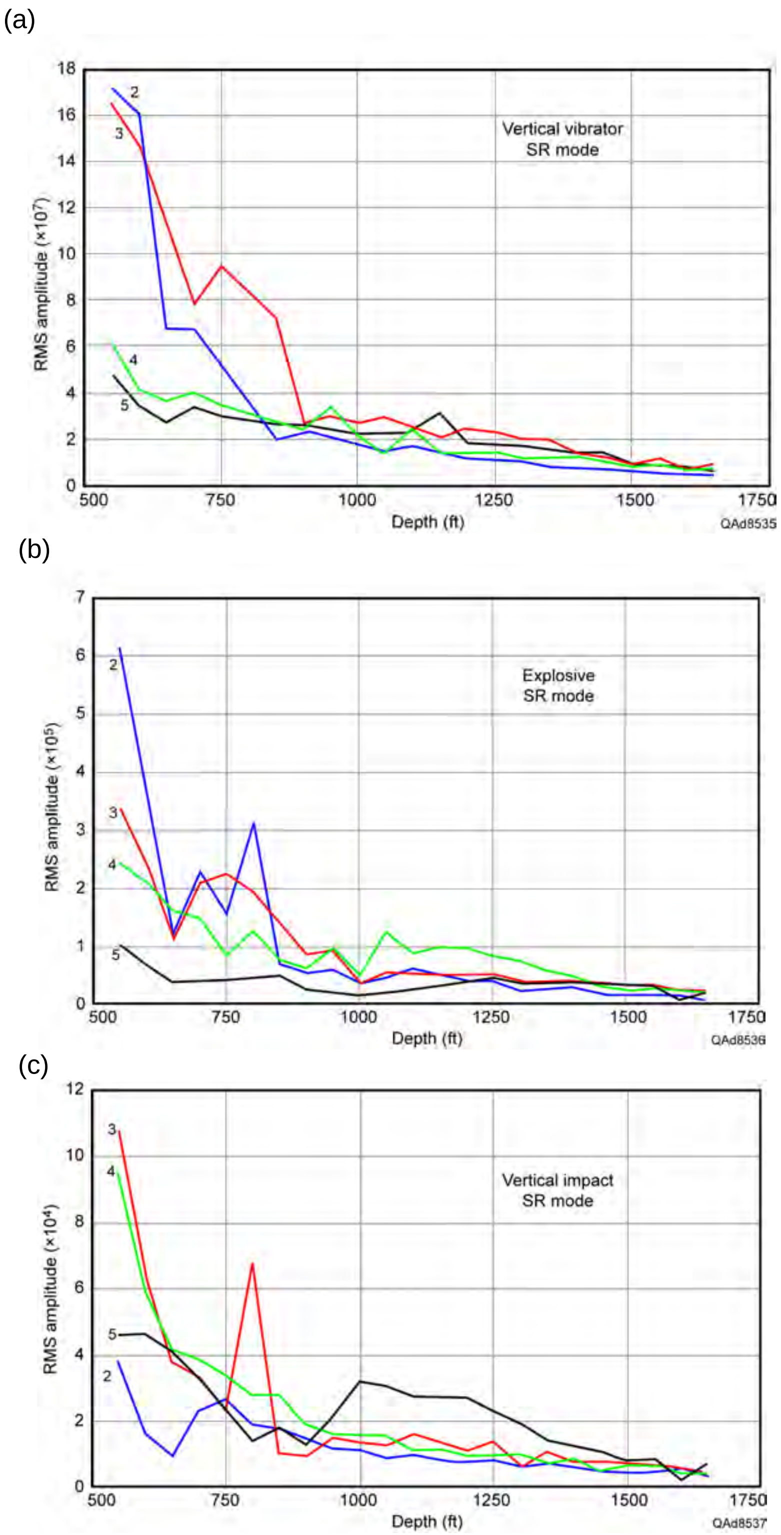

Figure 6.14. Root-mean-square (rms) amplitudes of downgoing SR modes measured across the downhole vertical sensor array when sources are positioned at offset stations 2 through 5 (Fig. 6.3). Source station positions are indicated by the numbers on the curves. (a) Source is 60,000-lb (27,733-kg) vertical vibrator. (b) Source is 1 kg charge at depth of 6 m. (c) Source is an accelerated-weight impact delivering 22,276 ft-lb (30,202 joules) to the Earth.

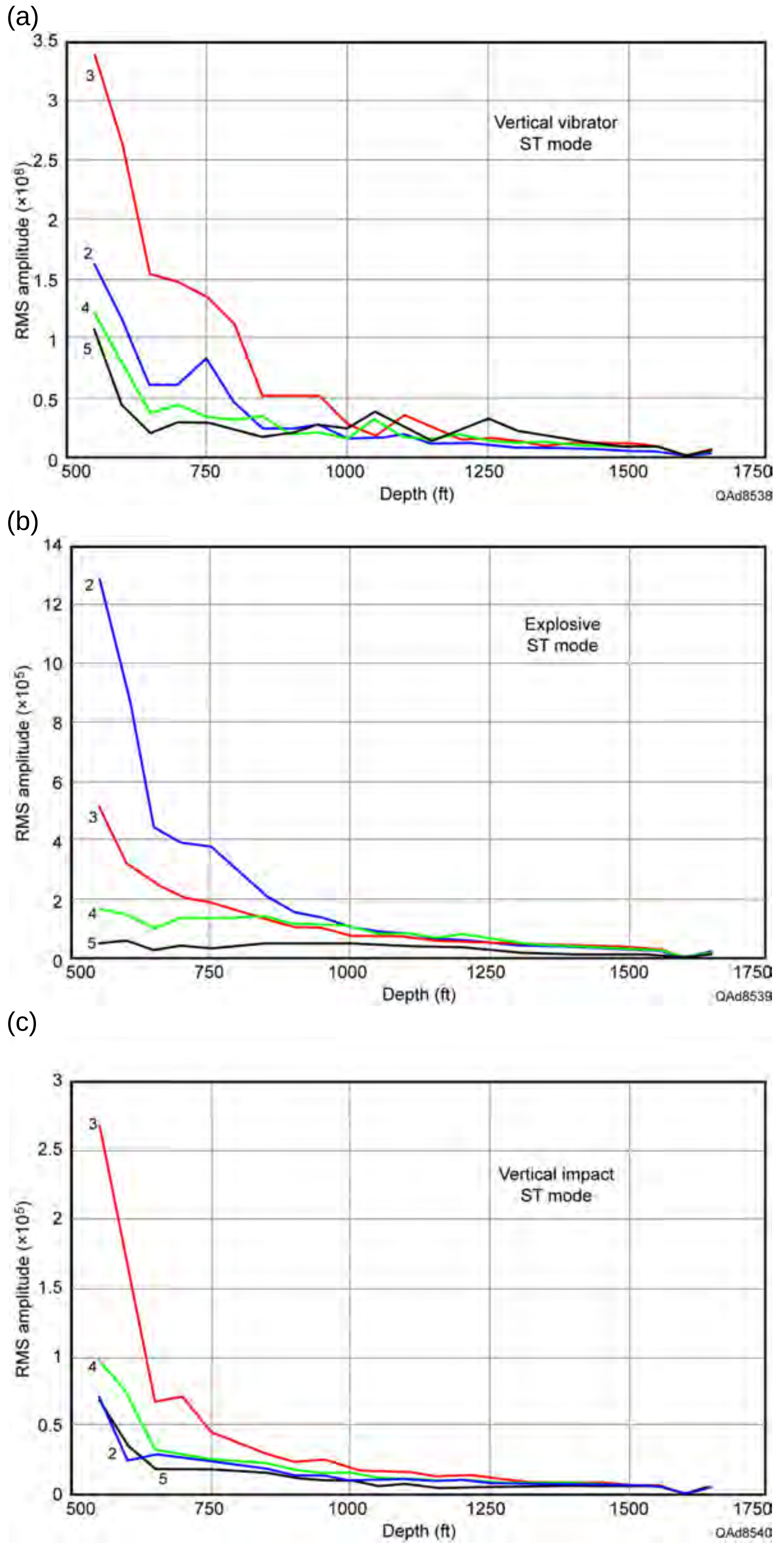

Figure 6.15. Root-mean-square (rms) amplitudes of downgoing ST modes measured across the downhole vertical sensor array when sources are positioned at offset stations 2 through 5 (Fig. 6.3). Source station positions are indicated by the number on the curves. (a) Source is 60,000-lb (27,733-kg) vertical vibrator. (b) Source is 1 kg charge at depth of 6 m. (c) Source is an accelerated-weight impact delivering 22,276 ft-lb (30,202 joules) to the Earth.

Important energy-related characteristics of the sources that were tested which should be kept in mind as data on Figures 6.10 through 6.15 are examined include the following specifications:

- Vertical vibrator: I/O AHV IV PLS 362 with a hold-down weight of 60,000 lb (27,733 kg). Linear 8-seconds sweep from 8 to 96 Hz.
- Explosive: One kilogram (2.2 lb) placed at a depth of 6 m (20 ft).
- Vertical impact: 33,000-lb vehicle with 1000-psi nitrogen-spring weight-acceleration system that delivers impact energy of 22,276 ft-lb (30,202 joules).

.

QAd7462(a)

Figure 6.16. VSX™ accelerated-weight impact source provided by Vecta Technology and United Services Alliance. This source can deliver a vertical impact to the Earth, or an inclined force vector can be applied in any azimuth direction and at any incident angle between 0 and 45 degrees without moving the vehicle. Vehicle weight is 33,000 lb. Its compressed-nitrogen spring system delivers 22,276 ft-lb (30,202 joules) of energy to the Earth.

The vertical vibrator used in the test is shown in both photos of Figure 6.4. The accelerated-weight impact source from United Service Alliance, which is powered by a compressed-nitrogen spring, is shown as Figure 6.16. These photos, together with the source characteristics just listed, imply the vertical vibrator is quite powerful and should put more energy into the ground than does either the explosive shot or the vertical-impact source. Test data exhibited as Figures 6.13 through 6.15 confirm this expected energy advantage of the vibrator, with the amplitudes of vibrator-produced wave modes being approximately 1000 times larger than the amplitudes of corresponding modes produced by the weight-impact source and approximately 100 times stronger than amplitudes of modes produced by a 1-kg explosive detonated at a depth of 6 m.

Frequency attributes of the wave modes produced by the sources are illustrated as Figures 6.17 through 6.19. These analyses show the narrow data windows spanning the downgoing illumination wavelets where frequency spectra were calculated. These data windows differ slightly from those used to measure the wavelet amplitude curves exhibited as Figures 6.13 through 6.15. The data within each shaded analysis window are almost pure wave-mode signal and have a minimal amount of non-mode noise. For this reason, each frequency spectrum is assumed to be a reasonable indication of the signal-frequency content in each downgoing illumination wavelet. Amplitudes that are more than 20 dB below the peak of an amplitude spectrum are assumed to be too small to make significant contributions to images and are ignored. The position of the -20 dB cutoff line that indicates frequency bandwidth is labeled on each spectrum. The effective signal-frequency content of each wave mode is defined as the frequency spectrum extending above each 20 dB cutoff line. Defining effective signal frequency with a 20 dB cutoff is only an approximation, because this assumption results in some signal energy extending beyond the limits of the 8 to 96 Hz sweep of the vertical vibrator (Fig. 6.17).

Frequency and amplitude-strength characteristics of wave modes measured by the downhole vertical-receiver array are summarized on Table 6.1. On this table, the amplitude measures displayed on Figures 6.13 to 6.15 are listed as “order of magnitude” quantities rather than as specific numerical values. In contrast to the amplitude information that was analyzed at four source stations (stations 2, 3, 4, 5) on Figures 6.13 to 6.15, the frequency characteristics summarized on Table 6.1 relate to data generated only at source station 3. Key principles defined by these tabulated amplitude and frequency characteristics are:

1. The ST (transverse S) mode is the most energetic mode produced by each source, with ST amplitudes often tending to be almost 10 times larger than P and SR amplitudes (Table 6.1).

2. Explosive-source wave modes have amplitudes approximately 100 times smaller than the amplitudes of vertical-vibrator wave modes (Table. 6.1).

3. Vertical-impact wave modes have amplitudes approximately 1,000 times smaller than the amplitudes of vertical-vibrator wave modes (Table 6.1).

4. All three vertical-force sources (vibrator, explosive, impact) produce robust P and S wave modes, and each source would be effective for many P and S imaging objectives.

5. For the vertical vibrator, the signal frequencies of SR and ST wave modes are essentially the same as the signal frequencies of the P mode. The frequency bandwidths of all vibrator wave modes are constrained by the 8–96 Hz sweep used to generate the data (Fig. 6.17).

6. For the explosive source, the signal frequency bandwidth of the P mode (approximately 5 to 200 Hz) is approximately twice the signal bandwidths of the SR and ST shear modes (Fig. 6.18). However, the 5 to 80 Hz (approximate) bandwidths of the SR and ST signal frequencies exceed the bandwidths of S modes that experience shows can be produced with horizontal vibrators, which tend to be about 4 to 50 Hz (or less).

7. The vertical-impact source (Fig. 6.19) produces a P mode that has a bandwidth (5 to 130 Hz) that is approximately twice that of the bandwidths of the SR mode (5 to 60 Hz) and the ST mode (5 to 70 Hz). However, P-mode frequencies greater than 50 Hz are significantly weaker in amplitude than frequency components less than 50 Hz (Fig. 6.19), causing all three modes (P, SR, ST) generated by the impact source to have approximately the same "effective" bandwidth. The ST shear mode has much of its energy concentrated in the frequency range between 30 and 50 Hz, which interestingly causes the amplitude of that mode to be 4 dB to 6 dB greater than the amplitudes of the P and SR modes.

Table 6.1. Amplitude and frequency attributes of wave modes measured by downhole sensors.

Source	P mode		SR mode		ST mode	
	Amplitude	Freq (Hz)	Amplitude	Freq (Hz)	Amplitude	Freq (Hz)
Vertical vibrator	10^7	8–96	10^7	8–96	10^8	8–96
Explosive	10^5	5–200	10^5	5–80	10^5	5–80
Vertical impact	10^4	5–130	10^4	5–60	10^5	5–70

Amplitude properties taken from Figures 13 - 15 for source stations 2, 3, 4, and 5.
Frequency properties taken from Figures 17 – 19 for source station 3 only.

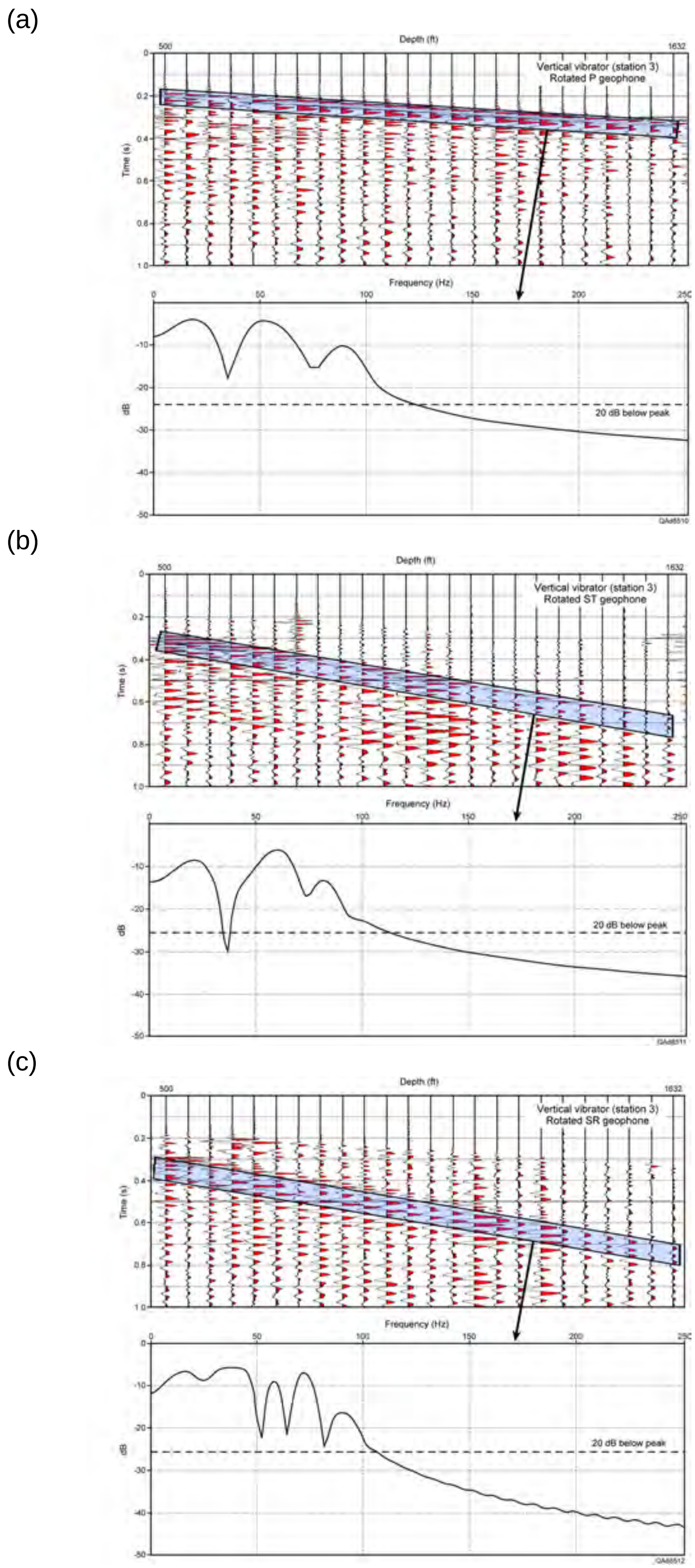

Figure 6.17. Frequency analysis of elastic wave modes produced by the 60,000-lb (27,733-kg) vertical vibrator at source station 3 and recorded by the downhole vertical array. (a) P mode. (b) ST mode. (c) SR mode. Amplitudes of the frequency spectra indicate relative strengths of the wave modes propagating away from the source station.

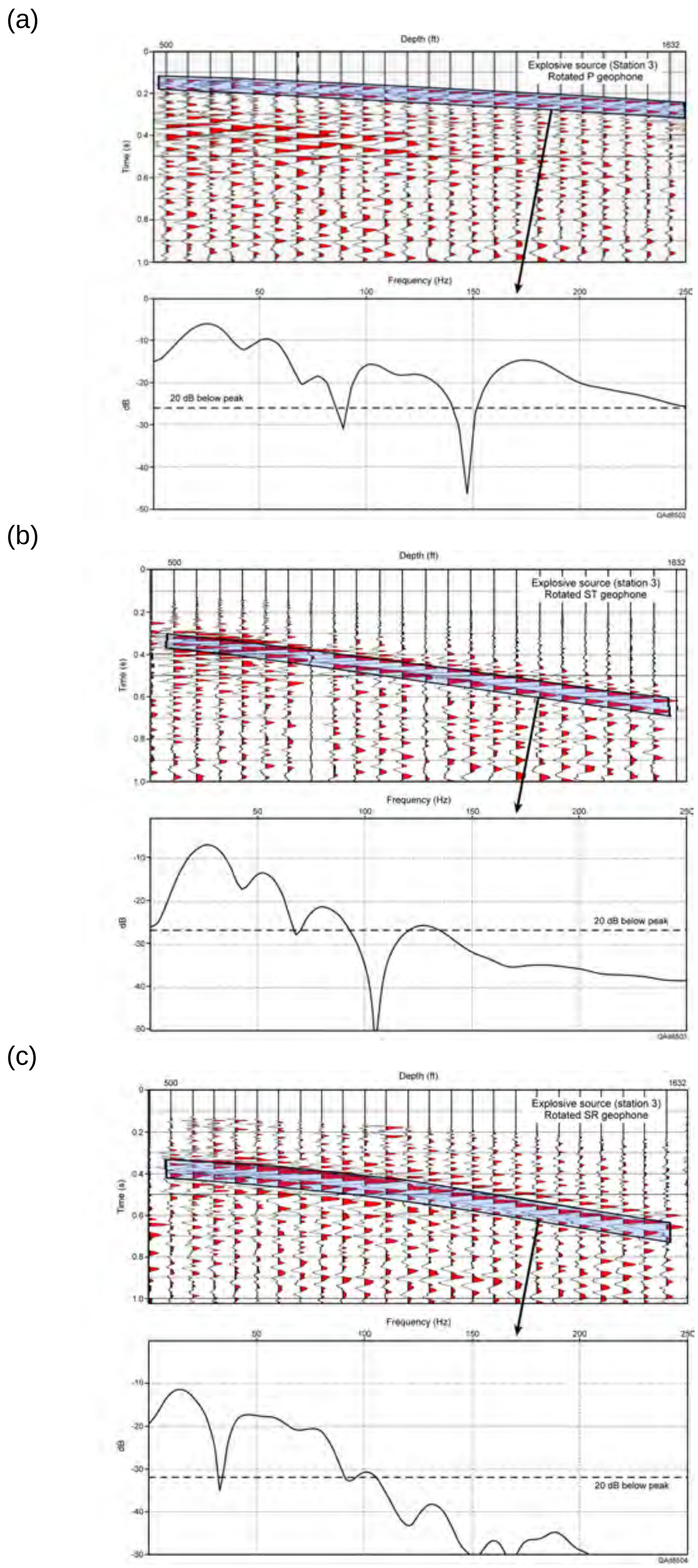

Figure 6.18. Frequency analysis of elastic wave modes produced by a 1-kg explosive shot at a depth of 6 m at source station 3 and recorded by the downhole vertical array. (a) P mode. (b) ST mode. (c) SR mode. Amplitudes of the frequency spectra indicate relative strengths of the wave modes propagating away from the source station.

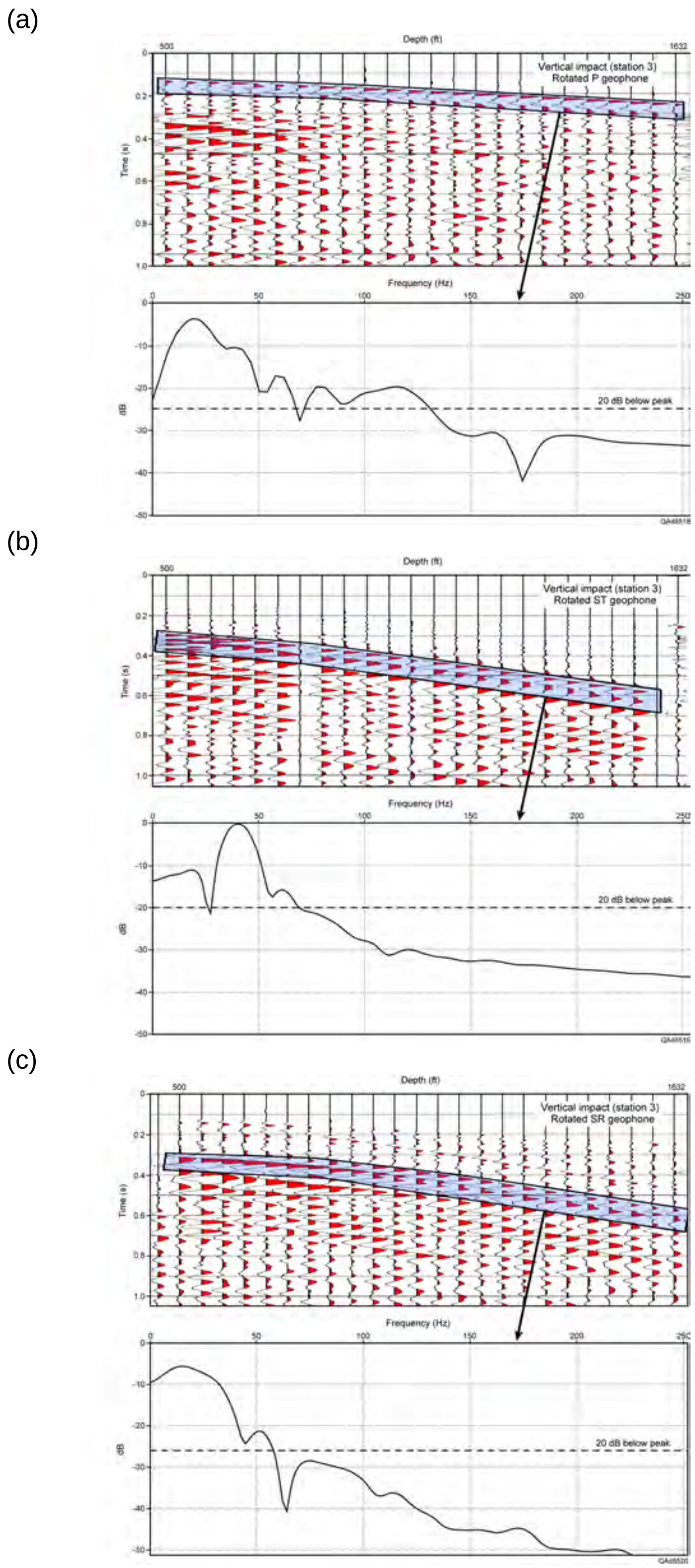

Figure 6.19. Frequency analysis of elastic wave modes produced by a vertical-impact source delivering 22,276 ft-lb (30,202 joules) of energy at source station 3 and recorded by the downhole vertical array. (a) P mode. (b) ST mode. (c) SR mode. Amplitudes of the frequency spectra indicate relative strengths of the wave modes propagating away from the source station.

Surface Array Measurements of Wave-Mode Amplitudes and Frequencies Produced by Test Sources

Offset distances of source stations from receiver Well 4 are defined on Table 6.2. Except for the first (No. 1) and last (No. 9) stations in this list, sources were offset at uniform distance increments of 250 ft (76.2 m) from the vertical receiver array in Well 4. These source-station intervals are the same distance as the dimension of the 25-station horizontal arrays of surface receivers. A graphical illustration of this tabulated source and receiver geometry is illustrated on Figure 6.3.

Table 6.2. Source station offsets.

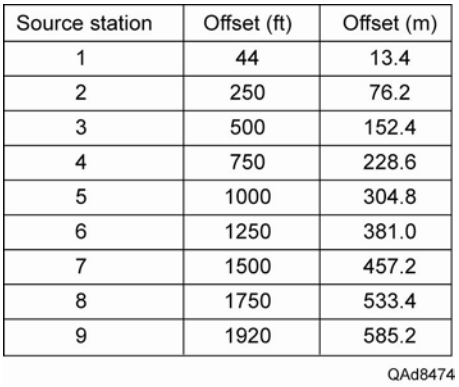

Source station	Offset (ft)	Offset (m)
1	44	13.4
2	250	76.2
3	500	152.4
4	750	228.6
5	1000	304.8
6	1250	381.0
7	1500	457.2
8	1750	533.4
9	1920	585.2

With this source geometry, data acquired by orthogonal X,Y,Z sensors deployed across the 25-station surface receiver array can be represented as 192-trace, single-fold field records having trace spacings of 10 ft (3 m) and extending 1920 ft (585.2 m) from the vertical receiver array. Examples of field records produced when the vertical impact source was positioned at source stations 2 through 9 are displayed on Figure 6.20a. For each sensor profile, static shifts occur in 25-trace blocks along the source line because no P or S source-station static corrections have been applied to the individual common-source gathers. The convex-shape of P-wave refraction arrivals within each 25-trace common-source segment is caused by intra-array P-wave receiver statics across the 250-ft (76.2 m) interval spanned by the surface receiver spread.

These same data are displayed as Figure 6.20b with P-wave static adjustments applied to each trace of the 192-trace record. P-wave refractions, and by inference P-wave reflections, none of which are obvious in the data displays, are now reasonably phase aligned. However, discontinuities in S-wave refractions still exist between adjacent source gathers because S source statics differ from P source statics. Likewise, within each common-source gather, S-wave refractions have nonlinear moveouts because intra-array S-wave statics across the 250-ft (76.2 m) distance spanned by the surface receivers differ from P-wave statics. Additional static corrections are required to create optimal alignment of S events.

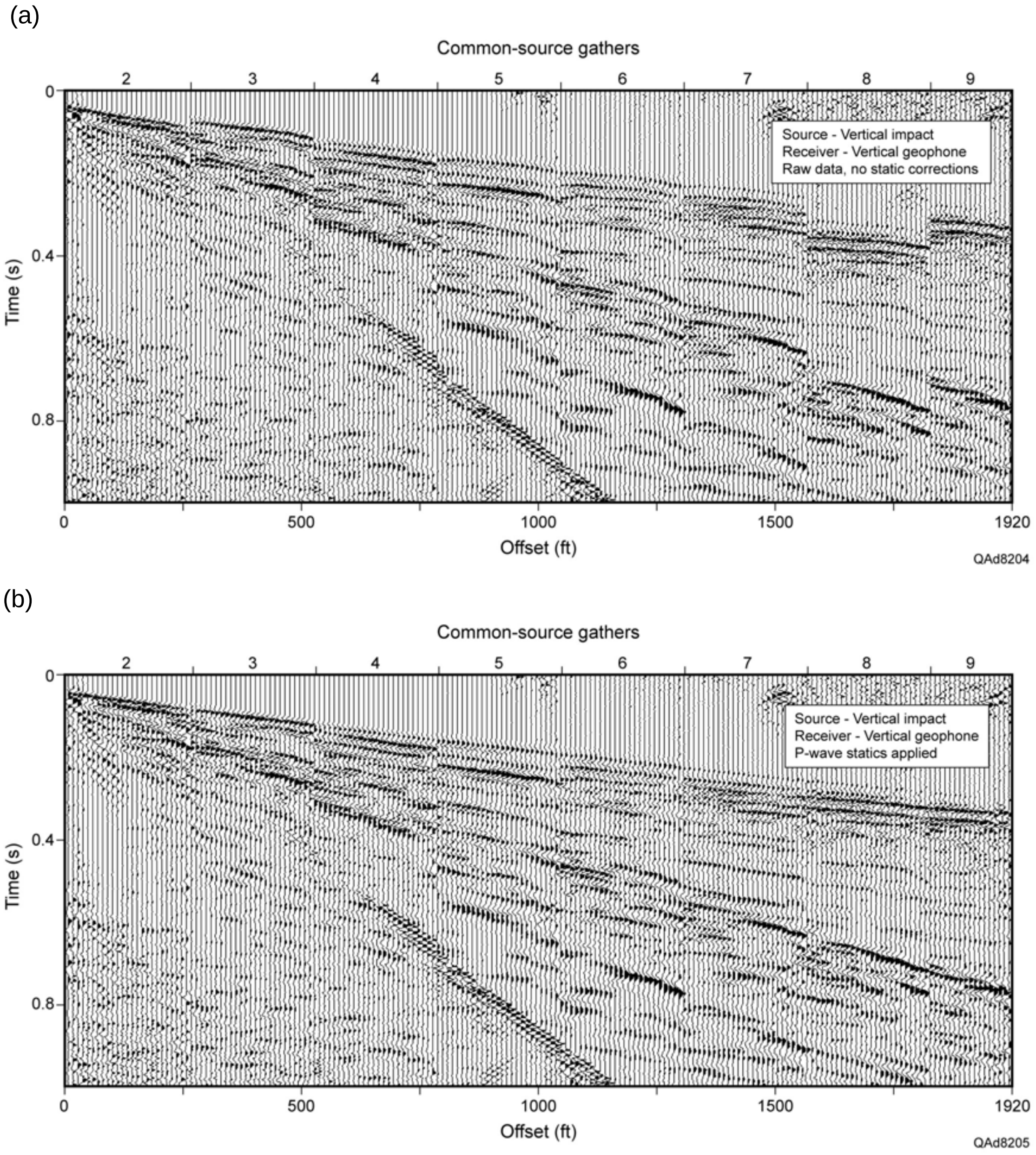

Figure 6.20. (a) Data generated by a vertical weight-impact source positioned at source stations 2 through 9 and recorded by surface vertical geophones. Discontinuities between each 25-trace group of source-station gathers are caused by source-station statics and variations in time-zero for this impact source. (b) Same data with adjustments made to align the earliest P-wave refraction arrivals.

Test data acquired with surface-based 3C geophones and Sigma cable-free boxes are analyzed in this section to compare the energy content and frequency bandwidth of P and S modes produced by each of the three tested vertical-force source types. The data windows illustrated on Figures 6.17 through 6.19 consist of downgoing target-illuminating P and S wavelets that are essentially pure signal and have minimal noise contamination. In contrast, the data on Figures 6.21 through 6.29 were acquired by a surface-positioned horizontal sensor array and contain not only P and S reflections and refractions, but also intrabed multiples and horizontally traveling surface-wave noise. The signal-to-noise ratio of downgoing target-illumination wavelets acquired by downhole vertical receiver arrays (Figs. 6.17 to 6.19) is high; whereas, the signal-to-noise ratio of reflection data acquired with surface-based horizontal receiver arrays (Figs. 6.21 to 6.29) is much lower.

Because the surface-array data are only 1-fold and the short length of the profile does not allow significant reflection curvature to be recognized, it is difficult to identify reflection signal in the data shown on Figures 6.21 through 6.29 by visual inspection. For this reason, a simple analysis procedure is used in which amplitude strengths and frequency bandwidths are calculated for refracted P, S, and surface waves that sweep across the horizontal receiver array. Reflection signal analyses of these surface-recorded data will be shown and discussed in a following section of this chapter.

Analyses of vertical-vibrator data are shown as Figures 6.21 to 6.23; explosive source data are analyzed on Figures 6.24 to 6.26; and vertical-impact source results are presented as Figures 6.27 to 6.29. For each source, separate analyses are done for vertical geophones, inline-horizontal (radial) geophones, and crossline-horizontal (transverse) geophones. For each geophone orientation, wave-mode velocity and frequency characteristics are calculated in data windows constrained to span only interpreted P, S, or surface-wave modes.

Velocity and frequency behavior are displayed as frequency-wavenumber (FK) spectra. On these FK plots, the vertical axis defines how energy embedded in a wave mode is distributed as a function of frequency. The horizontal axis spans a positive half-plane of wavenumber space (K) and a negative half-space. The negative-K half-space defines events that propagate left-to-right from zero offset to an offset of 1920 ft. This left-to-right direction is the propagation direction for all wave modes that are analyzed. The positive half-plane defines events that propagate right-to-left, from an offset of 1920 ft back to zero offset. In this display format, no events propagate right-to-left, so no energy appears in positive wavenumber half-space in any figure. The slope of energy distribution on these FK plots defines the propagation velocity of a wave mode, with steeper slopes implying higher wave-mode propagation velocities.

Data acquired with vertical and radial-horizontal geophones have three embedded wave modes: a P-wave mode (labeled **P**), A radial shear mode (labeled **SR**), and a surface Rayleigh wave (labeled **R**). Data acquired with transverse-horizontal geophones have only two wave modes: a transverse shear mode (labeled **ST**) and a surface Love wave (labeled **L**). No effective P-wave energy appears on transverse horizontal geophones.

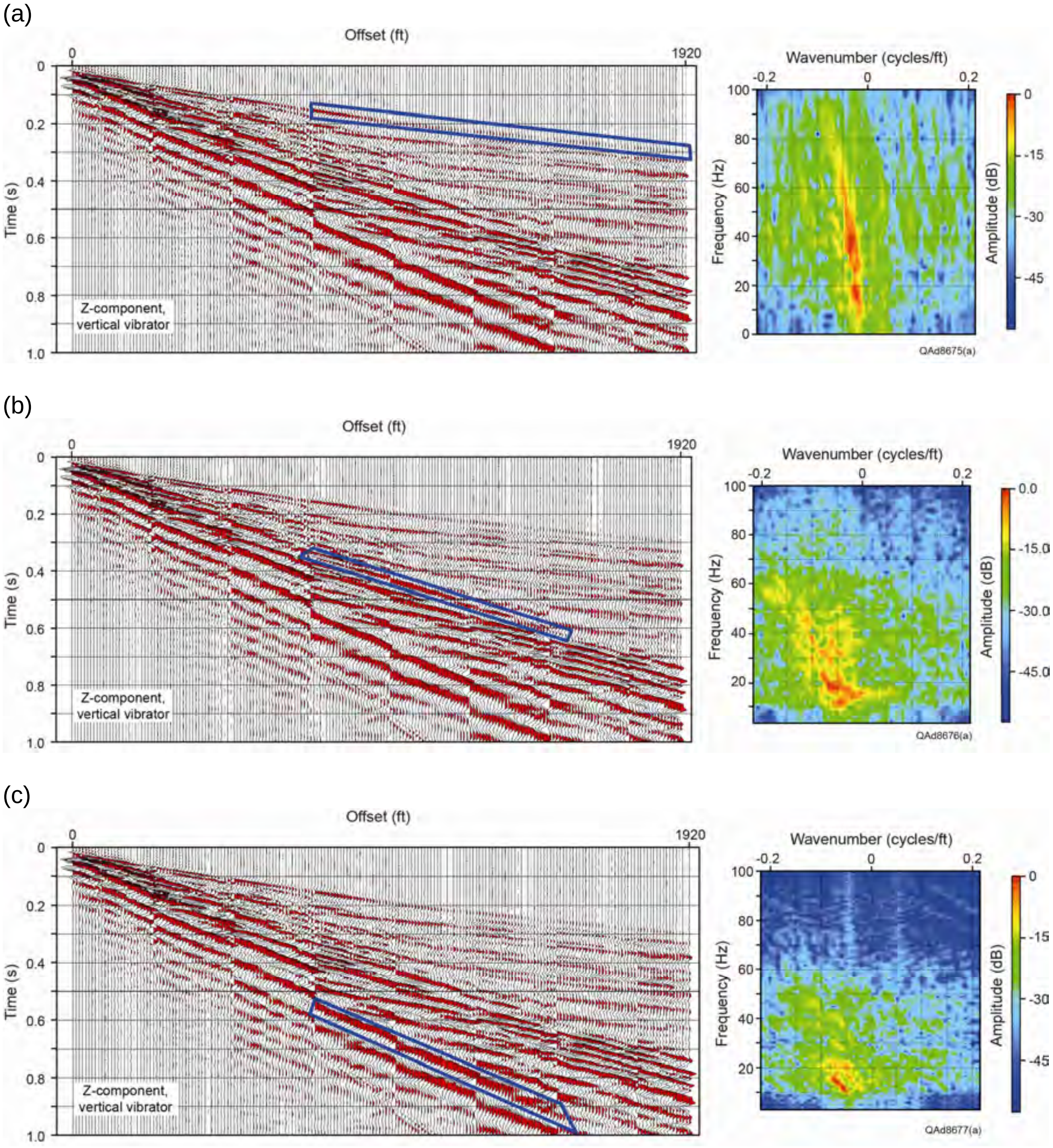

Figure 6.21. Analysis of refracted P, S, and Rayleigh wave modes produced by a vertical-vibrator source and recorded by vertical geophones deployed as a surface-based horizontal array. (a) Compressional mode, P. (b) Radial shear mode, SR. (c) Rayleigh wave mode, R. Data recorded by Sigma cable-free boxes.

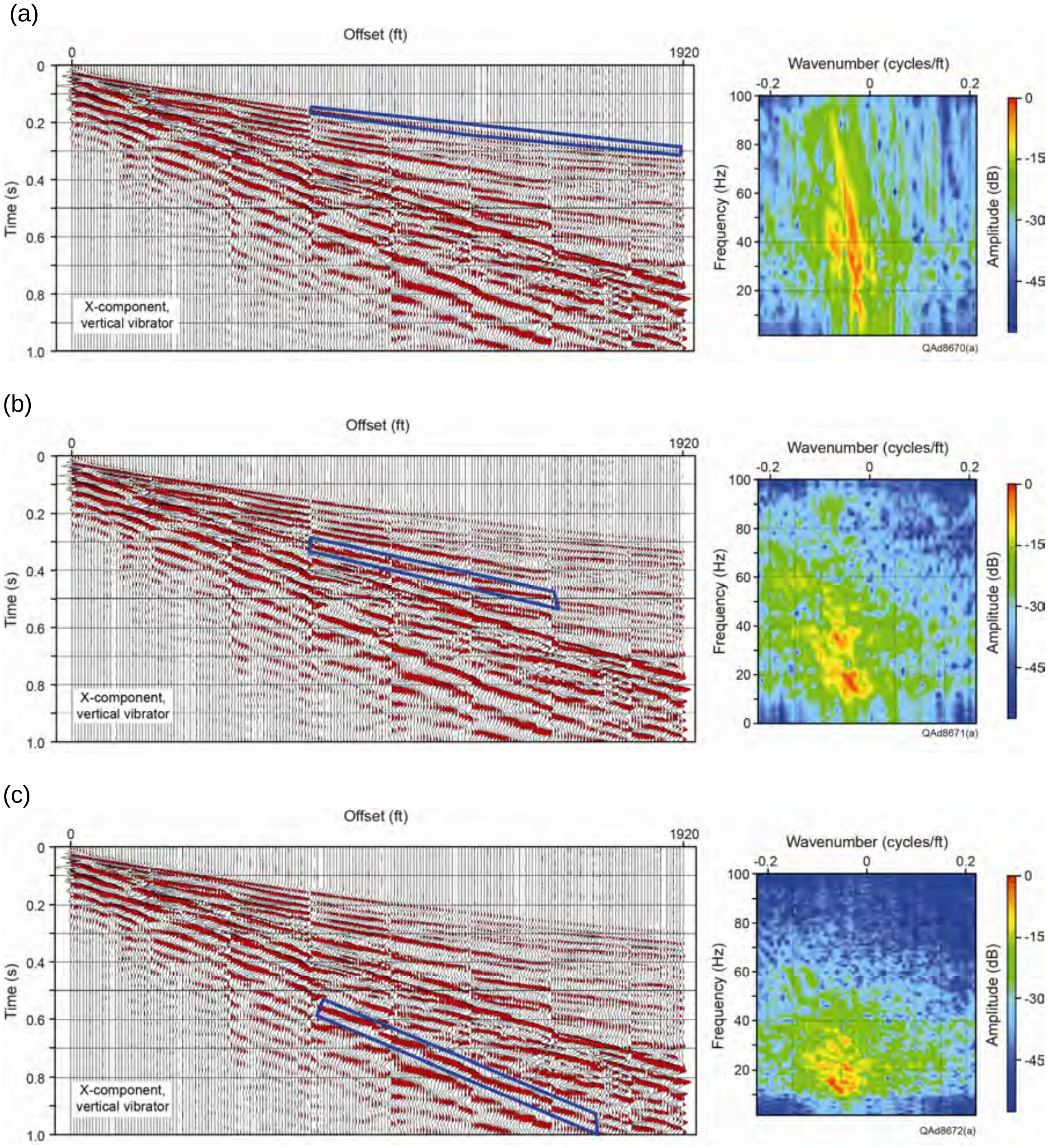

Figure 6.22. Analysis of refracted P, S, and Rayleigh wave modes produced by a vertical-vibrator source and recorded by inline-horizontal (radial) geophones deployed as a surface-based horizontal array. (a) Compressional mode, P. (b) Radial shear mode, SR. (c) Rayleigh wave mode, R. Data acquired by Sigma cable-free boxes.

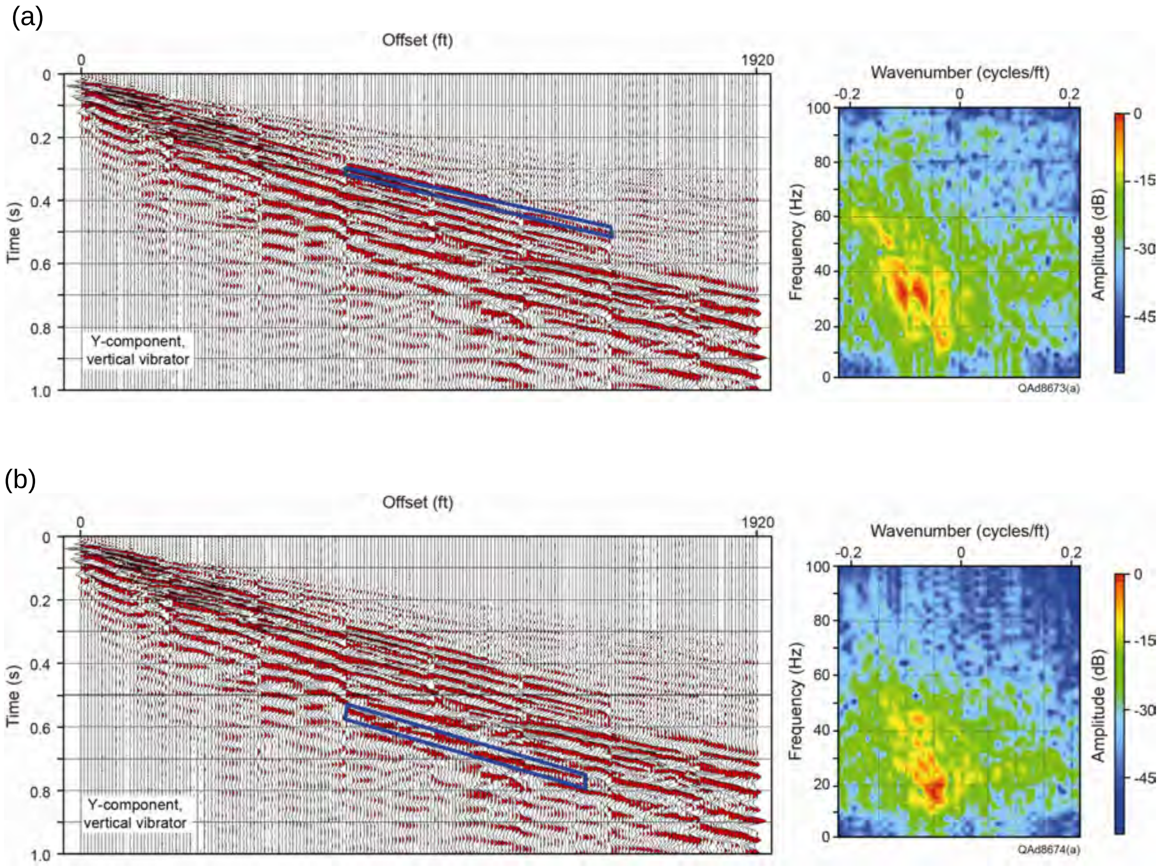

Figure 6.23. Analysis of refracted S and Love wave modes produced by a vertical-vibrator source and recorded by crossline-horizontal (transverse) geophones deployed as a surface-based horizontal array. (a) Transverse shear mode, ST. (b) Love wave mode, L. No P mode is recorded by transverse horizontal geophones. Data recorded by Sigma cable-free boxes.

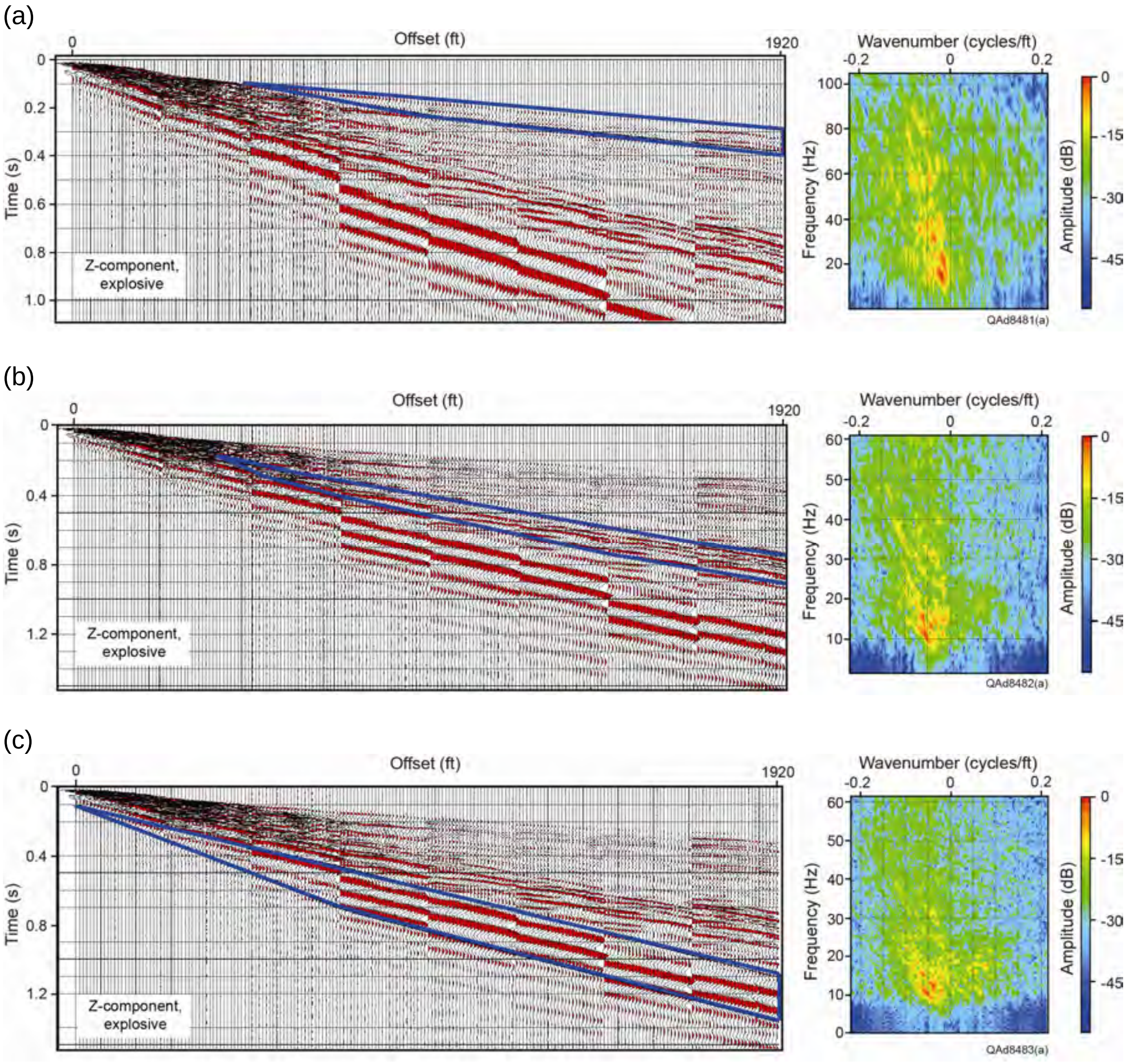

Figure 6.24. Analysis of refracted P, S, and Rayleigh wave modes produced by an explosive source and recorded by vertical geophones deployed as a surface-based horizontal array. (a) Compressional mode, P. (b) Radial shear mode, SR. (c) Rayleigh wave mode, R. Data recorded by Sigma cable-free boxes.

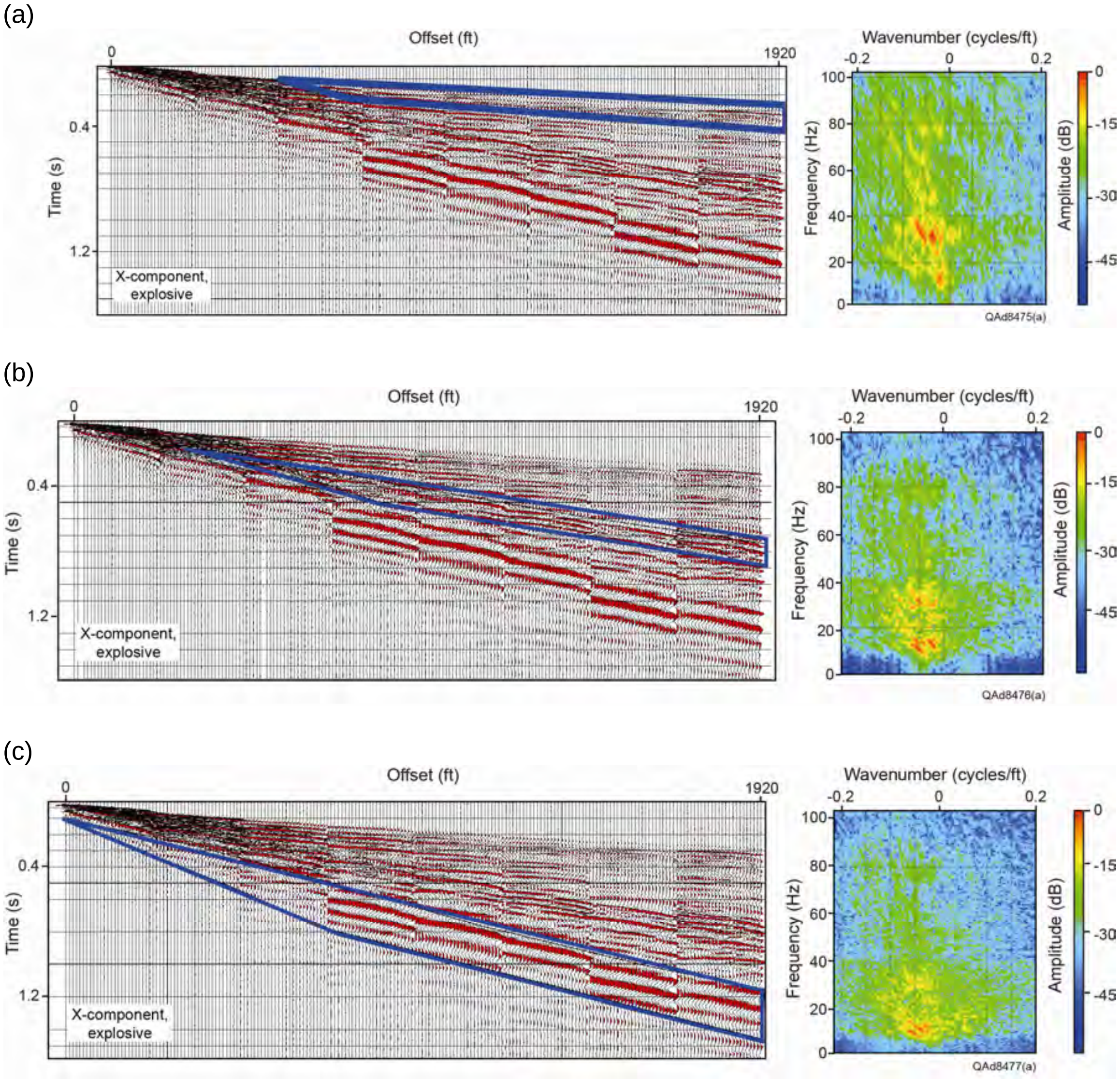

Figure 6.25. Analysis of refracted P, S, and Rayleigh wave modes produced by an explosive source and recorded by inline-horizontal (radial) geophones deployed as a surface-based horizontal array. (a) Compressional mode, P. (b) Radial shear mode, SR. (c) Rayleigh wave mode, R. Data recorded by Sigma cable-free boxes.

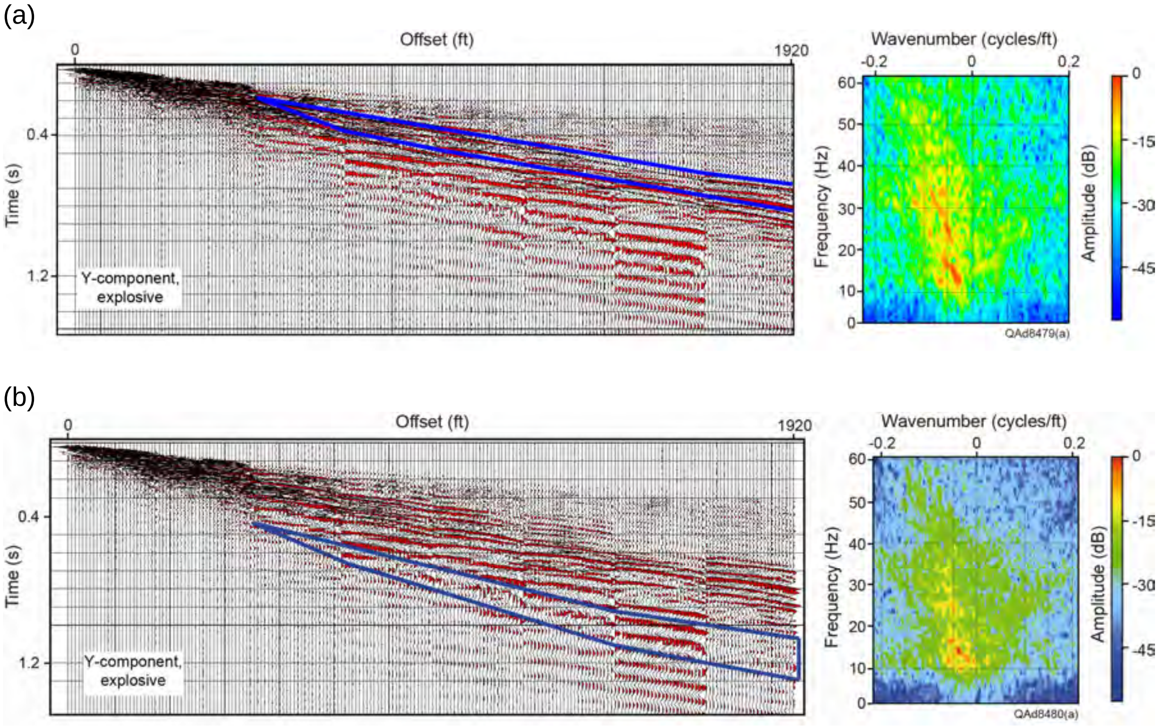

Figure 6.26. Analysis of refracted S and Love wave modes produced by an explosive source and recorded by crossline-horizontal (transverse) geophones deployed as a surface-based horizontal array. (a) Transverse shear mode, ST. (b) Love wave mode, L. No P mode is recorded by transverse horizontal geophones. Data recorded by Sigma cable-free boxes.

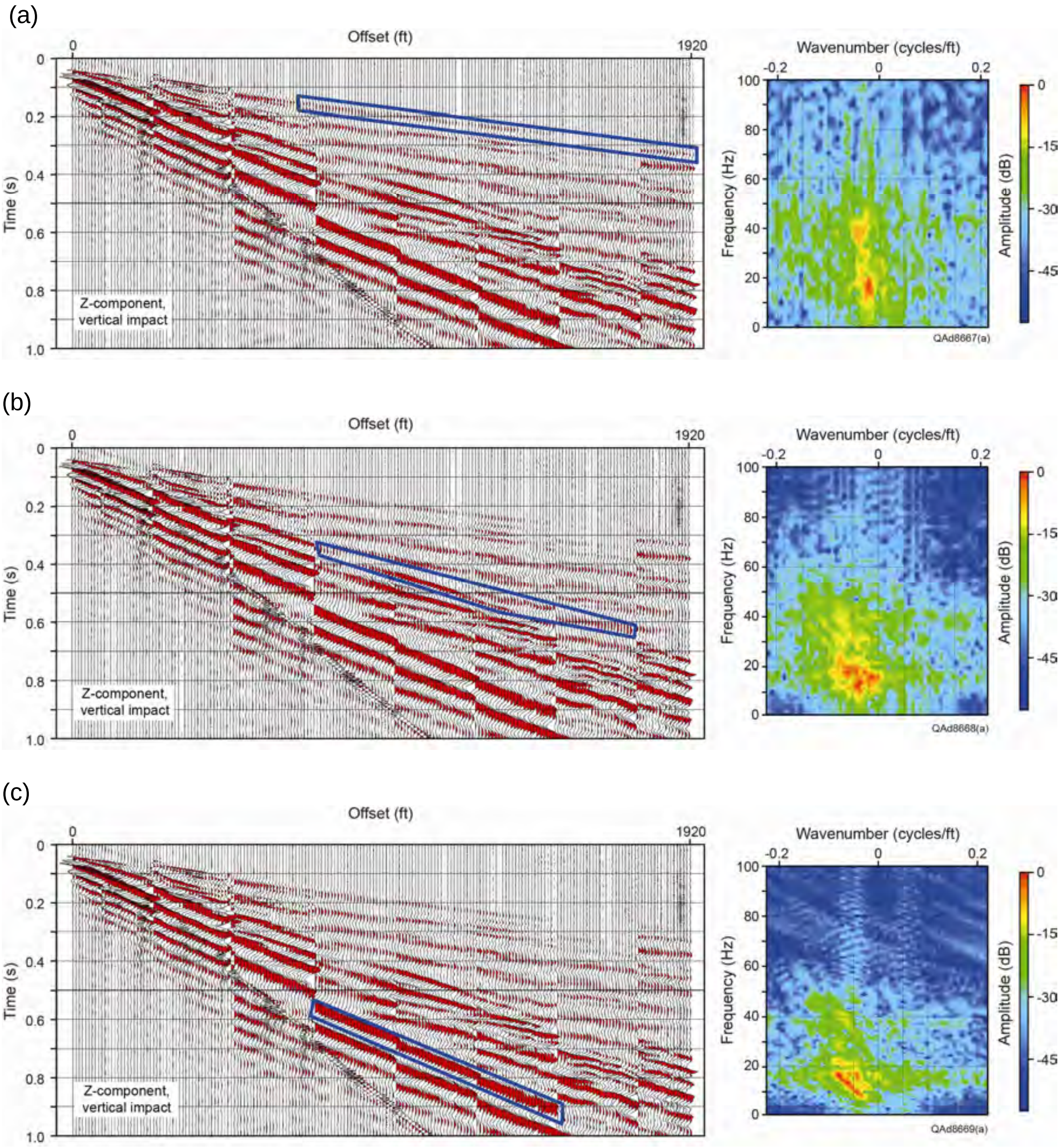

Figure 6.27. Analysis of refracted P, S, and Rayleigh wave modes produced by a vertical-impact source and recorded by vertical geophones deployed as a surface-based horizontal array. (a) Compressional mode, P. (b) Radial shear mode, SR. (c) Rayleigh wave mode, R. Data recorded by Sigma cable-free boxes.

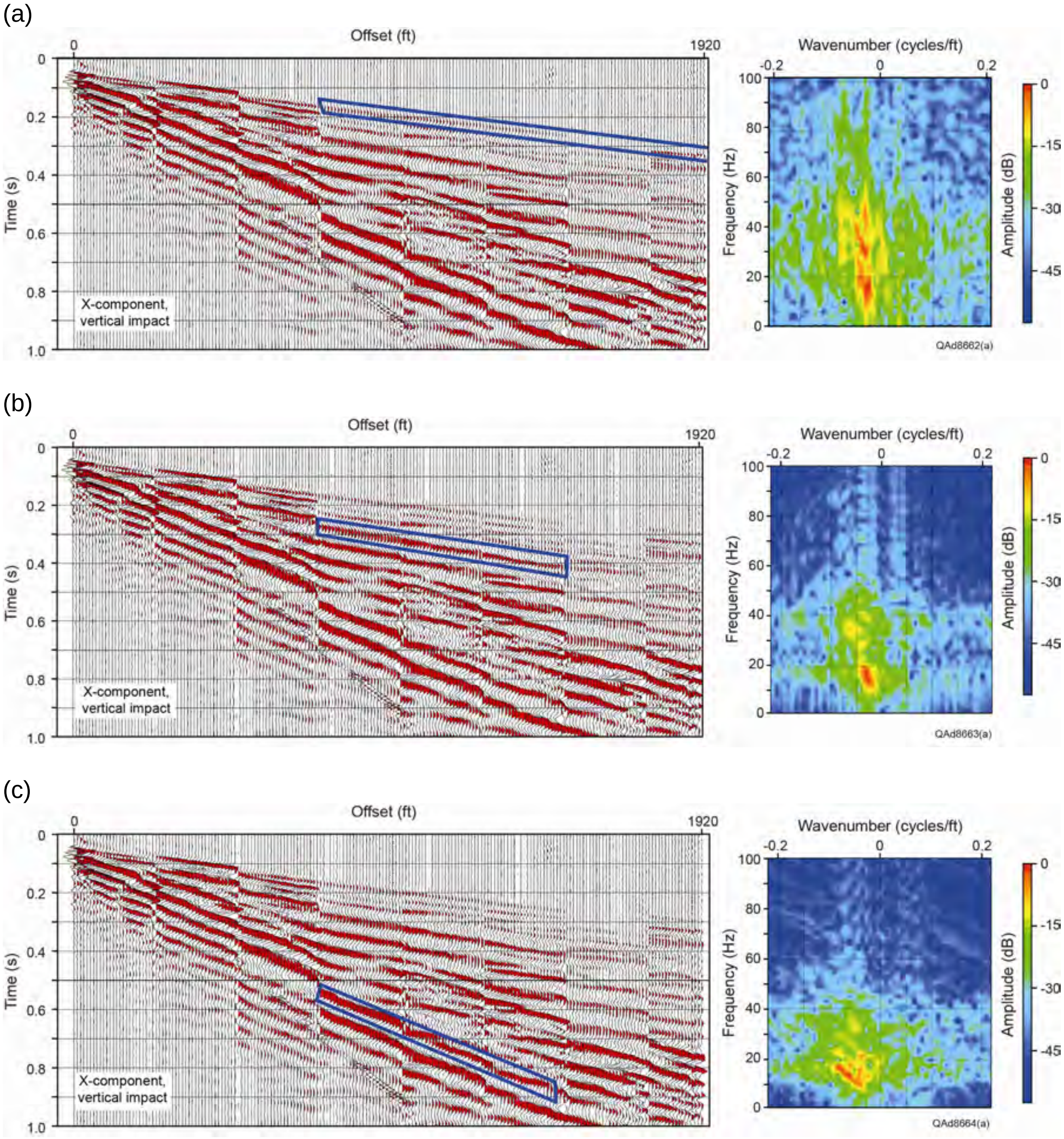

Figure 6.28. Analysis of refracted P, S, and Rayleigh wave modes produced by vertical-impact source and recorded by inline-horizontal (radial) geophones deployed as a surface-based horizontal array. (a) Compressional mode, P. (b) Radial shear mode, SR. (c) Rayleigh wave mode, R. Data recorded by Sigma cable-free boxes.

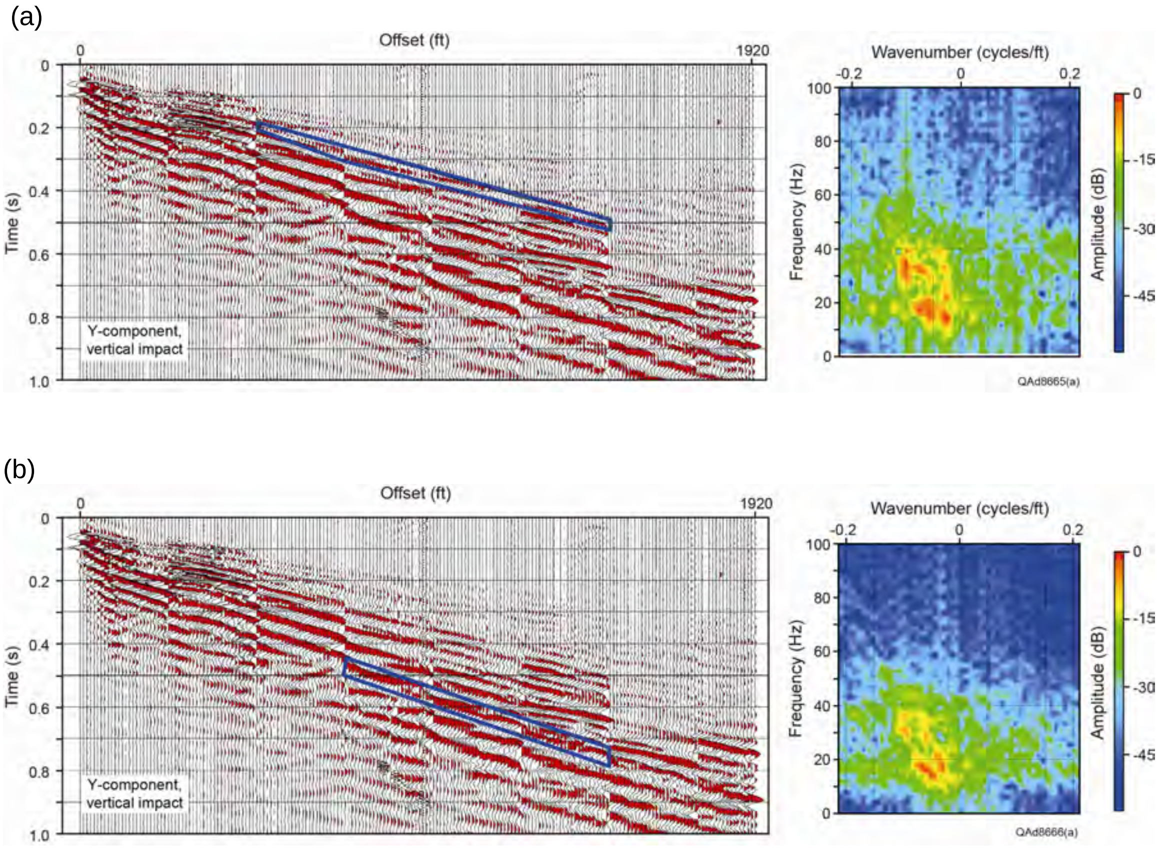

Figure 6.29. Analysis of refracted S and Love wave modes produced by vertical-impact source and recorded by crossline-horizontal (transverse) geophones deployed as a surface-based horizontal array. (a) Transverse shear mode, ST. (b) Love wave mode, L. No P mode is recorded by transverse horizontal geophones. Data recorded by Sigma cable-free boxes.

Source-specific amplitude and frequency characteristics of P, S, and surface-wave modes (either Rayleigh waves or Love waves) that can be inferred from these horizontal-array data are summarized below:

1. By visual inspection of the wiggle-trace data, refracted waves segregate into rather obvious P, S, and surface-wave modes for each source, allowing mode-specific data analysis windows to be positioned on the data.

2. FK spectra calculated for P, S, and surface-wave data windows vary from source to source.

3. Surface-wave modes are lower frequency than P and S modes for all sources, both by visual inspection of wiggle-trace data and by comparison of calculated FK spectra.

4. Examination of FK spectra shows P-mode spectra calculated for vertical geophones and inline-horizontal geophones are approximately equivalent for vertical vibrator and explosive sources (Figs. 6.21 and 6.24). P-mode spectra produced by the vertical impact source span a frequency band approximately 70-percent (one-third less) than that of the vertical vibrator and explosive sources, with diminished energy content occurring at the higher-frequency end of the impact-source spectra (Fig. 6.27).

5. FK spectra calculated from horizontal-transverse geophone data (Figs. 6.23a, 6.26a, 6.29a) show ST-mode spectra are roughly equivalent for the vertical vibrator and explosive sources. ST spectra for the vertical impact source span a frequency band slightly less than that of the vertical vibrator and explosive sources.

When horizontal vibrators are used to generate S-wave data, S-wave modes have frequencies that usually extend to only 50 Hz. This upper-frequency constraint is caused by mechanical limitations of horizontal vibrators. Although a horizontal vibrator can sweep to frequencies higher than 50 Hz, numerous mechanical problems develop if a large number of high-frequency sweeps are done. For this reason, S-wave data generated by horizontal vibrators typically have frequency spectra that span 4 to 48 Hz or 5 to 50 Hz so that S-wave data can be acquired at a large number of source stations with minimal down time for vibrator repair. In contrast to the S-wave frequency limitation imposed by traditional S-wave sources, an important research finding provided by these test data is that S modes produced by vertical-force sources have frequency spectra that exhibit appreciable energy for frequencies higher than 50 Hz. Examples of broadband S-wave data produced by vertical vibrator and explosive sources are displayed as Figures 6.21b, 6.22b, 6.23a, and 6.26a. S-mode spectra calculated for the impact source (Figs. 6.27 through 6.29) span a frequency bandwidth equivalent to that usually generated by horizontal vibrators.

Each of the vertical-force sources (vertical vibrator, shot-hole explosive, vertical impact) creates good-quality elastic wavefields. Specifically, each source produces more S-wave energy than P-wave energy, and although energy output varies from source to source, the ratio of S-wave energy to P-wave energy is approximately the same for each source. Some sources can image deeper geology simply because they are more energetic. For example, the 60,000-lb vertical vibrator used in these tests produced wave-modes having amplitudes approximately 1000 times greater than wave-mode amplitudes produced by the impact source and approximately 100 times greater than wave-mode amplitudes created by the explosive source. As a result, this particular vertical vibrator should image deeper geology than what can be imaged with the vertical-impact source or the shot-hole explosive source. However, any of the three vertical-force sources can provide P and S images extending to depths of principal targets across most oil and gas prospects. Our test data do not cause us to conclude that one type of vertical-force source should be used to the exclusion of other vertical-force sources. Source selection will be dictated by factors such as surface conditions across a prospect, source availability, source cost, and target depth.

Comparisons of Geophones and Accelerometers as 3C Sensors

One objective of the equipment tests done at the Devine Test Site was to compare P and S wave modes acquired with 3C accelerometers and 3C geophones to determine if one type of sensor provided more attractive multicomponent data than the other. Several factors were considered when analyzing these sensor data, with key requirements being:

1. Geophones and accelerometers had to be planted in the same sediment,

2. All sensors had to be coupled to the Earth in the same manner,

3. All sensor outputs had to be recorded by the same recording system, and

4. Geophones and accelerometers had to record data generated by the same seismic source.

These four data constraints were addressed by: (Requirement 1) placing geophone stations and accelerometer stations side-by-side within 1 meter of each other (Fig. 6.4); (Requirement 2) taking care to bury all sensors flush with the ground surface and tamping soil around each sensor with the same consistency; (Requirement 3) recording geophone and accelerometer data with the same data-acquisition system—a cable-based Sercel 428, and (Requirement 4) recording data generated by only an explosive source.

As a result of these field test procedures, it is reasonably correct to assume that differences in P and S wave modes observed in data outputs from test-site geophone arrays and accelerometer arrays should be caused by the type of sensor that recorded the seismic wavefields rather than by other factors.

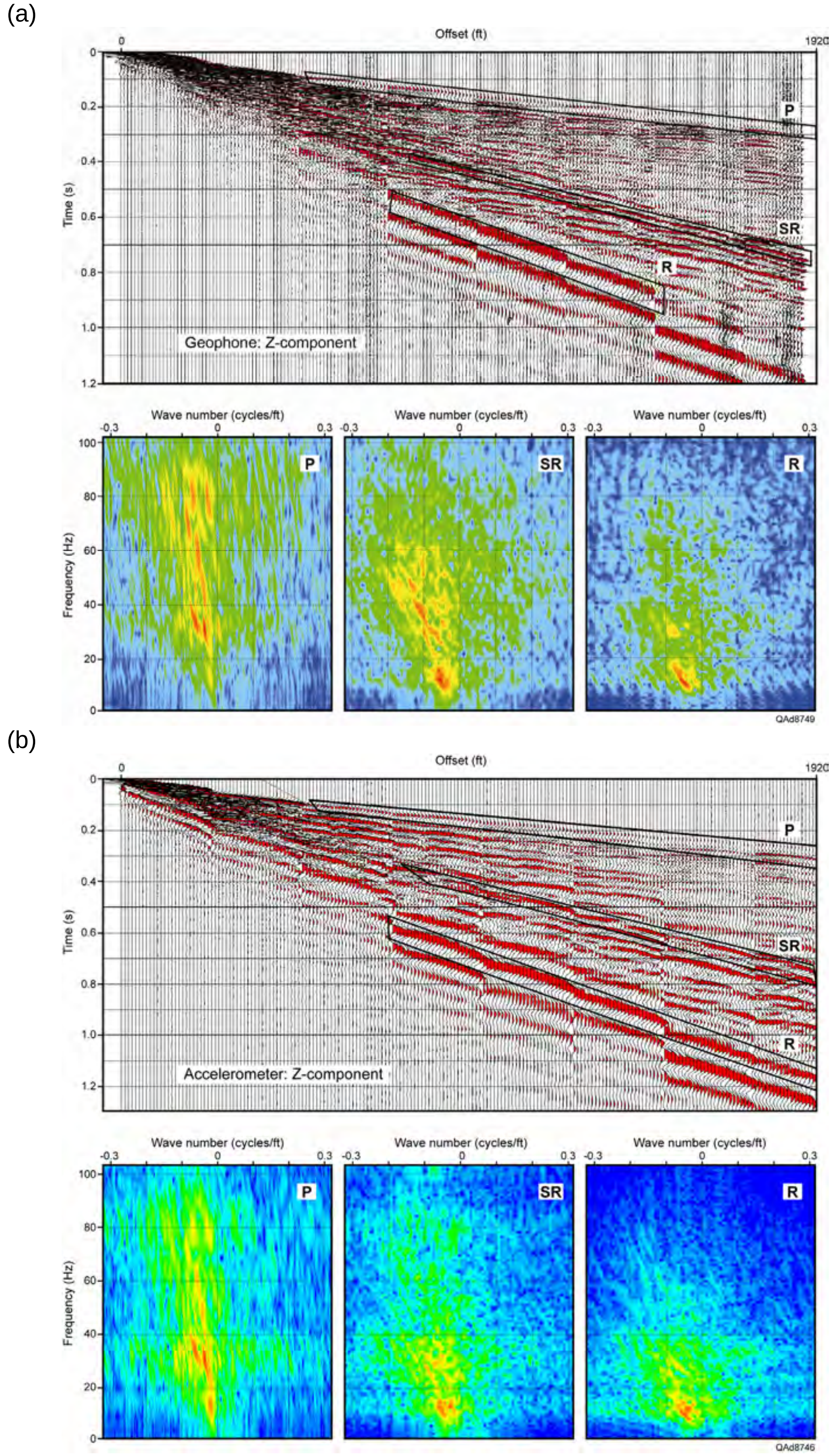

Figure 6.30.Comparison of seismic sensor data. (a) Response of vertical component of 3C geophones. (b) Response of vertical component of 3C accelerometers. P = P-wave mode. SR = radial shear mode. R = Rayleigh surface wave.

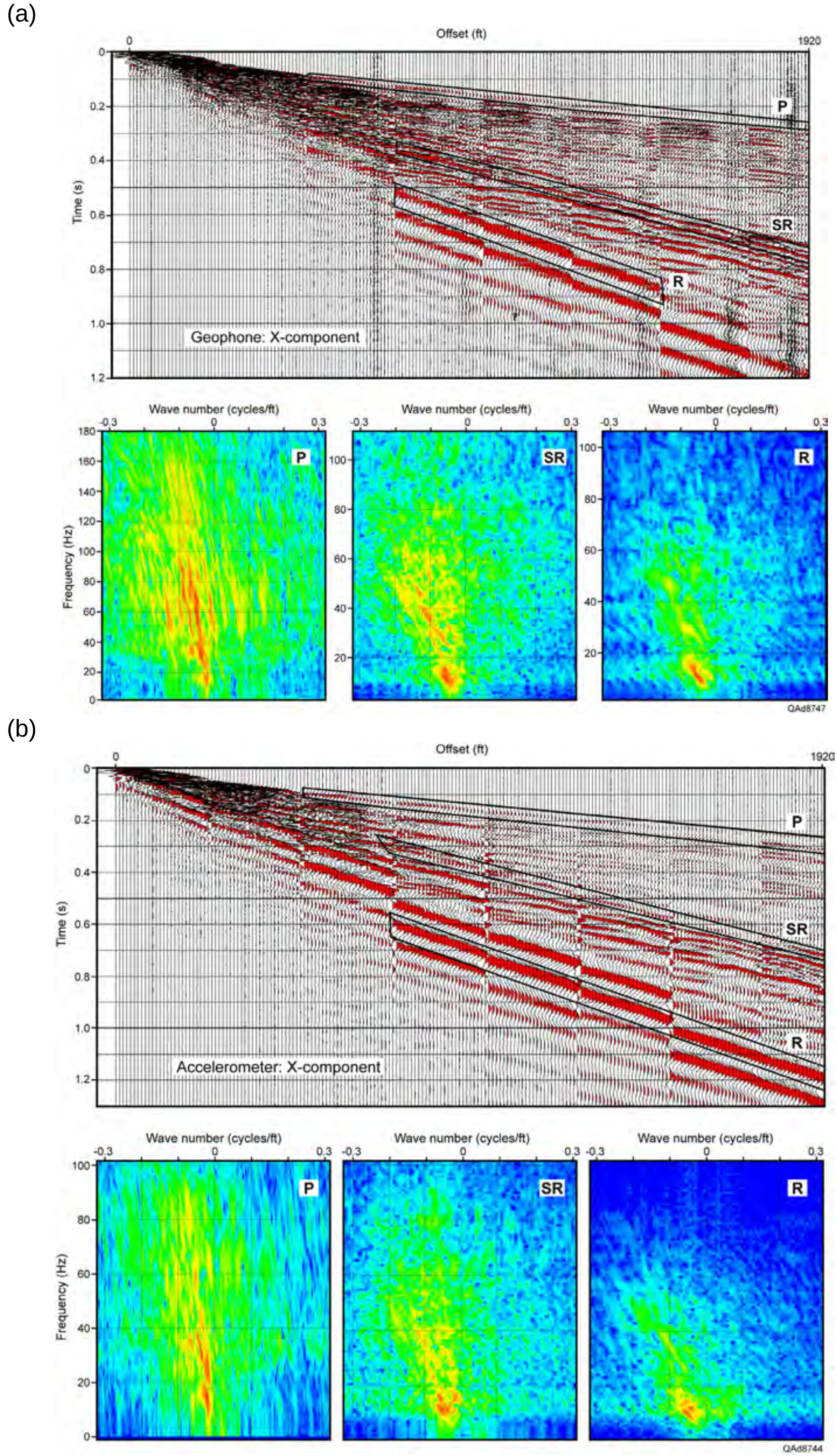

Figure 6.31.Comparison of seismic sensor data. (a) Response of horizontal-radial component of 3C geophones. (b) Response of horizontal-radial component of 3C accelerometers. P = P-wave mode. SR = radial shear mode. R = Rayleigh surface wave.

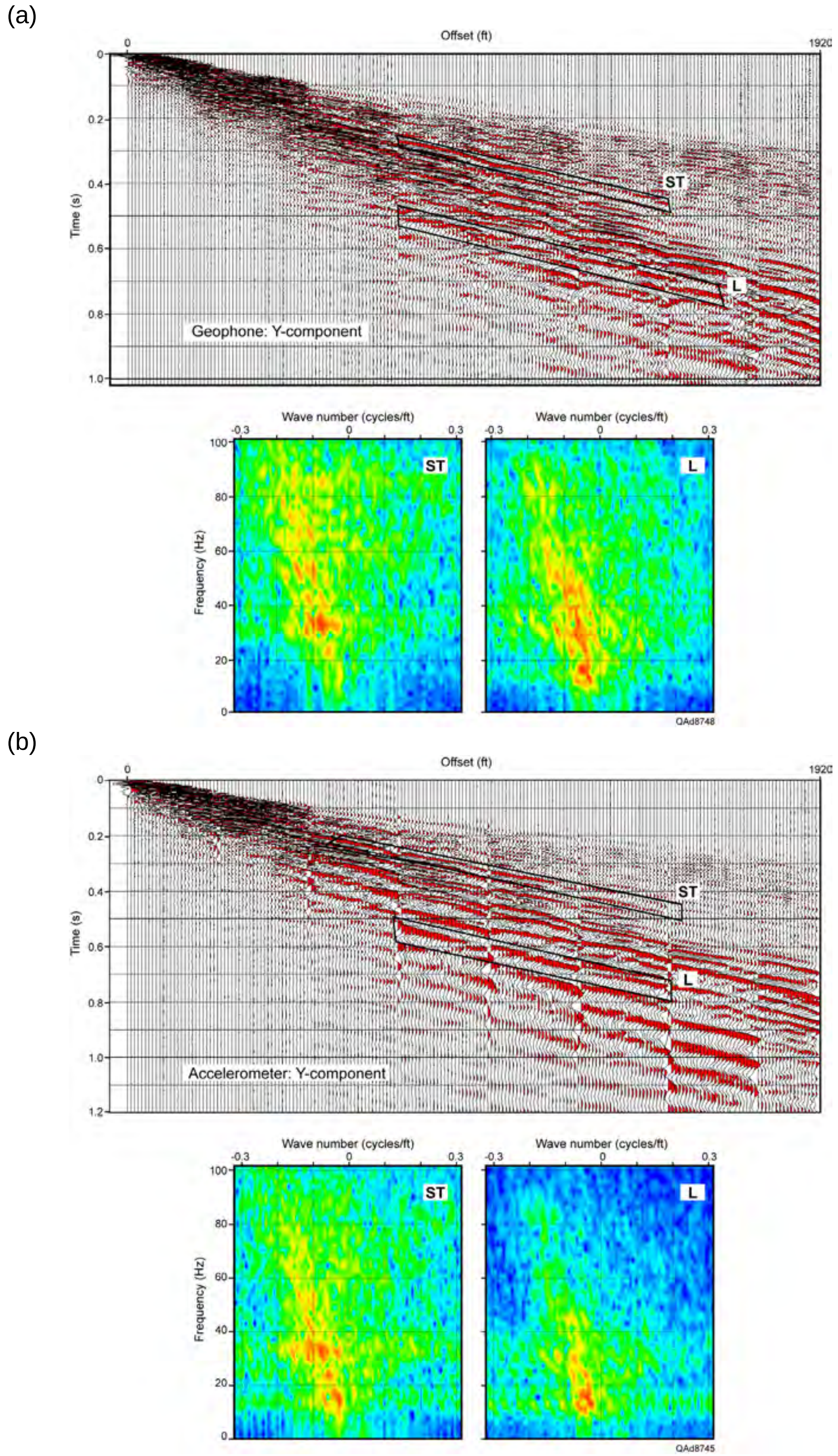

Figure 6.32.Comparison of seismic sensor data. (a) Response of horizontal-transverse component of 3C geophones. (b) Response of horizontal-transverse component of 3C accelerometers. ST = transverse shear mode. L = Love wave.

Test data acquired by 3C geophones and 3C accelerometers are compared on Figures 6.30 through 6.32. The geophones deployed for the test were Oyo Geospace Model 20DX types (10-Hz resonance suspension spring). The accelerometers were Sercel DSU3 MEMS solid-state sensors. The energy source that generated the sensor test data was a 1 kg (2.2 lb) explosive charge detonated at a depth of 6 m (20 ft).

Visual inspection of the wiggle-trace test data displayed on Figures 6.30 through 6.32 implies accelerometers record slightly more robust low-frequency components than do geophones. This distinction in sensor frequency response is verified by most (not all) of the FK spectra that accompany the wiggle-trace plots. In any multicomponent seismic application where it is essential to emphasize low frequencies, serious consideration should be given to using accelerometers rather than geophones for data acquisition.

A unique attribute of MEMS solid-state accelerometers is that they function as gravity meters when they are not reacting to Earth vibrations. The benefit of this gravity meter behavior is that a 3C accelerometer can identify which of its three sensors is in a vertical orientation. As a result, any of the three orthogonal accelerometers in a 3C accelerometer package can be the vertical sensor. An advantage of this sensor physics is that in situations where ground conditions make it difficult to plant a MEMS sensor package in its normal vertical orientation, the sensor package can be laid on its side, covered with a small sandbag or mound of dirt, and still record high-quality data. In our field tests, this property of MEMS sensors was utilized at two receiver stations located 20 and 30 ft (6 and 9 m) from the receiver well. At these locations, a thick layer of coarse gravel prohibited deploying a DSU3 sensor package in its normal vertical orientation. The DSU3 package was laid on its side at these two stations and covered with dirt-filled bags to make a reasonable sensor-to-Earth coupling. The internal electronics of the MEMS data-acquisition system switched the definitions of vertical, radial horizontal, and transverse horizontal to the appropriate accelerometers. The data acquired at these two receiver stations look identical to data acquired at all other receiver stations and cannot be identified when inspecting the wiggle-trace data on Figures 6.30 to 6.32. Thus there is considerable appeal to using MEMS 3C accelerometers to acquire multicomponent seismic data across areas where it is difficult to plant geophones in a vertical orientation, for example across prospects covered with hard rock outcrops.

In most seismic data-acquisition projects, vertical orientation of 3C geophones is not a serious handicap. Also for most studies, it is not necessary that amplitudes of low-frequency components (less than 10 Hz) be greater than the amplitudes provided by 3C geophones. In such conditions, there is no significant difference between multicomponent data acquired with 3C geophones and data acquired with 3C accelerometers.

An important principle of S-wave physics demonstrated on Figures 6.30 to 6.32 has nothing to do with the type of sensor that recorded the data. This principle is that FK spectra show the frequency bandwidth of an ST shear mode is significantly broader than the frequency bandwidth of an SR shear mode. Examples of this frequency difference are shown by comparing ST spectra on Figure 6.32, where high-energy frequency components extend from 10 to 100 Hz, with SR spectra on Figures 6.30 and 6.31, where high-energy frequency components extend from 10 Hz to only 40, 60, or 80 Hz, depending which sensor data are considered (vertical sensor data or horizontal-radial sensor data).

Comparisons of Cable-Based and Cable-Free 3C Data

The third objective of the equipment test program was to compare P and S wave modes acquired with cable-based and cable-free data acquisition systems to determine if equivalent data are acquired with each recording system. Constraints placed on data subjected to this analysis were:

1. Identical sensors (3C Oyo Geospace Model 20DX geophones [10-Hz resonance suspension spring]) generated the data inputs to the two recording systems, and

2. Sensor arrays recorded by each system were planted side-by-side in equivalent sediment and with equivalent sensor-to-earth coupling (Fig. 6.4).

3. The geophone responses that were input to each recording system were produced by the same source (a shot-hole explosive).

The cable-based recording system was a Sercel 428. Two cable-free systems were utilized: EUnite boxes provided by Sercel and Sigma boxes provided by Seismic Source and iSeis.

As a result of the three field test procedures listed above, any differences in P and S wave modes observed in the test data should be caused by the type of data-acquisition system that recorded the wave modes rather than by differences in sensor type, sensor coupling, source wavefields, or other factors.

Test data acquired by these three data-acquisition systems are compared on Figures 6.33 through 6.35. In these displays, data are segregated according to geophone orientation. Vertical geophone responses are shown in Figure 6.33, horizontal-radial geophone responses are displayed on Figure 6.34, and horizontal-transverse geophone responses are on Figure 6.35. As was the case for seismic sensor comparison (Figs. 6.30 to 6.32), the energy source that generated the data was 1 kg (2.2 lb) of explosive detonated at a depth of 6 m (20 ft).

Comparing FK spectra on each figure leads to the conclusion that data acquired with the 428 cable-based system have wider frequency spectra than data acquired with either cable-free system. This difference is particularly obvious for P-wave spectra where 428-system frequencies extend above 100 Hz (Fig. 6.34 in

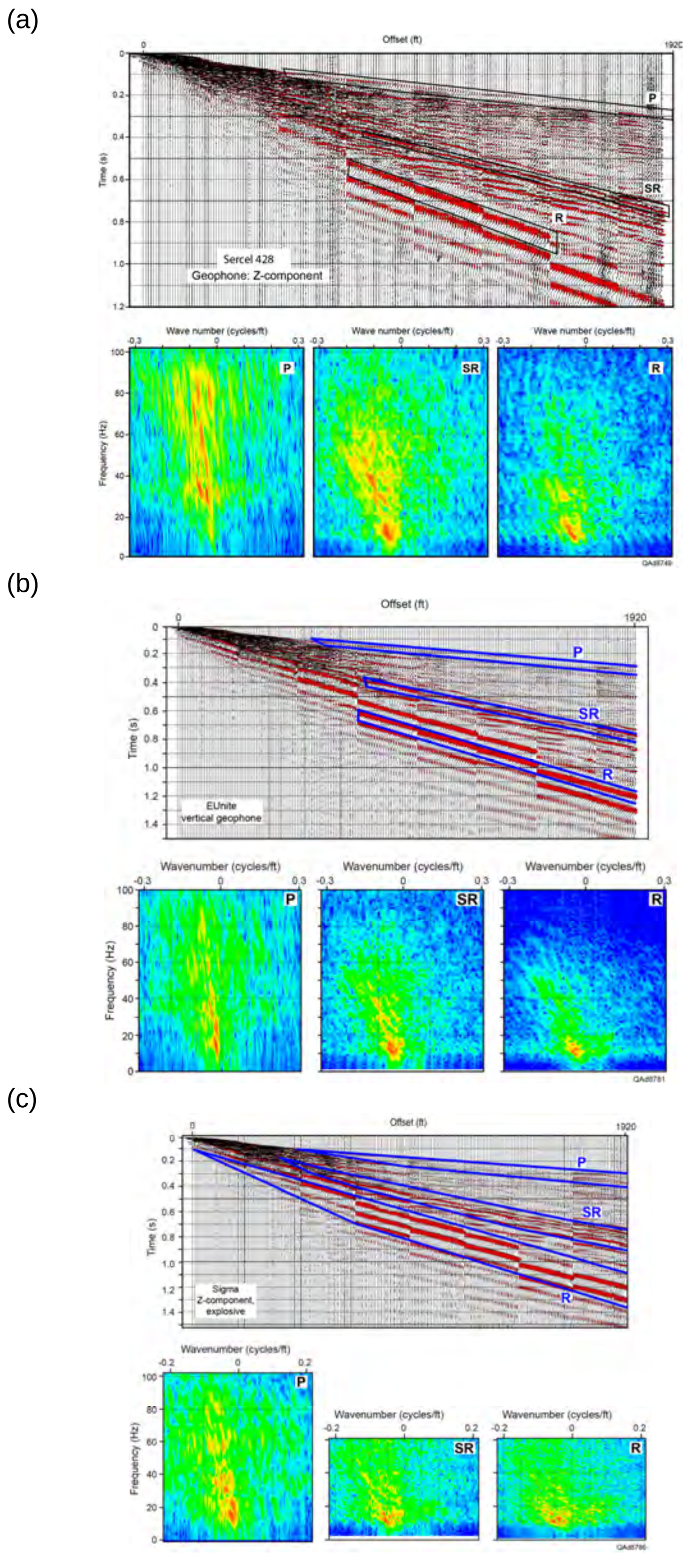

Figure 6.33. Comparison of vertical-geophone data acquired with a cable-based recording system and cable-free recording systems. (a) Vertical component data acquired with cable-based Sercel 428. (b) Vertical component data acquired with cable-free EUnite system. (c) Vertical component data acquired with cable-free Sigma system. P = P-wave mode. SR = radial shear mode. R = Rayleigh surface wave.

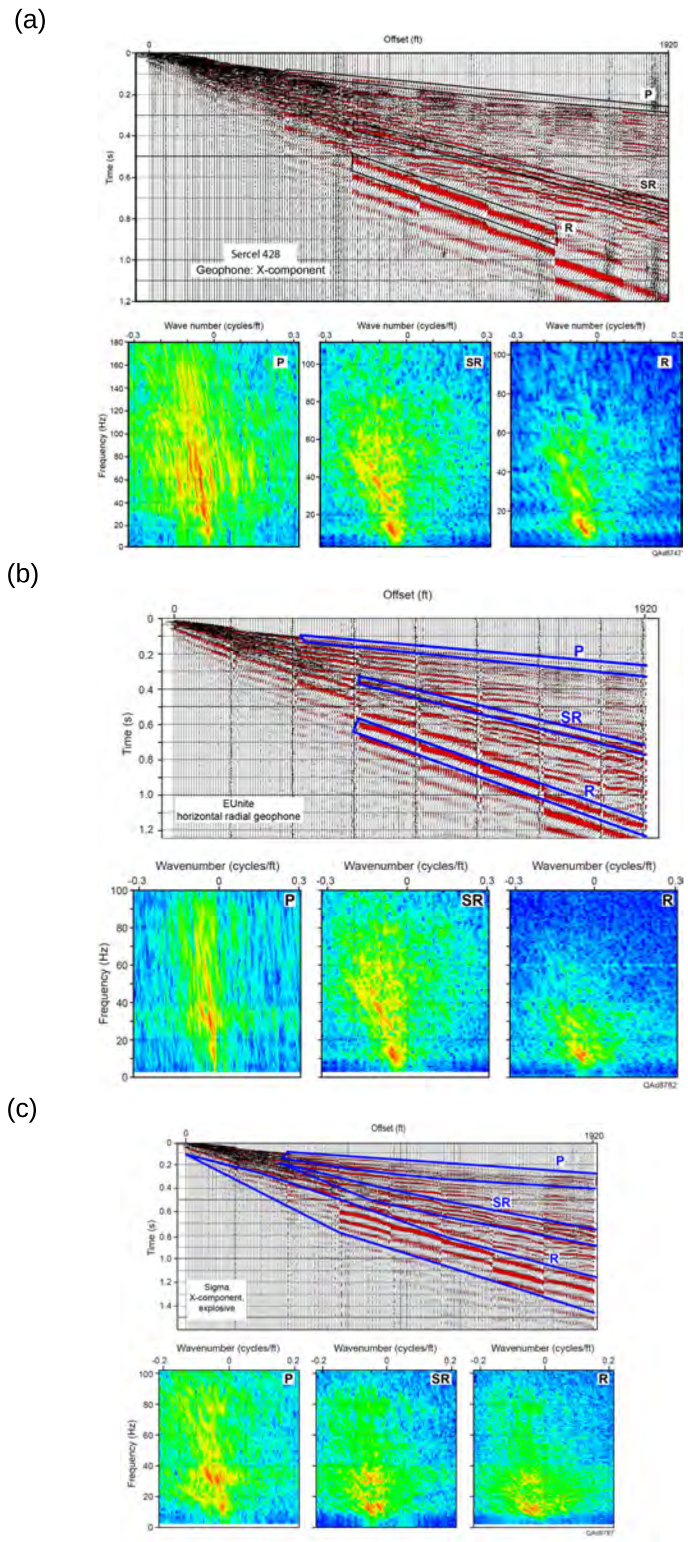

Figure 6.34. Comparison of horizontal-radial-geophone data acquired with a cable-based recording system and cable-free recording systems. (a) Horizontal-radial component data acquired with cable-based Sercel 428. (b) Horizontal-radial component data acquired with cable-free EUnite system. (c) Horizontal-radial component data acquired with cable-free Sigma system. P = P-wave mode. SR = radial shear mode. R = Rayleigh surface wave.

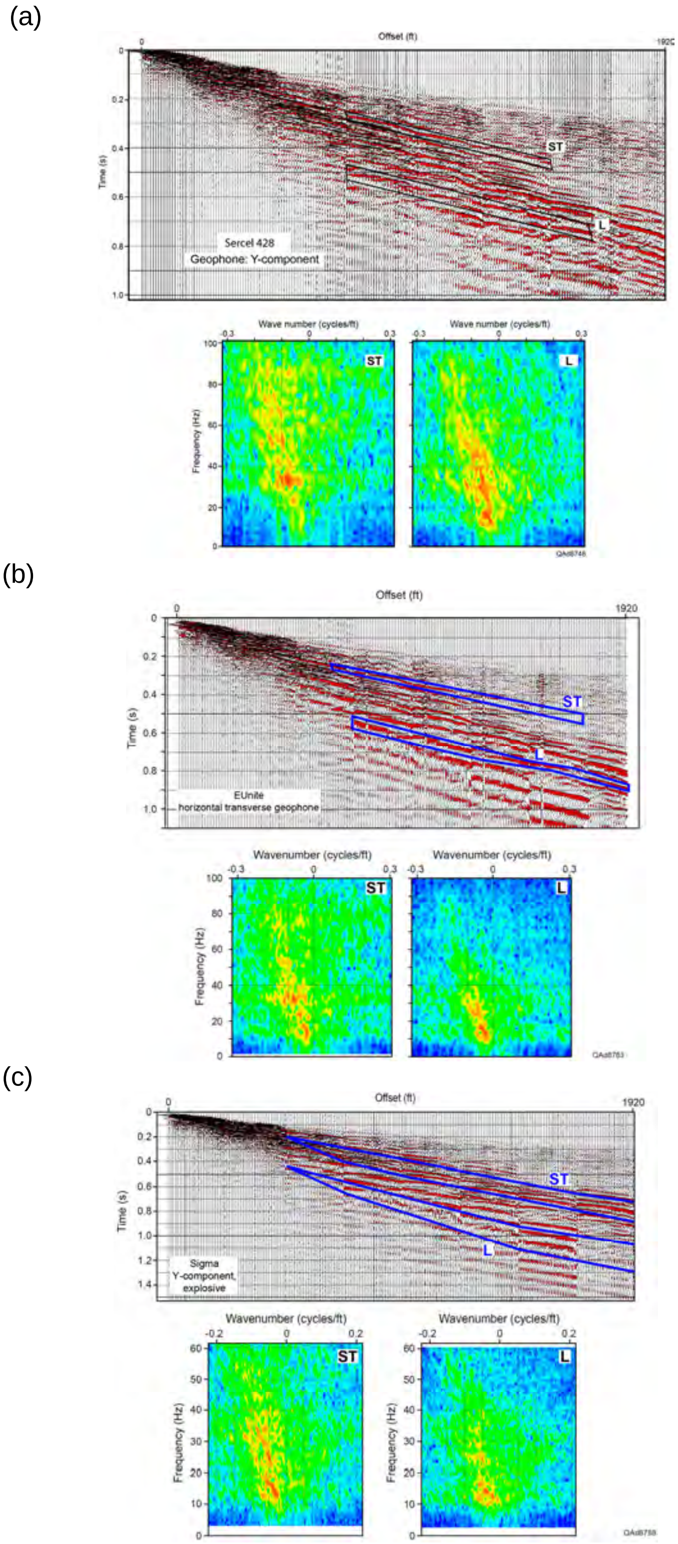

Figure 6.35. Comparison of horizontal-transverse-geophone data acquired with a cable-based recording system and cable-free recording systems. (a) Horizontal-transverse component data acquired with cable-based Sercel 428. (b) Horizontal-transverse component data acquired with cable-free EUnite system. (c) Horizontal-transverse component data acquired with cable-free Sigma system. ST = transverse shear mode. L = Love surface wave.

particular), but Sigma-system and EUnite-system frequencies extend to only 100 Hz (or less). Extensions of energy to higher-frequency components also occur for SR and ST shear modes acquired with the cable-based system.

Extracting P and S Reflections from Surface-Array Data

Downgoing P and S wave modes can be observed in displays of unprocessed vertical-force-source data acquired with downhole vertical-receiver array (Figs. 6.10 through 6.12). However, P and S reflection events are not obvious in displays of unprocessed data acquired with horizontal receiver arrays (Figs. 6.21 through 6.35). It is problematic that reflections can be identified in the 1-fold source gathers displayed in these latter figures. To search for reflections, surface-array data were processed using a patented hyperbolic Radon transform algorithm available from RARE Technology (Wood, 2004a, 2004b). This algorithm is particularly effective at finding weak signal embedded in relatively high noise.

Examples of surface-array data after application of hyperbolic Radon filtering are displayed as Figures 6.36 through 6.38. The velocity range over which the algorithm searched when filtering the data to extract P-wave signal was 6,000 to 18,000 ft/s (1828 to 5486 m/s). The algorithm was constrained to a velocity range of 2,000 ft/s to 6,000 ft/s (610 to 1828 m/s) when searching for S-wave signal.

Inspection of Figures 6.36 to 6.38 shows P and S reflection events were recorded on vertical component, horizontal-radial component, and horizontal-transverse component sensors for all three types of vertical-force sources – vertical vibrator, vertical impact, and shot-hole explosive. This result demonstrates two important concepts:

1. RARE’s hyperbolic Radon transform is a powerful velocity filter for extracting reflection signal from noisy seismic data, and

2. P, SR, and ST wave modes exist in surface-recorded data produced by vertical-force sources just as they do in downhole sensor data.

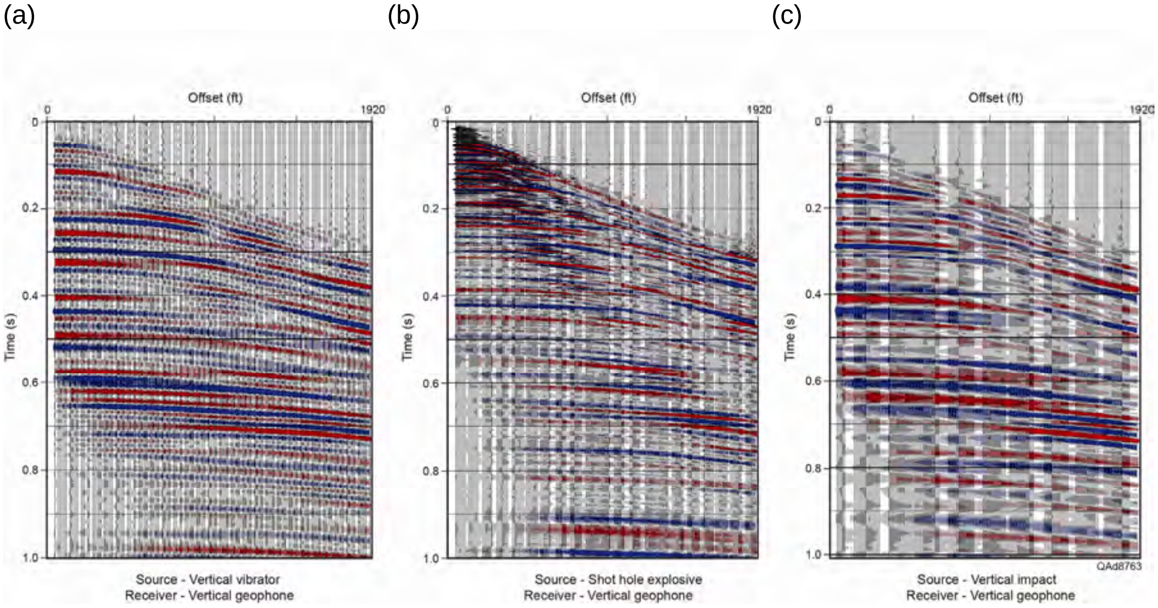

Figure 6.36. P-wave reflections and intra-bed multiples extracted from vertical-geophone response for (a) vertical vibrator, (b) shot-hole explosive, and (c) vertical impact.

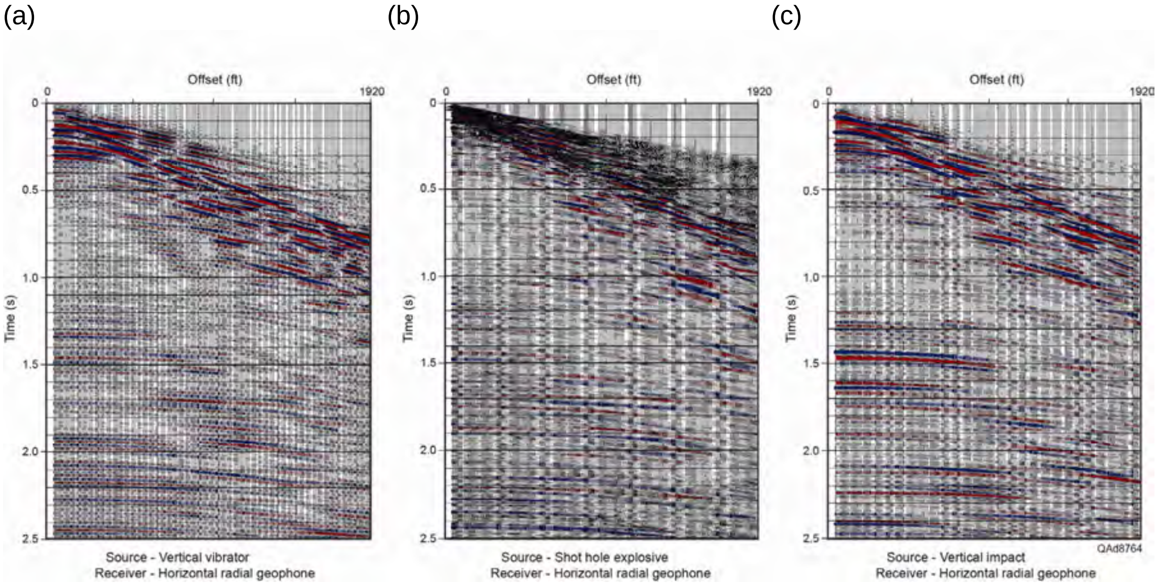

Figure 6.37. SR-wave reflections and intra-bed multiples extracted from horizontal-radial-geophone response for (a) vertical vibrator, (b) shot-hole explosive, and (c) vertical impact.

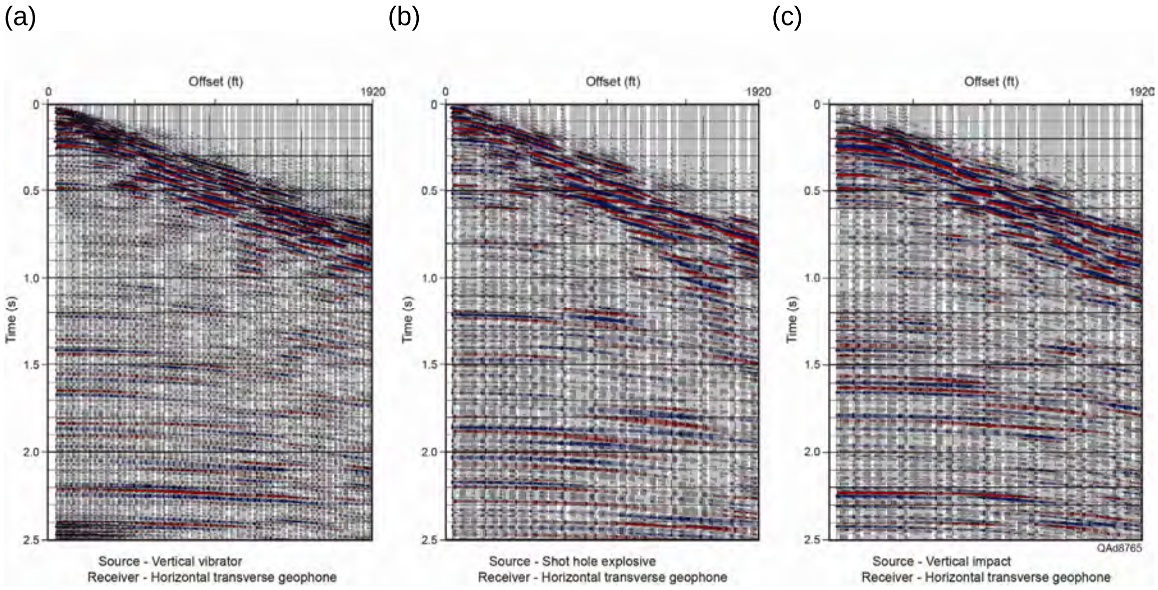

Figure 6.38. ST-wave reflections and intra-bed multiples extracted from horizontal-transverse-geophone response for (a) vertical vibrator, (b) shot-hole explosive, and (c) vertical impact.

Conclusions

The equipment test program implemented at the Devine Test Site focused on three objectives:

1. Record and analyze P and S modes produced by vertical-force, horizontal-force, and inclined-force seismic sources,
2. Compare data acquired by geophones and accelerometers, and
3. Determine whether seismic data acquired with a cable-based recording system are equivalent to data acquired with cable-free data-acquisition systems.

This field test was one of the success stories of this project. The no-cost contributions of companies who provided the equipment and engineers that allowed the tests to be done were invaluable. Sixty researchers, engineers, and technicians assembled at our Devine Test Site to assist. As a result, we did all tests in two days rather than in the anticipated four days. In subsequent short courses and workshops, the information presented in this chapter has been some of the more popular material according to attendees. Specific comments about aspects of the field test follow.

Source comparisons

Vertical-force sources can be classified into three generic types: vertical vibrators, shot-hole explosives, or vertical impacts. A representative source from each of these three general source classes was deployed for the test program conducted at the Devine Test Site. The fundamental physics documented by these tests was ***all vertical-force sources produce full elastic wavefields having robust compressional (P), radial shear (SR), and transverse shear (ST) modes***. One conclusion reached in this study is that these full-elastic wavefields are created directly at the point where each source applies its vertical force vector to the Earth. This observation should be a fundamental hypothesis in multicomponent seismic projects.

Wave modes propagating away from each source station are best seen if they are captured by a vertical array of downhole receivers. Vertical-array data define the properties of downgoing wave modes that illuminate subsurface targets, thus analyzing vertical-array data is the preferred way to evaluate seismic source performance. Analysis of vertical-array data acquired at the Devine Test Site shows all three tested sources (vertical vibrator, shot-hole explosive, and vertical impact) are effective for multicomponent seismic data acquisition. Encouraging aspects of these data are that each source generates radial (SR) and transverse (ST) shear modes in addition to the expected P mode, and that the energy content of these S modes equals or exceeds the energy content of the P mode.

Although vertical-array data show high-quality P and S modes propagate into the subsurface, it is important to analyze horizontal-array data acquired by surface-based sensors to evaluate the amount of surface-wave noise produced by each source and the P and S reflection-signal quality associated with each source. Horizontal-array data acquired during the test program show that P, SR, and ST modes exist in surface-sensor data and, even though some sources are more energetic than others, the relative ratios of the amounts of P, S, and surface-wave mode energy embedded in surface-recorded data do not greatly differ from source to source.

A continuing topic of research will be to compare SR and ST shear modes produced with a vertical-force source with SV and SH modes produced by horizontal-force sources to determine similarities and differences between S-wave modes produced by these two fundamentally different seismic sources. For example the ST mode observed in vertical-force test data may not be a true SH mode but a split shear mode created when an SV shear mode, known to be produced by a vertical-force source, propagates in an azimuthally anisotropic near-surface layer local to a source station.

Sensor comparisons

Only minor differences were found when comparing multicomponent seismic data acquired with 3C geophones against data acquired with 3C accelerometers. One difference was that the energy content of frequency components less than 8 Hz was higher for accelerometer data than for geophone data, which may be important in some studies. A second difference between geophones and accelerometers is that where ground conditions do not allow a 3C sensor package to be planted in a normal vertical orientation, a 3C accelerometer package can be placed horizontally on the Earth surface and still acquire good quality data if adequate weight is placed atop the package to ensure good sensor-to-Earth coupling. In contrast, 3C geophones cannot be deployed in this manner. This ability to deploy a 3C sensor in a vertical orientation, or on the ground surface in a horizontal orientation, allows 3C data to be acquired across hard ground surfaces where it is difficult to embed vertical 3C sensors so they have good sensor-to-Earth coupling.

In the majority of seismic data-acquisition programs, there is no particular advantage to which type of sensor—3C geophone or 3C accelerometer—is used to acquire multicomponent seismic data.

Recording system comparisons

We were surprised to see P and S wave modes acquired with a cable-based data-acquisition system had broader frequency spectra than data acquired with cable-free systems. The increase in higher-frequency content is significant, being of the order of 20-percent or more, depending on which wave mode is considered. These test results warrant more study. More comparisons of data acquired with cable-based systems and with cable-free systems will be done in future projects.

Chapter 7

Multicomponent Seismic Data Acquisition

Introduction

Multicomponent seismic data were the essential part of the research database needed for this study. Numerous attributes of seismic data, and particularly attributes of multicomponent seismic data, are affected by the source-receiver geometry that is deployed across a survey area and the field procedures that are used to acquire the data. Specifically, an acquisition geometry should create adequate stacking folds not only for common-midpoint (CMP) P-P and S-S data but also for common-conversion point (CCP) P-SV and SV-P data. In addition, a seismic data-acquisition geometry must create a full range of source-to-receiver offsets and azimuths for all P and S wave modes. Full-offset and full-azimuth data are particularly important if fracture intervals are to be detected and quantified, or if stress fields and geomechanical rock properties are to be analyzed.

This chapter describes how the 3D P and S seismic data used in this study were acquired and illustrates stacking-fold magnitudes, offset distributions, azimuth dependence, and other multicomponent seismic data properties that influence rock and fluid information extracted from P and S wave modes.

Survey Design

The 3D multicomponent seismic survey that was to be implemented in this research was intended to be an orthogonal brick pattern in which 13 receiver lines spaced 880 ft (268 m) apart were deployed northwest-to-southeast to form a 2 mi × 2 mi (3.2 km × 3.2 km) square of 3C geophone stations, with 97 receiver stations spaced at intervals of 110 ft (33.5 m) along each receiver line. The total number of planned receiver stations was 1261. This receiver grid was to be positioned in the center of a 5 mi × 5 mi (8 km × 8 km) square array of source stations arranged in a southwest-to-northeast brick pattern in which 41 source lines were spaced 660 ft (201 m) apart. Each source line consisted of a sequence of four source stations spaced at intervals of 220 ft (67 m) with a gap of 880 ft (268 m) between successive 4-station groups. This source-station pattern created 60 source stations per line, with a total of 2460 source points across the survey area. Each source involved a 1-kg (2.2 lbs) explosive positioned at a depth of 6 m (20 ft). This pre-survey design geometry is illustrated on Figure 7.1a.

Pre-survey geometry can rarely be implemented in practice because numerous constraints exist that prohibit source and receiver stations being positioned at regularly spaced intervals. Among these constraints are pipelines,

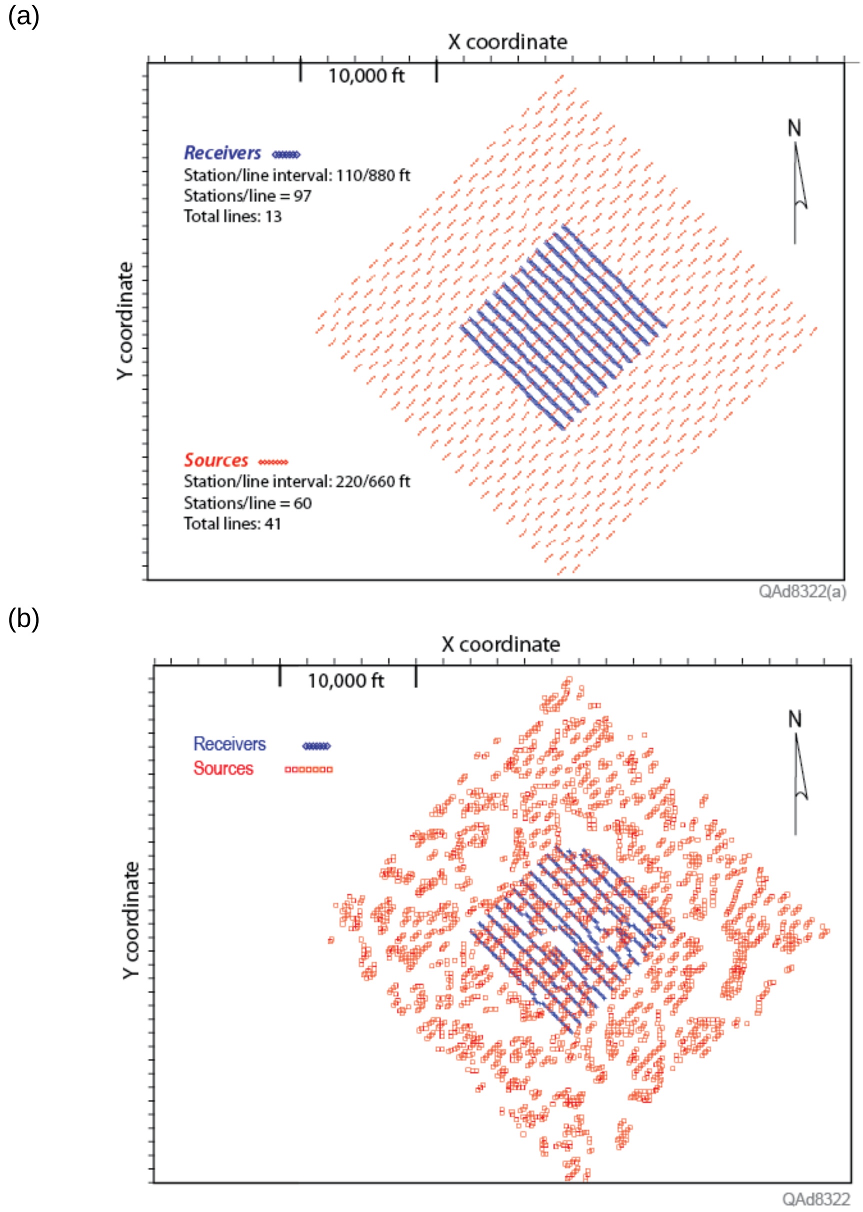

Figure 7.1. (a) Pre-survey design that was intended to be used to acquire the 3C3D seismic data for this study. The objective was to deploy source and receiver stations as a uniform, regular geometry in which there were consistent distances and azimuths between source-receiver lines and stations. Source and receiver line spacings and station spacings are labeled on the plot. (b) Post-survey geometry that was actually implemented. Source station positions were not at regular intervals. Although receiver stations were positioned with some degree of regularity, distances and azimuths between source-receiver station pairs were irregular and random.

electrical power lines, water wells, roads, buildings, agricultural crops, streams, marshes, dense forests, impassable topography, and an endless list of similar barriers. Topography, streams, and timber were principal barriers across our study site. As a result of surface constraints, the actual source and receiver station geometry that was implemented (Fig. 7.1b) differed from the pre-survey design. The number of actual source stations was 2350, not the planned number of 2460. The number of receiver stations that were deployed was 1225, not the planned number of 1261.

Two adjectives are used by geophysicists to describe the basic properties of the pre-survey and post-survey source-receiver geometries illustrated on Figure 7.1. Because of the consistent distances and azimuths between source/receiver lines and stations, the pre-survey geometry (Fig. 7.1a) is called a **regular geometry**. The post-survey geometry (Fig. 7.1b) is referred to as a **random geometry**. There are advantages to introducing a modest amount of randomness into the positioning of source and receiver stations in a 3D seismic data-acquisition grid (Alkan, 2007; Alkan and Hardage, 2007). The amount of randomness exhibited by the actual source-receiver geometry used to acquire our multicomponent seismic research data created several attractive data properties, as will be shown.

Fold Attributes

Stacking fold is usually the first attribute of a 3D data-acquisition design that geophysicists examine to decide if the design is appropriate for imaging specific geologic targets. If proper fold is not created by the source-receiver geometry utilized in the design, the quality of seismic images will not be adequate for many geologic applications. The magnitude of stacking fold that should be created across a particular prospect area is often not an easy decision to make. Proper stacking fold varies from prospect to prospect depending on the depth of the principal target that needs to be imaged, the strength of the energy source that is used, and the nature of the signal-to-noise ratio exhibited by propagating wave modes.

Two types of stacking fold were considered in this study: (1) common-midpoint (CMP) fold, and (2) common-conversion point (CCP) fold. CMP fold affects images made from wave modes that have the same propagation velocity on their downgoing and upgoing travel paths. CMP modes utilized in this study were P-P (pure compressional) data. In contrast to CMP fold, CCP fold affects images made from wave modes that have a different propagation velocity on their downgoing travel path than they do on their upgoing travel path. CCP wave modes considered in the survey design analysis in this report involve P-SV data (downgoing P and upgoing converted-SV) and SV-P data (downgoing SV and upgoing converted-P).

CMP stacking folds are considered first. CMP folds created by the proposed regular-station geometry when offsets are restricted to 5,000 ft

(1,524 m), 10,000 ft (3,048 m), 15,000 ft (4,572 m), and 26,000 ft (7,925 m) are shown in Figure 7.2. CMP folds created by the implemented random-station geometry for these same offset conditions are presented as Figure 7.3. Folds associated with these four offset ranges are important because they represent CMP stacking folds expected for target depths of 2,500 ft (762 m), 5,000 ft (1,524 m), 7,500 ft (2,286 m), and 13,000 ft (3,962 m), respectively, based on the principle that a target at depth H is appropriately imaged using source-receiver

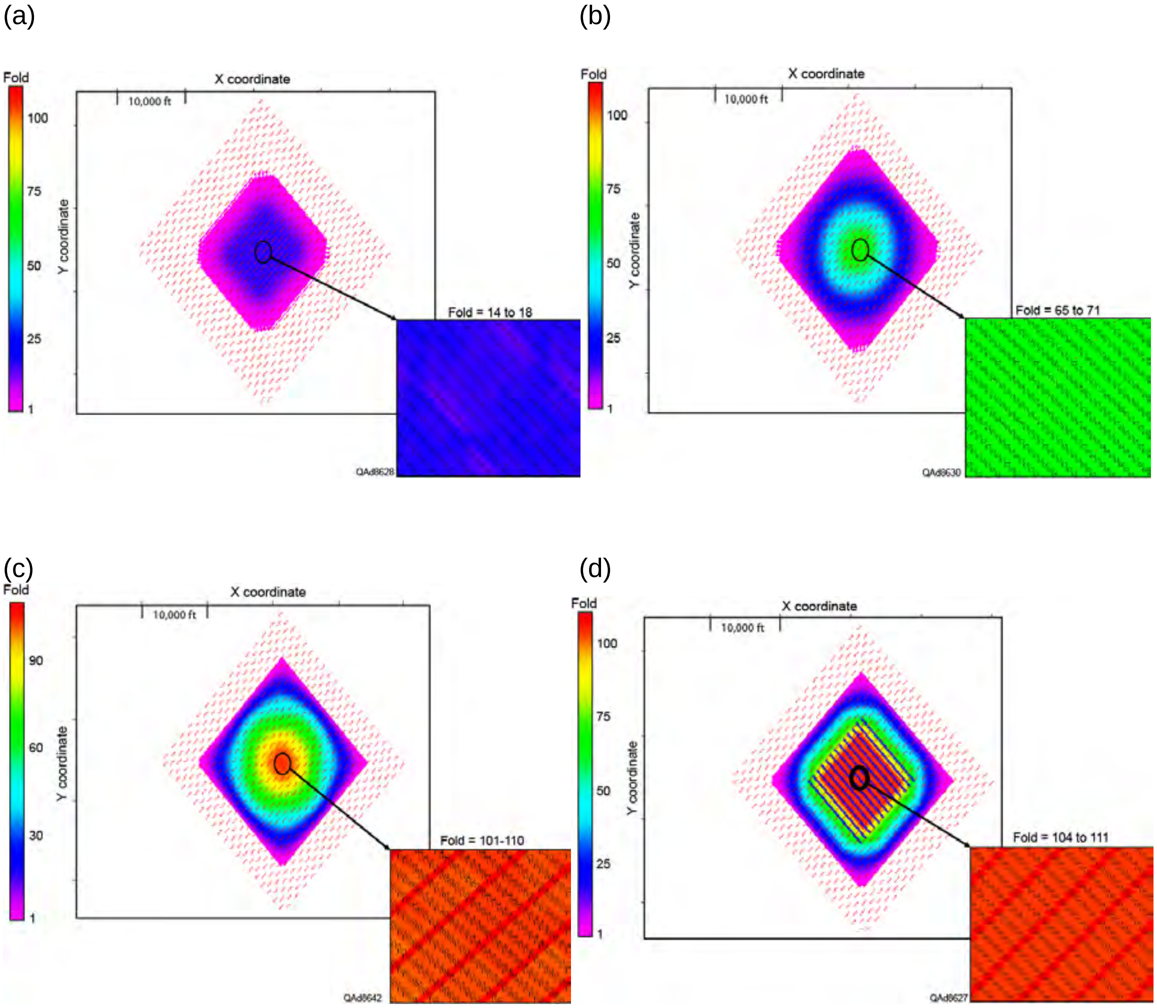
(a) (b) (c) (d)

Figure 7.2. Stacking fold for P-P and S-S CMP modes that would have occurred if the pre-survey source-receiver geometry could have been implemented. (a) CMP fold when source-to-receiver offsets do not exceed 5,000 ft (1,524 m). (b) CMP fold when source-to-receiver offsets do not exceed 10,000 ft (3,048 m). (c) CMP fold when source-to-receiver offsets do not exceed 15,000 ft (4,572 m). (d) CMP fold when all source-to-receiver offsets are used, an offset range extending to 26,000 ft (7,925 m).

offsets that range from 0 to 2H. Targets of interest in this study, numerous porous sandstones and carbonates that could be CO_2 sequestration reservoirs, are positioned over a depth range of 3,000 to 13,000 ft (914 to 3,962 m). Seismic basement is thought to be approximately 13,000 ft (3,960 m) deep across our study area.

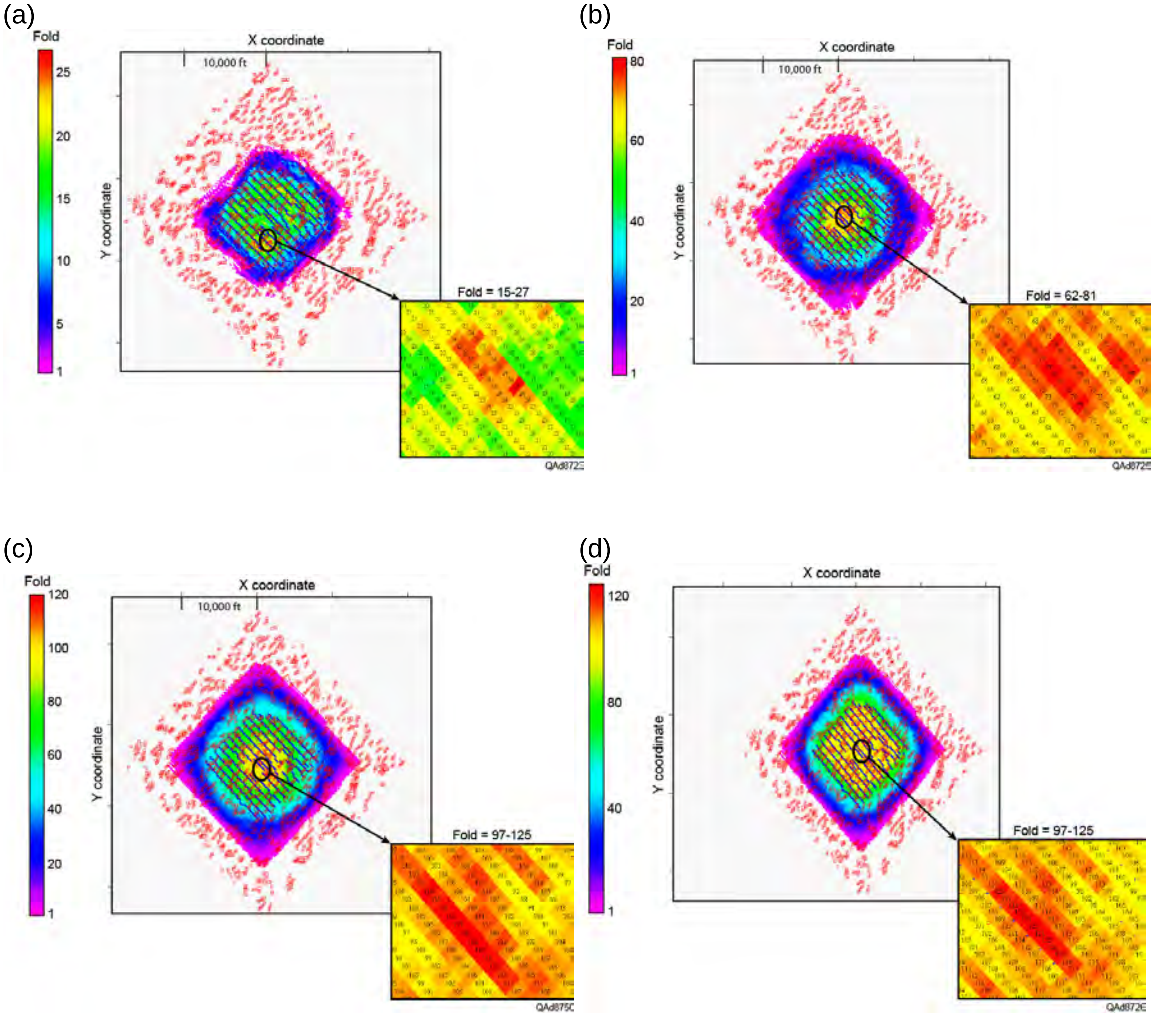

Figure 7.3. Stacking fold for P-P and S-S CMP modes when the actual post-survey source-receiver geometry was implemented. (a) CMP fold when source-to-receiver offsets do not exceed 5,000 ft (1,524 m). (b) CMP fold when source-to-receiver offsets do not exceed 10,000 ft (3,048 m). (c) CMP fold when source-to-receiver offsets do not exceed 15,000 ft (4,572 m). (d) CMP fold when all source-to-receiver offsets are used, an offset range extending to 26,000 ft (7,925 m).

CCP stacking folds created by the two survey designs are presented as Figures 7.4 (regular geometry) and Figure 7.5 (random geometry). These displays are fold maps for the P-SV converted shear mode that is commonly utilized when 3C3D data are acquired. CCP fold patterns are controlled by the

V_P/V_S velocity ratio of the propagation medium, and fold maps change when the magnitude of a V_P/V_S ratio varies by only small amounts of ±0.1 or ±0.2. Examination of dipole sonic-log data acquired in the calibration well at the center of the seismic image space (Figs. 4.1 and 4.7) suggested a V_P/V_S value of 1.6 to 1.7 should be appropriate for much of the stratigraphic depth of interest. A velocity ratio of 1.6 was used for the CCP fold calculations shown on Figures 7.4 and 7.5.

Because a single value of V_P/V_S is used for the entire propagation paths that downgoing and upgoing modes traverse in these CCP fold calculations, the fold patterns and magnitudes shown on the maps are those associated with **asymptotic bins**, which are deep bins in CCP image space (Hardage et al., 2011). Even though the fold calculations do not apply to shallow targets, they are still valuable for selecting a data-acquisition geometry that produces appropriate CCP stacking fold at critical target depths. During data processing, data-dependent V_P/V_S velocity ratios that vary as a function of image time (vertically) and X-Y image coordinates (laterally) are calculated at several locations across seismic image space. These spatially and dynamically varying V_P/V_S functions allow accurate stacking of CCP data to be done throughout the entirety of 3D image space. As a result, the asymptotic-bin approximation used in survey design is abandoned when CCP data are converted to images, and true CCP binning is used to create P-SV images. In summary, asymptotic-bin fold calculations are useful for evaluating a data-acquisition design but have little value in seismic data processing or interpretation.

Part of our research focus was to illustrate that an additional CCP mode—the SV-P mode—can be used for evaluating CO_2 reservoir systems. To date, SV-P data have not been utilized by geophysicists. This mode is the inverse of the popular P-SV mode presented on Figures 7.4 and 7.5. A P-SV mode involves a downgoing P mode and an upgoing SV mode. In contrast, an SV-P mode involves a downgoing SV mode and an upgoing P mode. SV-P fold maps produced by the two data-acquisition geometries are displayed on Figure 7.6 (regular geometry) and Figure 7.7 (random geometry). As was the case for P-SV fold calculations, a V_P/V_S velocity ratio of 1.6 is assumed for the entire thickness of the propagation medium, and the SV-P stacking fold conditions shown on the figures are those associated with asymptotic bins.

Several seismic imaging principles are revealed when comparing stacking-fold maps shown on Figures 7.2 through 7.7.

1. CCP fold is more erratic than CMP fold. Some of the oscillating behavior of CCP fold is caused by forcing the fold to be asymptotic-bin fold and by not using optimal values of V_P/V_S for calculating CCP coordinates. However, even if spatially varying and time varying V_P/V_S ratios were used, CCP fold would still not be expected to be as smooth and uniform as CMP fold across seismic image space.

2. For the data-acquisition geometry used to acquire these 3C3D data, where the source-station area is larger than the receiver-station area, SV-P data produce images that span a larger portion of XY coordinate space than do P-SV data. If source stations and receiver stations were exchanged, the opposite would be true, and P-SV data would span a larger area than SV-P data.

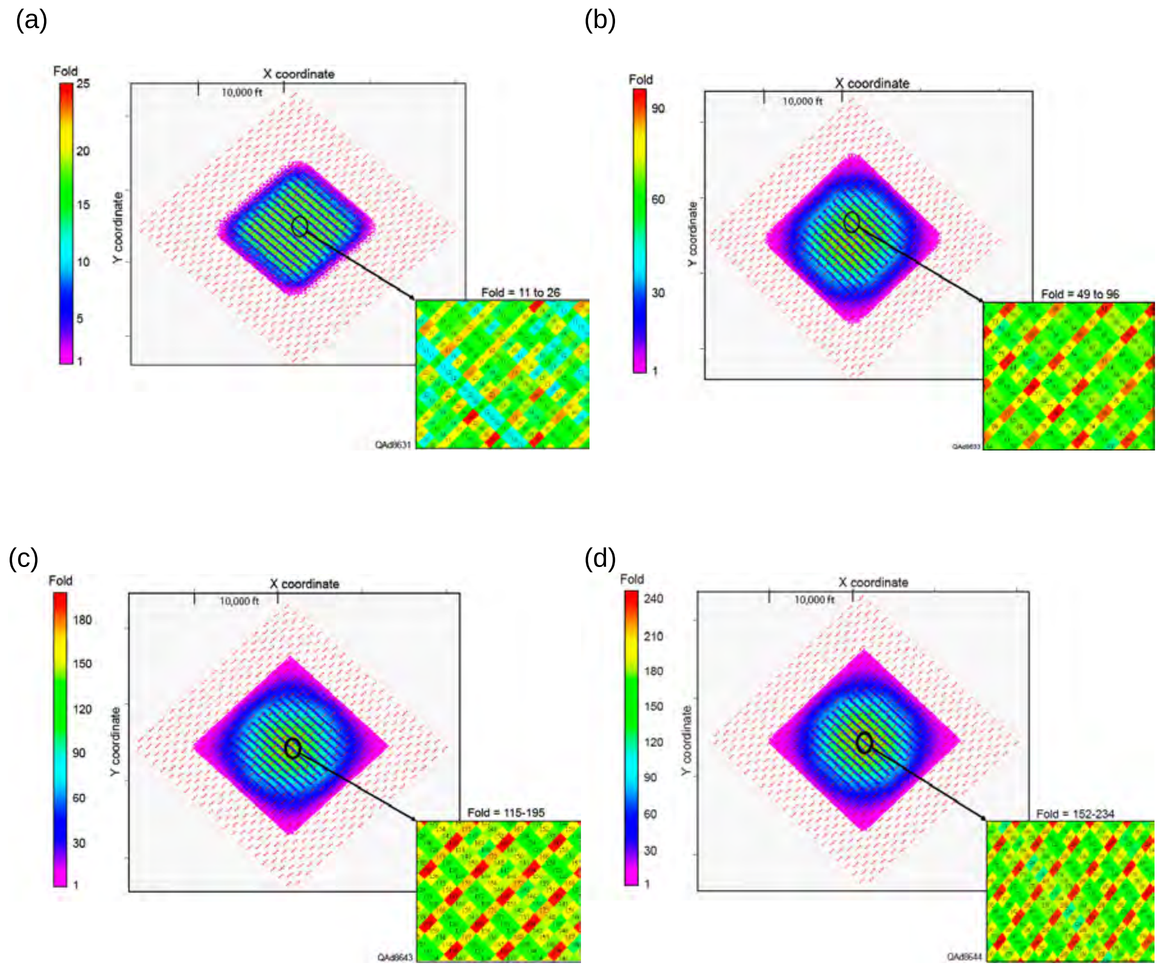

Figure 7.4. Stacking fold for CCP P-SV modes that would have occurred if the pre-survey source-receiver geometry could have been implemented. (a) CCP fold when source-to-receiver offsets do not exceed 5,000 ft (1,524 m). (b) CCP fold when source-to-receiver offsets do not exceed 10,000 ft (3,048 m). (c) CCP fold when source-to-receiver offsets do not exceed 15,000 ft (4,572 m). (d) CCP fold when source-to-receiver offsets are extended to 26,000 ft (7925 m). The stacking bin properties shown are those associated with asymptotic bins.

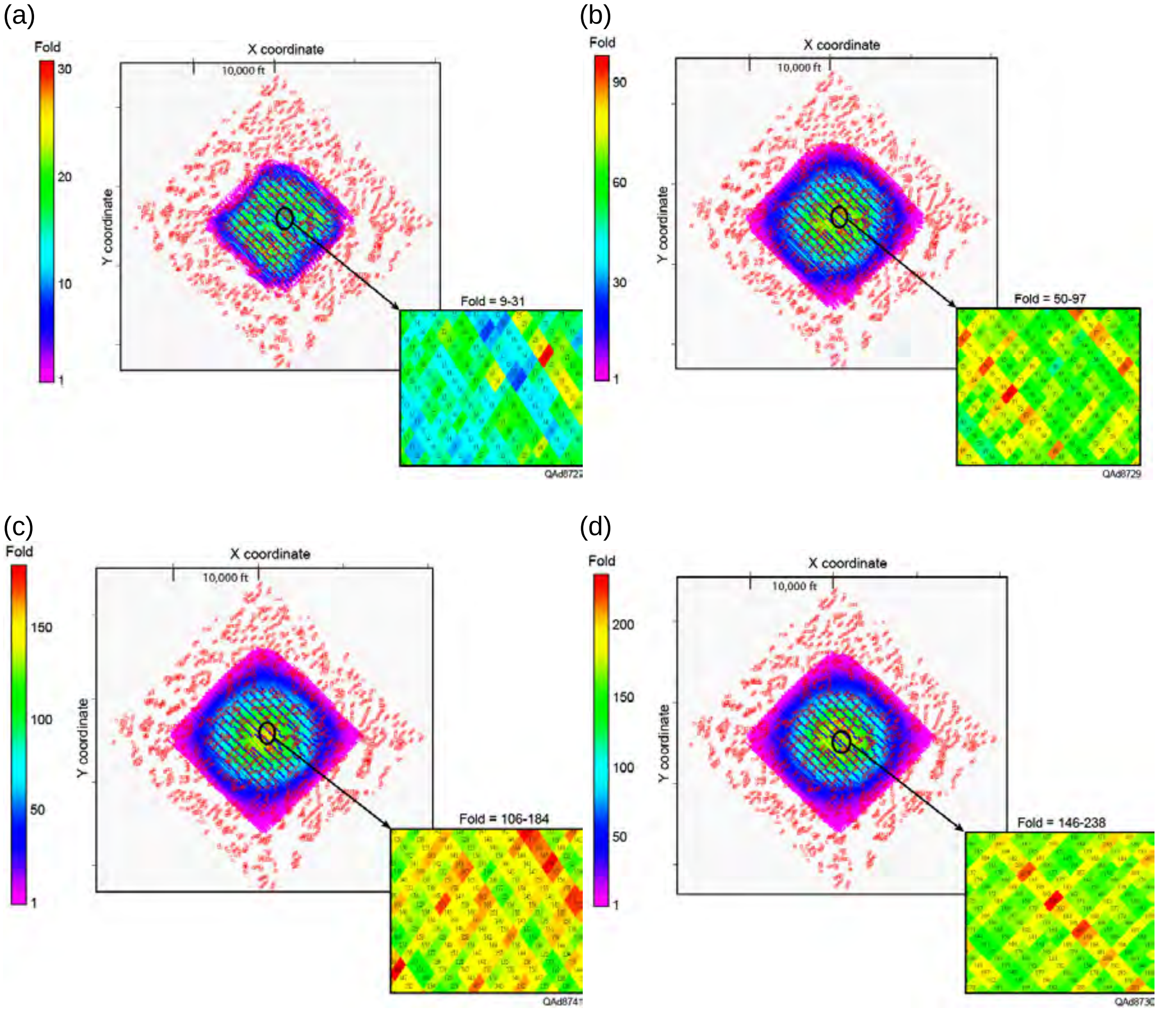

Figure 7.5. Stacking fold for CCP P-SV modes when the actual post-survey source-receiver geometry was implemented. (a) CCP fold when source-to-receiver offsets do not exceed 5,000 ft (1,524 m). (b) CCP fold when source-to-receiver offsets do not exceed 10,000 ft (3,048 m). (c) CCP fold when source-to-receiver offsets do not exceed 15,000 ft (4,572 m). (d) CCP fold when source-to-receiver offsets are extended to 26,000 ft (7,925 m). The stacking bin properties shown are those associated with asymptotic bins.

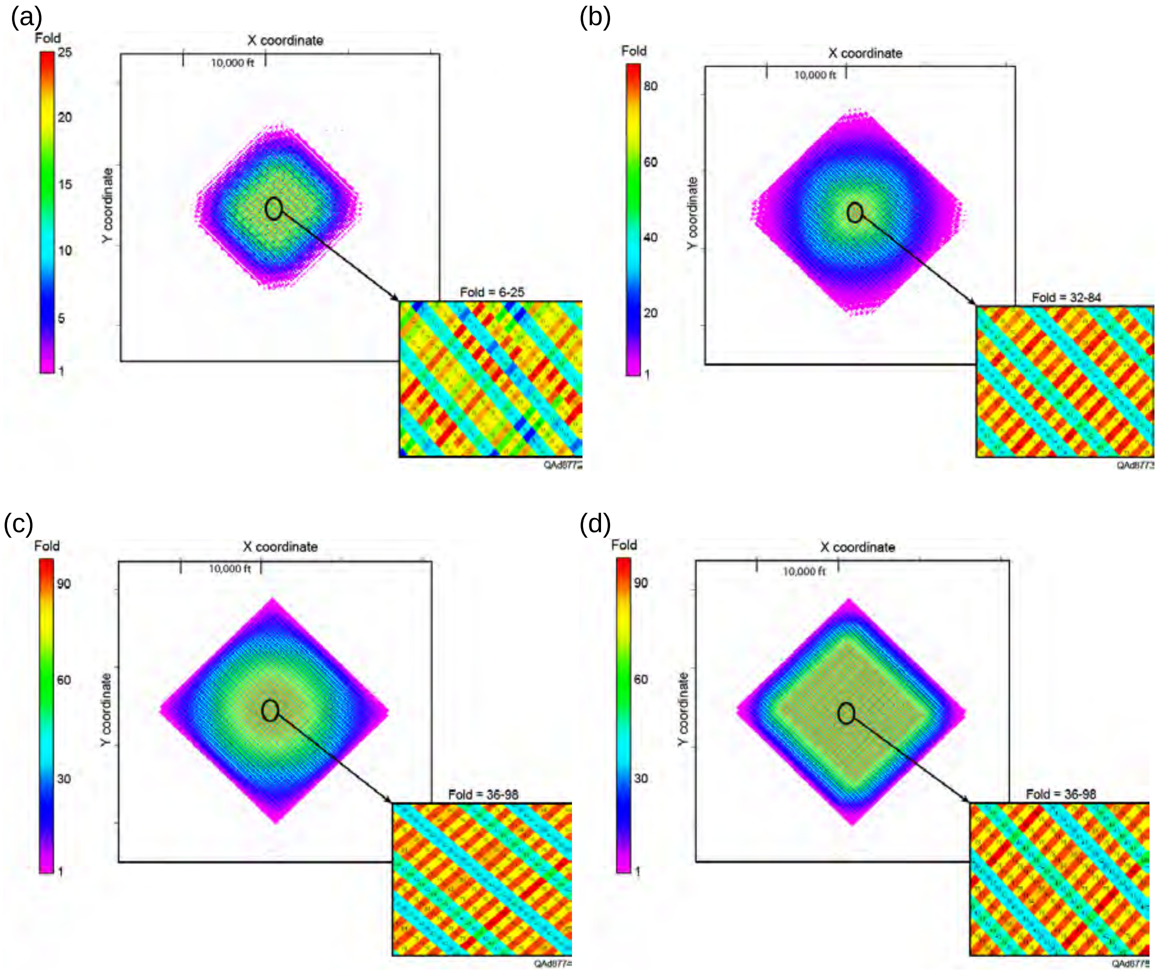

Figure 7.6. Stacking fold for CCP SV-P modes that would have occurred if the pre-survey source-receiver geometry could have been implemented. (a) CCP fold when source-to-receiver offsets do not exceed 5,000 ft (1,524 m). (b) CCP fold when source-to-receiver offsets do not exceed 10,000 ft (3,048 m). (c) CCP fold when source-to-receiver offsets do not exceed 15,000 ft (4,572 m). (d) CCP fold when source-to-receiver offsets are extended to 26,000 ft (7,925 m). The stacking bin properties shown are those associated with asymptotic bins.

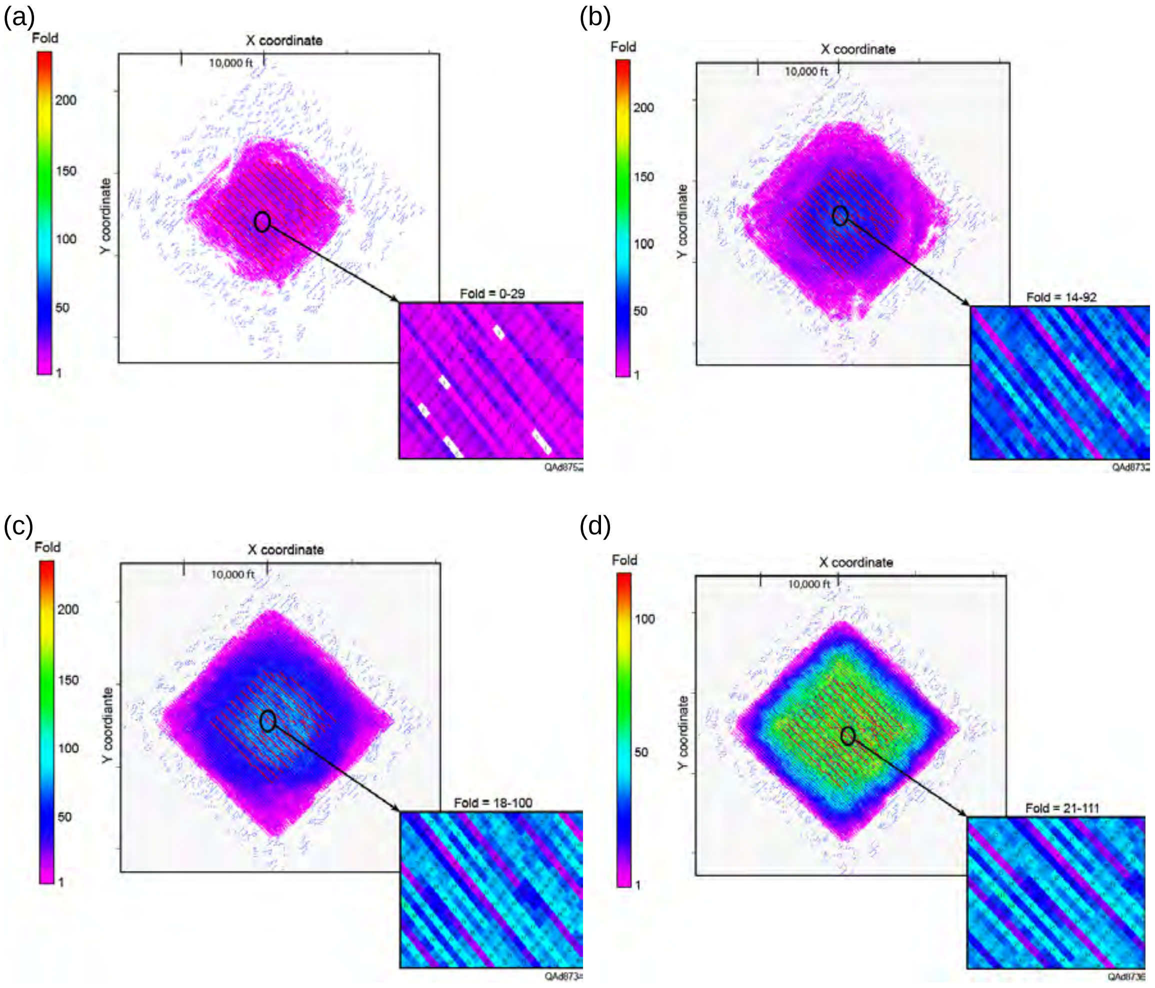

Figure 7.7. Stacking fold for CCP SV-P modes when the actual post-survey source-receiver geometry was implemented. (a) CCP fold when source-to-receiver offsets do not exceed 5,000 ft (1,524 m). (b) CCP fold when source-to-receiver offsets do not exceed 10,000 ft (3,048 m). (c) CCP fold when source-to-receiver offsets do not exceed 15,000 ft (4,572 m). (d) CCP fold when source-to-receiver offsets are extended to 26,000 ft (7,925 m). The stacking bin properties shown are those associated with asymptotic bins.

Offset Attributes

Each data trace recorded during a 3D seismic survey involves a propagation path from a particular source station to a specific receiver station. The horizontal, straight-line distance between the source-receiver pair that generates a seismic data trace is referred to as source-receiver **offset**. To create the maximum amount of rock and fluid information in seismic data, it is important to construct trace gathers in every azimuth direction that have offsets that vary from near-zero to a value that equals or exceeds twice the depth of the deepest target that needs to be imaged. Such full-offset trace gathers allow wave mode reflectivities to be evaluated at targeted interfaces for wide ranges of incident angles and permit wave-mode images to be made using traces having narrow incident-angle ranges to better emphasize selected rock/fluid conditions. The benefits are improved estimations of porosity, pore fluid type, mineral percentages, fracture properties, and other rock/fluid properties that affect angle-dependent wave mode reflectivity.

Optimal 3D seismic survey designs create smooth, continuous distributions of offsets in trace gathers created at critical image coordinates across seismic image space. In sub-optimal surveys, trace gathers summed at image points have erratic offset distributions where there are large trace populations in a few narrow offset ranges and other offset ranges where there are no data traces. To show the influence of 3D survey design on source-receiver offsets, the offset distributions associated with the pre-survey, regular-geometry design that was intended to be deployed across our study area is compared on Figure 7.8 with the offsets created by the post-survey random geometry that was actually implemented.

Because of the compressed horizontal scale used in these plots, the line segments connecting adjacent data points are essentially vertical. Thus the vertical extent of each plot at each offset coordinate indicates how the number of data traces varies as offset distance increases from 0 to 26,000 ft (7,925 m). If plotted data have a large vertical dimension, the number of traces available for analysis and imaging behaves in an erratic manner between adjacent offset bins, with a small number of traces occurring at one offset increment and a large number of traces occurring in the adjacent offset increment. The result is a tall, quasi-vertical line connecting two different trace populations, a small population and an adjacent large population, in the plot scale used for Figure 7.8.

In contrast, if data span a small vertical plot dimension, there is a reasonably smooth distribution of data traces across source-receiver offset space, with small variations in trace populations in adjacent offset increments. Comparison of the data plotted on Figure 7.8 shows trace populations exhibit more erratic behavior when source and receiver stations have consistent, regular spacings (pre-survey design) than they do when they are positioned so there is randomness in the distances and azimuths between station pairs (post-survey design). This conclusion has been documented by Alkan (2007) and Alkan and Hardage (2007).

Note also that no data point of the offset distribution for the post-survey random-station geometry drops to zero, which means data traces exist for every offset value. In contrast, many data points drop to zero, or near to zero, for the pre-survey regular-geometry design, showing that no data traces are available for analysis for numerous offset values. A conclusion made from these plots is that randomness in station positions across a 3D seismic data-acquisition area is desirable and beneficial from the viewpoint of creating a smoother and more continuous distribution of source-to-receiver offset distances.

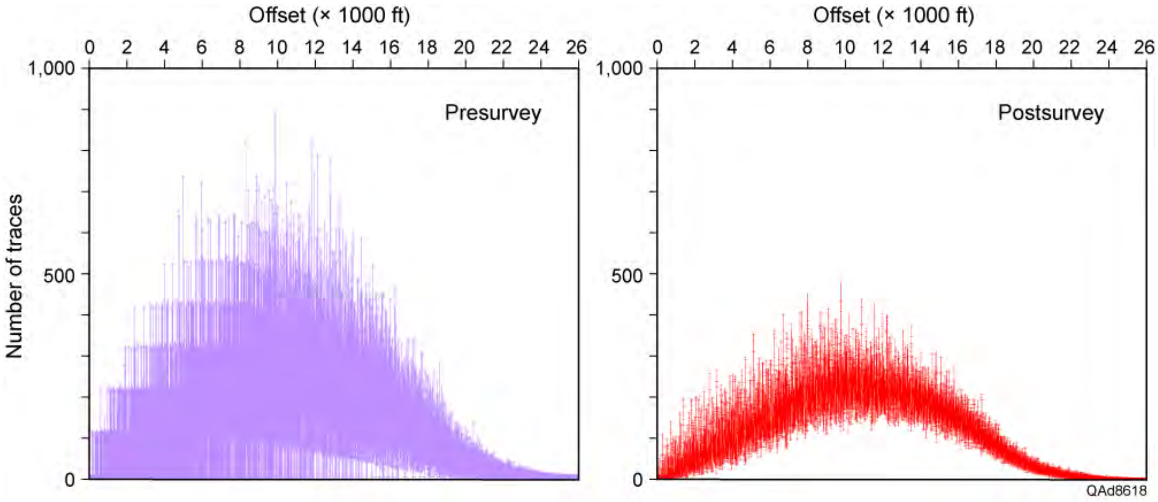

Figure 7.8. Distribution of source-receiver offsets for the pre-survey, regular-geometry design (left) that was planned for deployment, and for the post-survey, random-station geometry that was actually implemented (right).

Azimuth Attributes

Numerous seismic properties exhibit azimuth-dependent behavior. Of foremost importance is the possibility that seismic propagation velocities of P and S modes vary with azimuth. It is therefore important that a 3D seismic data-acquisition geometry be implemented that allows azimuth-dependent analysis of pre-stack seismic velocities and reflectivities to be done for all wave modes.

Azimuth relationships between all source-receiver pairs embedded in the two survey design options are compared on Figure 7.9. Both designs show essentially the same azimuth dependency for data traces recorded by the two source-receiver geometries. The curves on the figure are separated from each other vertically because the number of traces involved in the random-geometry data acquisition is less than the number of traces involved in the regular-geometry design. Examination of the source-receiver geometries displayed on Figure 7.1 verifies fewer source and receiver stations were used to record the data than were considered in the regular-geometry design. Thus fewer source-receiver pairs were available to generate independent data traces in the actual post-survey random-geometry deployment.

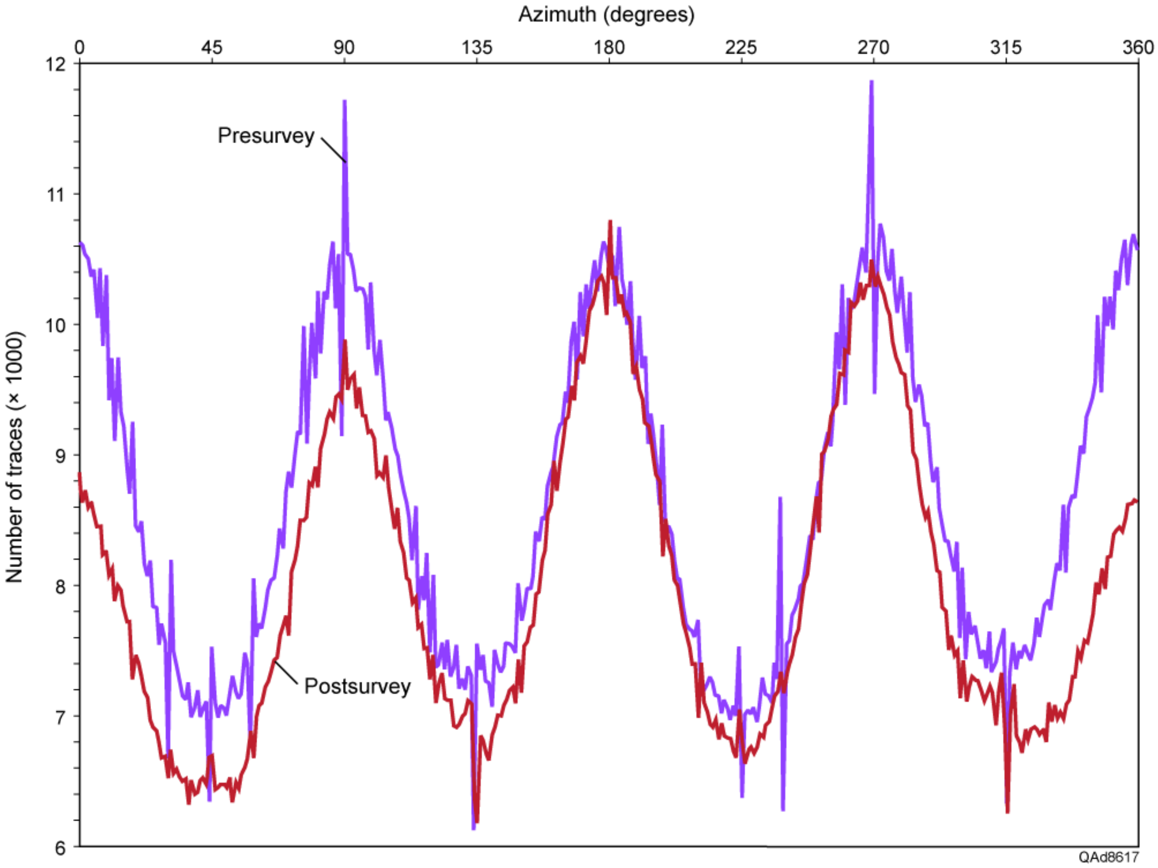

Figure 7.9. Relationship between number of data traces and the source-to-receiver azimuths that raypaths traveled to generate the traces. The random-geometry (post-survey) curve (red curve) is lower magnitude because fewer source and receiver stations were used than were intended in the original regular-geometry (pre-survey) design (blue curve).

Offset-Azimuth Maps

An informative way to display offset and azimuth properties related to seismic survey designs is a map format that shows offset behavior in all azimuth directions. Offset-azimuth attribute maps developed in this study are presented as Figure 7.10. These maps show how trace populations are distributed as a function of offset for narrow 10-degree azimuth corridors. Offsets are longer in north-south and east-west directions than in other azimuths because those directions are the diagonals of the square source-receiver grids (Fig. 7.1). Although the regular-geometry offset distribution shown on Figure 7.8 implies there are offsets that have zero trace populations, the distance and azimuth scales used on Figure 7.10 do not show these small areas of zero-trace occurrence. Every fifth circle is emphasized on the maps, and every tenth circle is labeled to allow quick recognition of offset distance in any azimuth direction. All distance labels have units of 1000-ft, thus “15” is equivalent to 15,000 ft.

An encouraging message provided by the map describing the offset-azimuth properties of the actual recorded data (Fig. 7.10b) is that there are full offset distributions in all azimuth directions. Thus the 3C3D data should be appropriate for prestack azimuth analysis of trace gathers to determine azimuth-dependent velocities and the existence of fast/slow S-wave modes.

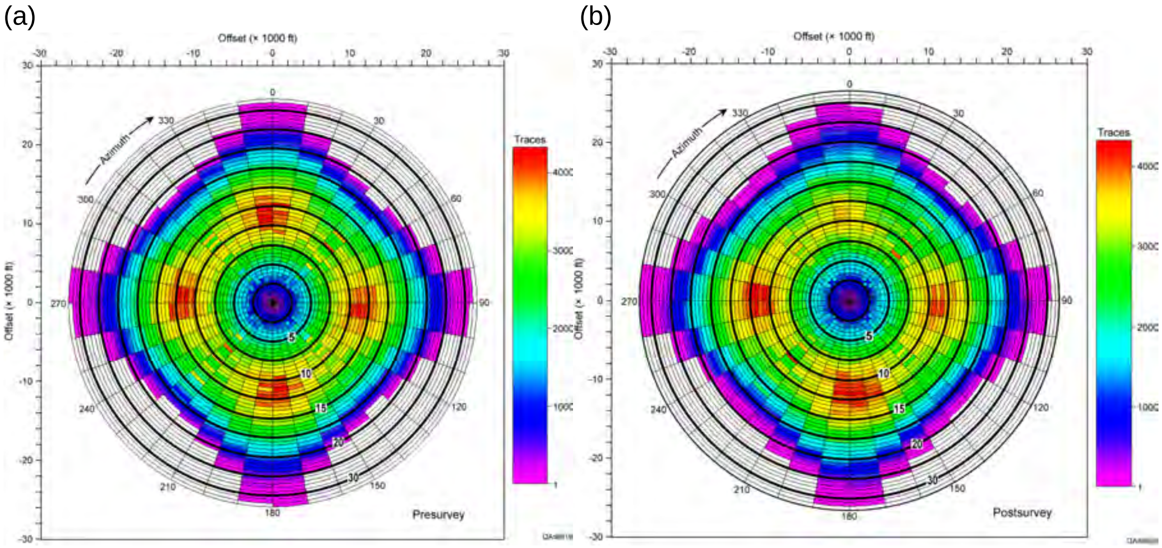

Figure 7.10. Maps of offset and azimuth attributes for (a) the intended regular-station geometry, and (b) the implemented random-station geometry. The numbered circles indicate offset distance in units of 1000-ft. Azimuth effects are shown in 10-degree corridors.

Conclusions

Our previous multicomponent seismic research has caused us to champion the principle of acquiring data with a source/receiver grid in which source and receiver stations are positioned with a modest amount of randomness rather than being at consistent incremental spacings as most geophysicists seek to achieve. Although we did not design the seismic data-acquisition used in this study, the surface conditions across the survey area forced random distributions of source/receiver stations. We could not have been more pleased if we had designed the survey ourselves. The resulting data quality is the best we have worked with in our 12 years of multicomponent seismic research. We used this seismic survey to analyze fold, azimuth, and offset atgtributes of the SV-P mode and compare those with similar attributes of the P-SV mode that was interpreted in this study. Because no one has to date utilized the SV-P mode, our intent is to continue to study attributes of SV-P data and to determine uses and applications of this mode compared to those of its popular and important P-SV companion mode.

The uniform line spacing and uniform station spacing that was intended to be used to acquire 3C3D seismic data in Bradford County could not be implemented. Instead, surface constraints (rough topography, buildings, water wells, electrical lines, roads, agricultural activity, etc.) forced source stations to be positioned in a random pattern across the seismic grid. Several receiver stations also had to be positioned at irregular intervals. The end result was a post-survey source-receiver geometry that differed significantly from the intended pre-survey geometry. This outcome is typical of most land seismic surveys. Actual post-survey distributions of sources and receivers are almost always different from what is assumed for station distributions when planning a 3D survey.

The randomness that local field conditions forced on the Bradford County seismic program had a positive influence on data quality, not a negative effect. A reasonable amount of randomness in positioning source and receiver stations in a 3D seismic program has minimal impact on stacking fold and results in smoother distributions of source-receiver offsets and azimuths. These smoother offset/azimuth distributions tend to allow offset-dependent and azimuth-dependent seismic attributes to be more reliably extracted from P and S data, which is an important benefit for estimating rock and fluid properties with seismic data.

The seismic data-acquisition geometry used to acquire the Bradford County 3C3D data had an appropriate amount of randomness. As a result, the P and S modes embedded in the data are well suited for the research objectives of this study.

A unique objective of this study was to consider the SV-P converted mode, which seismic data processors have not attempted to do to date. Based on the numerical analysis presented in this chapter, fold maps calculated for the SV-P converted mode are more erratic than fold maps for the conventional P-SV converted mode. This erratic fold is a factor that requires careful attention during data processing if viable SV-P data are to be produced.

Chapter 8

Multicomponent Seismic Data Processing

Introduction

Many seismic data processors think the term “seismic image” should be used to describe only data that have been migrated. In this discussion, we will be more flexible in our terminology and use the word “image” to describe stacked, but unmigrated, data as well as migrated data. Stacked data are an image; the data are simply a distorted and inaccurate image until they are migrated.

Two different concepts have to be implemented to create stacked, unmigrated images of multicomponent seismic data. One concept is based on common-midpoint (CMP) imaging concepts. The second concept is based on common-conversion-point (CCP) imaging principles. CMP imaging applies when the propagation velocity of an upgoing wavefield reflecting from a geologic target is the same as the propagation velocity of the downgoing wavefield that illuminated the target. CMP data processing has been used for decades to image geology with single-component P-wave seismic data. CMP data-processing procedures can also be used to create SH-SH and SV-SV shear wave images when SH and SV shear modes are produced directly at a source station.

CCP data-processing procedures are used when the propagation velocity of an upgoing reflected wavefield differs from the propagation velocity of the downgoing wavefield that produced the reflected wavefield. The most common use of CCP data processing is to create converted-SV (or P-SV) images, which involve a downgoing P-wave mode and an upgoing SV mode. In this study, traditional CCP data processing was used to produce P-SV images. In theory, an altered form of CCP imaging can be used to create a converted-P (or SV-P) image when an SV mode is produced directly at a source station. SV-P data involve a downgoing SV illumination wavefield and an upgoing P reflected wavefield. In practice, no one has generated a SV-P image, or at least no such image has been shared with the geophysical community.

Seismic data can be migrated before or after stacking the data. Post-stack migration is more common than prestack migration because post-stack migration is lower cost. However, prestack migration is more accurate than post-stack migration unless inaccurate or insufficient velocities have been supplied to the migration algorithm.

Prestack migration can be done as either a time-based procedure or as a depth-based procedure. The cost of time-based prestack migration is becoming more common as data-processing groups expand computational capabilities. Depth-based migration is relatively expensive because it requires many hours of machine time to perform the calculations, and the procedure may have to be done several times to create an appropriate layered-Earth model with appropriate layer velocities. Our multicomponent seismic data from Bradford County, Pennsylvania, were prestack time migrated.

Coordinate Data Spaces

Several different coordinate systems are used when processing multicomponent seismic data. Three coordinate systems that are utilized are shown on Figure 8.1. The map view on this figure shows a seismic source station and a receiver station positioned on the Earth's surface above a fracture system. When acquiring 3D multicomponent seismic data, a common practice is to deploy source lines orthogonal to receiver lines. An orthogonal source-line and receiver-line geometry was used to acquire the 3C3D seismic data used in this study, as discussed in Chapter 7.

In geophysical terminology, the direction in which receiver lines are deployed is called **inline**. The direction orthogonal to inline (usually the source line direction) is called **crossline**. The inline/crossline directions used on Figure 8.1 are indicated by axes with subscripts **i** (for inline) and **x** (for crossline). Together, these two axes—inline and crossline—define a seismic data-acquisition coordinate system. Axes and terminology other than orthogonal inline and crossline directions can be used to describe seismic data-acquisition geometry. For simplicity, inline and crossline terminology will be used to identify data-acquisition space in this discussion.

During seismic data processing, data are usually transformed to a second coordinate system referred to as **radial/transverse**. For the source-receiver pair drawn on Figure 8.1, this coordinate transformation is achieved by mathematically rotating inline and crossline axes by angle β so one axis is in the vertical plane passing through the source and receiver stations. The coordinate axis rotated into this vertical plane is the radial axis for this particular source-receiver pair. The axis normal to this vertical plane is the transverse axis for the same source-receiver pair. Angle β differs for each source-receiver pair and is calculated from GPS coordinates defining locations of source and receiver stations across a survey area. On Figure 8.1, radial and transverse axes are identified by axes labeled with subscripts **r** (for radial) and **t** (for transverse). Together, these two axes—radial and transverse—define a seismic data-processing coordinate system.

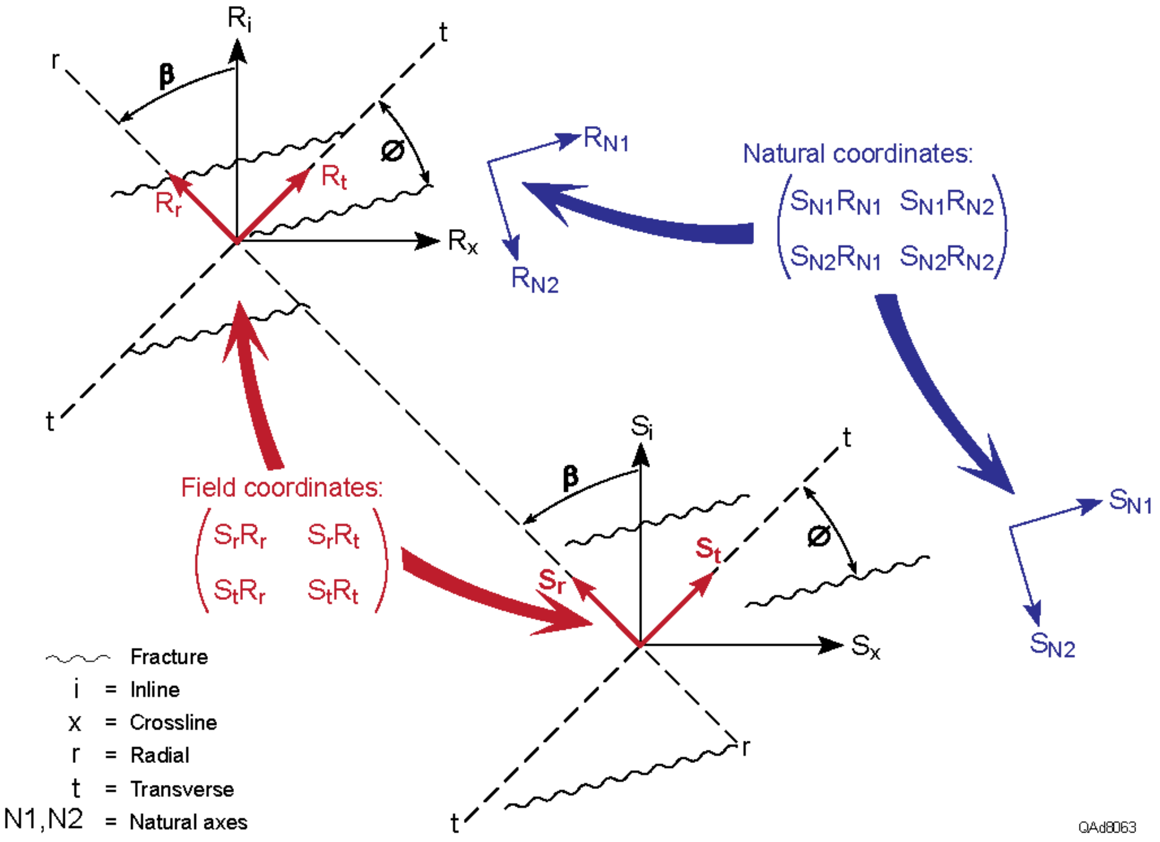

Figure 8.1. Vectors and quantities labeled R relate to a receiver station. Vectors and quantities labeled S relate to a source station. This map view illustrates three coordinate systems encountered when using multicomponent seismic technology to analyze fracture systems. The first coordinate system is an inline and crossline geometry used to deploy sources and receivers for data acquisition (subscripts i and x). The second coordinate system is a radial-transverse system created when processing data (subscripts r and t). The third coordinate system is the natural coordinate system that needs to be determined to interpret fracture properties (subscripts N1 and N2).

The third coordinate system will be called **natural coordinates** in this report. Natural coordinates align with principal anisotropy axes of the Earth. For this reason, the axes are referred to as **principal axes** in some technical papers. For the fracture system depicted on Figure 8.1, the principal anisotropy within the Earth is a system of aligned fractures. The challenge of utilizing multicomponent data in fracture analysis is to rotate radial and transverse data-processing axes to natural coordinate axes. On Figure 8.1, natural coordinate axes and natural coordinate data terms are identified by subscripts **N1** and **N2**. Together, these two axes—natural coordinate axis N1 and natural coordinate axis N2—define a seismic data-interpretation coordinate system. The prestack converted-SV shot gathers that Geokinetics provided our research team were data that had been rotated to natural coordinate data space appropriate for our study area in Bradford County, Pennsylvania.

Techniques used to determine the azimuths of natural coordinate axes depend on whether the azimuth of maximum horizontal stress σ_1 within the seismic propagation medium is known. There are several procedures by which the azimuth of maximum horizontal stress can be determined. For example, when wells are drilled through rock layers subjected to horizontal stress, a cross section of a well bore shows the hole is elliptical, not circular. The azimuths of the long axes of these elliptical cross sections of stressed wells define the azimuth of σ_1. As a second procedure, when wells are hydraulically fractured, the direction in which the largest population of induced fractures is oriented is the direction of σ_1. A third procedure is to determine the azimuths of dilational fractures in borehole image logs. An interpretation of fracture distributions from a Marcellus borehole image log acquired inside the image space of the 3C3D seismic data used in this study is included in Chapter 9 to show an interpretation of the azimuth of σ_1.

When the azimuth of σ_1 is known by one of these methods, or by an alternate technique, or simply by guessing, one natural coordinate axis is defined to have the same azimuth as σ_1, and the azimuth of the second natural coordinate axis is defined to be perpendicular to σ_1. Based on σ_1 azimuths known from Marcellus Shale drilling, the converted-SV shot gathers that Geokinetics provided our research team were rotated to natural coordinate axes determined to be approximately east-west and approximately north-south local to our study site in Bradford County, Pennsylvania. At the location of our study site, natural coordinate axis N1 (the polarization direction of the fast-S mode), as determined from an analysis of the horizontal-radial and horizontal-transverse geophone data, was oriented 80 degrees clockwise from North. Natural coordinate axis N2 (the polarization direction of the slow-S mode), as indicated by the seismic data, was oriented 170 degrees clockwise from North, perpendicular to the N1 axis. These natural-coordinate axis azimuths agree reasonably well with the log-based σ_1 azimuth information displayed in Chapter 9.

When the azimuth of σ_1 is not known, a popular procedure that allows natural coordinates axis azimuths to be determined is the Alford rotation procedure. Although Alford rotation was not used in this study, the technique is explained in the following section to make a complete documentation of natural-coordinate analysis procedures.

Alford Rotation

The Alford rotation procedure for estimating the orientations of natural coordinate axes was described publically as an oral presentation at the 56th Annual Meeting of the Society of Exploration Geophysicists (SEG). The

Expanded Abstract of that SEG presentation (Alford, 1986) is one of the more widely cited references in geophysical literature. A detailed explanation of the logic and physics embedded in the coordinate transformation procedure was later published as U.S. Patent 4,817,061 (Alford et al., 1989).

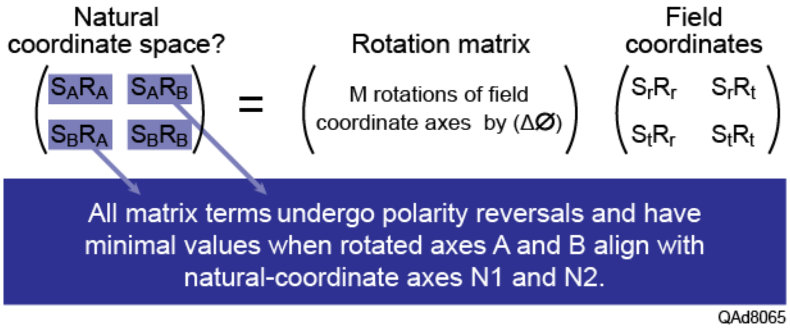

Figure 8.2. The Alford rotation procedure used to define natural coordinate data space. S is a source displacement vector; R is a receiver orientation vector. Subscripts r and t define radial/transverse coordinate space (or data-processing data space). Subscripts A and B define axes rotated from radial and transverse axes by azimuths that successively increase by small increments of $\Delta\theta$. When this coordinate rotation aligns axes A and B with natural coordinate axes N1 and N2, the terms in the left-hand-side matrix undergo polarity reversals and tend to assume minimal values. At this same azimuth, each diagonal term represents data propagating in one of the two natural coordinate directions.

Once a fracture target is illuminated with orthogonal S-wave displacement vectors, Alford rotation techniques can be used to estimate natural coordinate axes oriented parallel and orthogonal to fracture trends. The mathematics of Alford rotation is illustrated on Figures 8.2 and 8.3. The right-hand-side matrix of the equation displayed on these figures defines data components created by orthogonal S-wave source displacements and recorded by orthogonal S-wave sensors. Radial and transverse data (subscripts **r** and **t**) are used on Figures 8.2 and 8.3, but the calculation procedure can utilize inline and crossline data, or data defined by any orthogonal field-coordinate axes. The fundamental requirement for applying Alford rotation is that a fracture system be illuminated with orthogonal S-wave vectors and the Earth response be recorded with orthogonal S-wave sensor elements.

The target-illuminating data (right-hand-side matrix) are repeatedly transformed to a new coordinate system (left-hand-side matrix), in which axes are rotated in small azimuth increments of $\Delta\theta$. This calculation is typically done over an azimuth range of 180° (or 360°) at increments of 1, 5, or 10° of azimuth, depending on the preferences of a data processor. For each new choice of azimuth, the left-hand-side matrix defines the azimuth orientation of a “possible” natural coordinate system having one axis parallel to a fracture trend and one axis orthogonal to that trend. If $\Delta\theta = 1°$, these 180 (or 360) possible choices for the orientation of a natural coordinate system are analyzed to determine which azimuth value caused the terms of the left-hand-side matrix to undergo polarity reversals. The rotation angle at which terms exhibit a phase reversal defines the azimuth of a natural coordinate axis. Often terms will also exhibit minima values in addition to phase reversals when a data-space rotation sweeps past a natural-coordinate axis azimuth.

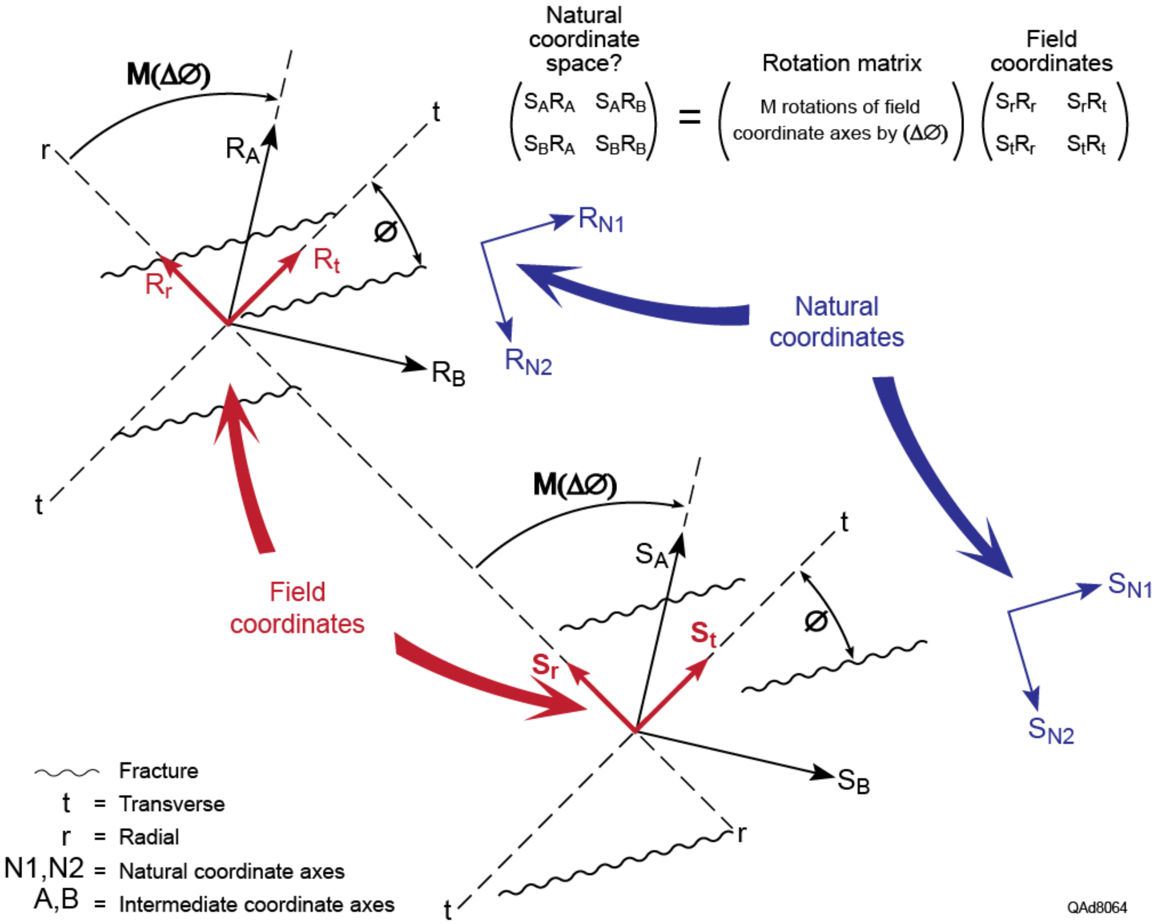

Figure 8.3. Graphical description of the Alford rotation procedure described on Figure 8.2. Axes with subscripts A and B have been rotated from radial/transverse axes by M increments of Δθ. At each new rotated coordinate position, the left-hand-side matrix is calculated and saved. When this calculation is done over an appropriate azimuth range, typically 180° (or 360°), these matrices are examined to find which azimuth rotation caused the terms of the matrix to undergo polarity reversals. When that polarity reversal occurs, axes A and B should be aligned with natural coordinate axes N1 and N2, and matrix terms S_AR_A and S_BR_B define data propagating in the two natural coordinate axis directions. Quantities using label R are associated with a receiver station, and quantities labeled S are associated with a source station.

Some data processors prefer to produce Alford rotation results for a full 360° rotation rather than a half-circle rotation of 180° so that they see a second confirmation of the azimuths at which off-diagonal terms exhibit phase reversals. Either rotation angle range (360° or 180°) is sufficient, depending on a data processor's preference.

Imaging Strategies

The concept of **common-midpoint** imaging was developed in the 1950's to produce P-P stacked images of the Earth's subsurface. In a flat-layered Earth, when the velocity of the downgoing wavefield that illuminates a geologic target is the same as the velocity of the upgoing reflected wavefield from that target, as it is for P-P data, the reflection point (image point) is half way between the source and the receiver. Hence the terms "common midpoint" or "CMP" are used to describe this imaging concept.

When seismic images are made using a downgoing illuminating wavefield that has a velocity that differs from the velocity of the upgoing reflected wavefield, a different concept called **common-conversion-point imaging** is used to construct stacked images of geologic targets. The abbreviation "CCP" is used to indicate this seismic imaging strategy. CCP imaging techniques are required to construct stacked images from SV-P data because the downgoing SV mode has a velocity that differs from the velocity of the upgoing P mode.

CMP and CCP imaging raypaths are illustrated on Figure 8.4. The source in the figure applies a vertical force to the Earth to simulate the force applied by the shot-hole explosive source that generated the 3C3D seismic data used in this study. Both P and SV modes are shown propagating away from the source to conform to the test-data findings discussed in Chapter 6.

In the example shown on Figure 8.4, P-P imaging (a CMP type of imaging) is compared with one type of CCP imaging—that involving the SV-P mode. Segments of downgoing and upgoing raypaths are labeled either P or SV to indicate the specific wave mode that travels along each segment of each raypath. Circled arrows on each raypath segment identify the direction in which the wave mode acting on that raypath segment displaces the Earth. The data polarities indicated by these particle displacement vectors agree with the polarity conventions defined by Aki and Richards (1980). The upgoing events that arrive at a receiver station are P-wave events for both P-P and SV-P modes.

The imaging principles of P-SV and SV-P modes illustrated on Figure 8.5 emphasize that an SV-P mode images geology closer to a source station than to a receiver station. In contrast, a P-SV mode images geology closer to a receiver station than to a source station. For our Bradford County study area, receivers occupied an area smaller than did source stations (Fig. 7.1b). Although no SV-P data were extracted from the Bradford County 3C3D data by Geokinetics and Geophysical Pursuit, if such data had been processed, the image space covered by P-SV data (Fig.7.5) would have been smaller than the image space covered by SV-P data (Fig.7.7), as demonstrated on Figures 7.5 and 7.7 of Chapter 7.

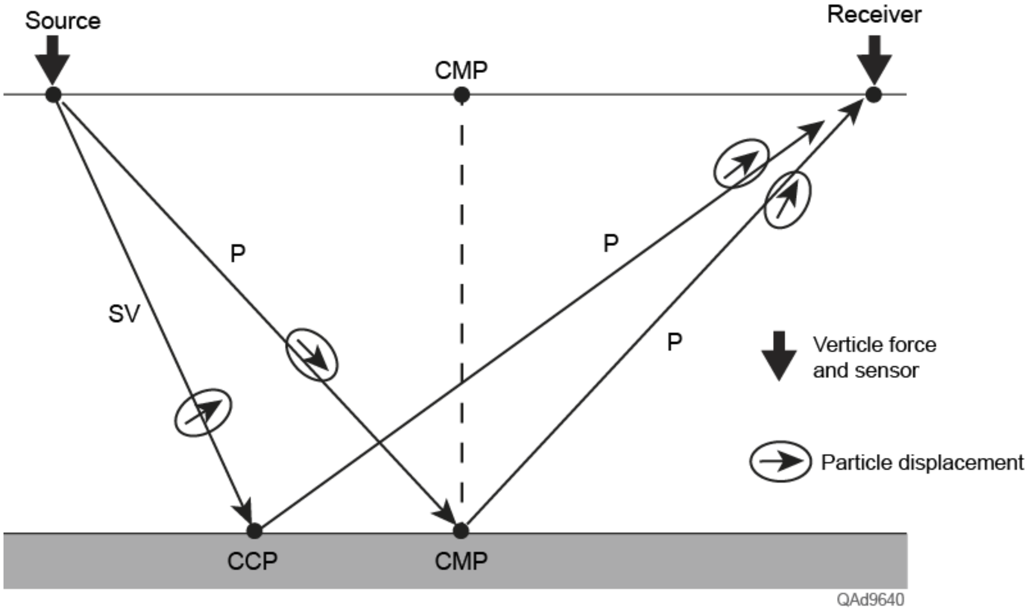

Figure 8.4. Comparison of P-P and SV-P imaging of subsurface geology. Point CMP is the common midpoint (image point) for P-P data for this source-receiver pair. Point CCP is the common-conversion point (image point) for SV-P data.

Velocity Analysis

Velocity analysis is a crucial data-processing step when constructing seismic images. An extensive set of literature exists that discusses methods used to estimate seismic-mode velocities from seismic reflection data. The discussion here will not attempt to summarize this literature but will focus on velocity concepts involved in processing converted-mode seismic data

When CMP data are processed, it is not necessary to be concerned about which offset domain (positive or negative) data reside in when performing velocity analyses. If the velocities of downgoing and upgoing wave modes are the same (CMP data processing), the same velocity behavior occurs in both offset directions. However, when converted modes are involved, it is essential to do two velocity analyses—one analysis for positive-offset data and a second analysis for negative-offset data.

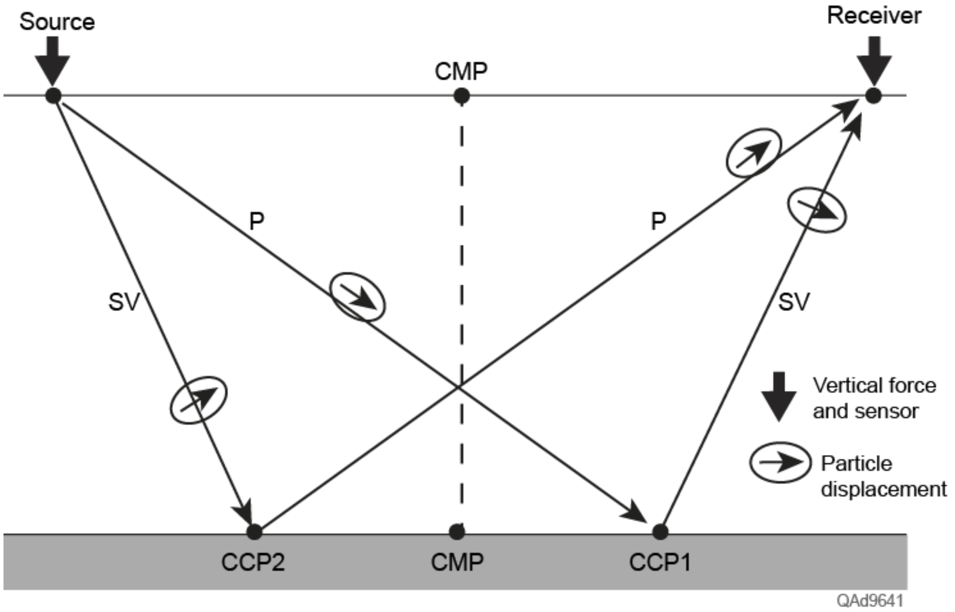

Figure 8.5. Comparison of P-SV and SV-P raypaths. The image points for these converted modes are common-conversion points CCP1 and CCP2. An image point for a P-SV mode (CCP1) is closer to the receiver station than to the source station. The image point for an SV-P mode (CCP2) is closer to the source station than to the receiver station.

The reason for this dual-domain velocity analysis is illustrated on Figure 8.6 which shows two distinct rock facies between two surface-based source and receiver stations. Laterally varying rock conditions such as shown on this diagram are common in many areas. For purposes of illustration, assume the P and S velocities in Facies A are significantly different from the P and S velocities in Facies B. The traveltime required for a positive-offset SV-P event to travel raypath SV_A-P_A is not the same as the traveltime for a negative-offset SV-P event to travel raypath SV_B-P_B. This difference in traveltime occurs because the SV_A mode is totally in Facies A, but the SV_B mode is almost entirely in Facies B, Likewise, all of mode P_B is in Facies A, but mode P_A has significant travel paths inside Facies A and Facies B. Because traveltimes differ in positive-offset and negative-offset directions, one velocity analysis has to be done on positive-offset data, and a separate velocity analysis has to be done for negative-offset data. This same requirement of dual-domain velocity analyses is known by people who process P-SV data, so the concept should not be considered as being novel to processing SV-P modes.

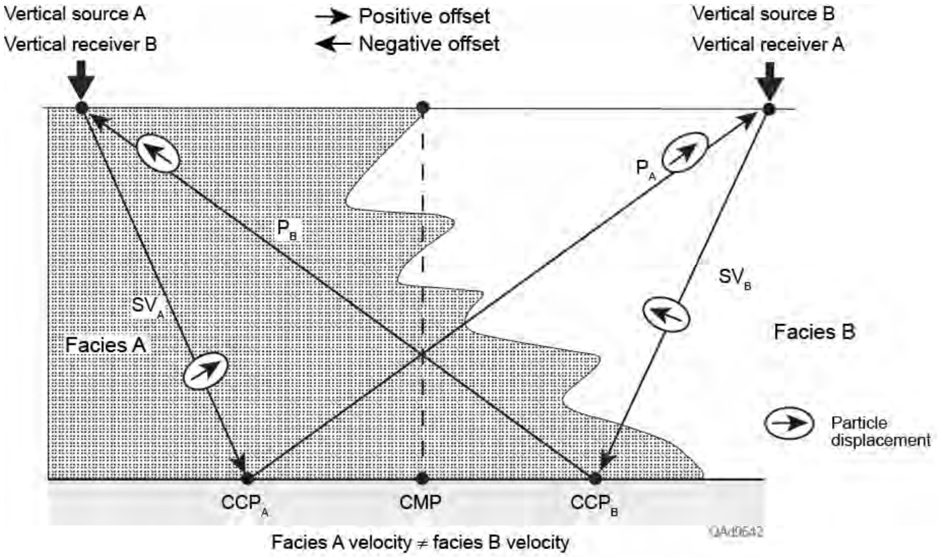

Figure 8.6. Positive-offset and negative-offset domains for SV-P data. V_P and V_S velocities in Facies A are different than they are in Facies B. Straight raypaths are drawn for simplicity.

In this diagram, SV-P data generated at Source A and recorded at Receiver A are labeled SV_A for the downgoing SV mode and P_A for the upgoing P mode. The offset direction from Source A to Receiver A is arbitrarily defined as **positive offset**. When the positions of source and receiver are exchanged, creating Source B and Receiver B, the offset direction reverses and is defined as **negative offset.** The raypath for negative-offset SV-P data is labeled SV_B for the downgoing SV mode and P_B for the upgoing P mode. The polarities shown for the downgoing SV particle-displacement vector conform to the polarity convention established by Aki and Richards (1980).

Constructing Converted-Mode Images

Converted-mode imaging can be done in two ways: (1) by CCP binning and stacking of P-SV and SV-P reflections, followed by post-stack migration of the stacked data, or (2) by implementing prestack migration of SV-P and P-SV reflections. Method 2 (prestack migration) is the more rigorous approach, but method 1 (CCP binning/stacking and post-stack migration) is the more common strategy because of its lower cost. To perform CCP binning and migration of converted-mode data, it is important to note CCP coordinates of SV-P image points are mirror images of CCP image points associated with P-SV data, as illustrated on Figure 8.7.

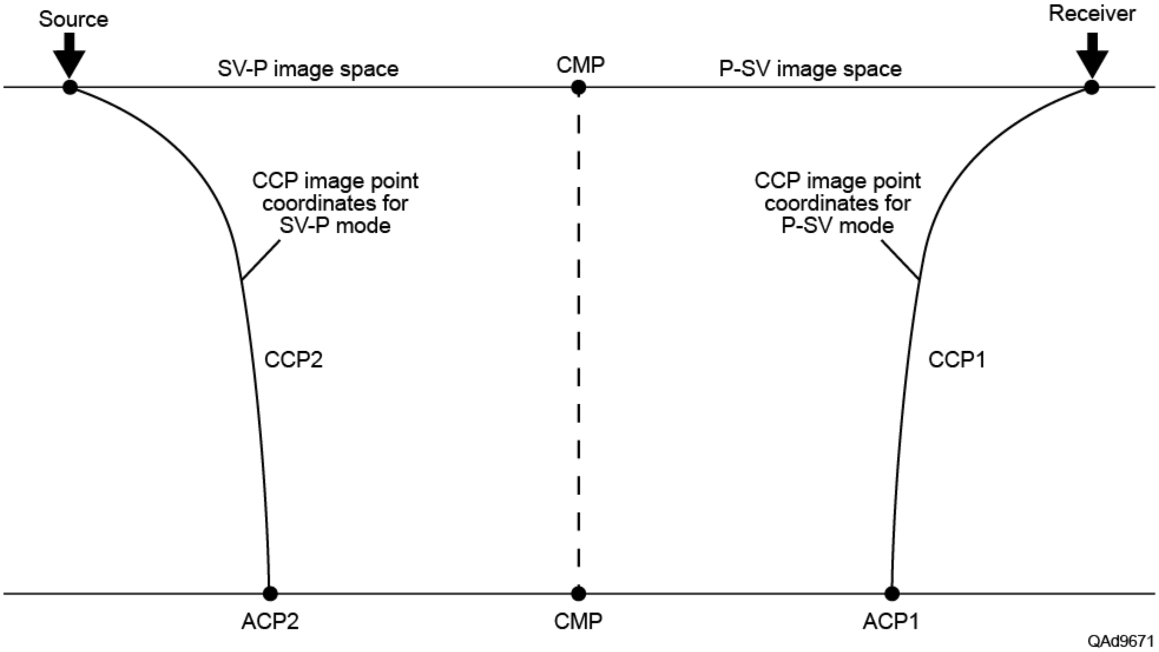

Figure 8.7. SV-P and P-SV CCP imaging principles. Curve CCP1 shows the trend of common-conversion points for P-SV data. Curve CCP2 shows the trend of common-conversion points for SV-P data. ACP1 and ACP2 are asymptotic conversion points for trends CCP1 and CCP2, respectively. CCP1 and CCP2 are mirror images of each other relative to the common midpoint CMP for this source-receiver pair.

Because positive-offset and negative-offset converted-mode data have different velocity behaviors, two separate CCP binning/stacking steps need to be done to create a converted-mode stacked image. In Step 1, positive-offset data are binned and stacked into an image using velocities determined from positive-offset data, and in Step 2, negative-offset data are binned and stacked into a second image using velocities determined from negative-offset data. The final image is the sum of these two opposing-offset images. This same dual-image strategy is implemented when binning and stacking P-SV data. All three stacked images should be migrated and used in geological applications. As documented by Hardage et al. (2011) relative to P-SV imaging, some geologic features are sometimes better seen in one of these three images than in its two companion images. Thus all three stacked and migrated images of SV-P and P-SV data are used in geological interpretations.

Imaging Option 1—CCP Binning, Stacking, and Post-Stack Migration

Regarding commercial seismic data-processing software that can be purchased or leased by the geophysical community, none of these software packages calculates true CCP image points. Instead, leased software calculates converted-mode image coordinates called **asymptotic conversion points**, which are abbreviated as **ACP**. An ACP is an image coordinate where the trend of correct CCP image points for a specific source-receiver pair becomes quasi-vertical (Fig. 8.7). Deep geology is correctly imaged using P-SV data binned by ACP principles, and would also be correctly imaged by SV-P data binned using ACP concepts that are adjusted for SV-P data. However, shallow geology is not correctly imaged for either P-SV data or SV-P data when ACP binning methods are used. Only true CCP binning produces correct stacked images of both shallow and deep geology for converted modes appropriate for post-stack migration. On Figure 8.7, the asymptotic conversion point for the P-SV mode is labeled ACP1, and the asymptotic conversion point for the SV-P mode is labeled ACP2. Neither image point is correct except where their associated CCP binning profile is quasi-vertical (i.e., for deep targets). As emphasized above, these two image points are mirror images of each other relative to the common midpoint (point CMP on Figure 8.7) for any source-receiver pair involved in a seismic survey.

Imaging Option 2—Prestack Migration

Prestack migration can be done to create a time-based seismic image or a depth-based seismic image. For convenience of discussion, this material will be limited to a brief description of prestack time migration of seismic data. Referring to Figure 8.8, prestack migration is done by numerically propagating a specific seismic wavefield downward from each source station to illuminate geologic targets, and then numerically propagating a specific seismic wavefield upward from reflecting interfaces to each receiver station.

To simplify the discussion, the specific wavefields used in prestack migration that are considered on Figure 8.8 are created by applying velocity filters to data recorded by only vertical geophones. After appropriate velocity filtering, reflection events having only a specific velocity behavior remain in the data. The specific velocity behaviors of interest for vertical-geophone data are those associated with the following seismic modes: P-P, P-SV, SV-SV, and SV-P. If 3C geophones are used in combination with a vertical-force source, a fifth velocity filtering option is to extract SH-SH reflection events (as documented by the test data discussed in Chapter 6). However, this latter option requires that the filtering action be applied to data recorded by transverse horizontal geophones. The result is an image of geologic interfaces seen by each specific seismic mode. For simplicity, only one source station and only one receiver station are shown on Figure 8.8.

The table on Figure 8.8 considers only wave modes produced by a vertical-force source (to simulate the shot-hole explosive source used in this study) and, for simplicity, only the responses of vertical geophones. For an Earth with isotropic velocity layers, there are five possible combinations of downgoing (D) and upgoing (U) modes. These possibilities are labeled Option 1 through Option 5 in the figure table.

As indicated by the table on Figure 8.8, prestack migration software can create a SV-P image if the velocity of the downgoing wavefield is that for a propagating SV wavefield and the velocity of the upgoing wavefield is that for a P wavefield.

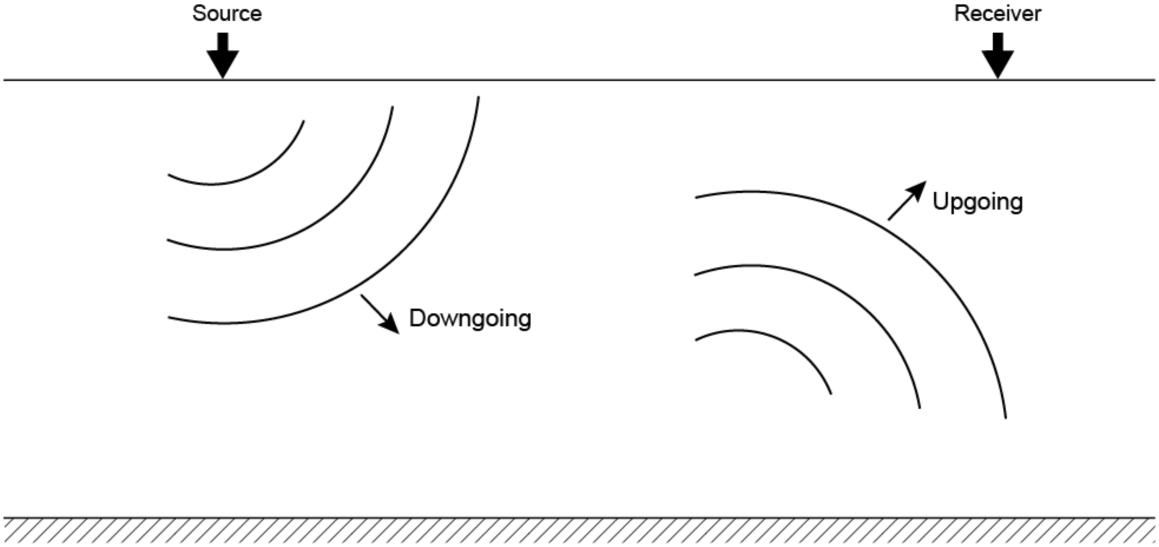

Option	Velocity of D	Velocity of U	Seismic image
1	V_P	V_P	P-P
2(1)	V_P	V_{SV}	P-SV
3	V_{SV}	V_P	SV-P
4(1)	V_{SV}	V_{SV}	SV-SV
5(2)	V_{SH}	V_{SH}	SH-SH

QAd9672

(1) Requires a high-velocity surface if vertical single-component geophones are used; otherwise requires 3C geophones.

(2) Always requires 3C geophones.

Figure 8.8. Simple illustration of prestack migration. A time-space distribution of velocities for a specific seismic mode is defined so that a specific downgoing wavefield (D) can be propagated through this Earth velocity model from every source station to illuminate targets. A second time-space distribution of velocities for a second specific seismic mode is then imposed to propagate that specific reflected upgoing wavefield (U) to every receiver station. The combinations of downgoing and upgoing velocities that can be implemented for a vertical-force source and vertical geophones are listed in the table.

Prestack Time Migration

Prestack time migration of seismic data is done by constructing common-source trace gathers and calculating where individual data points in each trace of each shot gather need to be positioned in seismic image space. The fundamental calculation is illustrated as Figure 8.9. In this diagram, S is the position of a source station in migrated image space, R is the position of a specific receiver station in migrated image space, and A is the position of an image point that is being constructed.

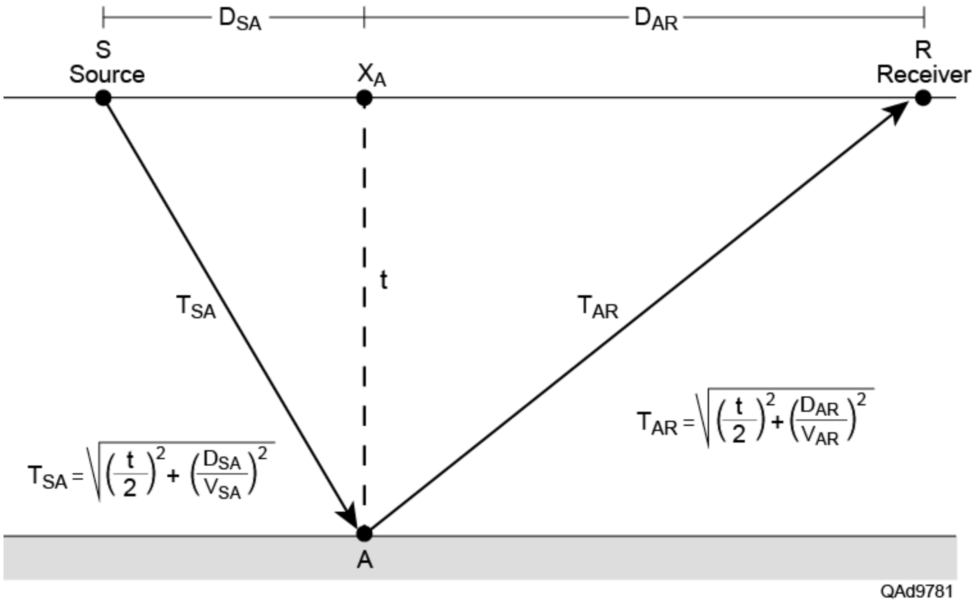

A = Image point
t = Image-trace time coordinate
X_A = Image-trace coordinate
D_{SA} = Horizontal distance from S to A
D_{AR} = Horizontal distance from A to R
T_{SA} = One-way time from S to A
T_{AR} = One-way time from A to R
V_{SA} = RMS velocity for downgoing mode at (X_A, t)
V_{AR} = RMS velocity for upgoing mode at (X_A, t)
$T = T_{SA} + T_{AR}$ = Time coordinate of data sample placed at image coordinates (X_A, t)

Figure 8.9. The double square root calculation used in prestack time migration of seismic data. Image coordinate X_A is defined by the data processor. Image time t varies from zero to the maximum time coordinate of the migrated data. Velocities V_{SA} and V_{AR} are rms velocities determined by a separate velocity analysis and preserved in a file that can be accessed to calculate time coordinate T of the data sample that needs to be moved to image coordinate at (XA, t).

The position of image point A is defined as space-time coordinates (X_A,t). To perform prestack time migration, coordinate X_A is defined by a data processor, and time coordinate t then is incremented from 0 to t_{MAX}, where t_{MAX} is the length of the migrated data trace. The diagram shows the migration of only one data point from only one trace of only one shot gather. The objective is to calculate the time coordinate T of the data sample from the S-to-R data trace that needs to be placed at image space coordinates (X_A,t).

The calculation is done by the two square root equations shown on Figure 8.9. One equation calculates one-way time T_{SA} for the downgoing raypath from S to A. The second equation calculates the one-way time T_{AR} for the upgoing raypath from A to R. The time coordinate T of the data sample from shot-gather trace S-to-R that needs to be placed at migration coordinates X_A, t is the sum of T_{SA} and T_{AR}. In geophysical literature, this prestack time migration procedure is called the **double-square-root** calculation. An important assumption built into the calculation is that down and up one-way traveltimes can be represented as traveltimes along straight, not curved, raypaths.

A broader view of prestack time migration is shown as Figure 8.10. In this diagram, prestack time migration is defined as a 5-step process. In step 1, a particular data trace recorded by receiver R of a particular Shot Record is selected for performing prestack time migration. Image coordinate X_A defined by the data processor may or may not coincide with the position of a receiver station. In this example, X_A is not coincident with a receiver station. In step 2, the data processor is building only one migrated image trace at space coordinate X_A. Time coordinate t is one time coordinate of this migrated data trace. Raypaths SA and AR shown relative to step 2 are the raypaths from Figure 1.

In step 3, the data processor accesses a velocity file that defines rms velocities at every coordinate in the migrated image space. In step 4, one-way traveltimes T_{SA} and T_{AR} defined on Figure 8.9 are calculated to define the time coordinate T of the input data trace that needs to be moved to image coordinates X_A, t. Step 5 is the simple procedure of moving the data sample from shot-gather data space to migrated image space.

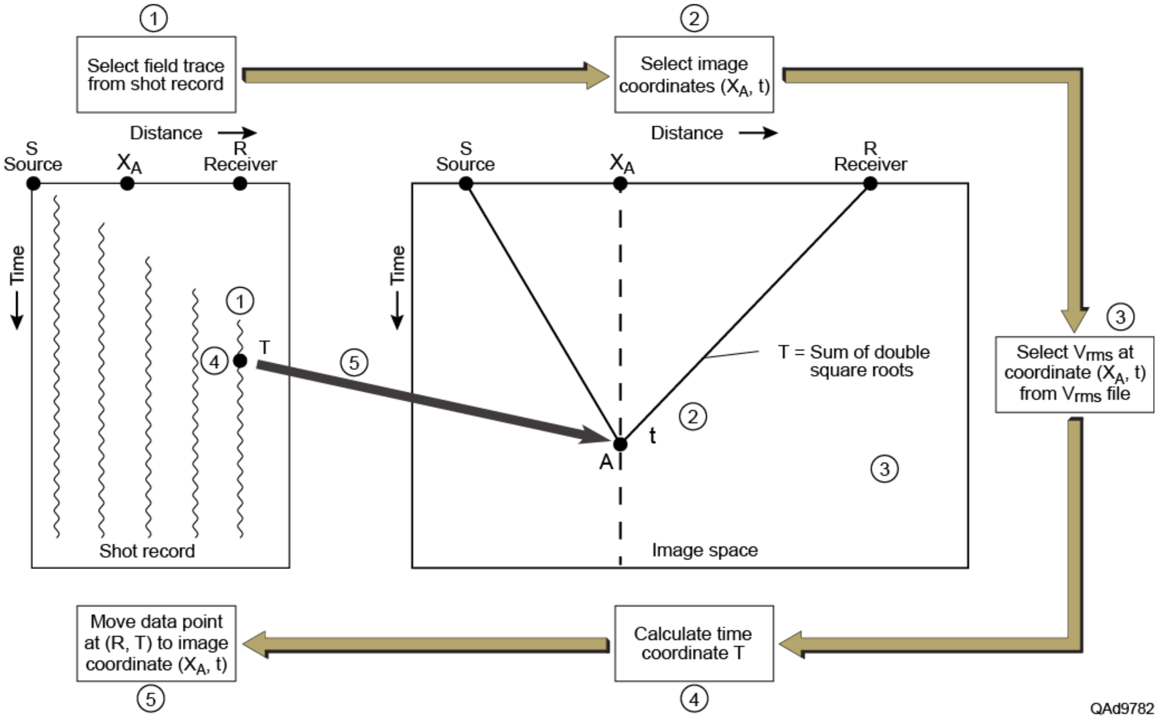

Figure 8.10. Prestack time migration illustrated as a five-step procedure.

Conclusions

It would require a full text book to do a thorough discussion of seismic data processing. To create a chapter that was informative, yet possible to read in a few minutes, only a few pertinent topics of seismic data processing germane to this study have been considered.

The data-coordinate spaces encountered when processing multicomponent seismic data confuse the uninitiated, thus a summary description of these data spaces and the unique terminology associated with each coordinate space seemed essential. Radial/transverse coordinates and natural-axis coordinates are not encountered when single-component P-wave seismic data are processed. The brief overview discussion of these data spaces provided in this chapter should help multicomponent seismic technology to be better understood among the CO_2 sequestration community.

Alford rotation was not used in processing the multicomponent seismic data used in this study because well-log data and regional drilling information provided reliable definitions of the azimuths of maximum and minimum horizontal stresses. If this stress-azimuth information had not been available, Alford rotation techniques would have been used to define fast-S and slow-S orientation azimuths for the 3C3D seismic data. Because Alford rotation procedures are encountered repeatedly when multicomponent seismic data and VSP data are utilized, a description of Alford rotation concepts was included to assist technology transfer to those who develop interests in using multicomponent seismic data to evaluate CO_2 reservoir systems.

The imaging step of seismic data processing was constrained to techniques used only for imaging converted-mode data. This approach was taken because CMP imaging has been practiced for decades and is well understood by any data-processing service, be it a small company or a large company. However, converted-mode data processing cannot be done by all data-processing services. Thus it seemed important to explain a few basic principles of converted-mode imaging that make the imaging distinctly different from the procedures used in CMP imaging.

Chapter 9

Interpretation of Multicomponent Seismic Data

Introduction

The 3D multicomponent seismic data used in this study were acquired as multi-client lease data by industry partners Geophysical Pursuit and Geokinetics. Geokinetics processed the data to produce three time-migrated data volumes—a conventional P-wave volume, a fast-S converted-shear (P-SV_1) volume, and a slow-S converted-shear (P-SV_2) volume. Each data volume consisted of 30,448 data traces. Data traces were 4 seconds long. Image bin dimensions were 110-ft × 110-ft (33.5-m × 33.5-m). The seismic images spanned an area of approximately 23.8 km^2 (9.3 mi^2).

Important geologic calibration data were recorded in a well positioned at the center of the seismic image space spanned by the 3D data volumes. Vertical seismic profile (VSP) data acquired in this calibration well were invaluable for depth registering P and S seismic data. Additional calibration data acquired in this central-image well were a full suite of modern logs that provided rock and fluid properties needed for modeling P and S reflectivities. A log of particular value was the dipole-sonic log, which measured P, fast-S, and slow-S velocities, indicated fast-S and slow-S polarization azimuths, and estimated S-wave anisotropy. These dipole-sonic log data were used to generate P-wave and S-wave synthetic seismograms that aided depth registration of P and S data and identified key geologic targets in seismic images. As a result of having high-quality geologic calibration data, we achieved excellent time-to-depth correlations of geology with P-P, P-SV_1, and P-SV_2 images and developed confidence in the rock and fluid properties interpreted from seismic data.

Seismic Data Quality

Analysis of P-P, P-SV_1, and P-SV_2 data volumes showed S-wave data volumes were more distorted by migration irregularities along the edges of image space than was the P-wave volume. These S-wave migration artifacts produced greater structural dips, as well as more reflection smearing, than were present in the P-wave volume (Figs. 9.1a, 9.1b, 9.1c). All three data volumes had small blank-out areas inside the image space where landowners would not grant permission for their subsurface to be leased. To protect these no-permit areas, data across these no-lease properties were deleted from each data volume. To ensure these data gaps created no migration artifacts, data were deleted after, not before, wavefield migration.

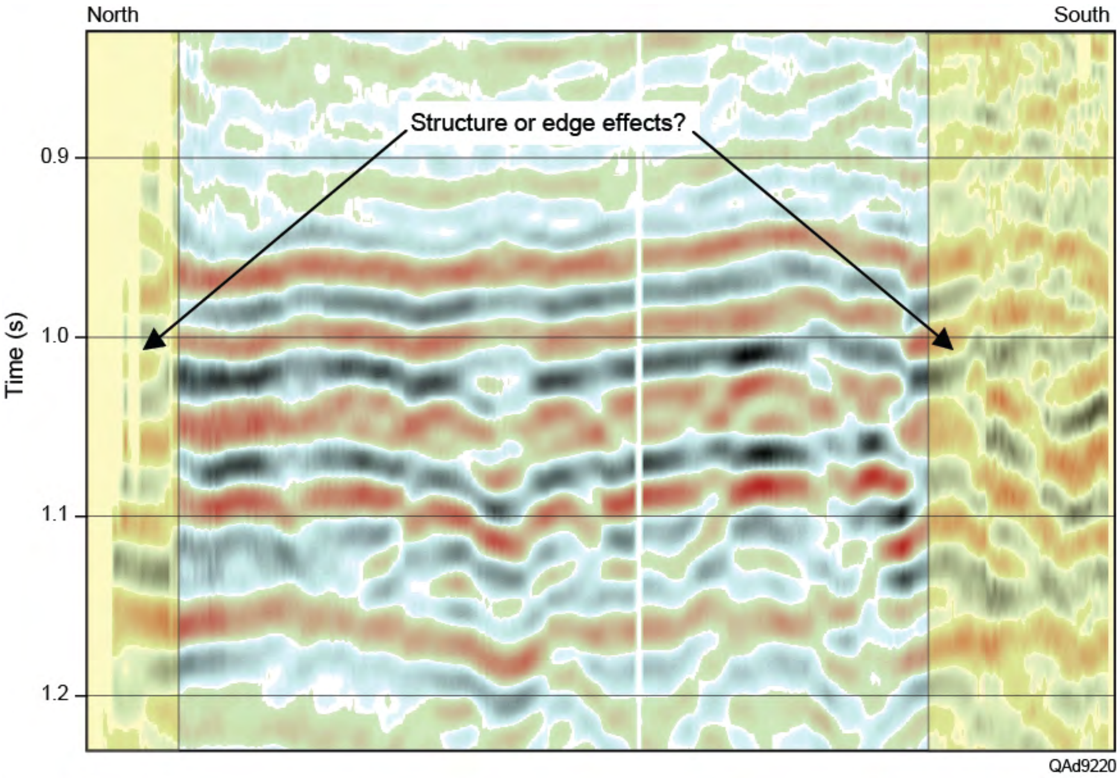

Figure 9.1a. Profile showing migration artifacts (shaded areas) along the edges of P-P image space.

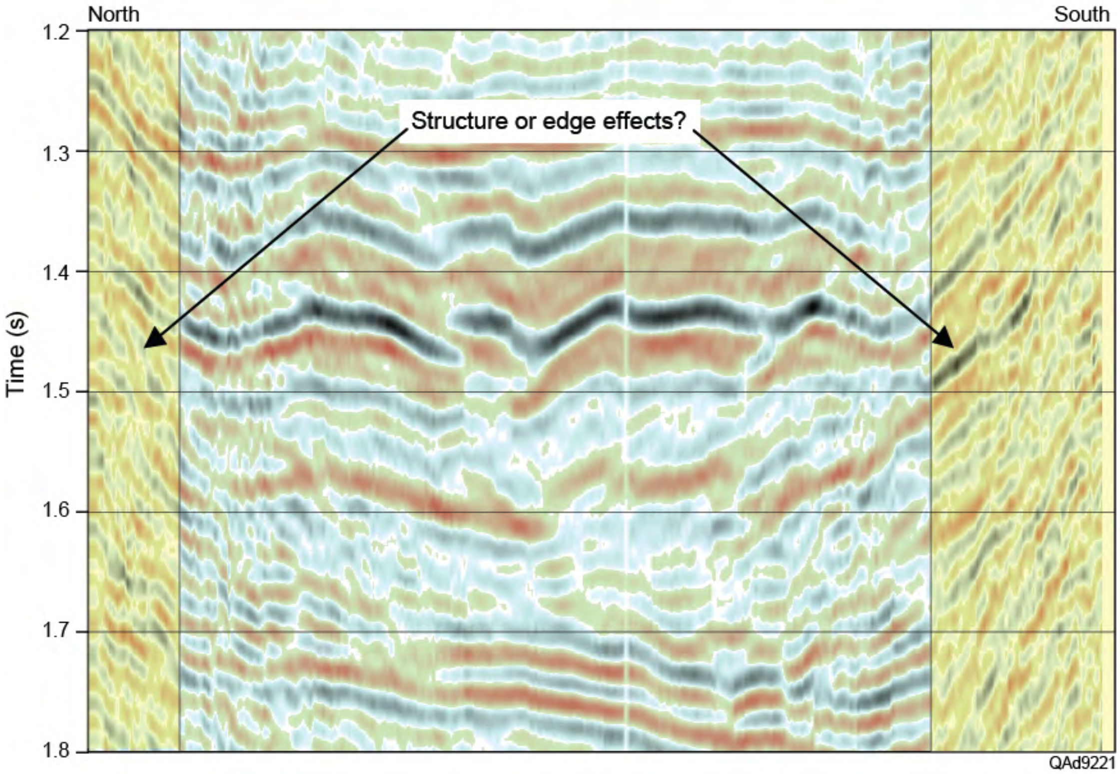

Figure 9.1b. Same profile as (a) showing migration artifacts (shaded areas) along the edges of P-SV_1 (fast-S) mage space. Note the increase in reflection dip inside the shaded areas.

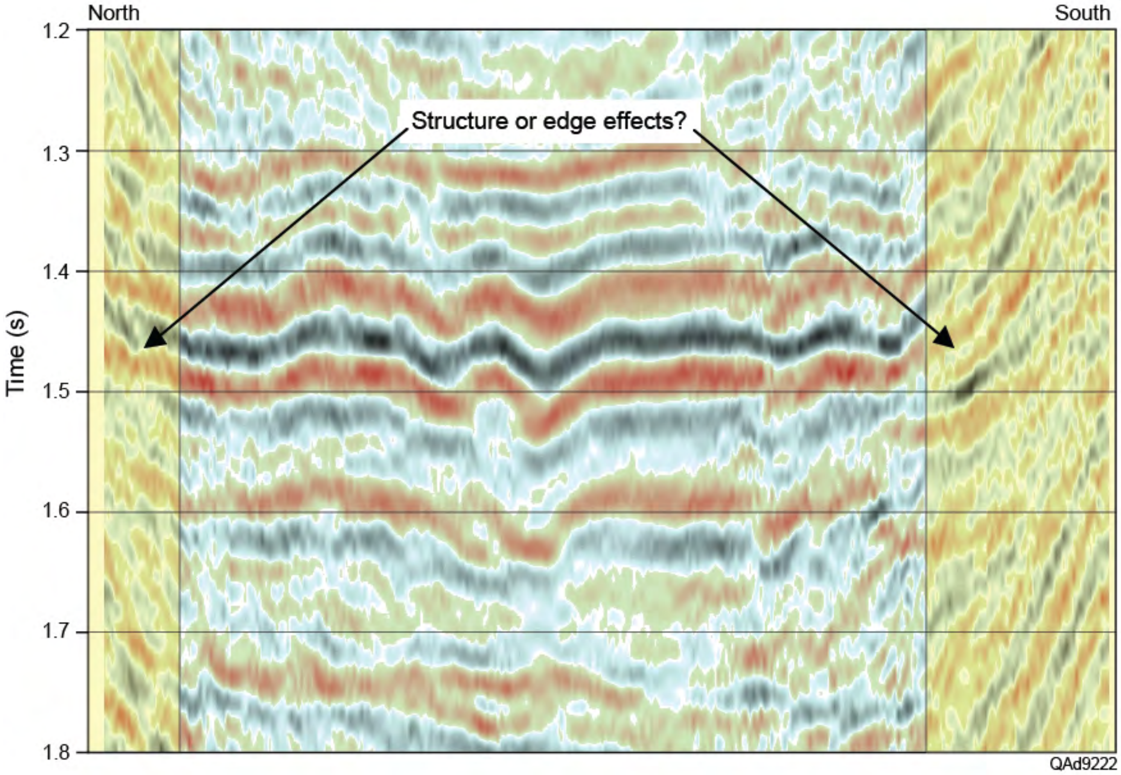

Figure 9.1c. Same profile as (a) showing migration artifacts (shaded areas) along the edges of P-SV_2 (slow-S) mage space. Note the increase in reflection dip inside the shaded areas.

Seed Horizons

A geologic horizon interpreted along a seismic reflection event marks a chronostratigraphic surface. When a reflection event has good signal-to-noise character, there is increased confidence in the accuracy and validity of its associated interpreted horizon. These high-confidence horizons form the basis of a chronostratigraphic section that can be defined vertically and laterally throughout 3D seismic image space. These high-quality, high-confidence, interpreted chronostratigraphic surfaces are called **seed horizons**.

Seed horizons are interpreted along inline and crossline profiles separated by intervals Δx and Δy, respectively, where the magnitudes of Δx and Δy are selected by an interpreter based on her/his confidence that a seed horizon will not jump to an incorrect reflection event when switching interpretation analysis from profile to profile. In our interpretation of post-stack data volumes, Δx and Δy were usually every fifth profile in both the inline and crossline directions. A few profiles that cut across image space at arbitrary azimuths relative to inline and crossline directions were also interpreted to ensure the accuracy of our seed horizons.

P-wave and S-wave horizons were mapped simultaneously to ensure geology was depth registered in P and S image space and to establish optimal stratigraphic correlation between P and S data volumes. Mapping stratigraphic horizons at the edges of S-wave data volumes was difficult because of the migration inaccuracies illustrated on Figures 9.1b and 9.1c.Interpretation of a seed S-wave horizon along inline and crossline profiles was terminated where the time structure of that horizon deviated significantly from its depth-equivalent P-wave horizon time structure.

Seed horizons spanning targeted stratigraphic intervals were interpolated between interpreted profiles to create a continuous horizon surface across seismic image space. These continuous surfaces were used to guide calculations of depth-equivalent P and S seismic attributes. Interpolated horizons were mathematically extended across the full extent of the inline range and crossline range using a best-fit algorithm. Along the edges of seismic image space, interpolated horizons extending beyond the end points of seed horizons are considered to be only estimates of the correct time structure. Consequently, seismic attributes generated near the edges of 3C3D image space are less reliable than attributes calculated where reliable seed horizons were interpreted.

Frequency Spectra Analysis

Visual inspection of time-migrated volumes of Bradford County 3C3D seismic data indicated S-wave data produced better vertical resolution of geologic targets across our study area than did P-wave data. The profiles exhibited on Figures 9.1a through 9.1c demonstrate these differences in vertical resolution. Additional comparisons of P-wave and S-wave resolution of targeted geology will be shown throughout this chapter. Spectral analyses of time-domain P and S data volumes confirmed the frequency content of each 3D image was reasonably broad band. The P-wave data volume had a rather flat frequency spectrum between 10 and 40 Hz, with energy content then steadily reducing to -40 dB at 80 Hz (Fig. 9.2). Both S modes (P-SV$_1$ and P-SV$_2$) had spectra that were approximately flat from 8 to 35 Hertz, with reduced, but significant, energy content extending to almost 55 Hz (Figs. 9.3 and 9.4). The spectra shown on Figures 9.2 to 9.4 were calculated for trace lengths that extended from the Earth surface to slightly below what was interpreted to be seismic basement in each image space.

These spectral analyses introduce the concept that, for this particular geology, converted-SV data are superior to traditional P-P data for detecting and interpreting small-scale geological features. The real proof of whether one wave mode is superior to another wave mode for imaging thinner strata and smaller fault throws requires data comparisons be made in the depth domain rather in the time domain. These depth (spatial wavelength) comparisons are presented in a following section.

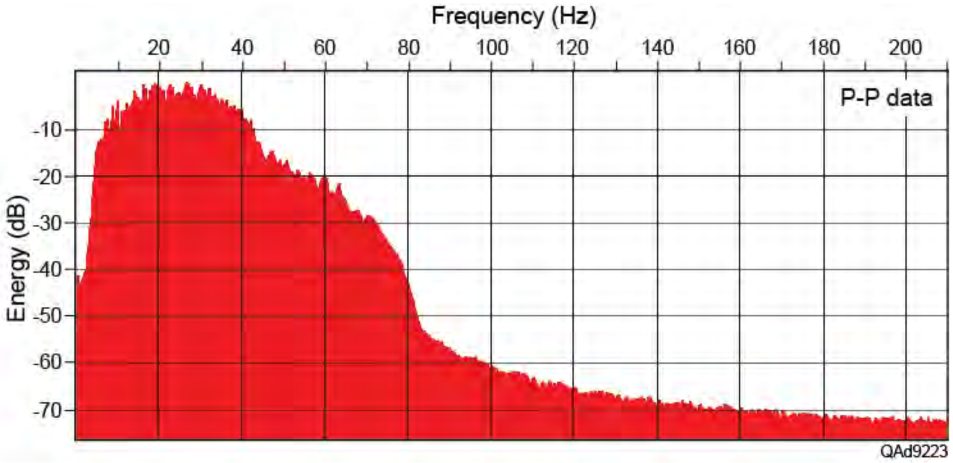

Figure 9.2. Frequency spectrum of P-P data.

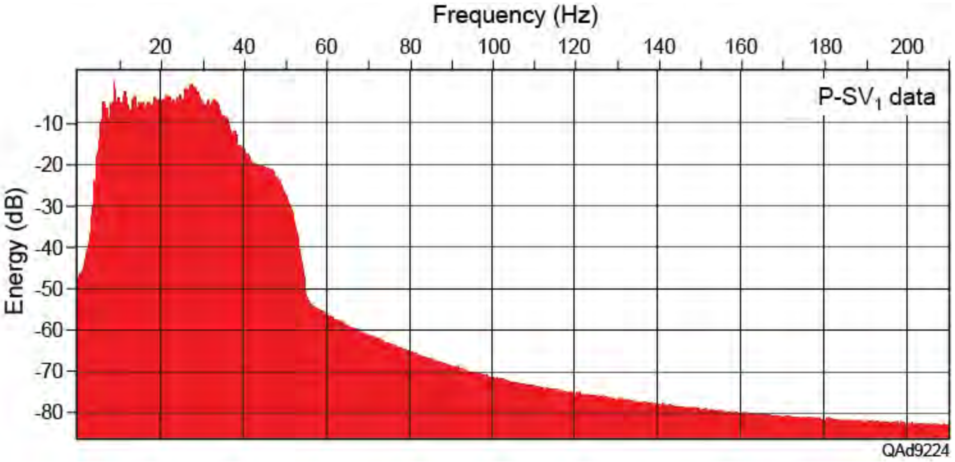

Figure 9.3. Frequency spectrum of P-SV_1 (fast-S) data.

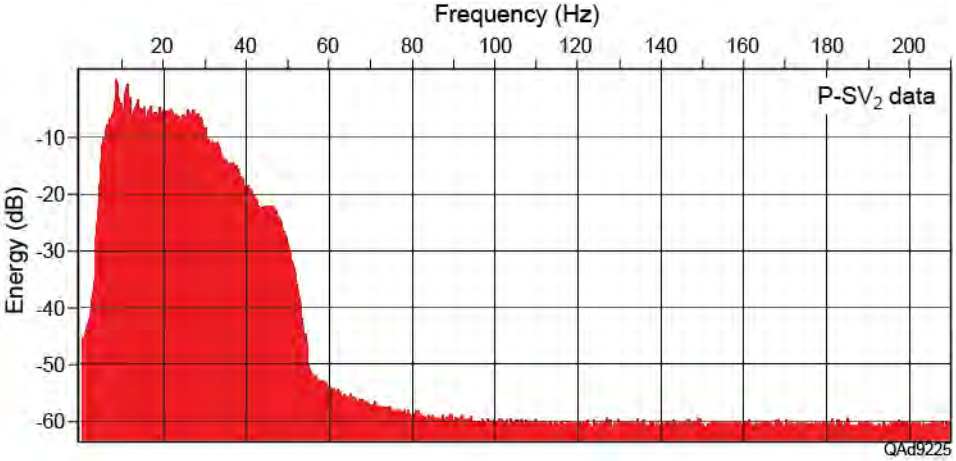

Figure 9.4. Frequency spectrum of P-SV_2 (slow-S) data.

Time to Depth Calibration

Before seismic interpretation is initiated, it is essential to determine which reflection events correlate with key geologic horizons. When interpreting multicomponent seismic data, time-to-depth calibrations must be established for P-wave data and for each S-wave mode involved in an interpretation. Data acquired in our central-image calibration well allowed two approaches to be implemented to establish time-to-depth correlations for the 3C3D Bradford County seismic data. The first approach was to utilize synthetic seismograms; the second approach was to use VSP time-based and depth-based images. We utilized the simpler, and more common, option of synthetic seismograms constructed from logs that use VSP data to establish accurate transformations from log depth to seismic-image time.

Depth Calibration Using Synthetic Seismograms

Velocity logs recorded in the central-image calibration well provided depth profiles of both P-wave velocity (V_P) and S-wave velocity (V_S). P-P and P-SV_1 synthetic seismograms were calculated by combining these velocity logs with the density log from the calibration well. These synthetic seismograms were our principal approach to defining depth-equivalent P and S reflection events as 3D P and S data volumes were interpreted. The correlations of seismic data and synthetic seismograms are shown on Figure 9.5 for P-P data and on Figure 9.6 for P-SV_1 data. The VSP-based calibration of log depth to seismic time defined depth-equivalent P and S horizons with high confidence.

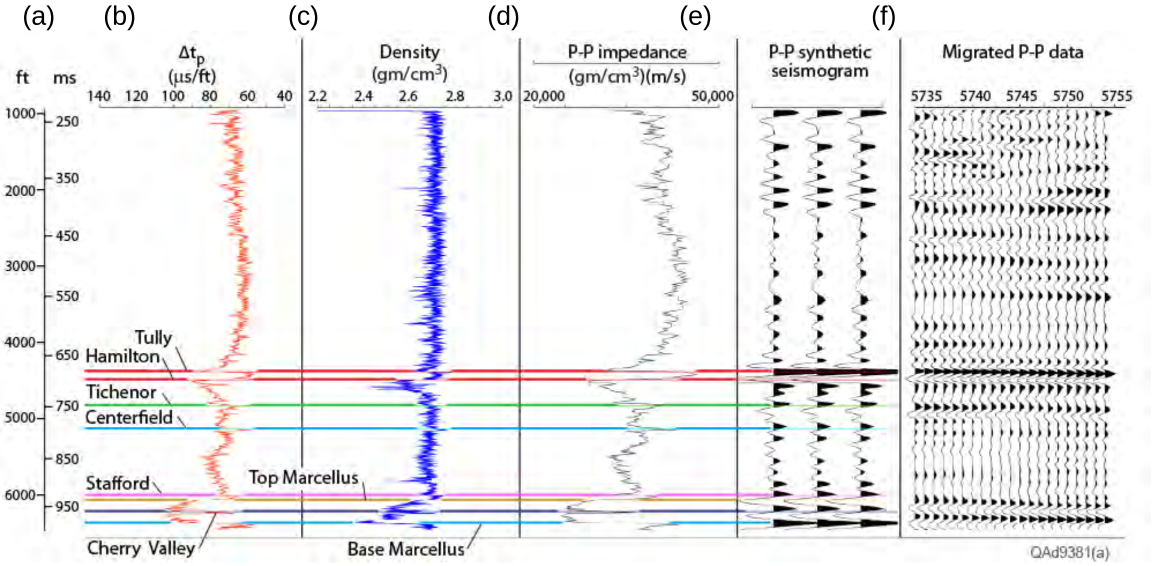

Figure 9.5. (a) Depth and P-P image time defined by VSP data. (b) P-wave sonic log. (c) Density log. (d) P-wave impedance. (e) P-P synthetic seismogram. (f) P-P seismic data local to the calibration well.

Additional confirmations of the accuracies of correlations between depth-based geology and time-based P and S images are shown on Figures 9.7 through 9.9 where the gamma-ray log recorded in the calibration well is displayed atop time-migrated P-P data (Fig. 9.7), P-SV_1 data (Fig. 9.8), and P-SV_2 data (Fig. 9.9). In each display, the depth-based gamma-ray curve is adjusted to the respective seismic image time using VSP time-depth information measured from VSP data acquired in the calibration well. Each significant change in gamma-ray magnitude correlates with a specific reflection event that allows depth-equivalent P and S horizons to be defined.

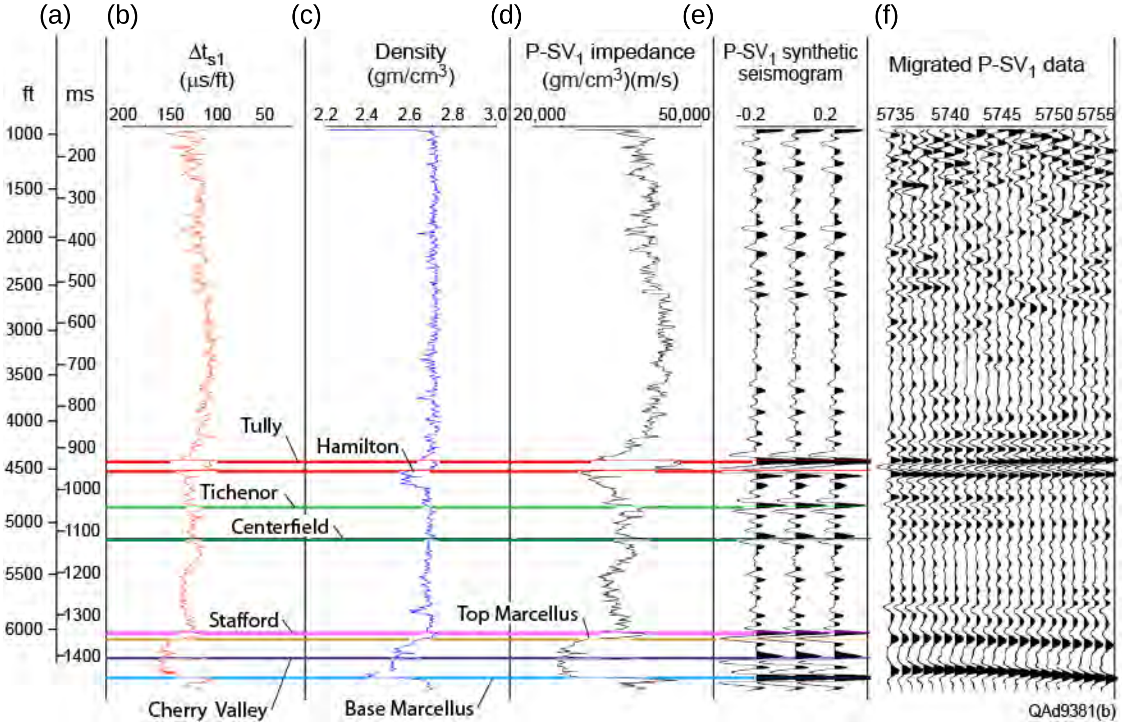

Figure 9.6. (a) Depth and P-SV_1 image time defined by VSP data. (b) S-wave sonic log. (c) Density log. (d) P-SV_1 impedance. (e) P-SV_1 synthetic seismogram. (f) P-SV_1 seismic data local to the calibration well.

The calibration well was drilled only to the Onondaga, immediately below the Marcellus, because the well was to be completed as a horizontal well in the Marcellus. Thus log-based and VSP-based calibration of P and S seismic data terminated at the base of the Onondaga. The position of the deeper Oriskany unit shown on Figures 9.7, 9.8, and 9.9 is speculative. The position of the Oriskany was determined by extrapolating log-based time-to-depth curves and assuming the Oriskany was 450 to 500 ft (137 to 152 m) below the Onondaga. As a result, the seismic reflection feature labeled “Oriskany” on each image is reasonable but may not be precise.

Defining seismic windows that span even deeper Cambrian sandstones involves considerable speculation, and no attempt was made to interpret data that could be assumed to be Cambrian-age rocks.

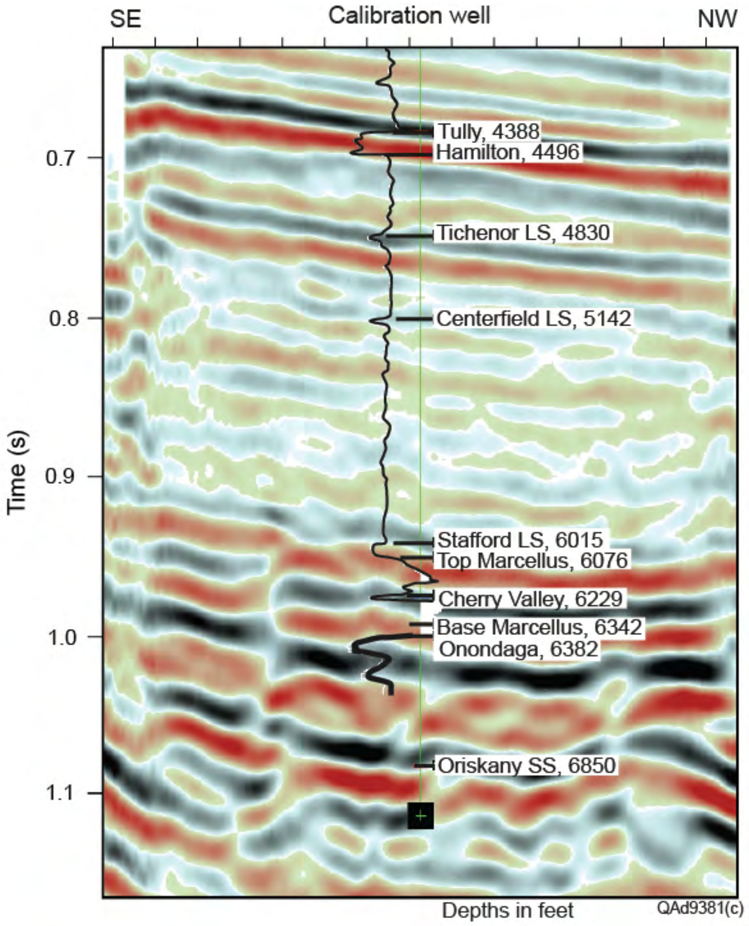

Figure 9.7. Time-migrated P-P data with gamma-ray log from the calibration well adjusted to VSP-defined P-P image time.

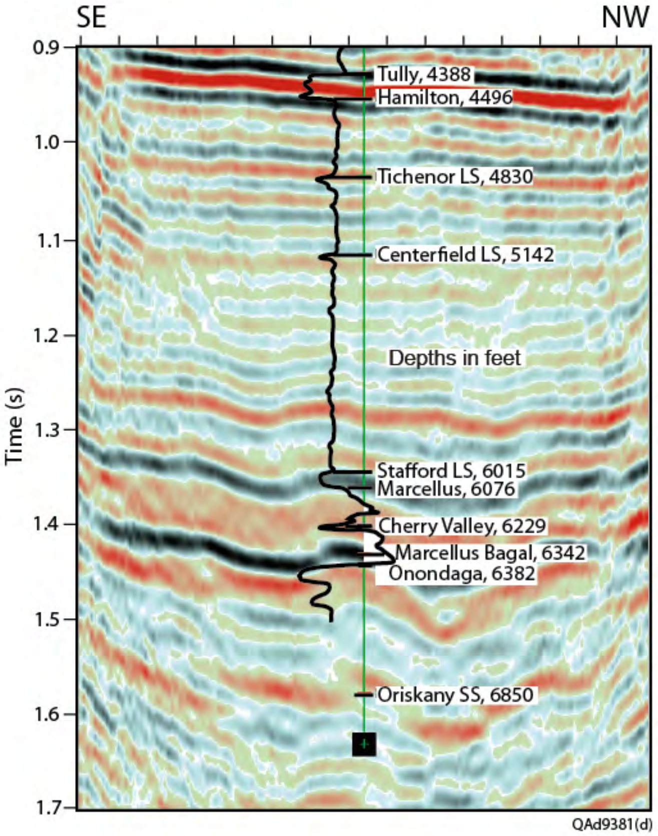

Figure 9.8. Time-migrated P-SV_1 data with gamma-ray log from the calibration well adjusted to VSP-defined P-SV_1 image time.

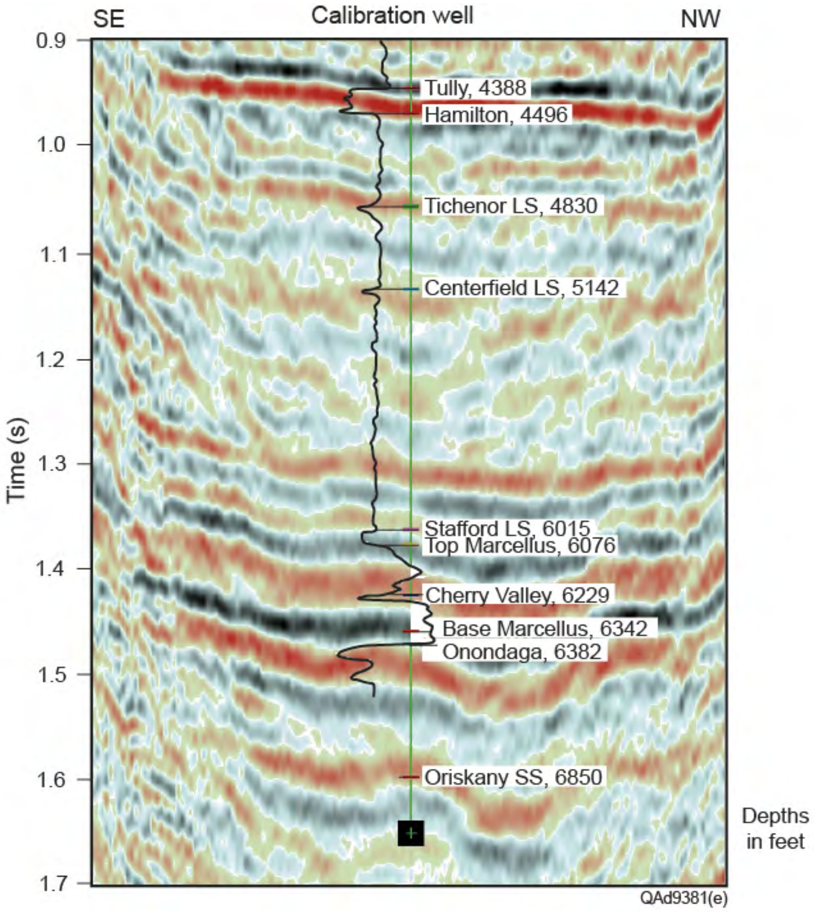

Figure 9.9. Time-migrated P-SV_2 data with gamma-ray log from the calibration well adjusted to VSP-defined P-SV_2 image time.

Depth-Converted P and S Data

A simple procedure was implemented to convert the Bradford County time-migrated P and S image volumes to depth (spatial wavelength) volumes. For each time-based volume, a single velocity function was calculated to convert image-time to depth across the entire 3D image space. Only one P-P time-to-depth conversion function was applied to the P-wave migrated-time volume. A spatially invariant V_P/V_S velocity ratio was then assumed and used to adjust this P-P time/depth relationship to create a P-SV time-to-depth conversion function. This single P-SV depth conversion was applied to both the P-SV_1 and P-SV_2 migrated-time data volumes.

Precise depth conversion requires several velocity functions, spaced at appropriate intervals across X-Y image space, be applied to a time-based seismic data volume. Because we used only a single time-to-depth conversion function across the entire image space of each data volume, our depth-converted data are only approximately correct. However, these approximate-depth volumes are sufficiently accurate to allow important observations to be made about the relative vertical resolution of P and S seismic data.

Vertical slices through the P-P and P-SV_1 depth-converted data volumes are displayed on Figure 9.10. The vertical distances between the interpreted Tully and Marcellus horizons are labeled on each profile. By counting the number of peaks and troughs across a depth interval, these depth-domain profiles show P-SV_1 shear data have considerably better resolution than do P-P data. On average, P-SV_1 data have a dominant spatial wavelength of 200 ft over the depth range of 4,000 to 9,000 ft (5,000 ft divided by 25 wavelength cycles). In contrast, P-P data have a longer dominant wavelength of 250 to 280 ft depending on where the number of reflection cycles is counted across this 5,000-ft span. These depth resolution comparisons provide considerable confidence in the value of S-wave data for evaluating smaller geologic features associated with CO_2 reservoir systems.

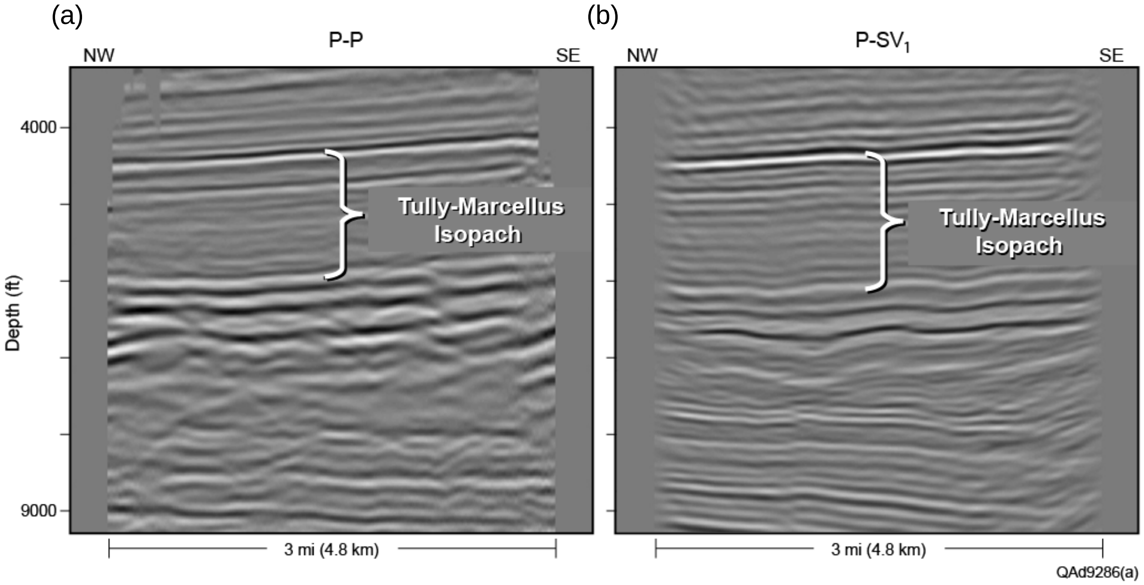

Figure 9.10. Equivalent profiles through depth-converted (a) P-P volume and (b) P-SV_1 volume.

Spectral analyses of depth-converted data volumes enforce these wiggle-trace comparisons of P-P and P-SV_1 spatial wavelengths. Spectral comparisons of depth-based P and S data are displayed as Figure 9.11. These spectra show depth-converted P-P data (Fig. 9.11a) are dominated by wavelengths of 100 to 800 ft; whereas depth-converted P-SV_1 data (Fig. 9.11b) are dominated by wavelengths of 40 to 400 ft.

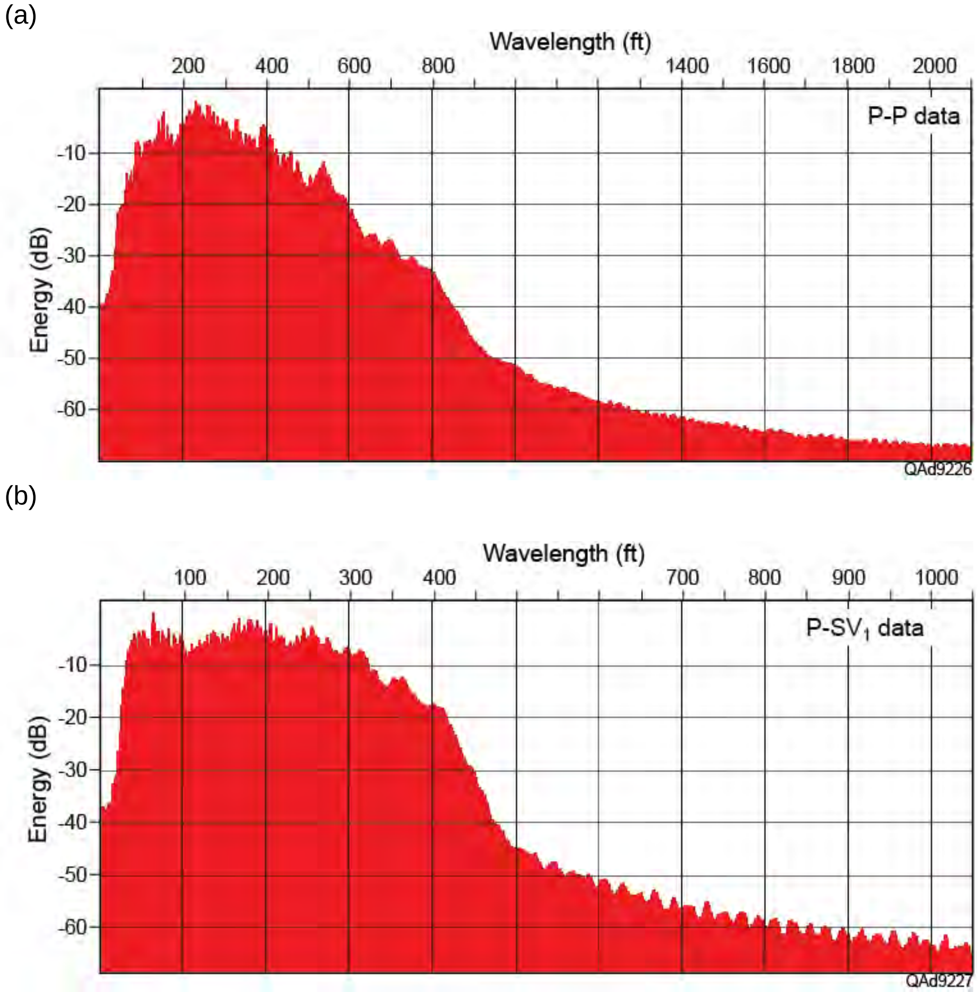

Figure 9.11. Spatial-wavelength spectrum of depth-converted (a) P-P data and (b) P-SV$_1$ data.

Interpreting Depth-Equivalent P and S Horizons

The greatest problem confronting interpreters of P and S seismic data is to determine which S reflection is depth equivalent to a targeted P reflection event. The importance of accurate depth correlation between P-wave and S-wave data cannot be overemphasized. Until depth-equivalent P and S horizons are established, P and S seismic attributes cannot be compared across targeted stratigraphic depth intervals to determine attribute combinations that optimize the detection of specific rock and fluid properties.

A common approach to determining depth-equivalent events in 3D P and S data volumes is to work in section views, using procedures similar to those followed when interpreting 2D seismic profiles. This vertical-section approach to interpreting 3D P and S seismic data is satisfactory if adequate precautions are taken to ensure miscorrelations of key stratal surfaces do not occur. We think our time-depth registration of P-P and P-SV data is accurate because our definitions of depth-equivalent P and S horizons were established using P and S travel times observed in VSP data acquired in the central-image calibration well (Fig. 4.1 of Chapter 4). P-P and P-SV travel times to key depth-based stratigraphic horizons penetrated by this VSP calibration well were marked at the well X-Y coordinates in each time-based data volume to define the P-P and P-SV reflection event associated with that horizon. Each horizon was then extended from this well-control point across all of P-P and P-SV image space.

Away from the VSP calibration well, inline and crossline sections of P-P and P-SV data were compared to define characteristic features that should be expected on both data sets and which would increase confidence that depth-equivalent horizons were being followed as interpretation proceeded farther from the VSP calibration well. Geometric features such as stratigraphic terminations and lap-outs, if observed in both P and S image space, were important for deciding how to constrain the interpretation to depth-equivalent P and S horizons. However, as will be emphasized later, P-SV seismic sequences often differ from P-P seismic sequences so this interpretation guideline must be used with discretion.

An attempt was made to use fault surfaces for P-to-S depth correlation. If faults cut across reflections at significant angles away from vertical, it is often possible to match depth-equivalent breaks in P and S reflections. In such cases, interpreted P and S horizons can often be verified as being depth equivalent by comparing fault maps of these interpreted horizons. In contrast, if faults are near-vertical, it is difficult to decide how much vertical shift should be applied to an S profile to make a P-SV horizon depth-equivalent to a targeted P horizon. For near-vertical faults, fault maps of P and P-SV horizons show minor changes in X-Y coordinate location over large vertical intervals of P and S data windows. This focus on fault interpretation is a valuable approach to depth registration of P and S images, but it was not productive for our study area because no significant faults were present inside our seismic image space.

Devonian Sandstone CO_2 Reservoir Interval

Previous studies indicate transgressive Devonian sandstones are often found in the stratigraphic interval immediately below the Tully Limestone (Bruner and Smosna, 1994; Diecchio, 1985; Kostelnik and Carter, 2009a, 2009b; Milici and Swezey, 2006). Because porous, brine-filled sandstones are good candidates for CO_2 storage reservoirs, we did a detailed interpretation of the interval between the interpreted tops of the Tully Limestone and Tichenor Limestone to determine how P and S seismic data react to these particular sandstone targets.

Time windows chosen for spectral analysis of the Tully-to-Tichenor interval for P-P, P-SV_1, and P-SV_2 data are shown on Figures 9.12a, b, and c, respectively. The Tully unit is characterized by a strong reflection peak (black) immediately followed by a high-amplitude wavelet trough (red) in all three data volumes and is easily mapped across the image area. In contrast, the Tichenor Limestone appears as a modest-amplitude reflection in the P-P data volume, and has an even lower amplitude response in both the P-SV$_1$ data (Fig. 9.12b) and the P-SV$_2$ volumes (Fig. 9.12c). Despite these weaker expressions of the Tichenor unit, depth-equivalent Tichenor horizons were interpreted across the image space in all three data volumes. Visual inspection of these side-by-side data windows leads to an important research finding – *P-SV data provide better resolution of stratigraphy across our study area than do P-P data*. An important implication is that this same advantage of S-wave data may occur across many shale-gas prospects.

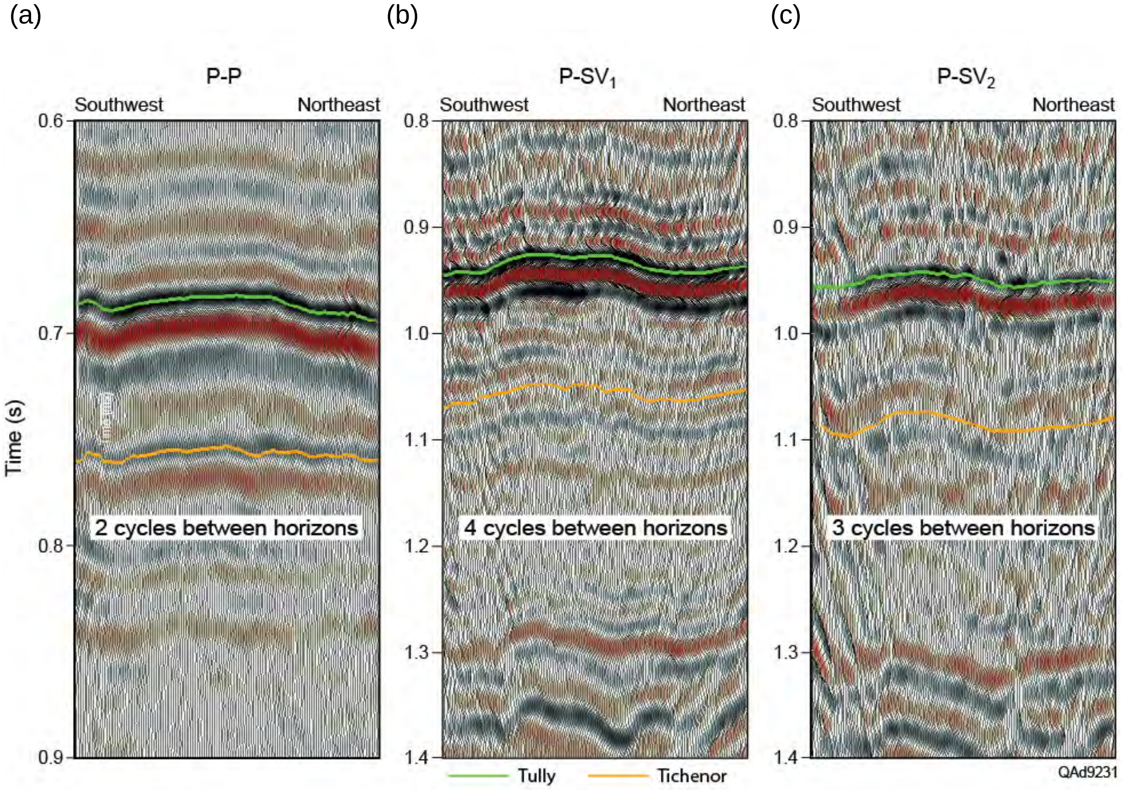

Figure 9.12. Profiles comparing Tully (green horizon) to Tichenor (orange horizon) intervals in (a) P-P, (b) P-SV$_1$, and (c) P-SV$_2$ image space.

P-P data show a marked decrease in the number of reflection cycles across the transgressive sandstone interval relative to the number of reflection cycles appearing in P-SV$_1$ and P-SV$_2$ images, another example of the improved spatial resolution of P-SV data compared to P-P data. P-SV$_1$ data provide the greatest stratigraphic detail after the three wave-mode volumes are time warped to equivalent time scales. Frequency analyses of the data after time warping are displayed on Figures 9.13a through 9.13c. These spectra show P-P data have good frequency content up to 50 Hz and then exhibit a sustained decline in

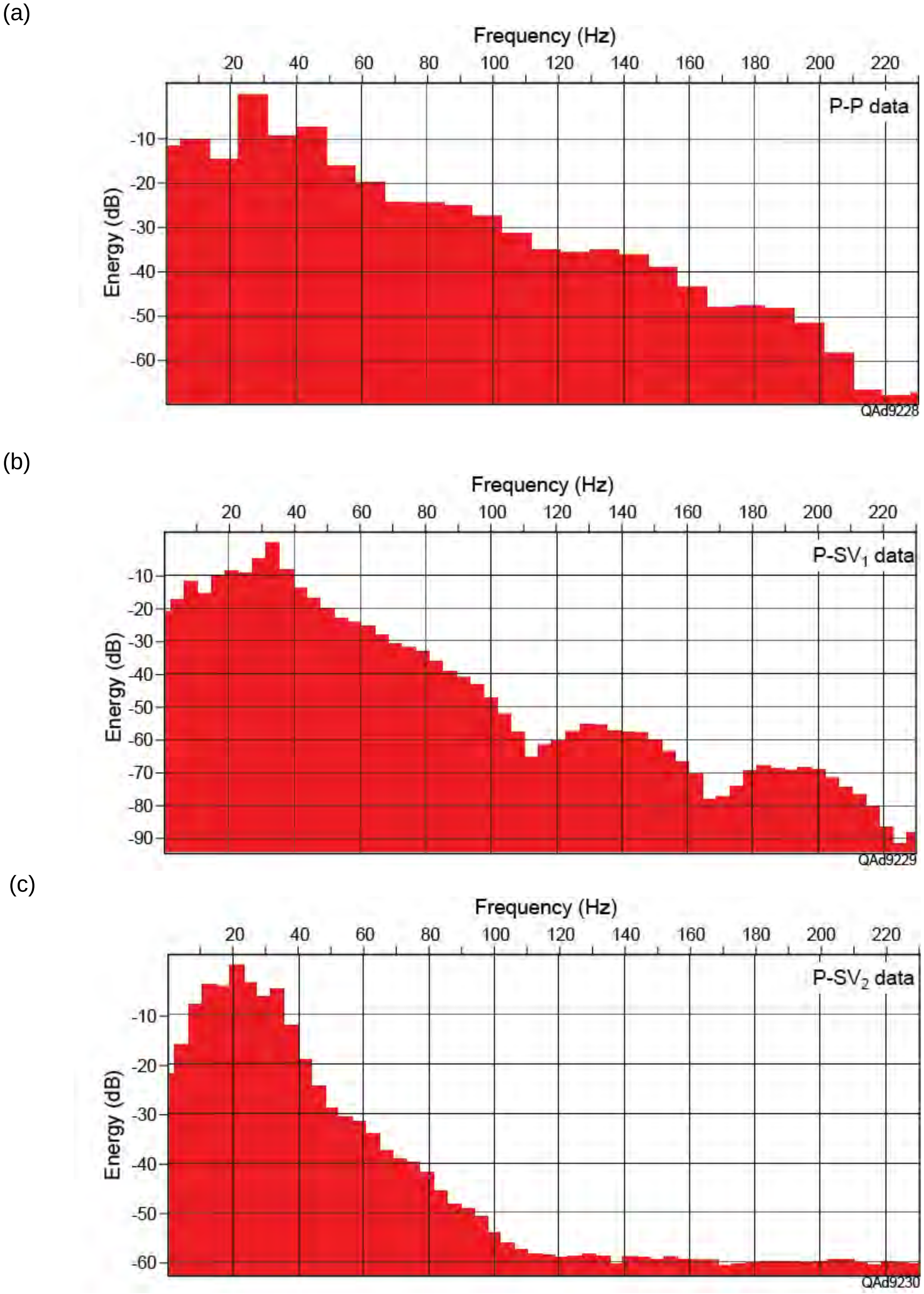

Figure 9.13. Frequency spectra across the Tully-to-Tichenor interval for (a) P-P data, (b) P-SV_1 data, and (c) P-SV_2 data.

energy content of approximately 5 dB for each 20-Hz increase in frequency. P-SV_1 data have good energy content up to 40 Hz and then lose energy content almost twice as fast as do P-P data (~5 db per 10-Hz interval). P-SV_2 data have good energy content up to 35 Hz and then decay in energy even faster than do P-SV_1 data.

Amplitude Attributes across Devonian CO_2 Reservoir Interval

Many attributes can be calculated from seismic data. In our elastic wavefield seismic stratigraphy interpretation across this prospect, we gave heavy weight to amplitude-based P and S attributes, with these attributes determined using depth-equivalent stratal surfaces. Amplitude horizon slices were extracted from P and S data volumes at 2-ms intervals. For the geology imaged by these Bradford County 3C3D seismic data, we found amplitude attributes failed to identify unique reflection patterns in P-P and P-S data that could be used for depth-correlation purposes, but they were valuable for evaluating subsurface structural trends and particularly valuable for detecting erosion-like features within the Tully-to-Tichenor interval.

Root-mean-square (rms) P-P reflection amplitudes across the Tully-to-Tichenor interval are shown in map view on Figure 9.14. Several small black areas occur across the color map. These black areas are no-lease properties where subsurface geological information cannot be shown, thus seismic information across these properties are deleted from the data volumes. Similar blank-out areas will be shown on numerous maps that follow. Basically, P-P reflection amplitudes show only minor variations across the image area of approximately 9 mi^2 (23 km^2). Amplitude variations appearing near the edges of image space are not given significant geological importance because of the edge-related migration artifacts discussed in association with Figures 9.1a through 9.1c.

An important research finding was that P-SV_1 data imaged a southwest to northeast trending feature within the Tully-to-Tichenor interval (Fig. 9.15) that appears similar to an eroded channel. However, the feature has no meandering character, and its linear geometry suggests there may be a genetic relationship to structure. This feature was not revealed by either P-P data (Fig. 9.14) or P-SV_2 data (Fig. 9.16). These amplitude-attribute comparisons are an example of the increased geological information provided by elastic wavefield seismic stratigraphy (joint interpretation of P and S data) compared to the amount of information provided by traditional seismic stratigraphy (which uses only single-component P-wave data). The erosion-like feature has a significant size, being approximately 0.25 mi (0.4 km) wide and extending across the full 3 mi (4.8 km) dimension of the image space.

The detection of this depositional feature has significant implications in evaluating CO_2 storage reservoirs. There is not sufficient subsurface information to define the type of lithological fill within this particular geobody. Thus the feature can be a lateral barrier to fluid flow, or it could enhance fluid flow, depending on the nature of its internal lithology, porosity, and permeability. In either case, it is essential that anyone who considers Devonian sandstones within this stratigraphic interval as possible CO_2 storage reservoirs be aware of this reservoir heterogeneity. The key point of this interpretation is that multicomponent seismic data provide a picture of reservoir compartmentalization that is not available if CO_2 sequestration projects utilize only single-component P-wave seismic data.

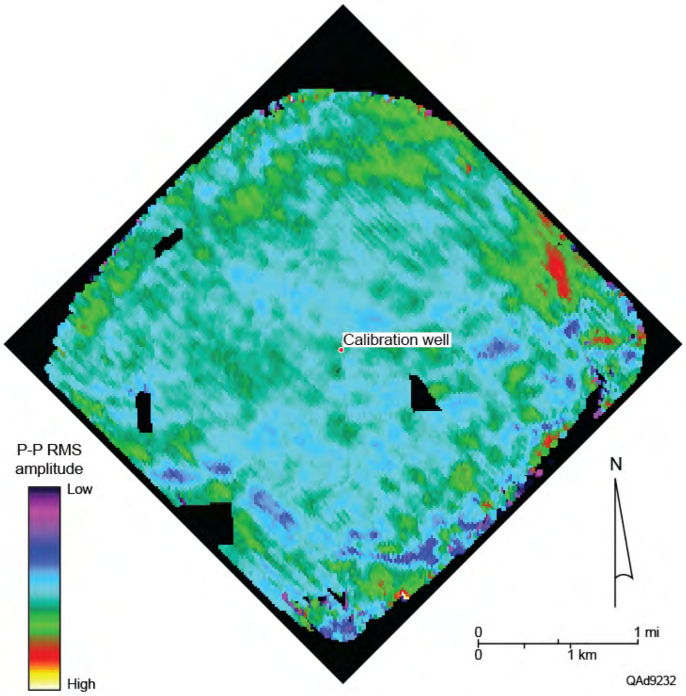

Figure 9.14. P-P rms amplitudes across the Tully-to-Tichenor interval. The black areas within the image space are no-lease properties where subsurface seismic properties cannot be shown. Amplitude anomalies near the edges of image space are not assigned significant importance because of migration artifacts that occur along the outer edges of 3D image space.

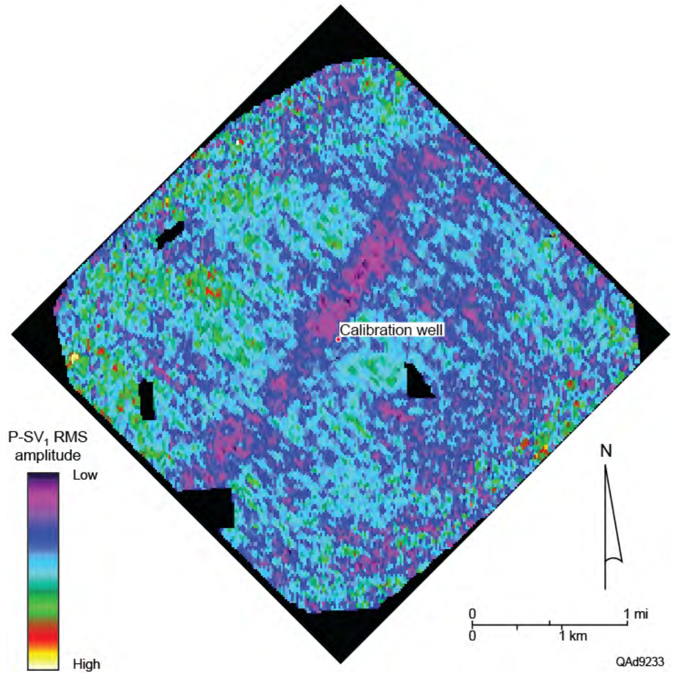

Figure 9.15. P-SV$_1$ rms amplitudes across the Tully-to-Tichenor interval showing an interpreted incised channel in purple (low-magnitude amplitudes). The black areas within the image space are no-lease properties where subsurface seismic properties cannot be shown. The southwest-to-northeast trending low-amplitude feature is given major interpretation importance because the amplitude effects extend across the central image space where migration artifacts have minimal effects on amplitude behavior.

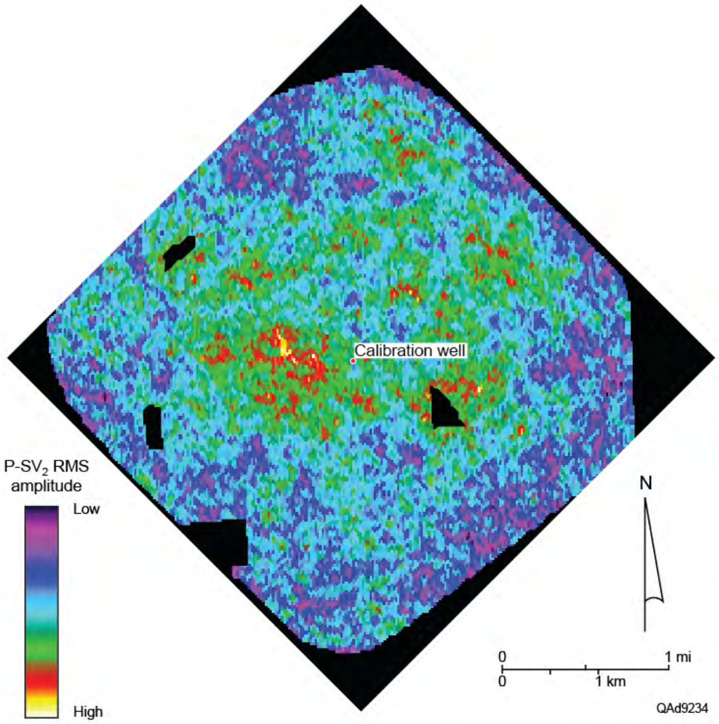

Figure 9.16. P-SV$_2$ rms amplitudes across Tully-to-Tichenor interval. The incised channel seen by the fast-S mode (Fig. 9.10) is not evident in this slow-S image. The black areas within the image space are no-lease properties where subsurface seismic properties cannot be shown.

P-SV$_1$ and P-P profiles across this stratigraphic feature are shown on Figure 9.17. A mounding geometry is associated with the feature on both profiles, but reflector dimming occurs within and below this mounding only on the P-SV$_1$ image. This reflector dimming creates the reduced rms amplitude values that appear as the purple low-amplitude corridor extending across the map on Figure 9.15.

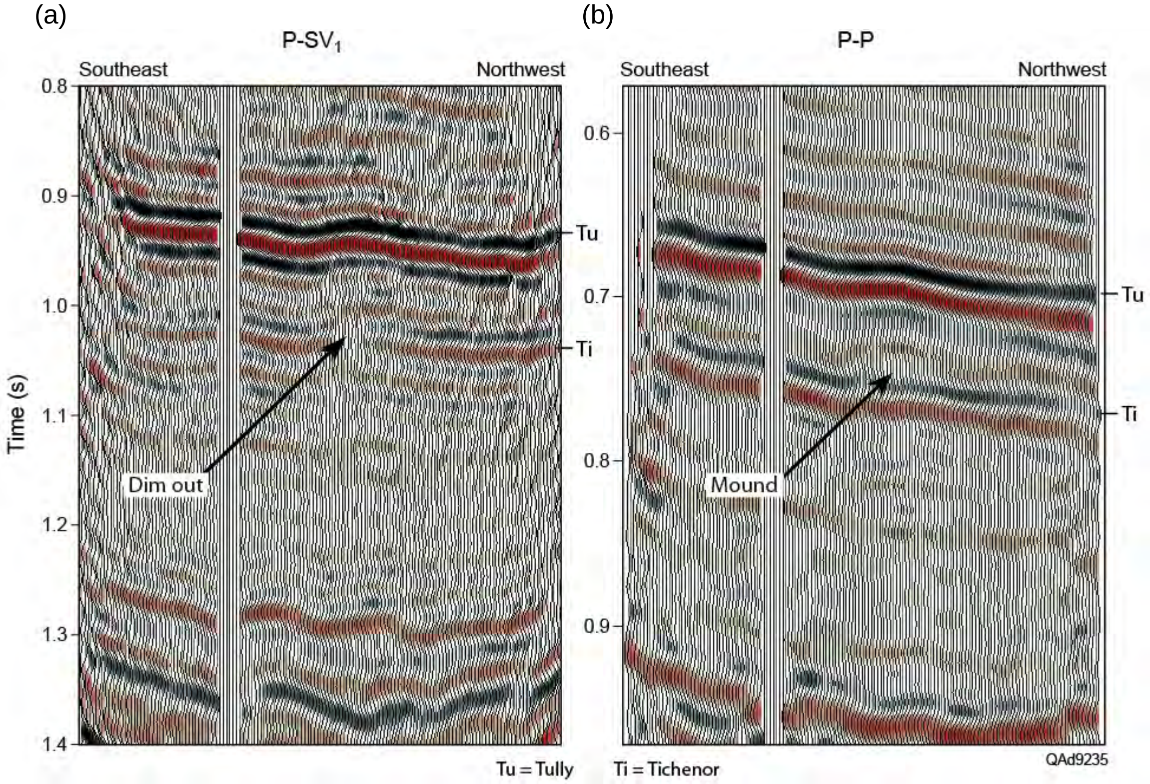

Figure 9.17. (a) P-SV$_1$ profile showing mounding (red trough) immediately above dim-out of peak (black) and trough (red). (b) P-P image along same profile shows mounding but no reflection dim-out.

Tully Structure

Because the sandstone-prone interval immediately below the Tully can contain units that could be CO_2 storage reservoirs, it was essential to verify if faults breached the Tully to create conduits that would allow injected CO_2 to migrate upward into shallow strata. A structural interpretation of the Tully was done to determine if evidence of breaching faults was present. No faults were found that disrupted the Tully Limestone in any of the three seismic data volumes. This time-based interpretation showed that across the 9.3 mi^2 (23.8 km^2) area of seismic image space, the Tully Limestone is structurally high in the southeast and dips northwest in a gentle, gradual manner. Structural maps of the Tully horizon interpreted from P-P, P-SV$_1$, and P-SV$_2$ data volumes are shown on

Figures 9.18, 9.19, and 9.20, respectively. A gentle structural ridge appears on each time-based structural map. The ridge-like feature is much smaller in P-P image space and has a different azimuth orientation than it does in either P-SV image space. An arrow is placed on each map to indicate the trend of this structural feature.

It must be emphasized that these maps were constructed from time-based seismic data, and thus differences between P and S time-based structure are expected. Time-based P and S structural maps will have similar geometry only if V_P and V_S velocities vary in synchronization across X-Y seismic image space. Because azimuth-dependent rock properties cause V_S velocity to vary with azimuth more than does V_P velocity, P and S velocities rarely vary in synchronization at all seismic image coordinates. In a rigorous seismic interpretation, P and S data should be converted to depth, using reliable seismic-based P and S velocities, so depth-based, not time-based, structure maps can be generated. We did not construct depth-based structural maps because there was no need to do so to achieve the basic research objectives of this study, or to determine if breaching faults eliminate the Tully Limestone as an effective seal for Devonian CO_2 storage reservoirs.

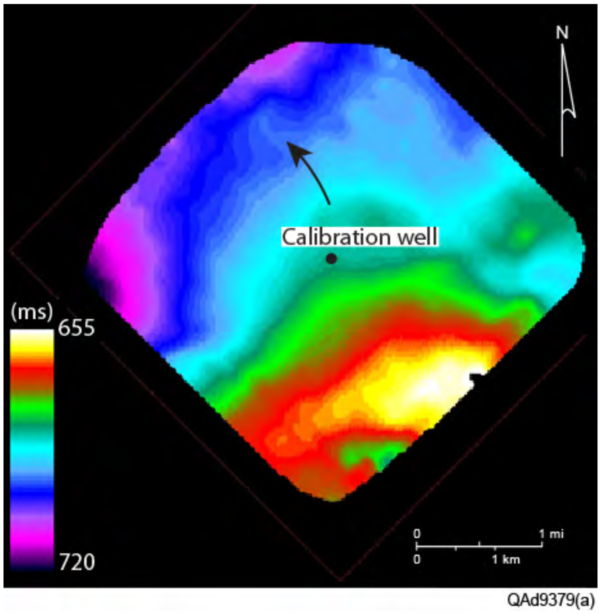

Figure 9.18. P-P time structure map of the Tully Limestone. The arrow emphasizes a modest ridge-like structure. The structure across this 24 km^2 area may look different when converted to depth.

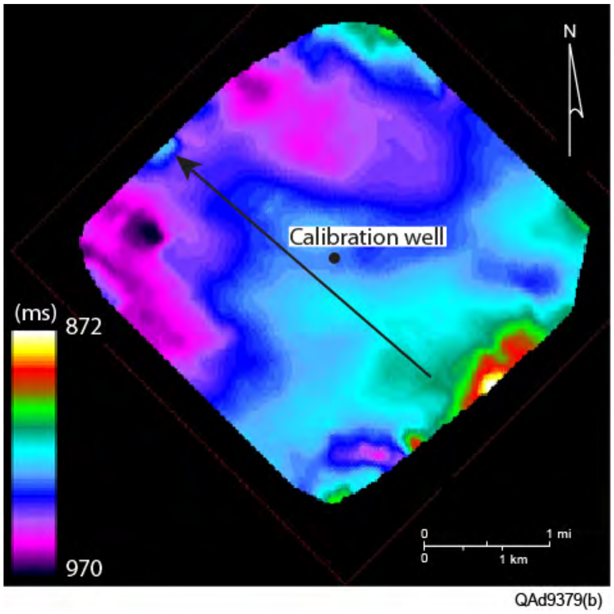

Figure 9.19. P-SV_1 time structure map of the Tully Limestone. The arrow emphasizes a structural ridge, which may have a different size and shape in a depth-based map.

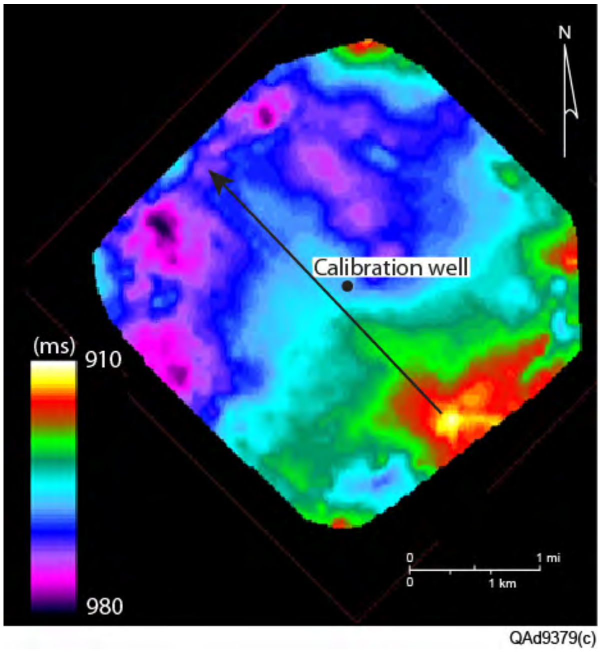

Figure 9.20. P-SV_2 time structure map of the Tully Limestone. The arrow emphasizes a structural ridge, which may have an altered shape in a depth-based map.

Tully to Tichenor Stratal Surfaces

A fundamental premise of seismic stratigraphy is that a seismic reflection event follows a **chronographic surface**, which is a depositional surface where geologic time does not change. Stated another way, a seismic reflection event defines a bedding surface, or **stratal surface**, which is a surface where geologic time is constant. All seismic stratigraphy studies are based on the principle that geologic time is constant along a horizon that follows a fixed seismic reflection phase. A corollary to this principle is that a seismic horizon that is conformable to a seismic reflection is also a surface along which geologic time is constant.

If the top and base of an interval is bounded by reflection events that are conformable to each other, it is rather simple to interpolate an arbitrary number of conformable horizons that span the interval between these two reflections. Seismic attributes calculated on each successive internal conformable surface describe stratigraphy within the interval at fixed increments of geologic time. A different strategy, developed by Zeng (2001, 2006), must be implemented if reflection events at the top and base of an interval are not conformable. In this approach, an interval having a time-varying thickness is divided into an arbitrary number of uniformly spaced sub-intervals as shown on Figure 9.21.

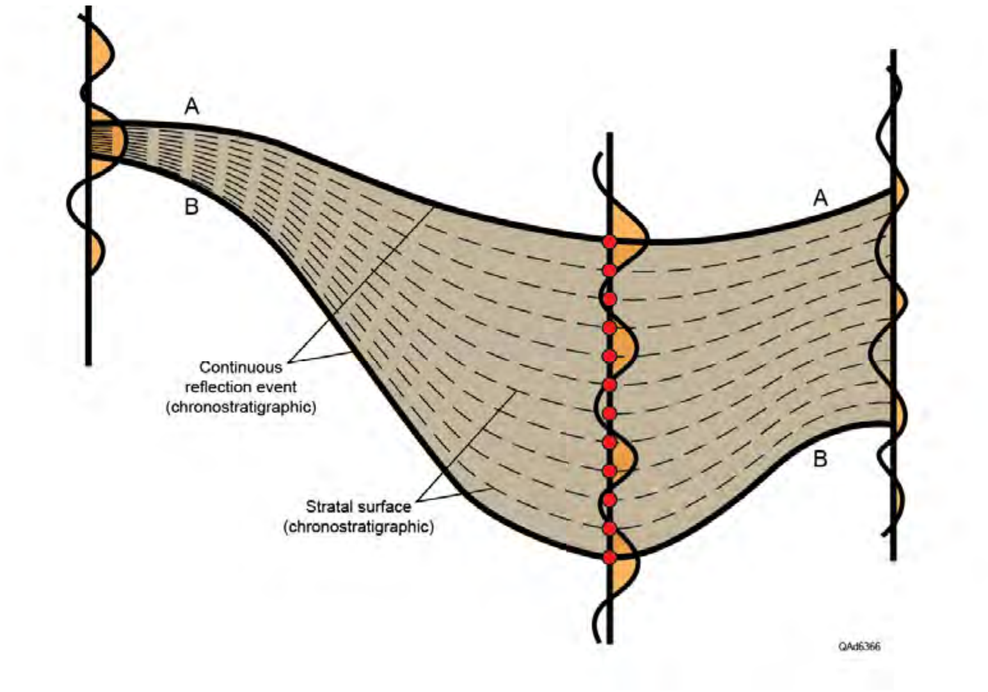

Figure 9.21. Stratal slices along a seismic profile where there are significant variations in the interval thickness between two chronostratigraphic reflections. AA and BB are continuous reflection events (chronostratigraphic surfaces).

At any two coordinates along this profile, the vertical spacing between adjacent interpolated surfaces differs in seismic time but is constant in geologic time. The result is a series of surfaces that define depositional features within the interval at fixed increments of geologic time. The creation of the interpolated surfaces between Reflections AA and BB on Figure 9.21 is called **stratal slicing**. In this example, the interval between Reflection AA and Reflection BB is divided into 11 sub-intervals. If the time interval at some point on the profile is 11 ms, each sub-interval is 1 ms thick at that image coordinate. If the interval from A to B is 110 ms thick at a second point on the profile, each subinterval is 10 ms thick at this second image coordinate. Even though the magnitude of seismic image time spanned by each sub-interval differs at these two points, the geologic time across each subinterval is MY/11 at both points, where MY is the difference in geologic times represented by Reflection AA and Reflection BB. Because of the interpolation technique used to create these sub-intervals, the creation of stratal slices is also called **proportional slicing**.

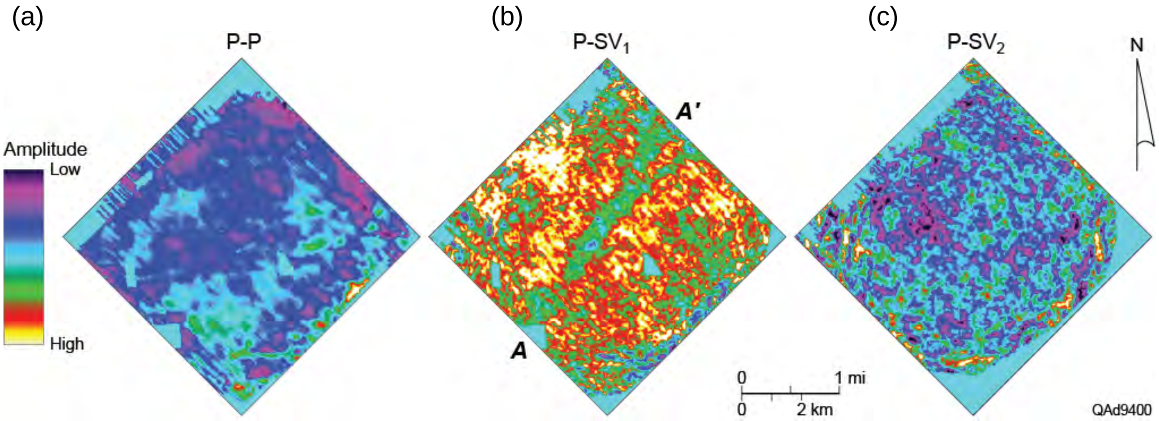

Figure 9.22. Stratal slice results showing depth-equivalent surfaces within the Tully-to-Tichenor interval. (a) P-P stratal slice. (b) P-SV$_1$ stratal slice. The channel-like image labeled A-A′ is a key reservoir compartmentalization feature not revealed in the other data volumes. (c) P-SV$_2$ stratal slice. The attributes displayed on each surface are reflection amplitude values scaled as shown by the color bar.

This stratal time slicing technique was applied to the Tully-to-Tichenor interval to expand knowledge of the internal architecture of rock units that might be used to store injected CO_2. All three data volumes (P-P, P-SV$_1$, and P-SV$_2$) were analyzed. Interpreted Tully and Tichenor horizons defined on Figures 9.7 to 9.9 were used as bounding seismic reflections to guide the stratal slicing. Example stratal slices from the volumes are exhibited on Figure 9.22. The heterogeneous feature internal to this interval revealed by amplitude analysis of P-SV$_1$ data (Fig. 9.15) is more prominent in this stratal-slice analysis (Fig. 9.22b). For example, stratal slicing shows a clear bifurcation of the feature at the northeast edge of the image space. This stratal-slice interpretation adds credence to the assumption that the channel-like feature contributes to reservoir compartmentalization. The interpretation also verifies the following important concept of elastic wavefield seismic stratigraphy—*one or more key depositional features not seen by one wave mode may be seen by another wave mode*.

In this instance, S-wave data see a feature that P-wave data do not see. In other instances, P-wave data will see features that S-wave data do not see.

Reflection Cycles across Devonian CO_2 Reservoir Interval

A second example demonstrates an instance where P-P data are more useful than P-SV_1 data for understanding the stratigraphy of the Tully-to-Tichenor interval. In this case, the number of reflection troughs within the Tully-to-Tichenor interval was counted in P-P and P-SV_1 data sets. Although P-P data had fewer reflection troughs across the interval than did P-SV_1 data, the number of P-P troughs changed in some portions of the image space (Fig. 9.23), which indicates alterations in bedding thickness or bedding geometry. In contrast, the number of P-SV_1 reflection troughs stayed constant across the image space (Fig. 9.24). P-P and P-SV_1 profiles following trends AB labeled on Figures 9.23 and 9.24 are exhibited on Figure 9.25 to illustrate the behavior of P-P and P-SV_1 reflectivity within the Tully-to-Tichenor interval.

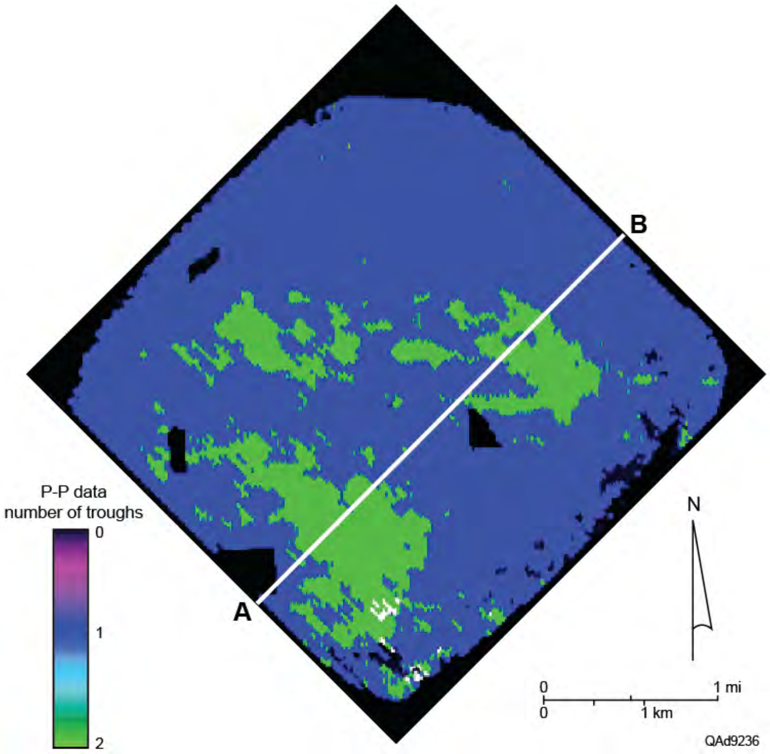

Figure 9.23. Number of P-P reflection troughs across the Tully-to-Tichenor interval. In some areas, the number of troughs increases from 1 to 2.

Although it has been emphasized that the spatial resolution of P-P data across our study area is less than the spatial resolution of P-SV_1 data, image coordinates where changes in the number of P-P reflection troughs occur must be considered as locations where there is a change in the internal compartmentalization of the Tully-to-Tichenor interval even if P-SV_1 data show little variation at the same coordinates. Thus maps of numerical counts of

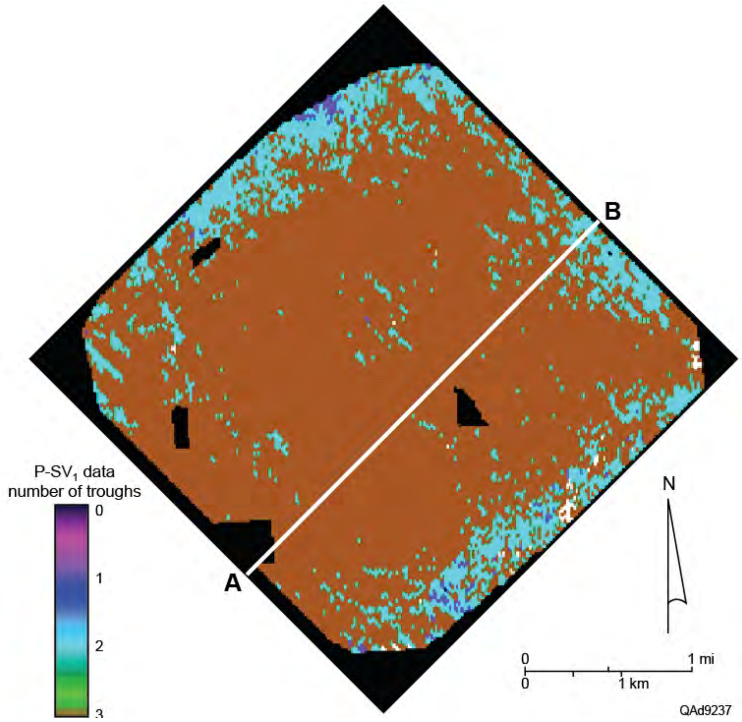

Figure 9.24. Number of P-SV_1 reflection troughs across the Tully-to-Tichenor interval. The number of troughs stays constant at 3 across the valid portion of image space. The reduced number of troughs near the edges of image space is ignored because of the migration artifacts that occur in these regions.

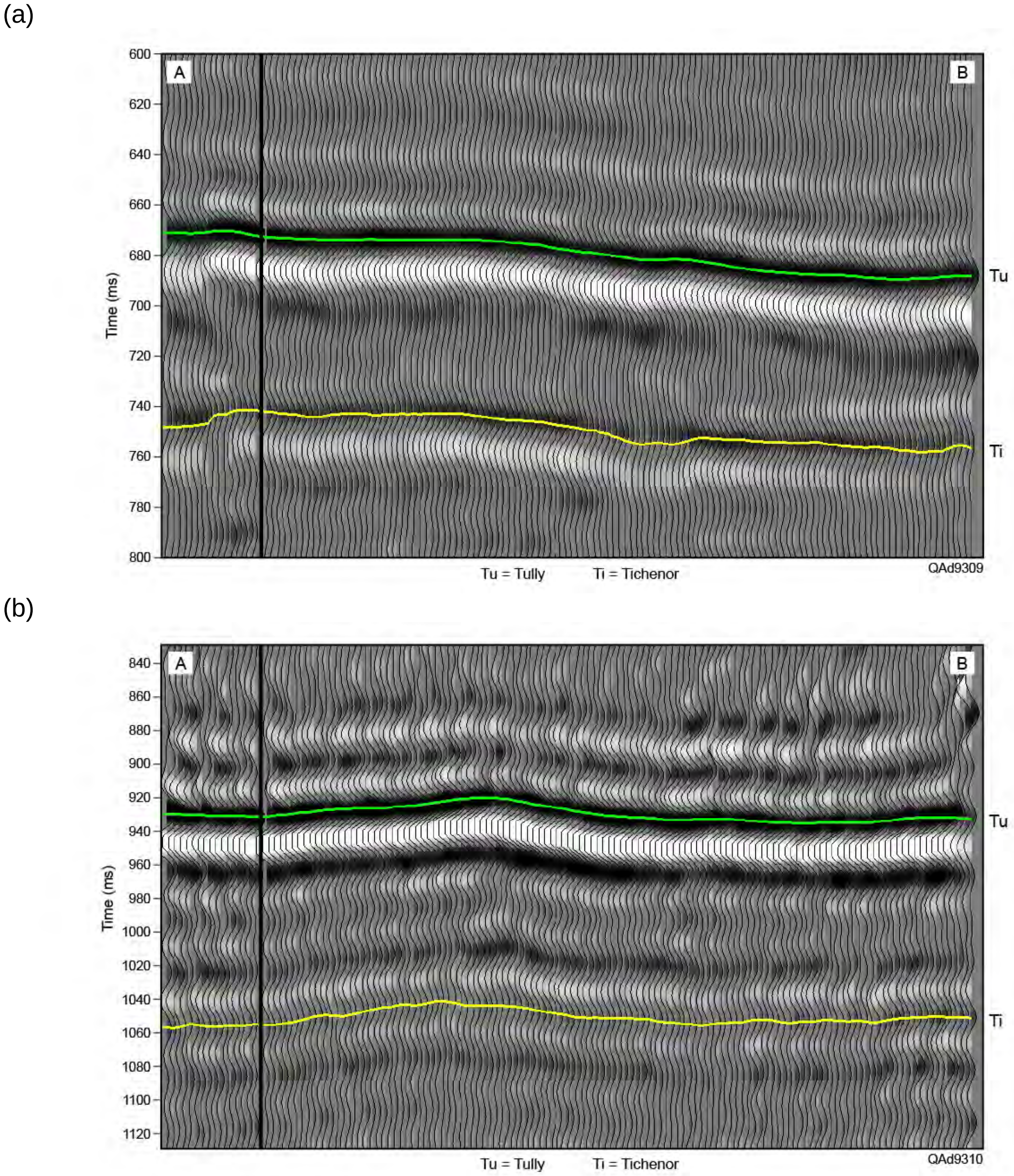

Figure 9.25. (a) P-P profile AB. (b) P-SV_1 profile AB.

reflection troughs (or peaks) across a stratigraphic interval are valuable in elastic wavefield seismic stratigraphy applications. It should also be emphasized that a constant number of reflection peaks and troughs across a target interval does not necessarily imply the internal layering of that interval is unchanging. Inspection of the P-P and P-SV_1 profiles on Figure 9.25 shows the amplitudes of peaks and troughs between the Tully and Tichenor horizons vary significantly at different image coordinates as reflection events are followed across the profile. Such amplitude variations are often caused by alterations in thick stacks of interfingering thin-bed layers. All seismic attributes must be combined to reach optimal stratigraphic interpretation, particularly when stacked thin beds are involved.

Marcellus Shale Interval

Because some scientists consider gas-shale units to be potential CO_2 sequestration reservoirs, we interpreted P-P, P-SV_1, and P-SV_2 data windows that spanned the Marcellus Shale to ensure all possible CO_2 storage targets imaged by the Bradford County multicomponent seismic data were analyzed. The Marcellus Shale is divided into two distinct units—the Upper Marcellus and the Lower Marcellus. The boundary between these two units is the Cherry Valley Limestone. To characterize the Marcellus interval, it was essential to accurately interpret depth-equivalent P-P and P-SV horizons that correlate with the Top of Marcellus, Cherry Valley Limestone, and Base of Marcellus. Examples of these depth-equivalent surfaces are illustrated on Figure 9.26.

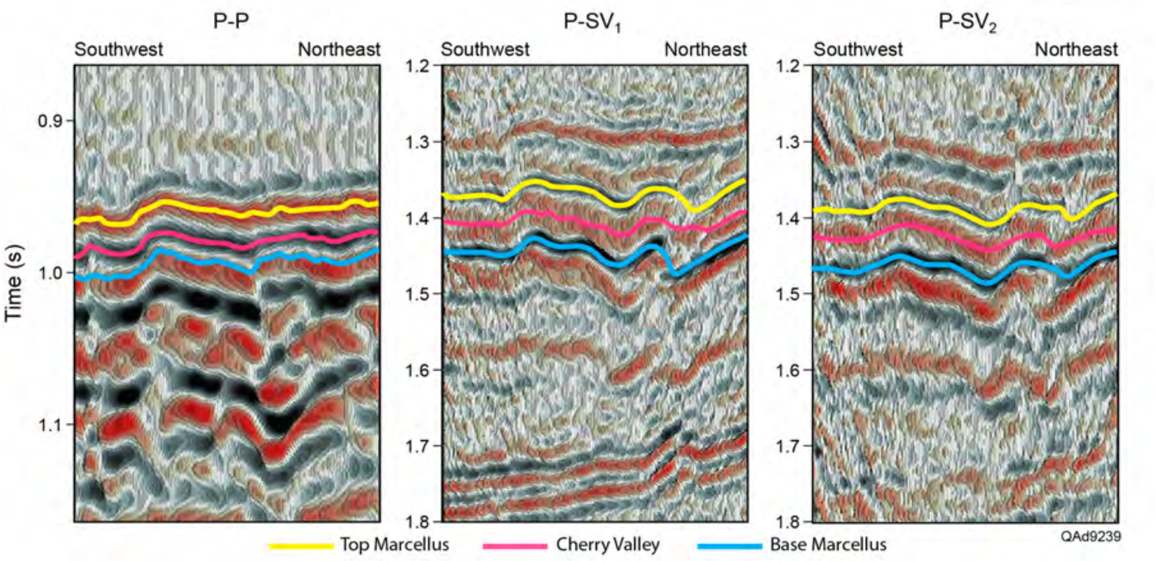

Figure 9.26. Profiles showing P-P, P-SV_1, and P-SV_2 images of the Marcellus interval.

Visual inspection of the profiles displayed on Figure 9.26 implies both P-SV modes have a better vertical resolution across the Marcellus interval than do P-P data. The improvement in spatial resolution provided by S-wave modes is another important research finding that encourages the use of multicomponent seismic technology in CO_2 sequestration studies rather than relying on only single-component P-P seismic data.

The profiles exhibited on Figure 9.26 show the top and base of the Marcellus interval are associated with bold reflection events in all three data volumes. However, mapping the Cherry Valley horizon posed problems. The Cherry Valley Limestone was not imaged as an individual reflection trough or peak in any seismic data volume, making any attempt to create a Cherry Valley horizon arbitrary. Automatic picking algorithms failed to track any consistent seismic feature related to the Cherry Valley Limestone, making it necessary to find a seismic attribute that might help discriminate the Cherry Valley unit from its surrounding Marcellus Shale units. After a series of trials, it was determined instantaneous phase was the best attribute to use to define the Upper Marcellus-Cherry Valley interface. An example profile from the P-SV$_2$ data volume is shown on Figures 9.27 and 9.28 to illustrate the advantage of using instantaneous frequency to map the Cherry Valley Limestone interface. Manual interaction was required to extend the Cherry Valley interface across some areas of image space.

Frequency spectra calculated in seismic windows dominated by the Marcellus interval are displayed on Figure 9.29. These spectra confirm the frequency content of P-SV$_1$ data across the Marcellus Shale interval spans a broader range (10-40 Hz) than do P-P data (15-30 Hz). This frequency comparison indicates P-SV$_1$ data should lead to improved resolution of reservoir and seal features. P-SV$_2$ data are characterized by a narrower frequency band dominated by lower frequencies (10-20 Hz). The lack of higher frequencies in P-SV$_2$ data indicates the P-SV$_2$ data volume will be the least valuable of the three post-stack volumes for analyzing the Marcellus interval. However, P-SV$_2$ data were never ignored in our interpretation. In particular, P-SV$_2$ data were essential for calculating azimuthal anisotropy behavior exhibited by fast-S and slow-S modes. Such anisotropy is critical for quantifying fractures and horizontal stress fields related to the Marcellus Shale.

The improved resolution of Marcellus geology provided by P-SV data compared to P-P data is more striking when wavelength spectra are considered. P-P wavelengths (λ_P) are defined as $\lambda_P = V_P/f$, where f = frequency, and P-SV wavelengths (λ_S) are defined as $\lambda_S = V_S/f$. Thus,

$$(9.1) \quad \lambda_S = \lambda_P \, (V_S/V_P).$$

Because the V_P/V_S velocity ratio within the Marcellus is approximately 1.6, this wavelength relationship simplifies to,

$$(9.2) \quad \lambda_S = 0.62\lambda_P.$$

P-SV wavelengths are thus significantly shorter than P-P wavelengths within the Marcellus Shale interval.

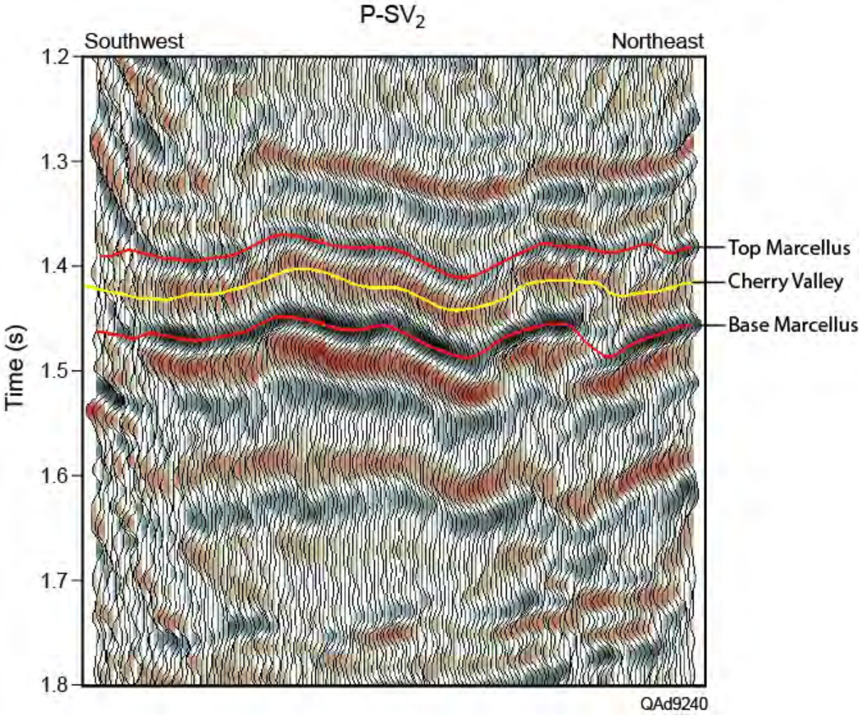

Figure 9.27. Variable-area wiggle-trace profile through P-SV$_2$ data volume with interpreted horizons across the Marcellus Shale interval.

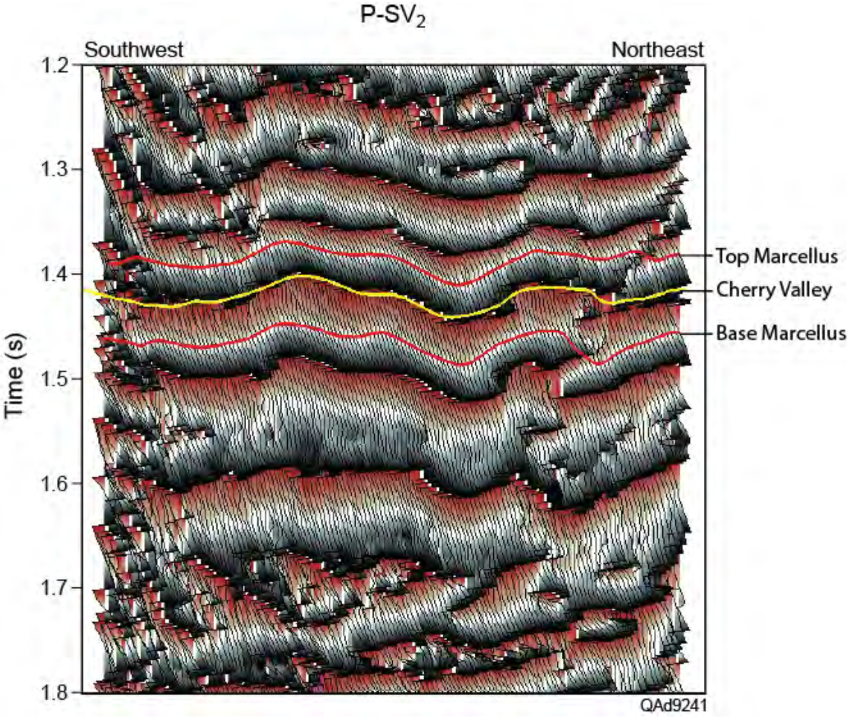

Figure 9.28. Instantaneous phase display along the profile of Figure 9.27. On this profile, the Cherry Valley correlates with a distinctive zero crossing in instantaneous phase. On other profile, manual interaction was required to define the interface.

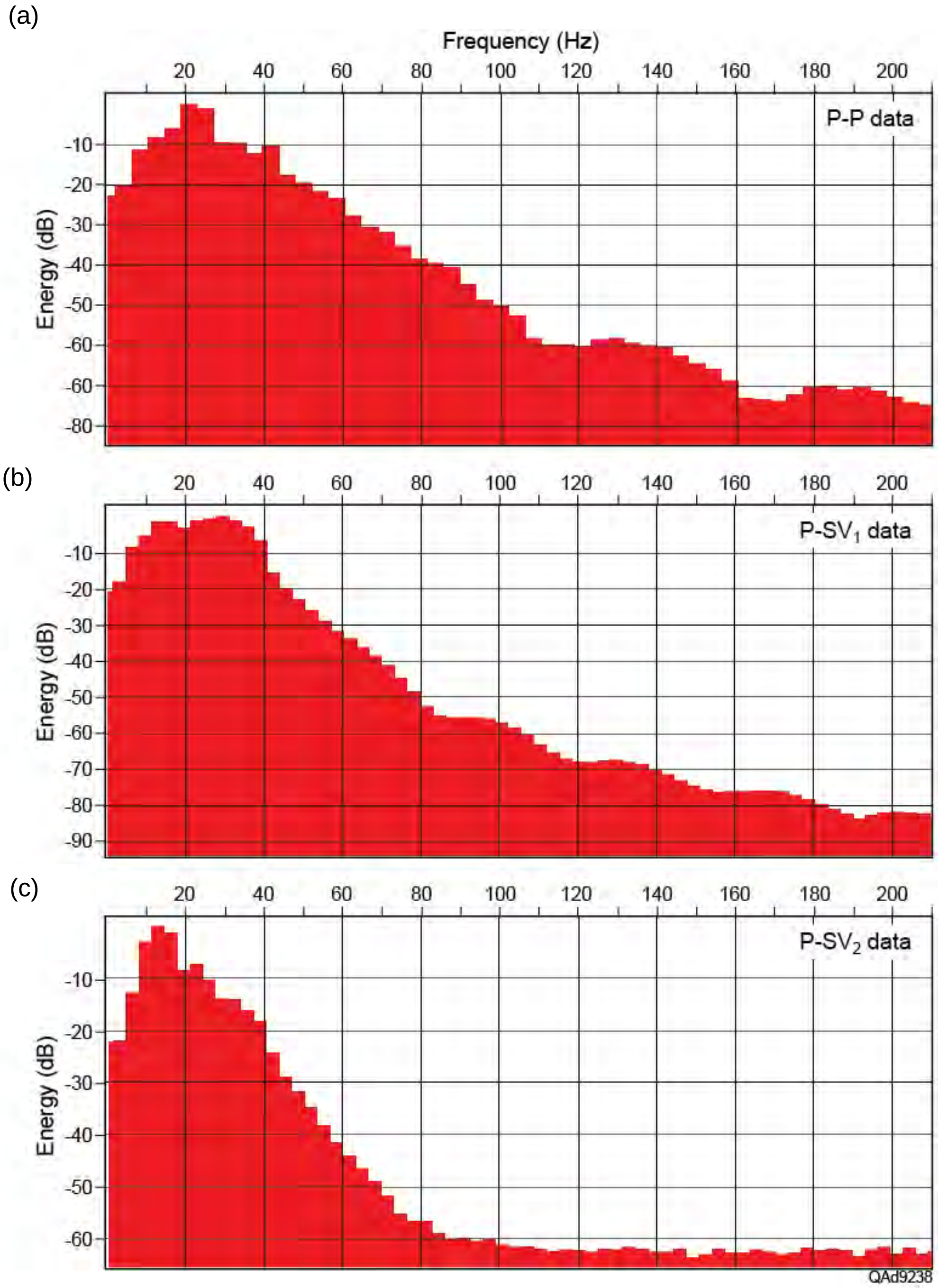

Figure 9.29. (a) P-P frequency spectrum across the Marcellus interval (900–1100 ms). (b) P-SV$_1$ frequency spectrum across the Marcellus interval (1300–1600 ms). (c) P-SV$_2$ frequency spectrum across the Marcellus interval (1300–1600 ms).

Marcellus Structural Interpretations

Structural complexity increased within the Marcellus interval across our study area. Both P-P and P-SV data showed the Marcellus has a strong structural-fold fabric trending east-to-west. These linear folds were mapped and correlated in both P-P and P-SV data volumes to better understand local effects of tectonic stress on the Marcellus. Although the natural fracture pattern within the Marcellus Shale is below the resolution of these post-stack seismic data, these structure maps provide a partial understanding of probable Marcellus fracture patterns. Understanding stress fields is useful for determining where natural fractures should be localized and for predicting how embedded fractures may behave when reactivated during hydraulic fracture treatments, or when pore pressure is altered because of fluid injections.

Similar fold patterns occur in both the Upper and Lower Marcellus units, but folds within the Lower Marcellus have slightly larger vertical relief than do their equivalents in the Upper Marcellus. These differences in fold height imply stresses acting on the Lower Marcellus may have been greater than stresses that generated folds in the Upper Marcellus. Folds are evident on P-P data (Fig. 9.30) but are more pronounced in P-SV_1 data (Fig. 9.31) and P-SV_2 data (Fig. 9.32). Because of the limited size of our 3D3C seismic survey (9 mi^2 [23 km^2] of image space), we cannot demonstrate that the structural complexities associated with the Marcellus Shale are associated with any specific regional orogenic event (for example, Taconian or Acadian), or if they are caused by more recent neotectonic joint systems formed during regional uplifting.

(a)

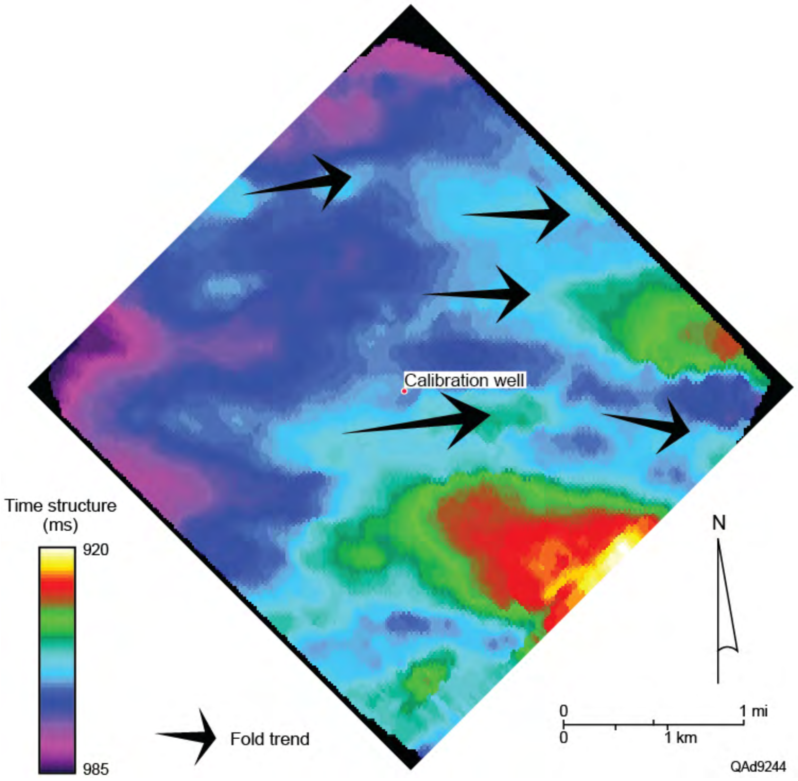

(b)

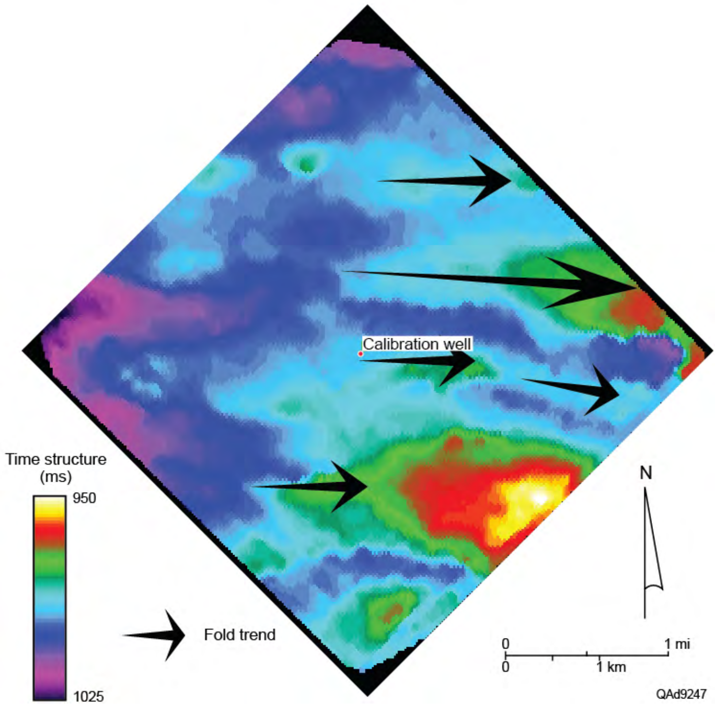

Figure 9.30. (a) Upper Marcellus Shale P-P time structure. (b) Lower Marcellus Shale P-P time structure. The arrows depict orientations of fold hinges.

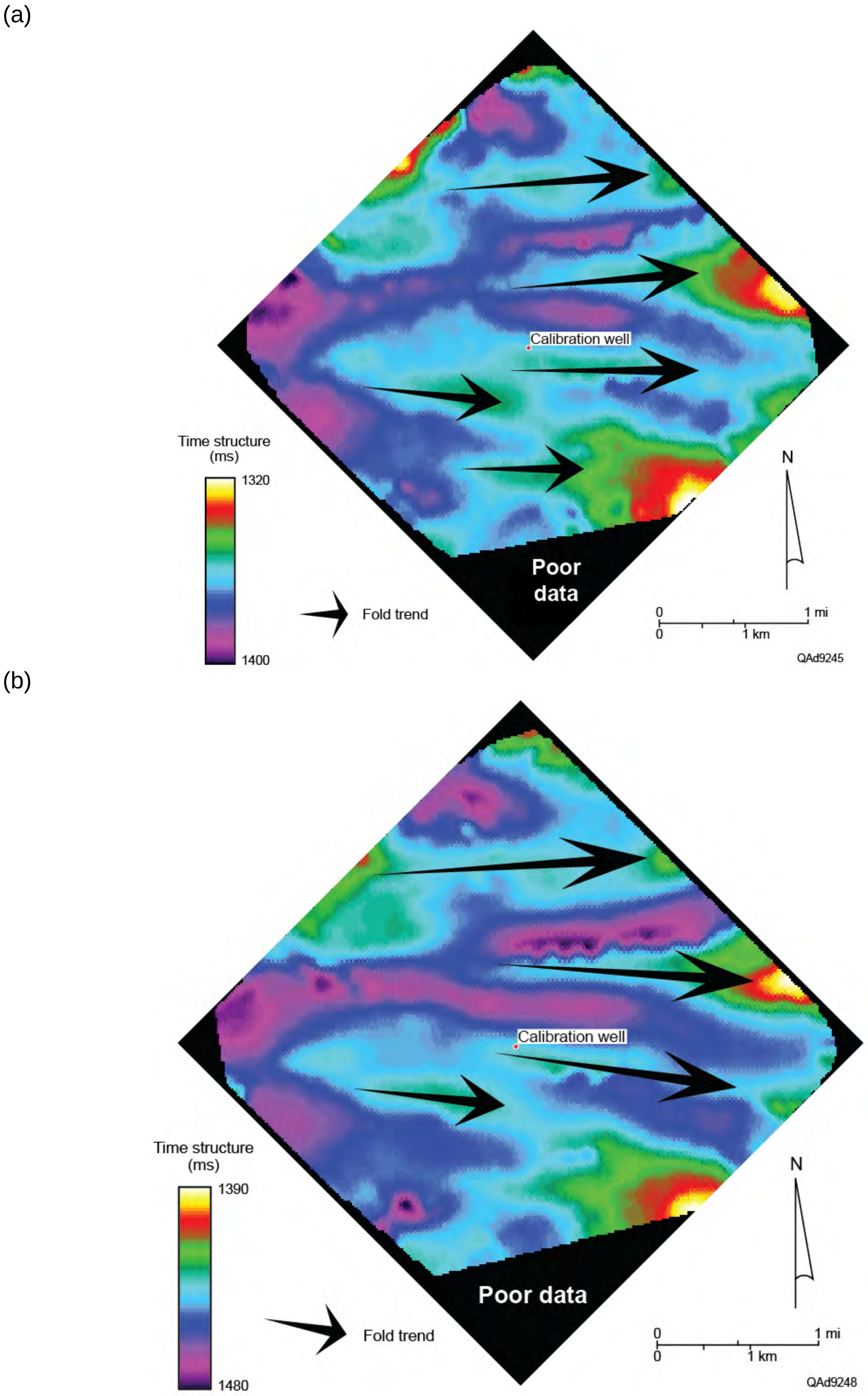

Figure 9.31. (a) Upper Marcellus Shale P-SV$_1$ time structure. (b) Lower Marcellus Shale P-SV$_1$ time structure. The arrows depict orientations of fold hinges.

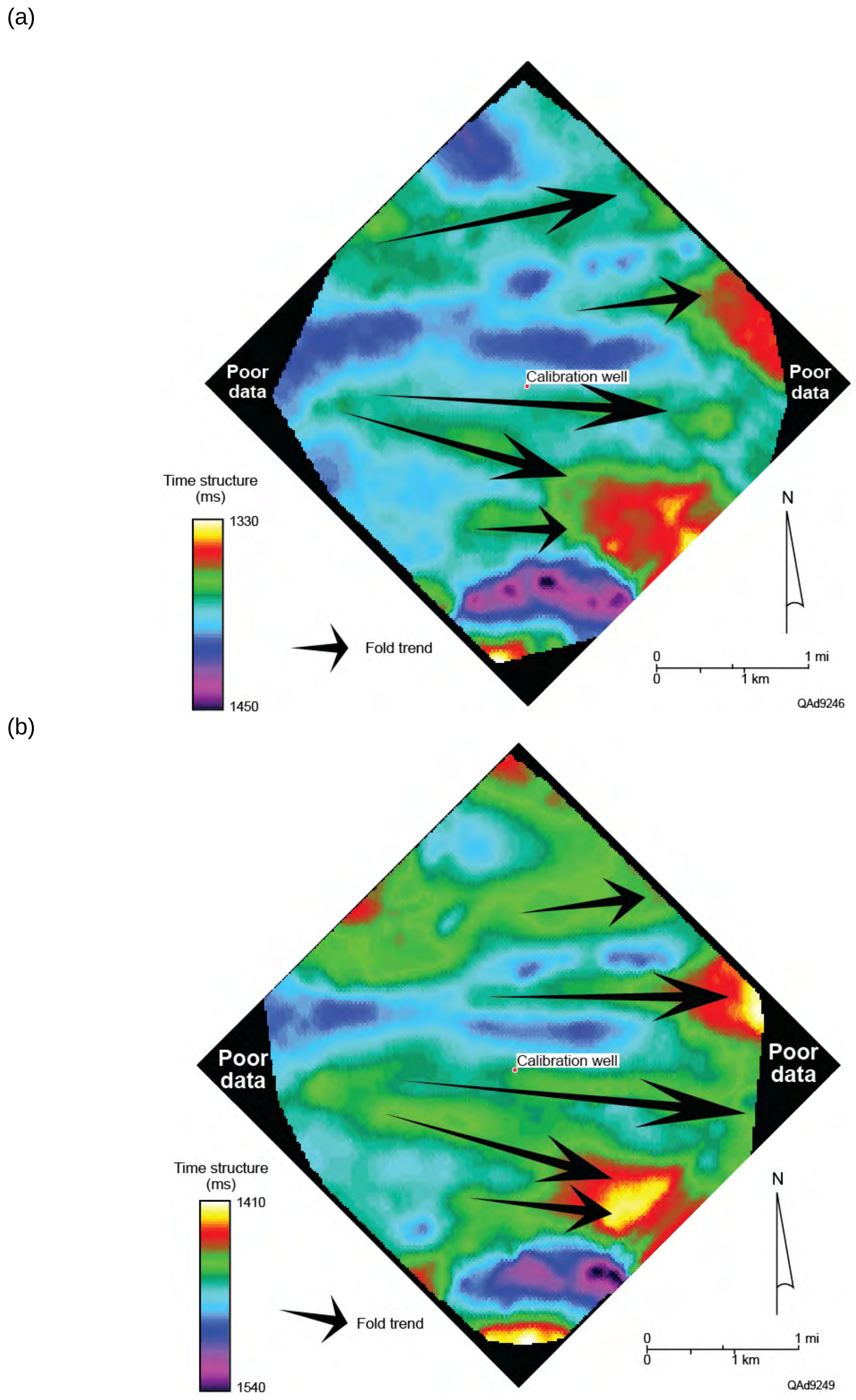

Figure 9.32. (a) Upper Marcellus Shale P-SV_2 time structure. (b) Lower Marcellus Shale P-SV_2 time structure. The arrows depict orientations of fold hinges.

The relationship between natural fracture orientations and present-day stress are important factors to consider for planning CO_2 injection. The orientation of natural fractures was evaluated in the central calibration well where a shear wave anisotropy log was acquired. Rose diagrams of interpreted fracture orientations generated by Halliburton, the logging contractor, show fracture orientations in the Upper Marcellus (Fig. 9.33a) and Lower Marcellus (Fig. 9.33b) range from slightly south of east-west to approximately 45-degrees north of east-west. The orientations of extensional fractures (σ_1) and shear fractures (A) drawn on the rose diagrams are our interpretations of the fracture patterns, not Halliburton's interpretation. If this fracture interpretation is implemented, maximum horizontal stress σ_1 would align with extensional fractures, making σ_1 have an orientation approximately 100-degrees from north. A significant fact implied by these rose diagrams and by the preceding structure maps is that most fractures within the Marcellus interval are oriented parallel to fold axes within the interval. Fracture set A labeled on each display is our interpretation of possible shear fractures, which typically are oriented approximately 30-degrees away from the extensional fractures created by maximum horizontal stress $\sigma_{1.}$

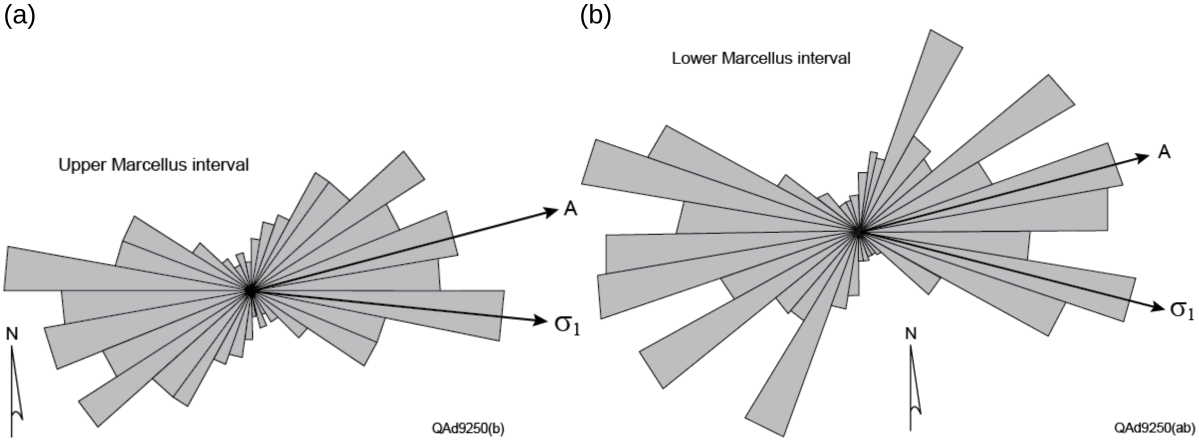

Figure 9.33. Rose diagrams calculated from borehole image logs acquired in the central-image calibration well for (a) Upper Marcellus and (b) Lower Marcellus. σ_1 defines the direction of maximum horizontal stress interpreted from these rose diagrams. Fractures along trend σ_1 should be extensional fractures. Shear fractures are oriented in a direction that is usually in a direction approximately 30-degrees away from σ_1, such as the fractures sets labeled A.

Marcellus Seismic Amplitude Attributes

Numerous horizon-constrained seismic attributes were generated during our interpretation of the Upper Marcellus and Lower Marcellus intervals. The objective of this amplitude-attribute analysis was to determine if any amplitude calculations derived from post-stack data volumes would provide additional evidence of faulting, fracturing, or jointing within the Marcellus Shale interval, which are features that would affect CO_2 injection behavior if the Marcellus Shale is considered for CO_2 sequestration.

We found no amplitude attribute that provided structural, faulting, or fracturing information about the Marcellus that differed from information shown by structural maps (Figs. 9.30 to 9.32). Amplitude attribute maps for the Lower Marcellus showed narrow trends of increased P-P and P-SV_1 reflectivities (Figs. 9.34b and 9.35b) that tracked the structural folds on corresponding structural-fold maps for these two seismic modes (Figs. 9.30b and 9.31b). We have no technical explanation why there is a good correlation between intra-Marcellus folds and P-P and P-SV_1 reflectivity within the Lower Marcellus and a poor correlation between these two properties for the Upper Marcellus. We document only our empirical observation of good-vs.-poor correlations for these two seismic attributes for each of the Marcellus units. No reflectivity pattern emerged from our interpretation of P-SV_2 data that had any structural or stratigraphic significance across the Marcellus interval (Fig. 9.36).

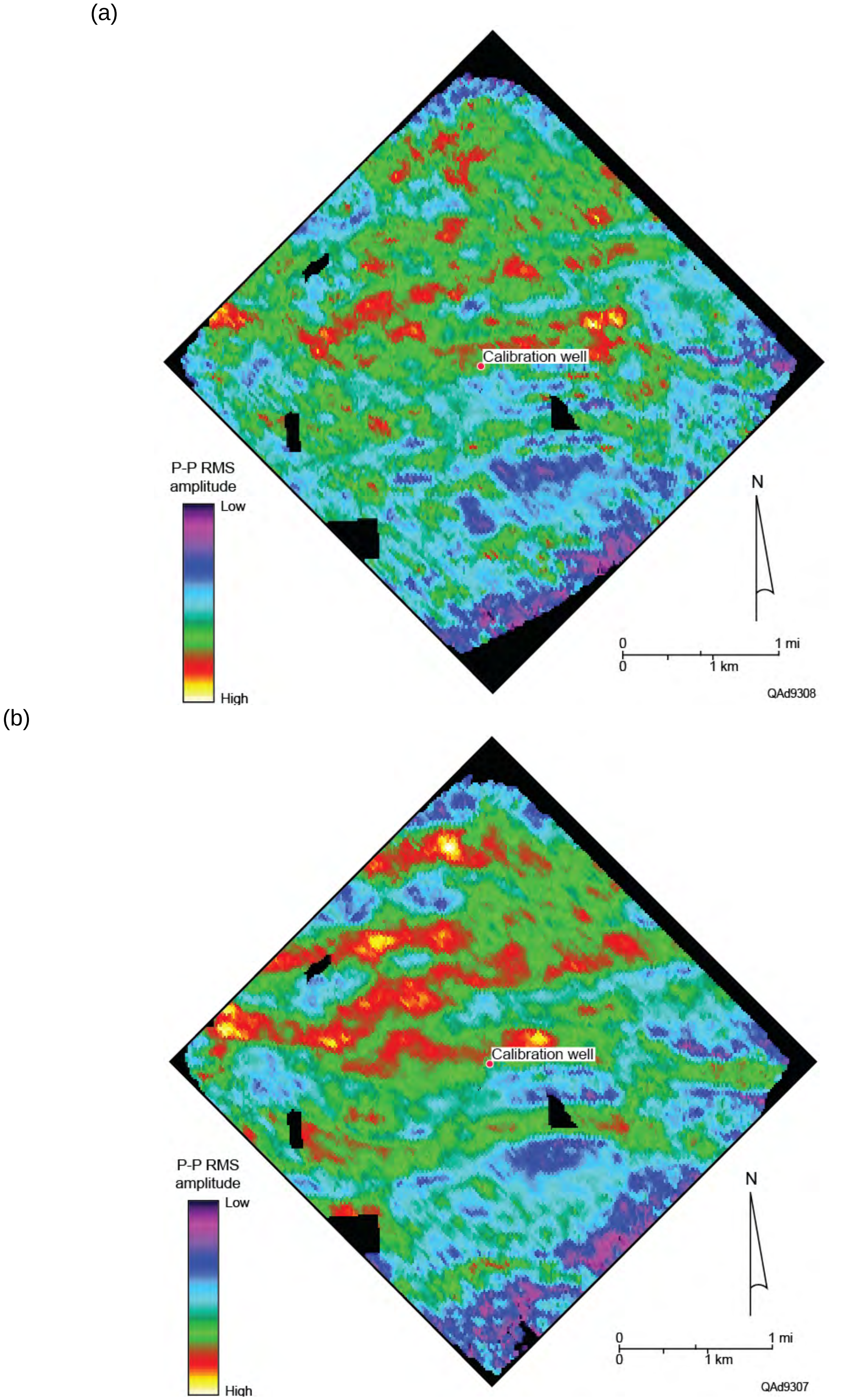

Figure 9.34. P-P rms amplitudes across (a) Upper Marcellus and (b) Lower Marcellus.

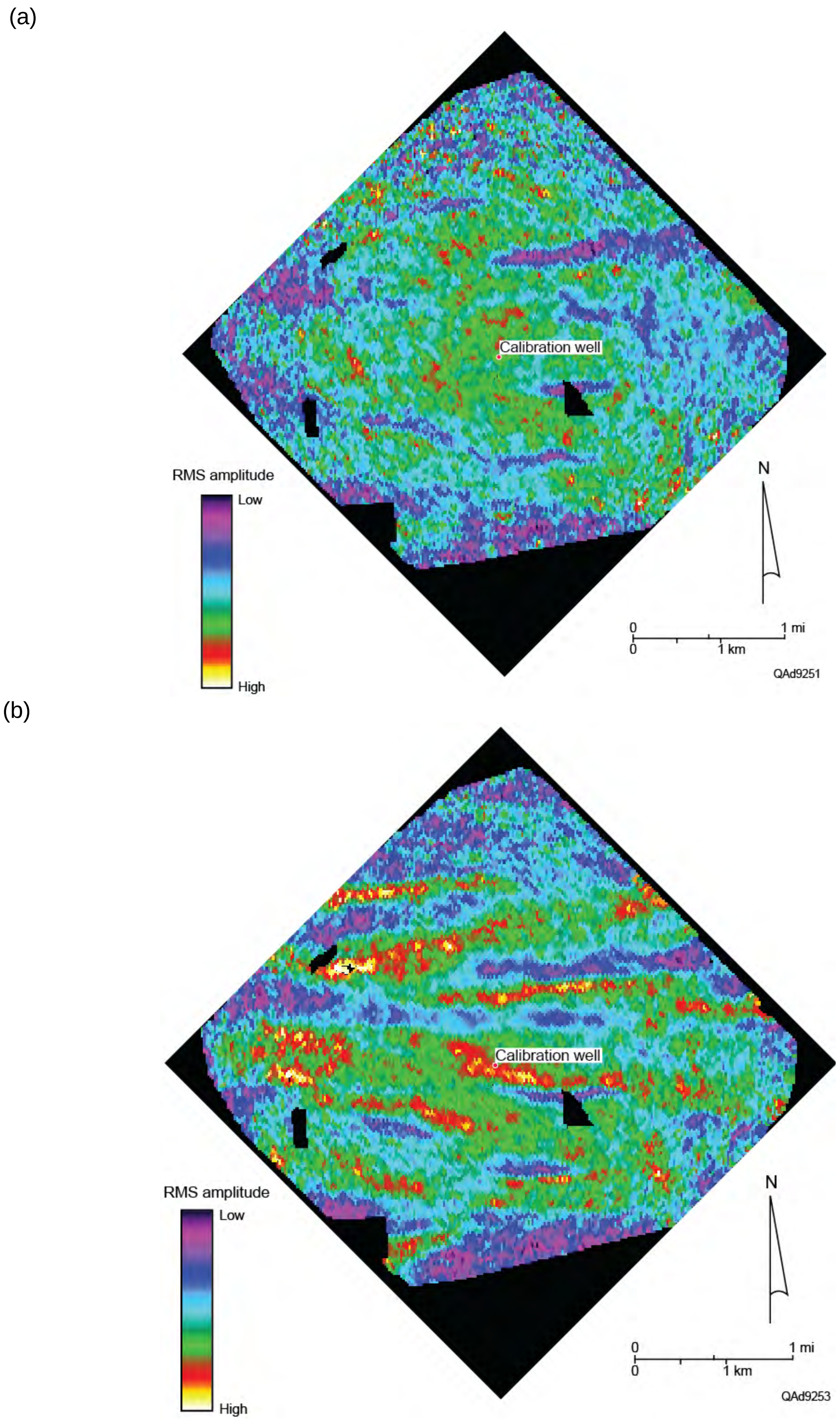

Figure 9.35. P-SV_1 rms amplitudes across (a) Upper Marcellus and (b) Lower Marcellus.

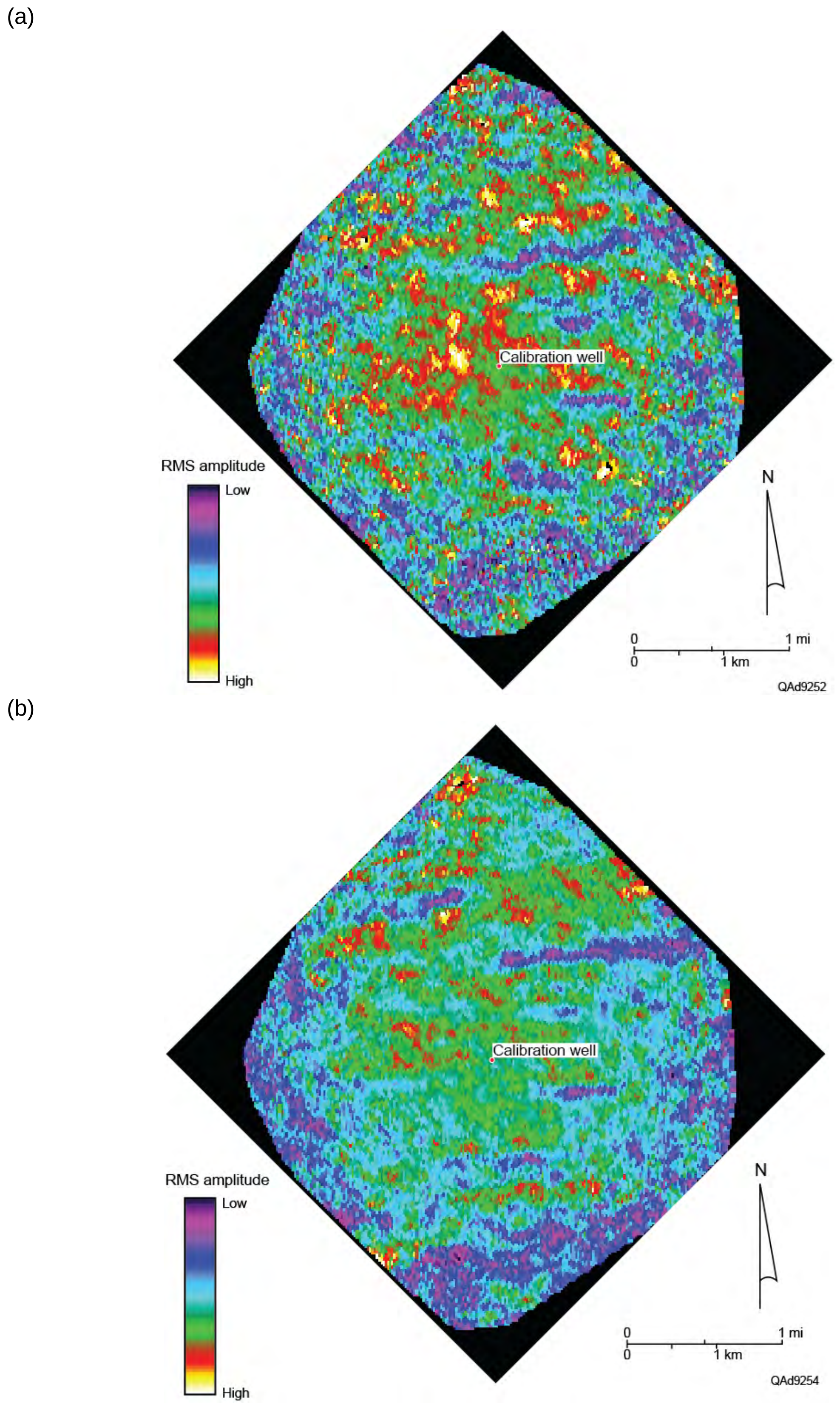

Figure 9.36. P-SV_2 rms amplitudes across (a) Upper Marcellus and (b) Lower Marcellus.

Marcellus Stratal Slices

The stratal slicing concept described by Figure 9.21 was applied to the Marcellus Shale interval to determine if a stratal-slice approach could find stratigraphic features not exhibited by other interpretations. Depth-equivalent stratal slices from each of the three data volumes are displayed on Figure 9.37. Each stratal slice shows amplitude anomalies that trend in the same direction as the structural folds exhibited on the maps displayed on Figure 9.30 to 9.32. This stratal slicing effort added confidence to the structural fold picture previously developed (Figs. 9.30–9.32) and provided no evidence that would make an interpreter suspect there was internal compartmentalization within the Marcellus. At the depth level chosen for this comparison, both S-mode volumes show stronger amplitudes than does the P-P mode. These example stratal slices are representative of those created across the full Marcellus interval in that amplitude anomalies trended along structural folds, and no subtle stratigraphic pinch-outs or other features were found.

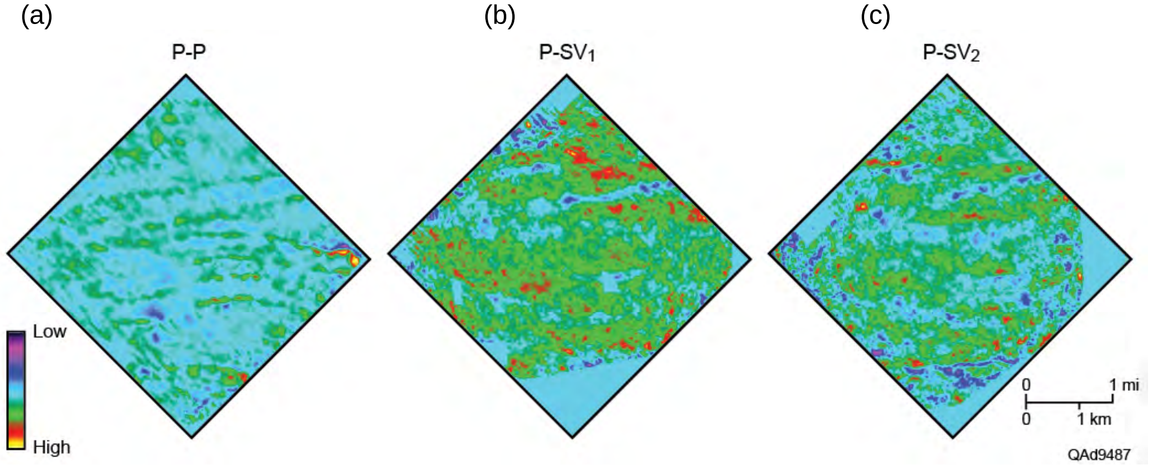

Figure 9.37. Comparisons of depth-equivalent stratal slices within the Upper Marcellus Shale. (a) P-P stratal slice. (b) P-SV_1 stratal slice. (c) P-SV_2 stratal slice. The attribute displayed on the slices is reflection amplitude.

Marcellus S-Wave Anisotropy

Vertical fractures, when consistently oriented across an interval, cause that interval to be an azimuthally anisotropic seismic propagation medium. Because the mechanical strength of such a medium is stronger parallel to fractures than it is perpendicular to fractures, a seismic mode exhibits a faster propagation velocity parallel to fractures than it does perpendicular to fractures.

This difference in propagation velocities is more pronounced for S waves than it is for P waves. For this reason, azimuthal anisotropy is often referred to as S-wave anisotropy. The quantity S_{ANI} will be used to indicate seismic-based S-wave anisotropy is defined as,

$$(9.3) \quad S_{ANI} = (V_1 - V_2) / V_2,$$

where V_1 is fast-S velocity and V_2 is slow-S velocity. If fast-S and slow-S images of a targeted anisotropic interval are available, seismic-based interval values of V_1 and V_2 can be approximated as,

$$(9.4) \quad V_1 = D / \Delta T_1 \text{ and } V_2 = D / \Delta T_2,$$

where D is the thickness of the interval, ΔT_1 is the time thickness of the interval on a fast-S image, and ΔT_2 is the time thickness of the interval on a slow-S image. Substituting Equation 9.4 into Equation 9.3 leads to a simple calculation that transforms fast-S and slow-S post-stack seismic data into estimates of seismic-based S-wave anisotropy:

$$(9.5) \quad S_{ANI} = (\Delta T_2 / \Delta T_1) - 1.$$

We calculated this quantity, S_{ANI}, across the Upper Marcellus and Lower Marcellus intervals. Maps of these seismic-based estimates of S-wave anisotropy are displayed on Figure 9.38.

Anisotropy measurements taken at the calibration well are: Upper Marcellus 1.7% and the Lower Marcellus 1.6%, respectively. At the location of the calibration well, the Upper Marcellus has an east-to-west trending anisotropy zone of approximately 2.5-percent immediately north of the well location. The Lower Marcellus shows a northwest-to-southeast trending anisotropy zone of approximately 2-percent that passes immediately south of the calibration well. The areas highlighted with green-red-to-yellow colors have slightly higher S-wave anisotropy and may define localized increases in fracture intensity.

The magnitudes of these seismic-based estimates of S-wave anisotropy agree with the magnitudes of S-wave anisotropy measured by dipole sonic-log data (Figure 4.8 of Chapter 4). This agreement between log data and seismic data has two implications:

1. It verifies the accuracy and reliability of the seismic data used in this study, and

2. It demonstrates a valuable rock property provided by multicomponent seismic data that cannot be provided by single-component P-wave data.

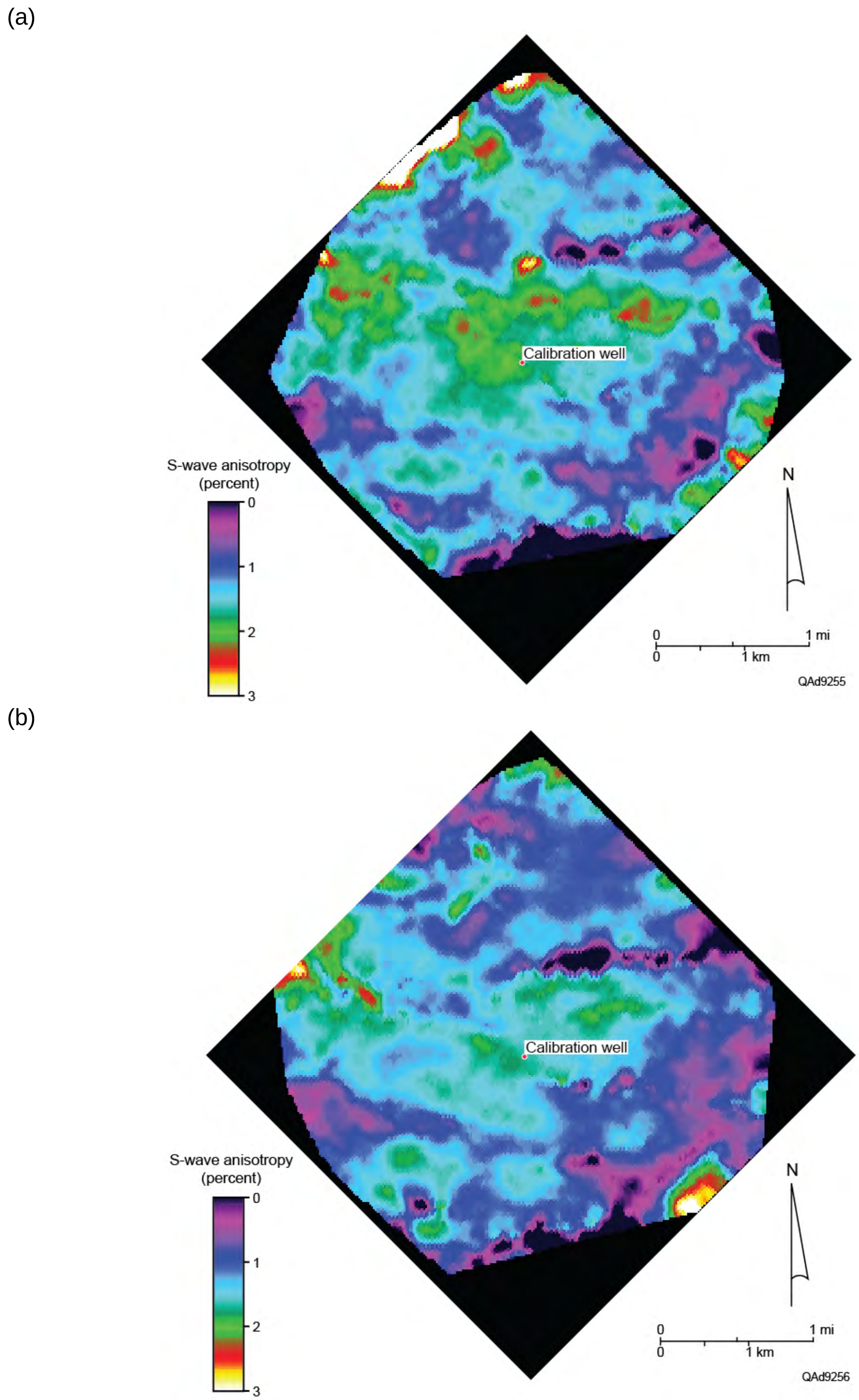

Figure 9.38. S-wave anisotropy calculated for (a) Upper Marcellus and (b) Lower Marcellus.

The S-anisotropy values shown on Figure 9.38 are sensitive to subtle variations in the position of the Cherry Valley interface that separates Upper and Lower Marcellus. Because the Cherry Valley Limestone could not be interpreted with automatic horizon-picking algorithms, manual intervention by an interpreter was required to define the position of this thin intra-Marcellus limestone. This interpreter action may introduce some ambiguity in the position of the boundary separating Upper and Lower Marcellus. Thus S-wave anisotropy was calculated across the total Marcellus interval to compare against results determined for the upper and lower units of the Marcellus. This total-Marcellus anisotropy is displayed as Figure 9.39 and shows anisotropy varies from 0.75 to 1.7 percent. For all practical purposes, S-wave anisotropy within the Marcellus Shale is too small to use traveltime differences in fast-S and slow-S modes to infer fracture density.

Again, as stated earlier, these seismic-based S-wave anisotropy numbers agree with S-wave anisotropy estimates calculated from log data (Fig. 4.8) and verify that multicomponent seismic data have value and applications that cannot be provided by P-wave seismic data.

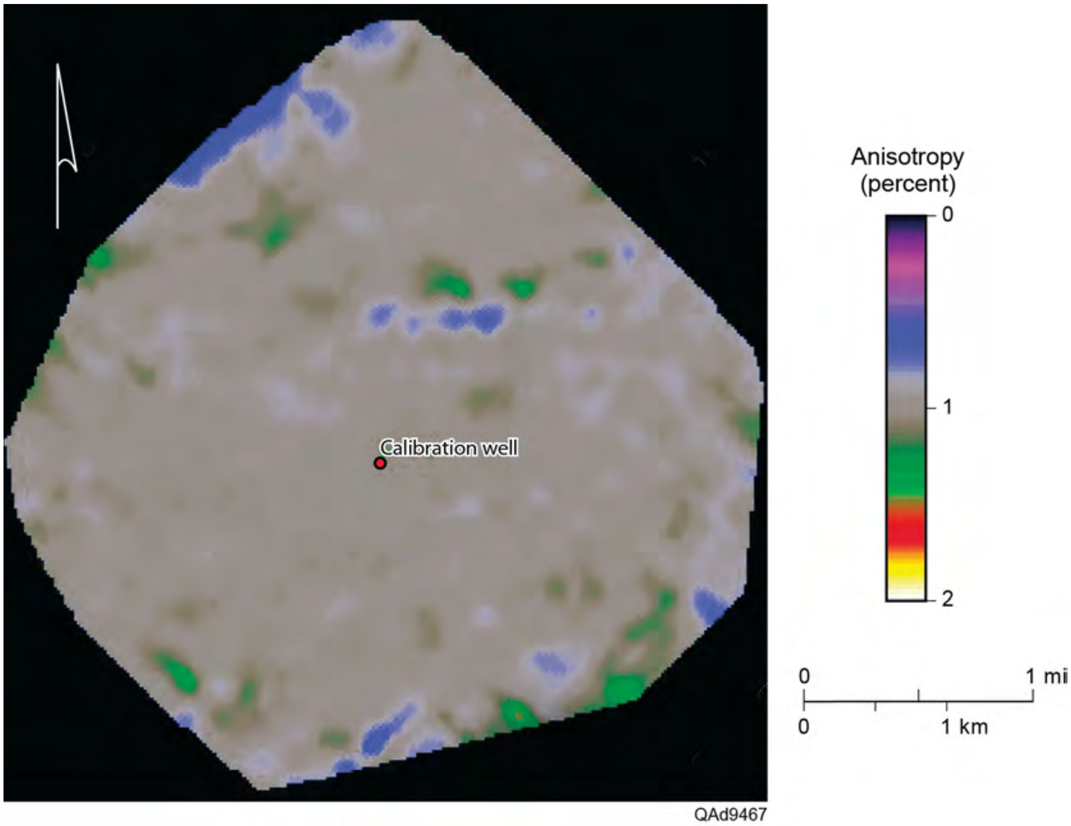

Figure 9.39. S-wave anisotropy across the total Marcellus interval.

Curvature

Curvature is a recent seismic attribute developed to aid interpreters. Two types of curvature can be calculated: (1) structural curvature, and (2) amplitude curvature. Amplitude curvature is a calculation that reacts to lateral variations in reflection amplitude strength along an interpreted horizon. Structural curvature is a calculation that describes lateral variations in the time (or depth) coordinate of a horizon. Here, the emphasis is on structural curvature, not amplitude curvature.

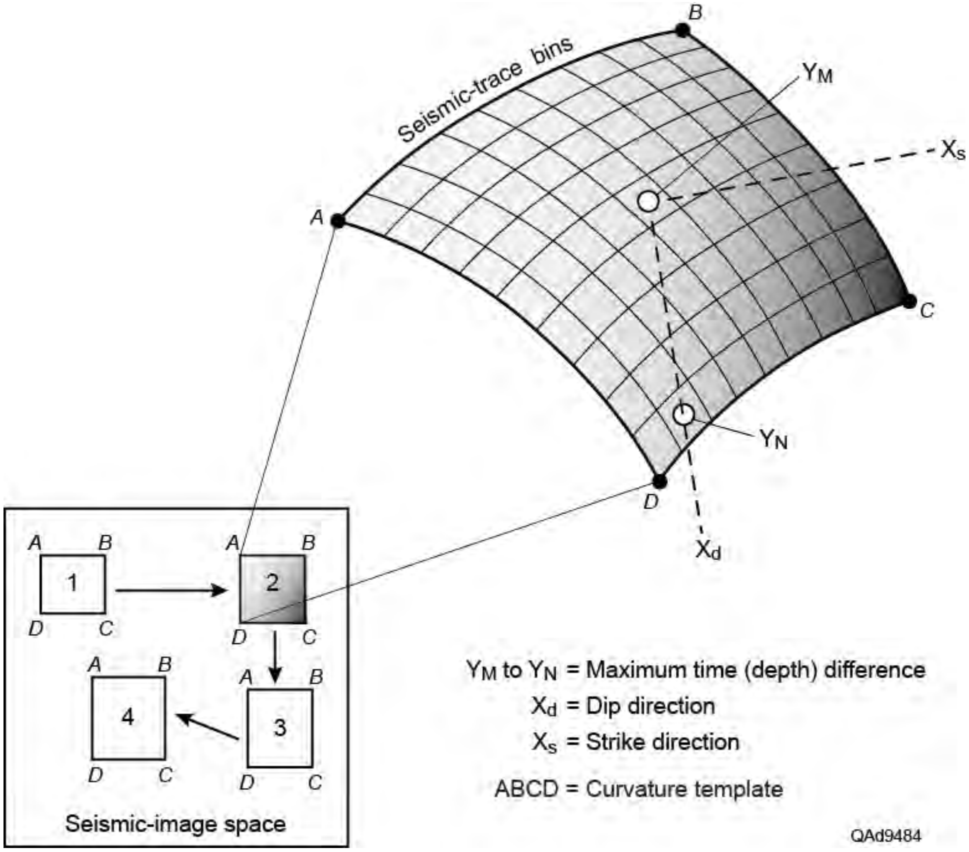

Figure 9.40. Procedure used to calculate local dip and strike directions. In this example, local dip and strike related to data point Y_M are calculated using a 9×9 analysis template ABCD. This template moves over the interpreted seismic horizon so that analysis point Y_M is positioned at every data point on the surface. The movement of the template to four different analysis points is shown at the lower left.

Structural Curvature

Structural curvature is calculated using time-based or depth-based seismic data that define geometrical configurations of subsurface structure. First and second time derivatives (time-based seismic data), or first and second depth derivatives (depth-based seismic data), can be calculated throughout a 3D volume of interest and then classified in a number of ways, such as most-positive curvature, most-negative curvature, minimum curvature, maximum curvature, mean curvature, Gaussian curvature, dip curvature, strike curvature, shape index, or azimuth curvature. The list of curvature attributes that can be calculated continues to grow as more people apply curvature concepts to seismic data interpretation. Any structural curvature attribute can be filtered to emphasize long-wavelength curvature or short-wavelength curvature, depending on what an interpreter wishes to see in an interpretation.

We found **dip curvature** and **strike curvature** to be valuable seismic attributes for the Marcellus interval. The manner in which these two curvatures is determined is illustrated on Figure 9.40. Surface ABCD represents a portion of a seismic interpreted horizon that exhibits structural curvature. This small square of image bins is the area over which curvature is calculated. The size of this analysis area is arbitrary and can be defined by a seismic interpreter. In the example drawn on Figure 9.40, the dimensions of the analysis template are (9 bins) X (9 bins), which is a typical template size. Change in structure is measured in all azimuth directions from the central image bin Y_M of template ABCD. The azimuth in which the largest time (depth) difference is measured is defined as the local dip, which on Figure 9.40 is dashed line X_d passing from point Y_M to point Y_N. Local strike is defined as the azimuth normal to the calculated local-dip azimuth. This analysis template moves over the complete interpreted horizon so local dip and strike are calculated at every image bin on the interpreted horizon as shown in the lower left of the figure.

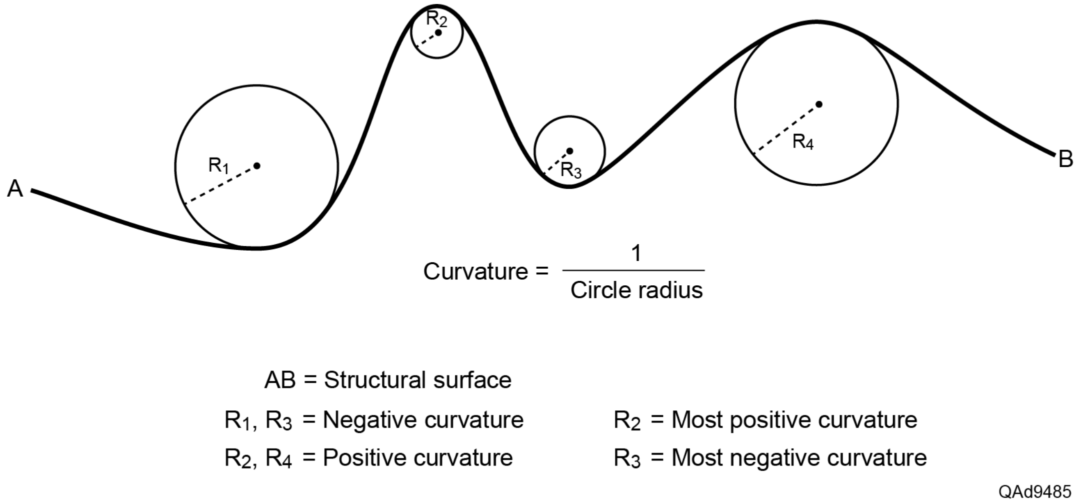

Figure 9.41. Estimating structural curvature by fitting circles to an interpreted structural horizon at each local point on the surface. This illustration is a 2D view along a selected profile traversing an interpreted surface.

After dip and strike directions are determined as continuous XY-coordinate functions across an interpreted horizon, dip and strike curvature are calculated by fitting circles to the structural surface as shown on Figure 9.41. When a circle of radius R is found such that its circumference makes maximum contact with local curvature of the structural surface, the inverse of the circle radius (1/R) is defined as an indicator of structural curvature. On Figure 9.41, there are illustrations of positive curvature, negative curvature, most-positive curvature, and most-negative curvature.

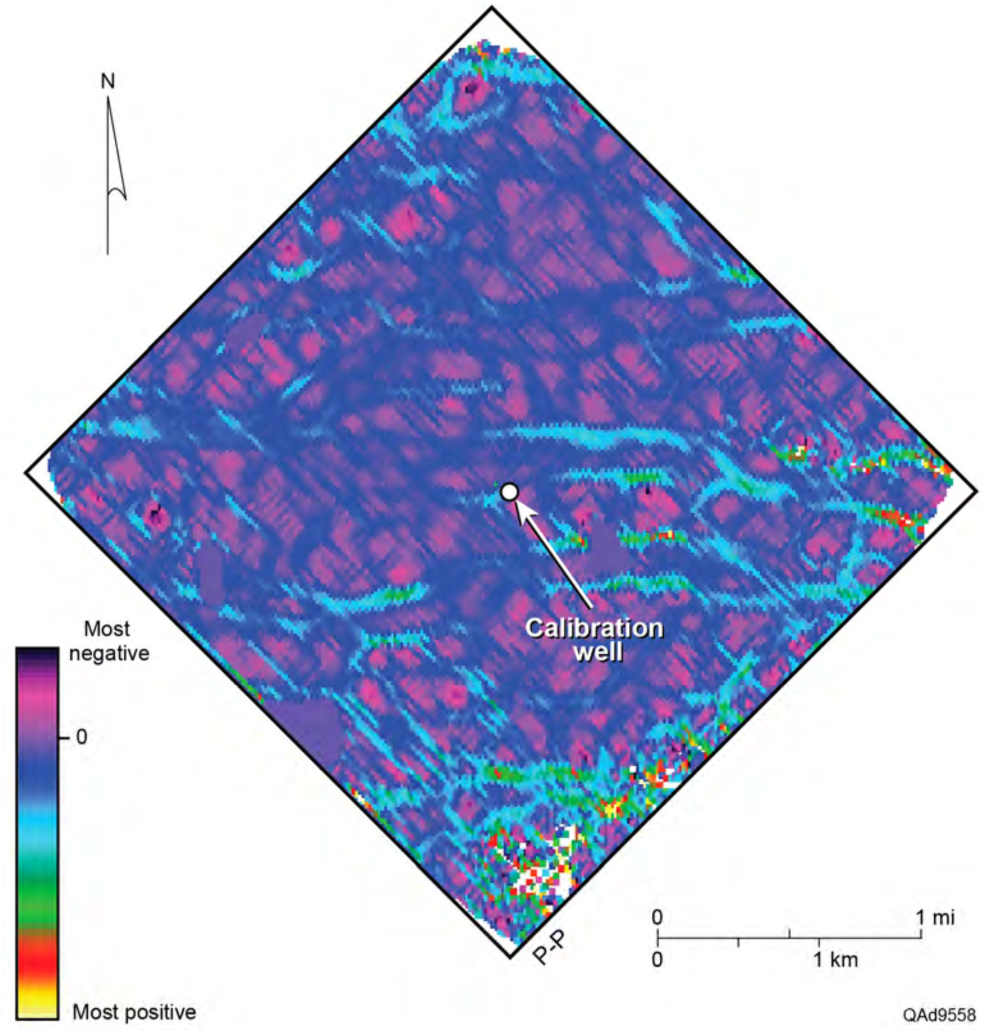

Figure 9.42. P-P dip curvature for the Upper Marcellus.

Marcellus Curvature

A structural curvature analysis was done for the Marcellus interval to identify trends of maximum curvature, which in turn, may correspond to trends of increased fracture intensity. Curvature was calculated in both dip and strike directions, as those attributes are defined on Figure 9.40. Results are displayed as Figure 9.42 for P-P data, Figure 9.43 for P-SV_1 data, and Figure 9.44 for P-SV_2 data. In each seismic image space, structural curvature calculated in the dip direction provided a map that exhibited less data-acquisition footprint effects than did curvature calculated in the strike direction. Thus the displays on

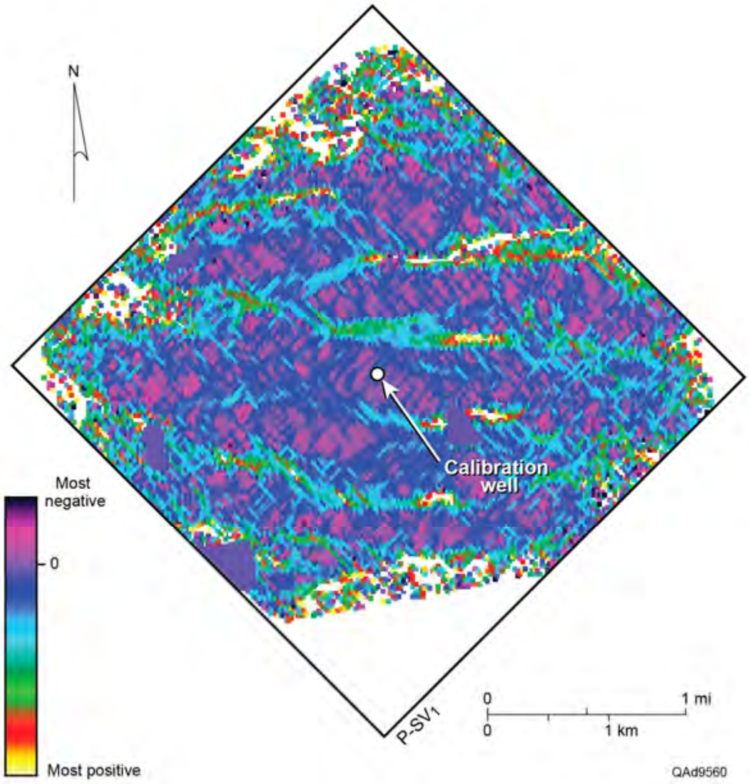

Figure 9.43. P-SV$_1$ dip curvature for the Upper Marcellus

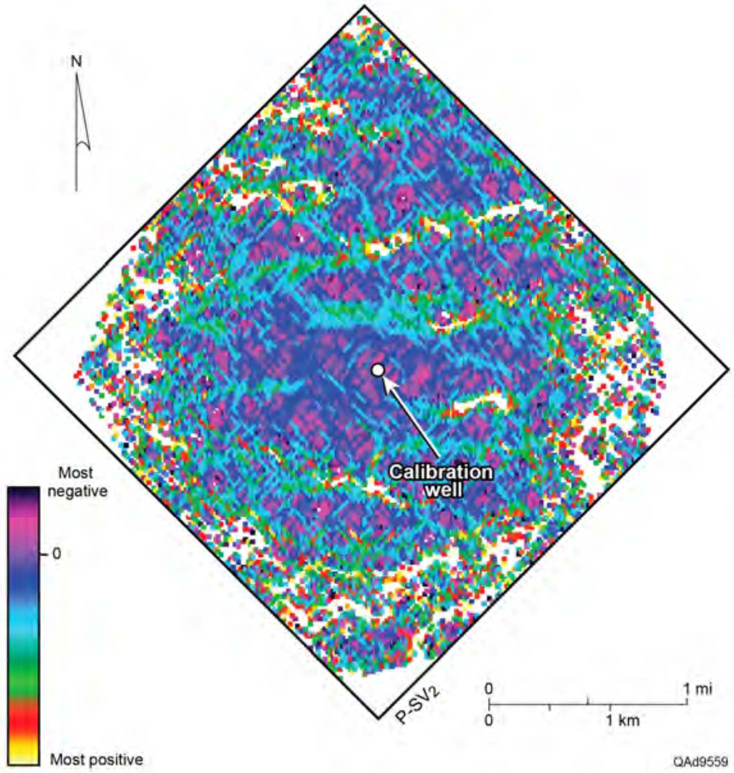

Figure 9.44. P-SV$_2$ dip curvature for the Upper Marcellus.

Figures 9.42–44 are restricted to curvature measured in the dip direction. These structural curvature results confirm the validity of the structural folds within the Marcellus displayed on Figures 9.30 through 9.32. The trends of maximum curvature (either most-positive or most-negative) are tentatively viewed as trends of enhanced fracture density.

Seismic Sequences within the Oriskany Sandstone

Examples showing distinctions between P-wave seismic sequences and facies and depth-equivalent S-wave seismic sequences and facies occur within the Onondaga and Oriskany intervals below the Marcellus Shale. These data displays are significant because of the potential importance of using the Oriskany Sandstone as a CO_2 sequestration reservoir.

A selected P-P profile across these depositional features is exhibited on Figure 9.45. Based on the VSP calibration log superimposed on the P-P seismic profile shown as Figure 9.7, we conclude with reasonable confidence that sequence **ON** is within the Onondaga interval, and sequence **OR** is within the Oriskany interval. Sequence **UT** is arbitrarily interpreted as being a Utica depositional unit. No time-to-depth calibration data are available across deep stratigraphic units to be confident where the Utica interval should be in P-P image space.

Using the log overlays on the P-SV_1 and P-SV_2 profiles of Figures 9.8 and 9.9 for correlation, we conclude sequences **ON** and **OR** labeled on Figure 9.46 and 9.47 are, respectively, Onondaga and Oriskany sequences that are depth-equivalent to the P-P sequences identified on Figure 9.45. The base of the **ON** sequence is a bold reflection in P-P image space (Fig. 9.45), but it is an invisible stratal surface identified only by terminating reflection events in P-SV_1 image space (Fig. 9.46). The base of the **ON** sequence is even more nebulous in P-SV_2 image space (Fig. 9.47) although some evidence of terminating reflection events is indicated by the labeled arrows. The geometrical shape of sequence **OR** differs in P-P and P-SV_1 image spaces. P-SV_2 data define the geometry of sequence **OR** in much the same way as do P-SV_1 data.

The fundamental assumption of elastic wavefield seismic stratigraphy is that all three images (P-P, P-SV_1, and P-SV_2) are correct until proven otherwise. If this assumption is true, distinctions in the seismic sequences and seismic facies in these three image spaces present dramatically different pictures of reservoir compartmentalization, which are insights required for rigorous evaluation of CO_2 sequestration targets. Without deeper well data to define rock properties needed to estimate P and S reflectivities, one can only speculate why P seismic sequences and S seismic sequences differ so radically.

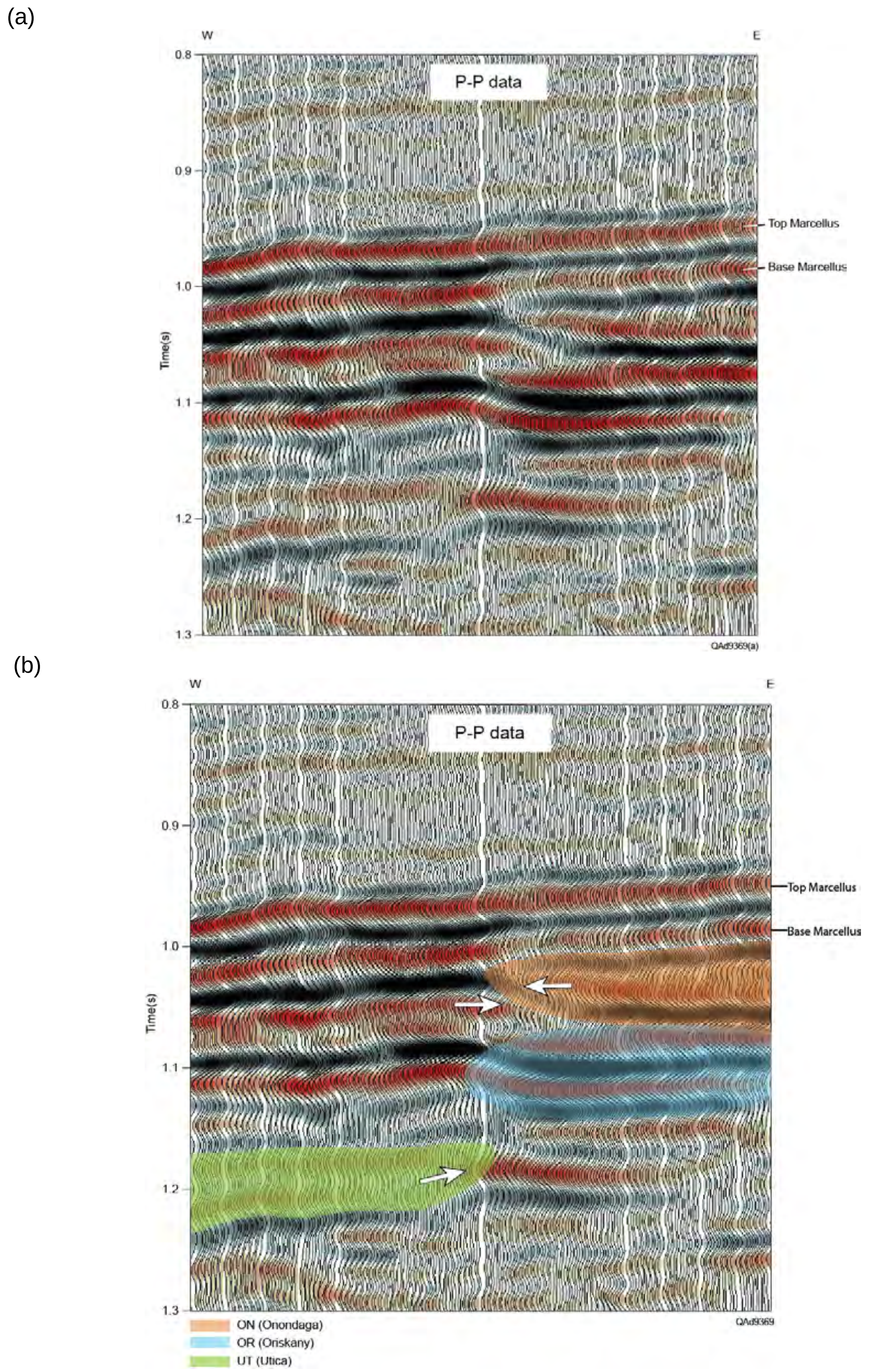

Figure 9.45. (a) P-P profile showing pre-Marcellus geology. (b) Same profile showing interpreted Onondaga sequence (**ON**), Oriskany sequence (**OR**), and Utica sequence (**UT**). The arrows define terminating reflections associated with sequence boundaries.

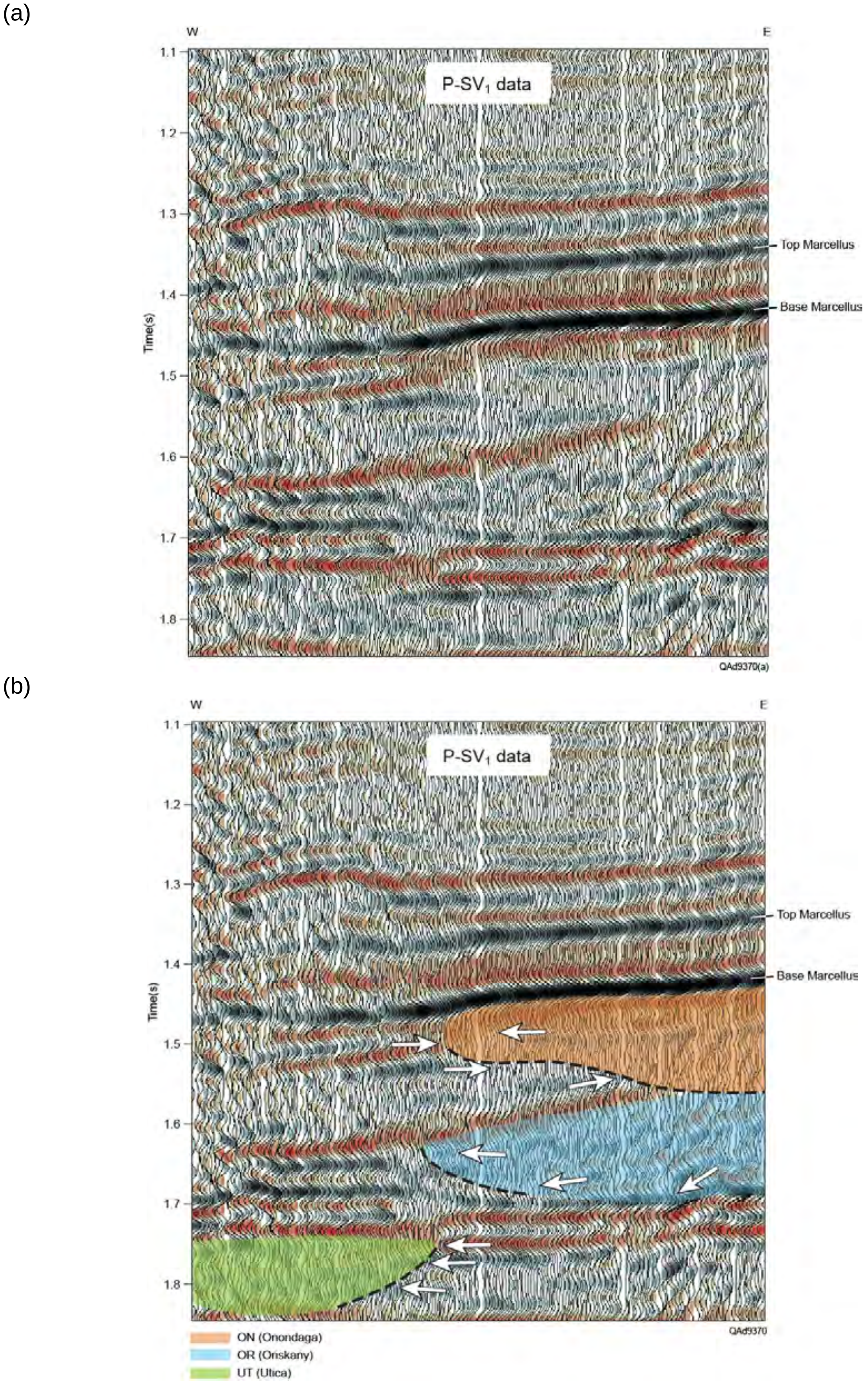

Figure 9.46. (a) P-SV$_1$ profile showing pre-Marcellus geology. (b) Same profile showing interpreted Onondaga sequence (**ON**), Oriskany sequence (**OR**), and Utica sequence (**UT**). The arrows define terminating reflections associated with sequence boundaries.

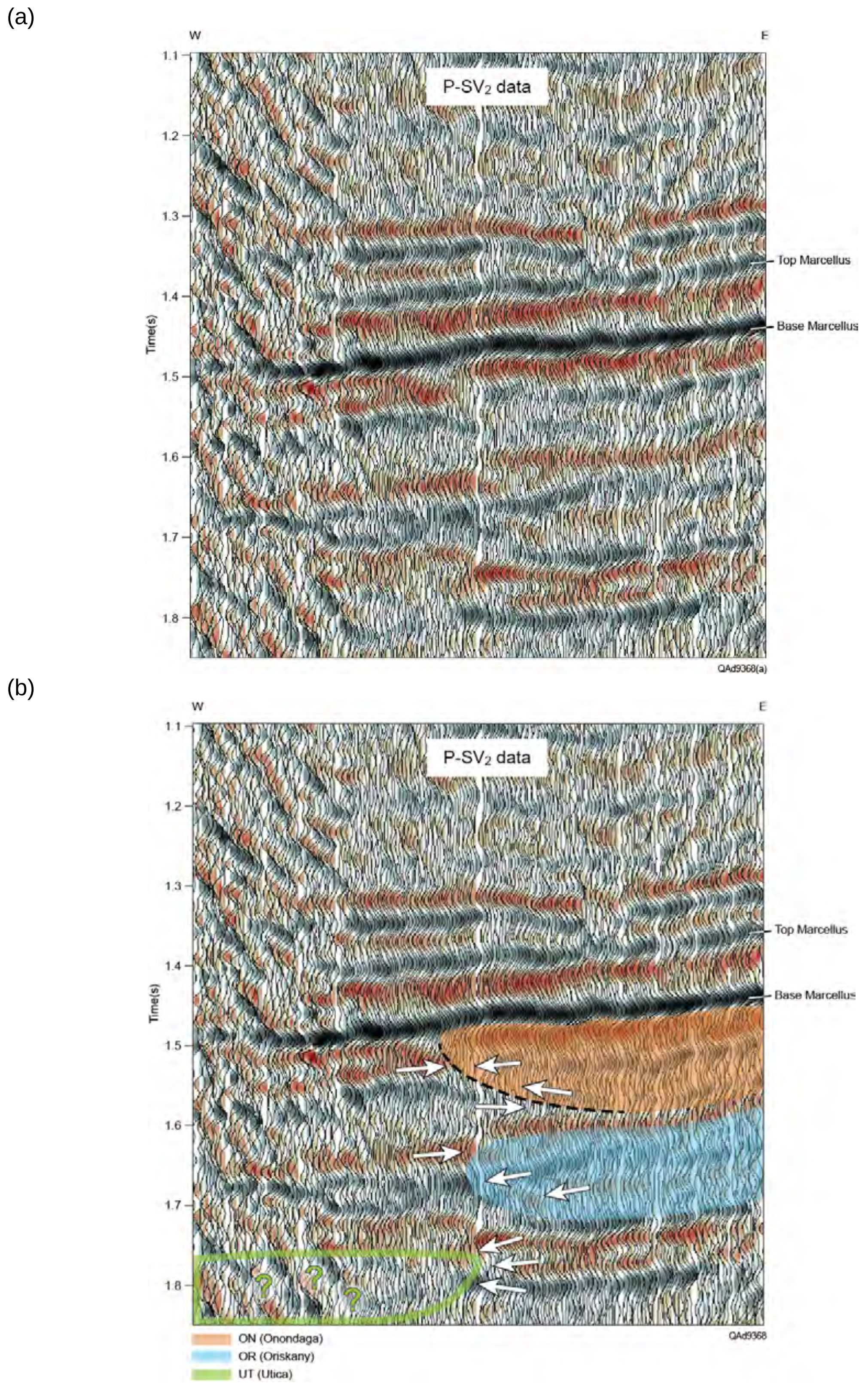

Figure 9.47. (a) P-SV$_2$ profile showing pre-Marcellus geology. (b) Same profile showing interpreted Onondaga sequence (**ON**), Oriskany sequence (**OR**), and Utica sequence (**UT**). The arrows define terminating reflections associated with sequence boundaries.

Conclusions

The outcome of our research activities in our data-interpretation task far surpassed our expectations when the project started. Briefly, the 3C3D seismic data used in this study provided the most dramatic contrast between P-wave and S-wave imaging of geologic targets that our research teams has observed in the 12 years our laboratory has been engaged in multicomponent seismic interpretation. The impressive aspect of these data was that both the P-SV_1 (fast-S) mode and P-SV_2 (slow-S) mode provided better spatial resolution of key geologic targets than did P-P (compressional) data. The latter data (P-P) are the principal seismic data used to evaluate CO_2 reservoir systems. The increase in P-SV_1 resolution over P-P resolution was particularly significant, with P-SV_1 wavelengths being approximately 40-percent shorter than P-P wavelengths. Research findings discussed in this chapter should be considered by all CO_2 sequestration projects across the Appalachian Basin so seismic interpreters can take advantage of the increased resolution of converted-shear modes relative to P-wave data.

In addition to S-wave data providing better resolution of geologic targets, we found S-wave images described reservoir heterogeneities that P-P data could not see. Specifically, a channel-like feature was imaged in the Tully-to-Tichenor interval by P-SV_1 data, and no indication of the feature existed in P-P data. This finding is important because this interval contains attractive sandstones that can be utilized as reservoirs for CO_2 sequestration. If units are considered for water-storage purposes, it is essential to know all heterogeneities internal to the unit to understand reservoir compartmentalization. We conclude it is essential that multicomponent seismic data be used whenever an Appalachian Basin operator is searching for potential CO_2 sequestration reservoirs.

All three data volumes (P-P, P-SV_1, and P-SV_2) showed linear folds existed in the Marcellus Shale. These fold trends were not observed in the stiff rocks above and below the Marcellus. The approximate east-west orientation of these folds agreed with the orientation of Marcellus fractures interpreted in borehole image logs acquired in the central-image calibration well. The consistent fold orientations across seismic image space imply Marcellus fracture properties should be reasonably consistent across the image area.

Isopach thicknesses of P-SV_2 and P-SV_1 images across the Marcellus were combined to estimate S-wave anisotropy within the Marcellus. This anisotropy attribute is important because it is a qualitative indicator of fracture intensity within a potential CO_2 sequestration interval. Seismic-based anisotropy values were small, of the order of 1 to 2 percent, which were the same values calculated from fast-S and slow-S modes measured with a dipole sonic log acquired in the central-image well.

Significant differences were observed between P-wave sequences and S-wave sequences in data windows interpreted to correspond to the Oriskany Sandstone, a popular unit considered for CO_2 sequestration. On the assumption that the P-P and P-SV images are correct, each seismic mode provides a distinct insight into reservoir compartmentalization. No deep-well data exist that allow P and S reflectivities to be analyzed for the Oriskany and its bounding rock units so that the validity of interpreted Oriskany sequence boundaries can be verified.

Technology Transfer and Products Developed

Chapter 10

Value of Study

Introduction

We conclude the research done in this study can have considerable impact on the direction multicomponent seismic technology proceeds in evaluating CO_2 sequestration systems. This view is summarized and documented in this closing chapter. Important principles emphasized by our research findings are:

- Simple, lower-cost, and widely used vertical-force seismic sources produce full-elastic wavefields,
- Elastic wavefield seismic stratigraphy provides more information about geological systems than does traditional single-component P-wave seismic stratigraphy, and
- When multicomponent seismic data are carefully acquired and processed, S-wave modes will often provide a better resolution of geologic targets than will P-wave seismic data.

The importance of these principles to the CO_2 sequestration community is both fundamental and significant. Viewpoints about the impacts and applications of our research findings follow.

Research Products and Technology Transfer

Patents

Four U.S. patents were written by the principal investigator and issued to the Board of Regents of the University of Texas during the period of this study. All of these patents deal with commercial applications of the principle that S-wave modes are produced directly at the point where a vertical-force seismic source applies its force vector to the earth. Even though the ideas for these patents originated before the start of this CO_2 sequestration study, the research findings achieved in this study supported the concepts of the patents and contributed important data examples that support the patent claims. We thus think it is appropriate to say that among the research products produced by this project are proofs of the validity of important seismic patents that will be commercialized by the University of Texas.

The university has established a company named VertiShear to commercialize the concepts claimed in these patents. This commercialization effort will be an important vehicle for technology transfer of research findings documented in this report

Public Data Base

The principal investigator was President of the Society of Exploration Geophysicists (SEG) during the final year of this project. During his presidency, the principal investigator established an SEG group named IQ Earth that has the objective of creating comprehensive digital databases across reservoir systems that will allow all disciplines involved in reservoir exploitation (geophysics, geology, engineering, petrophysics) to access the data, develop joint-discipline algorithms, share their ideas and developments with fellow researchers in all disciplines, and improve the quality of reservoir description and quantification. These data sets will be available through SEG to global researchers who wish to participate in developing IQ Earth technology and in sharing research results with colleagues in many countries. The principal investigator is working with DOE to communicate with all DOE-funded CO_2 sequestration researchers to transfer any public-domain data acquired with DOE funding into a database that will be maintained by the Society of Exploration Geophysicists for this IQ Earth project. This database effort is occurring only because of the project discussed in this report. Thus global access by a huge research community to DOE-produced CO_2 sequestration data sets is a product of this study and has the potential of being a huge technology transfer activity.

Publications

The principal investigator has also been instrumental in establishing a new peer-reviewed journal titled *Interpretation* at the Society of Exploration Geophysicists and sits on the Editorial Board. This journal will begin publication in mid-2013. No papers based on the research findings of this study have been published because all such papers are being held so they can be submitted to *Interpretation.* These paper submissions will occur after this project concludes. The principal investigator will work with DOE to contact principal investigators of all CO_2 sequestration studies funded by DOE to recruit additional manuscripts for this new journal. If these requests for case histories are successful, research products and technology transfer activities will expand beyond the boundaries of this study and will include products and publications produced by companion studies.

Impact of Research Findings

The research findings developed in this study impact CO_2 sequestration seismic technology in two important areas: (1) seismic data acquisition, and (2) geologic interpretation of seismic data.

Seismic Data Acquisition

When a decision is reached to acquire multicomponent seismic data across an onshore CO_2 sequestration area, traditional approaches are to do one of the following:

- Option 1: Use a commonly available vertical-force type of source (vertical vibrator, shot-hole explosive, or vertical impact) together with appropriate arrays of surface-positioned 3C sensors and record two wave modes – a P-P compressional wave mode and a P-SV converted shear mode.
- Option 2 : Use both a vertical-force source and a horizontal-force source (either a combination of vertical impact and inclined-impact sources or a combination of vertical vibrators and horizontal vibrators) together with appropriate surface arrays of 3C sensors and record a full-elastic wavefield. To most geophysicists, this option means acquiring three CMP modes, P-P, SH-SH, and SV-SV, and one converted-wave mode, the P-SV mode.

Option 2 is more expensive than Option 1 because of the necessity to use two types of sources to generate the required P and S wave modes. For this reason, most land-based multicomponent data acquisition involves Option 1. As a result, seismic interpreters have access to only converted-S (P-SV) shear modes and are penalized by not having access to CMP-based S-S wave modes created when S-waves are generated directly at each source station by horizontal-force sources.

The research accomplished in this study adds to evidence produced by our research team in previous studies over the past several years that demonstrates radial and transverse S-wave modes propagate directly from the point where a vertical-force source applies its force vector to the Earth. We are now convinced all of the wave modes listed in Option 2 can be acquired using only vertical-force seismic sources. Vertical-force sources are widespread, reasonably low cost, and all exploration-focused geophysicists are familiar with them. Perhaps more importantly, vertical-force sources can be used in a wider range of environments than can horizontal-force sources, which allows multicomponent seismic technology to be practiced in any CO_2 sequestration environment where standard P-wave seismic data can be utilized. For example, horizontal-force sources (horizontal vibrators or inclined impacts) cannot be deployed across swamps, marshes, dense timber, or rugged topography, but shot-hole explosives can. Thus not only do our research findings establish the concept that full-elastic seismic wavefields can be acquired with simpler, lower-cost sources than what have been traditionally used to acquire such data, but our findings also allow full-elastic wavefield data to be acquired across prospect areas where traditional horizontal-force sources cannot be used.

This research finding – that full-elastic wavefield data can be acquired with vertical-force sources - can have significant impact on the practice of the CO_2-sequestration seismic data-acquisition community and on the use of multicomponent seismic data in CO_2 sequestration applications.

Geological Interpretation of Seismic Data

Our research findings add to the evidence amassed by the Exploration Geophysics Laboratory at the Bureau of Economic Geology that elastic wavefield seismic stratigraphy is superior to common, single-component, P-wave seismic stratigraphy for extracting geological information from seismic data (Hardage, et al. 2006; Hardage, 2010b). Specifically, research documented in this project shows:

1. S-wave data often reveal depositional features that cannot be seen with P-P data (Fig.9.15).

2. Across some stratigraphic intervals, S-wave data have better vertical resolution of stratigraphic layering than do P-P data (Figs. 9.10, 9.12, and 9.26).

These two applications alone should convince seismic interpreters that there is great value in doing joint interpretations of P and S data. By combining P and S interpretations into an “elastic wavefield” seismic stratigraphy analysis, more information is created to define rock properties, fluid properties, depositional facies patterns, depositional sequence patterns, fracture orientation and intensity, and subtle faults across a prospect area.

A research finding that offers great potential is our evidence that previously unused seismic modes can be extracted from vertical-force wavefields and applied in geological interpretations. Specifically, these new seismic modes are the SR-SR (radial shear), ST-ST (transverse shear), and perhaps the SV-P (converted P) modes. The value of these previously unused wave modes is that each mode has a different reflectivity behavior at geologic interfaces than does its companion wave modes. As a result, any one of these shear modes can potentially reveal a rock property or fluid property that is difficult to see with its companion wave modes.

Applications to CO_2 Sequestration

Applications of our research findings to the CO_2 sequestration community can be quite important. We demonstrate that by applying multicomponent seismic technology to the evaluation of reservoirs and seals considered for CO_2 sequestration, the following benefits occur:

1. A large population of depositional features is revealed in stratigraphic intervals where potential CO_2-storage reservoirs could be located (Fig. 9.15 and 9.22). Some of these newly revealed depositional features can compartmentalize a reservoir and affect fluid movement within a reservoir system. The presence of an intra-compartment boundary can be a positive effect or a negative effect on sequestration efforts, depending on whether the facies change enhances or inhibits fluid flow. The important point is that it is essential to detect such depositional features, and across our study area, these intra-compartment heterogeneities could be detected with S-wave data but not with P-P seismic data (Fig. 9.15).

2. S-waves are much more responsive to the presence of fractures than are P-waves. Specifically, the polarization azimuth of the fast-S mode indicates fracture orientation. In addition, fast-S and slow-S seismic data can be combined to estimate S-wave anisotropy, and in this study, this seismic-based estimate of S-wave anisotropy had the same magnitude as S-wave anisotropy predicted by dipole-sonic log data. These S-wave anisotropy data are directly proportional to fracture intensity and provide a valuable fracture attribute for CO_2 reservoirs and seals that cannot be calculated from P-wave seismic data.

3. There is an increased resolution of shale-gas stratigraphy provided by P-SV seismic data relative to the resolution provided by P-P data. Across our study area, P-SV data provided approximately a 40-percent improvement in resolution of thin stratigraphic layering.

Conclusions

Research findings developed and documented in this study are significant. Several of our findings involving seismic modes emanating from vertical-force source stations address fundamental principles that will affect how future seismic data-acquisition will be done across CO_2 sequestration systems. Other findings add to the mounting evidence that elastic wavefield seismic stratigraphy should be practiced in reservoir characterization studies rather than traditional single-component P-wave seismic stratigraphy. Both of these impact areas are significant for evaluating CO_2 reservoir systems and have applications any study where it is essential to understand reservoir compartmentalization and to detect fluid-flow barriers.

References

Aki, K., and P.G. Richards, 1980, Quantitative seismology – theory and methods: W.H. Freeman and Co.

Alford, R.M., 1986, Shear data in the presence of azimuthal anisotropy: SEG Expanded Abstracts, 56th Annual Meeting, p. 476-479.

Alford, R.M., 1989, Multisource multireceiver method and system for geophysical exploration: U.S. patent 4,803,666.

Alkan, E., 2007, Multi-dimensional land seismic data acquisition techniques and random survey design: Master of Science Thesis in Geological Sciences, The University of Texas at Austin.

Alkan, E., and B. Hardage, 2007, Was that survey crew sober?: AAPG Explorer, v. 28, no. 10, p. 40-41.

Bruner, K., and D. Smosna, 1994, Porosity development in Devonian lithic sandstones of the Appalachian foreland basin: Northeastern Geology, v.16, p. 202-214.

Bruner, K., and Smosna, D., 2008. A trip through the Paleozoic of the Central Appalachian basin with emphasis on the Oriskany Sandstone, Middle Devonian shales, and Tuscarora Sandstone: Dominion Exploration and Production, INC

Castle, J.W., and A.P. Byrnes, 2005, Petrophysics of Lower Silurian sandstones and integration with the tectonostratigraphic framework, Appalachian Basin, United States: AAPG Bulletin, v. 89, p. 41-60.

DCNR (Pennsylvania Department of Conservation and Natural Resources), 2009a, Geologic carbon sequestration opportunities in Pennsylvania: Revision 1.1, 150 pages. http://www.dcnr.state.pa.us/info/carbon/reports-research.aspx.

DCNR (Pennsylvania Department of Conservation and Natural Resources), 2009b, Assessment of risk, legal issues, and insurance for geologic carbon sequestration in Pennsylvania: 401 pages. http://www.dcnr.state.pa.us/info/carbon/reports-research.aspx.

Diecchio, R.J., 1985, Regional controls of gas accumulation in Oriskany sandstone, Central Appalachian basin: AAPG Bulletin, v. 69, p. 722-732.

Hardage, B.A., M.M. Backus, M.V. DeAngelo, S. Fomel, K. Fouad, R.J. Graebner, P.E. Murray, R. Remington, and D. Sava, 2006, Elastic wavefield stratigraphy – an emerging seismic technology: Final Report, U.S. DOE Contract DE-PS26-02NT15375.

Hardage, B.A., 2009, Horizontal wave testing: AAPG Explorer, v. 30, no. 12, p. 26–27.

Hardage, B.A. 2010a, Vertical wave testing: AAPG Explorer, v. 31, no. 1, p. 32–33.

Hardage, B.A., 2010b, Elastic-wavefield seismic stratigraphy and reservoir characterization, *in* D.H. Johnston, ed., Methods and applications in reservoir geophysics, Chapter 6: The road ahead: SEG Investigations in Geophysics Series No. 15, p. 513-530.

Hardage, B.A., M.V. DeAngelo, P.E. Murray, and D. Sava, 2011, Multicomponent seismic technology: Geophysical References Series, No. 18, Society of Exploration Geophysicists, Tulsa, OK, 318 pages.

Harper, J.A., 1990. Leidy gas field, Clinton and Potter Counties, Pennsylvania, in Beaumont, E. and Foster, N.H., compilers Structural Traps I, Tectonic Fold Traps: AAPG Treatise of Petroleum Geology, Atlas of oil and gas Fields, p. 157-190.

Harper, J.A, 2005. An overview of carbon sequestration in Pennsylvania: wpweb2.tepper.cmu.edu/ceic/SeminarPDFs/Harper_CO2_Sequestration_4_28_05.pdf: Accessed October 8, 2011.

Harper J.A., and Kostelnik, J., 2010. The Marcellus Shale Play in Pennsylvania: Pennsylvania Department of Conservation and Natural Resources. http://www.marcellus.psu.edu/resources/publications.php Accessed October 15, 2011.

Harper, J.A., and D.G. Patchen, 1996, Play Dos (Devonian updip stratigraphic pinchout), the Lower Devonian Oriskany Sandstone structural play, in Roen, J.B. and Walker, B.J. (eds), The atlas of major Appalachian gas plays: West Virginia Geologic and Economic Survey Publication, v. 25, p. 118-125.

Harper, J.A., 2008, The Marcellus Shale – an old “new” gas reservoir in Pennsylvania: Pennsylvania Geology, Pennsylvania Bureau of Topographic and Economic Survey, v. 38, no. 1, p. 2-13.

Harper, J.A., 2011, An introduction to carbon sequestration – what’s being done in Pennsylvania: http://www.pbi.org/resources/rxtras/6364_ELF/Harper.pdf.

Kostelnik, J., and K.M. Carter, 2009a, The Oriskany Sandstone updip permeability pinchout: A receipe for gas production in northwestern Pennsylvania: Pennsylvania Geology, v. 39, no.4. p. 19-34.

Kostelnik, J., and K.M. Carter, 2009b, Unraveling the stratigraphy of the Oriskany Sandstone: A necessity in assessing its site-specific carbon sequestration potential: Environmental Geosciences, v. 16, no.4, p. 187-200.

Lash, G.C., 2007, Influence of basin dynamics on Upper Devonian Black Shale deposition, western New York state and northwest Pennsylvania: AAPG Search and Discovery Article #30050 (2007).

Laughrey, C.D., D.A. Billman, and M.R. Canich, 2004, Petroleum geology and geochemistry of the Council Run gas field, north central Pennsylvania: AAPG Bulletin, v. 88, p. 213-239.

Levin, F., 1979, Seismic velocities in transversely isotropic media I: Geophysics, v. 44, p. 918-936.

Levin, F., 1980, Seismic velocities in transversely isotropic media II: Geophysics, v. 45, p. 3-17.

Miall, A.D., and R.C. Blakely, 2009, The Phanerozoic tectonic and sedimentary evolution of North America in Miall, A.D. (ed) Sedimentary Basins of the World, Vol. 5, Chapter 1, p.1-28.

Milici, R.C., and Swezey, C.S., 2006. Assessment of Appalachian Basin oil and gas resources: Devonian shale- Middle and Upper Paleozoic total petroleum system: USGS Open File Report 2996-1237, 70p.

Nyahay, R., Leone, J., Smith, L.B., Martin, J.P., and Jarvie, D.J., 2007, Update on regional assessment of gas potential in the Devonian Marcellus and Ordovician Utica shales of New York: AAPG Search and Discovery Article 10136 (posted October 1, 2007 after presentation at the 2007 AAPG Eastern Section Meeting September 16-17, 2007, Lexington, KY).

Opritza, S.T., 1996, Lower Devonian Oriskany sandstone updip permeability pinch-out, in J.B. Roen and B.J. Walker, eds., The atlas of major Appalachian gas plays: West Virginia Geological and Economic Survey Publication, 25, p. 126-129.

Patchen, D.G., and J.A. Harper, 1996, The Lower Devonian sandstone combination traps play, in J.B. Roen and B.J. Walker, eds., The atlas of major Appalachian gas plays: West Virginia Geological and Economic Survey Publication, 25, p. 118-125.

Roen, J.B., and B.J. Walker, 1996, The atlas of major Appalachian gas plays: West Virginia Geologic and Economic Survey Publication, V. 25, 201 pages.

Rowan, E.L. J.E. Repetski, and R.T. Ryder, 2008, [Abstract] Evidence for paleo-fluid flow westward from the Appalachian basin: AAPG Eastern Section Meeting, Pittsburgh.

Sager, M. 2007. Petrologic study of the Murrysville sandstone in southwestern Pennsylvania. Unpublished Masters Thesis West Virginia University 1451665, 99 pages.

Skeen, J.C., 2010, Basin analysis and aqueous chemistry of fluids in the Oriskany Sandstone, Appalachian Basin, USA: Thesis submitted to Eberly College of Arts and Sciences, West Virginia University, 109 pages.

Smosna, R., and M.L. Sager, 2008, [Abstract] The making of a high-porosity, high-permeability reservoir - the Murrysville Sandstone of Pennsylvania: AAPG Eastern Section Meeting, Pittsburgh.

U.S. Department of Energy, 2008, 2008 carbon sequestration atlas of the United States and Canada, Second edition, 140 pages.

Wood, L., 2004a, Removal of noise from seismic data using improved Radon transforms: U.S. Patent 6,691,039 B1.

Wood, L., 2004b, Removal of noise from seismic data using improved tau-p filters: U.S. Patent 6,721,662 B1.

Zeng, H., 2001, From seismic stratigraphy to seismic sedimentology – a sensible transition: Gulf Coast Assoc Geol. Soc. Trans. v. 51, p. 412-420.

Zeng, H., 2006, Stratal slicing makes seismic imaging of depositional systems easier: AAPG Explorer, v. 27, no. 6, p. 26-27.

Glossary

3C3D: 3-component and 3-dimensional.

a: Crack radius

α: aspect ratio of cracks (ratio of short and long axes of a crack)

ANISO: magnitude of S-wave velocity anisotropy. Calculation procedure is defined by Equation 4.1.

anisotropy: a rock property that causes the magnitude of wave mode velocity, particularly the velocity of an S mode, to vary with direction of propagation. A more explicit term **azimuthal anisotropy** is used when wave-mode velocity varies with azimuth. Azimuthal anisotropy is important for detecting and quantifying fractured intervals.

asymptotic bin: a CCP stacking bin for a converted-mode (e.g. a P-SV mode) positioned at X-Y coordinates that do not vary as imaging depth increases. For shallow interfaces, the X-Y coordinates of a CCP vary rapidly with depth. Asymptotic bins appear in the deeper portion of seismic image space.

AVAZ: amplitude versus angle and azimuth

C: elastic stiffness tensor

C_{ij}^0: components of isotropic elastic-stiffness tensor

C_{ij}^1, C_{ij}^2: first-order and second-order corrections of elastic-stiffness tensor

CCP: common-conversion point. A point in the subsurface where a downgoing wave mode propagating with velocity V1 converts to an upgoing wave mode that propagates with a different velocity V2. See **CMP**. For a **P-SV** mode, a CCP coordinate for a given source-receiver pair is closer to the receiver station than to the source station. For an **SV-P** mode, the CCP is closer to the source station.

chronostratigraphic surface: a rock surface representing a fixed geologic time. Seismic reflections are assumed to follow chronostratigraphic surfaces. See **stratal surface**.

CMP: common midpoint. A point in the subsurface where a downgoing wave mode propagating with velocity V1 converts to an upgoing wave mode that propagates with the same velocity V1. In an Earth having flat horizontal layers, this reflection point is half way between a source and a receiver, hence the term "midpoint". See **CCP**.

crossline: the direction perpendicular to receiver lines. See **inline**.

e: fracture density

FD: fracture density

FK: a data space defined in terms of frequency versus wavenumber. A forward FK transform converts seismic data from the time-space domain to the frequency-wavenumber domain. An inverse FK transform converts data from the frequency-wavenumber data domain to the time-space domain. In FK data space, seismic modes are defined in terms of their frequency content and their propagation velocity. Wave mode propagation velocity V is given by V = F/K, the slope of a wave mode's energy trend in FK data space.

$\gamma^{(S)}$: vertical shear-wave splitting parameter

GR: gamma-ray log

horizontal transverse isotropy: a seismic propagation medium in which rock properties are isotropic in a direction perpendicular to a horizontal axis of symmetry. Such a medium describes a system of parallel, vertical fractures in a thick uniform layer. See **HTI** and **vertical transverse isotropy**.

HTI: horizontal transverse isotropy.

inline: the direction in which a receiver line is deployed. See **crossline**.

Love wave: a surface wave that propagates across the Earth-air interface with a particle-displacement vector that is: (1) parallel to the Earth surface, and (2) perpendicular to the direction the wave is moving. This particle displacement is an **SH** displacement, and this type of surface wave can be produced only by an **SH** source. Wave motion is confined to the Earth surface. A Love wave does not propagate into the Earth as a body wave. See **Rayleigh wave**.

MEMS: micro-electronic mechanical system. A solid state accelerometer concept used to acquire 3C seismic data.

MRCSP: Midwest Regional Carbon Sequestration Partnership.

N1: natural coordinate axis 1.

N2: natural coordinate axis 2.

natural coordinate axes: a data coordinate system within the Earth with its axes oriented in the directions of the natural anisotropy axes existing in the Earth's rock system. As S waves propagate in the Earth, their polarization directions adjust to be aligned with natural coordinate axes **N1** and **N2**.

N/V: number of cracks per unit volume

offset: the horizontal, straight-line distance between a seismic source and a seismic sensor.

orthorhombic: a seismic propagation medium consisting of thin-bed layering and (1) one set of parallel fractures normal to bedding, or (2) two sets of orthogonal fractures normal to bedding. An orthorhombic medium has three symmetry planes – one plane parallel to bedding, one plane normal to bedding and parallel to fractures, and the third normal to bedding and perpendicular to fractures.

Φ: porosity

P-P: conventional P-wave seismic data; P-wave down and P-wave up.

proportional slicing: the process of dividing a seismic interval into a series of surfaces that each follow a fixed geologic time. See **stratal slicing**.

P-SV: converted-shear data; P-wave down and SV-wave up. See **SV-P**.

P-wave: compressional wave

radial: the straight line direction from a source station to a receiver station. See **transverse**.

radial-shear: a shear displacement in the vertical plane passing through a source station and a receiver station. Also called **radial-S**, **SR**, or **SV**. See **transverse-shear**.

random geometry: a seismic data-acquisition geometry in which the distances and azimuths between receiver stations and source stations differ in a random manner across a data-acquisition grid. See **regular geometry**.

Rayleigh wave: A wave that travels along the Earth-air interface and produces both vertical and inline-radial displacement as it propagates. The resulting particle displacement motion is elliptical with the ellipse tilted toward the source point where the wave originated. This type of surface wave is produced by vertical-displacement sources. Wave motion is confined to the Earth surface, and a Rayleigh wave does not propagate into the Earth as a body wave. See **Love wave**.

regular geometry: a seismic data-acquisition geometry in which source and receiver lines occur at consistent spacings and source-station and receiver-station positions along these lines occur at consistent intervals. See **random geometry**.

S_1: fast S mode. In a fractured medium, an S_1 mode is polarized parallel to aligned fracture planes. In a stress field, S_1 is polarized parallel to maximum horizontal stress.

S_2: slow S mode. In a fractured medium, an S_2 mode is polarized perpendicular to aligned fracture planes. In a stress field, S_2 is polarized perpendicular to maximum horizontal stress.

sagital plane: a plane passing through a source station, a receiver station, and a reflection point produced by a wave mode propagating between that source and receiver.

seed horizon: a high-quality, high confidence chronostratigraphic surface interpreted across a 3D seismic volume

S-S: S-wave seismic data involving a downgoing S mode and the same upgoing S mode, where S can be **SH**, **SR**, **SV**, or **ST**.

S-wave: shear wave.

SH: shear mode having a horizontal displacement vector. See **ST** and **transverse-shear**.

SR: shear mode having a radial displacement vector. See **SV** and **radial-shear**.

ST: shear mode having a transverse displacement vector. See **SH** and **transverse-shear**.

stratal slicing: the process of creating a seismic horizon that follows a fixed geologic time. See **proportional slicing**.

stratal surface: a surface that follows a fixed geologic time. See **chronostratigraphic surface**.

SV: shear mode having a vertical displacement vector. See **SR** and **radial-shear**.

SV-P: converted P mode. SV-wave down and P-wave up. See **P-SV**.

transverse: the direction perpendicular to the vertical plane passing between a source station and a receiver station. See **radial**.

transverse-shear: shear displacement perpendicular to the vertical plane passing through a source station and a receiver station. Also called **transverse-S**, **ST**, or **SH**.

vertical transverse isotropy: a seismic propagation medium in which rock properties are isotropic in a direction perpendicular to a vertical axis of symmetry. Such a medium describes a system of stacked thin beds. See **VTI** and **horizontal transverse isotropy**.

VSP: vertical seismic profile.

VSX: an accelerated-weight seismic source patented by Vecta Technology and manufactured by United Service Alliance.

VTI: vertical transverse isotropy.

Acknowledgments

The seismic equipment tests done at the Devine Test Site could not have been done without the assistance of many sponsors of the Exploration Geophysics Laboratory. Mitcham Industries provided the MaxiWave system used for the vertical receiver array, as well as surface-based 3C geophones and DSU3 solid state MEMS sensors, a recording truck, and field technicians. Halliburton provided wireline services and engineers. Dawson Geophysical provided vibrators, support personnel, and transportation for other sources. Sercel provided a 428 recorder, supporting engineers, and EUnite cable-free boxes. Seismic Source and i-Seis combined to provide Sigma cable-free boxes, a Universal Encorder, and engineering staff. Austin Powder provided explosives and a licensed shooter. United Services Alliance and Vecta Technology provided their accelerated-weight (nitrogen spring) impact source and source operators. OyoGeospace provided a variety of special geophones, GSR cable-free boxes, and field personnel.

Neither could this study have been done without Geophysical Pursuit and Geokinetics providing access to their 3C3D seismic data in Bradford County, Pennsylvania. Proper analysis of these multicomponent seismic data was possible because Chesapeake Energy allowed access to log data acquired in a well they drilled inside this 3C3D seismic grid, and because Chesapeake and their partners, Anadarko Exploration, Statoil, and Southwestern Energy provided access to vertical seismic profile data acquired in this calibration well.

Our interpretations of the P-P and P-SV seismic data volumes were done with Landmark software. The seismic profiles, attribute maps, and synthetic seismogram calibrations displayed throughout this report are Landmark products. We at the Bureau of Economic Geology are indebted to Landmark for providing software licenses that allow students and academic research staff to do these types of investigations.